Università degli Studi di Firenze
Scuola di Ingegneria
DIEF - Department of Industrial Engineering of Florence

PhD School: *Energetica e Tecnologie Industriali ed Ambientali Innovative*
Scientific Area: ING-IND/09 - *Sistemi per l'Energia e l'Ambiente*

Combustion-Turbine Interaction in modern gas turbines: analysis and modelling of aerothermal phenomena

PhD Candidate: Ing. Stella Grazia Tomasello

Tutor: Prof. Ing. Antonio Andreini

Co-Tutor: Prof. Ing. Bruno Facchini

PhD School Coordinator: Prof. Ing. Giovanni Ferrara

XXXVI PhD School Cycle - 2020-2023

A mio papà Antonio,
A mia mamma Maria,
Al mio amore Lorenzo

Per un attimo vidi una pistola a terra, pensai di raccoglierla.
Ma non lo feci. Capii che io non ero come il mio assassino.
Da allora sono diventata donna libera e di pace.
- L. Segre

E l'amore ha l'amore come solo argomento
e il tumulto del cielo ha sbagliato momento.
- F. De André, Dolcenera

She teaches me that the world is made to be pounced on and enjoyed, and that there is absolutely no reason at all to hold back.
- A. Ernaux, A frozen woman

I solemnly swear that I am up to no good.
- J.K. Rowling, Harry Potter and the Prisoner of Azkaban

Acknowledgements

È arrivato infine la conclusione di questo percorso di dottorato. Sono sicuramente stati tre anni impegnativi, con qualche alto e basso, ma anche molto stimolanti. Credo che l'esperienza del dottorato sia unica nel suo genere e che raramente si riesca ad imparare così tanto in così poco tempo. Quello che personalmente ho imparato in questa avventura è che, seppur con fatica e con tempo, ogni difficoltà che può apparire insormontabile può essere superata, anche con l'umiltà di chiedere consiglio quando necessario.

Vorrei prima di tutto, ringraziare il Prof. Antonio Andreini, per essere stata una guida impareggiabile durante questi anni. Grazie per tutto quello che mi hai insegnato. Grazie per avermi offerto questa opportunità e questa occasione unica di fare ricerca su un argomento così attuale dal punto di vista scientifico. Grazie anche al Prof. Facchini, che, oltre ad essere un riferimento dal punto di vista professionale, ha sempre incoraggiato i suoi dottorandi quando necessario con grande empatia.

Vorrei ringraziare anche i miei ormai colleghi in Baker Hughes: grazie a Simone Cubeda, Luca Andrei e Vittorio Michelassi, per avermi fornito suggerimenti validissimi durante le attività di collaborazione. Un ringraziamento speciale anche a Roberto Meloni, che non mi ha mai negato un consiglio e un confronto in tre anni. Ho imparato tantissimo lavorando insieme durante questi anni. Grazie per tutto quello che mi hai insegnato!

Vorrei anche ringraziare Tommaso Diurno, prima collega di PhD e ora

collega nel reparto TUVA di Baker Hughes, che mi ha sempre incoraggiato durante questi mesi. Grazie per i tuoi consigli, sia lavorativi che non, e soprattutto grazie per la tua allegria e la tua positività, sei il miglior buddy del globo e grande genio supremo del vapore! Un ringraziamento particolare anche al mio manager, Damaso Checcacci, per aver creduto in me e avermi offerto un'opportunità irripetibile.

Un ringraziamento a tutto il gruppo HTC, sia ai vecchi membri che nuovi. È stato un onore e un piacere condividere con voi questa esperienza di dottorato! Un ringraziamento particolare a Tommaso Fondelli, Sabrina Giuntini, Matteo Poggiali, Pier Carlo Nassini, Daniele Pampaloni, Alberto Amerini, Leonardo Langone, appartenenti alla vecchia guardia, che mi hanno accolto appena arrivata. Ringrazio anche tutti i ragazzi del THT Lab, con cui ho lavorato fianco a fianco. Grazie soprattutto a Tommaso Bacci, non solo per i dati sperimentali che mi ha condiviso per validare la CFD, ma soprattutto per le opinioni e i consigli che mi ha dato durante tutti questi anni. Grazie, perché ho imparato tantissimo lavorando con te!

Infine, un ringraziamento a tutti i miei amici, sia di sempre che nuovi che siete sempre presenti nella mia vita.
Grazie a Sofia Brocchi, per aver condiviso con me un pezzo del percorso di dottorato e per essere diventata, oltre che una collega, anche una amica. Grazie per esserci stata in questi mesi.
Grazie a Sara Rizzi, per la sua recente amicizia e la sua presenza. Sono felice che le turbine a vapore ci abbiano fatto incontrare! Sono sicura che riuscirai a realizzare tutti i tuoi sogni!
Grazie a Sofia Panzera, amica milanese, compagna di letture con cui è sempre bello "spill the tea" su personaggi immaginari o su gente che nemmeno conosciamo. Non vedo l'ora di tornare a Milano per poterci riabbracciare, andare insieme alla bancarella dei libri scontati e fare i raid su Pokémon GO in piazza Duomo! Nel frattempo, mi godo il nostro esclusivissimo club del libro, dal ritmo serratissimo, tramite il quale, tra una pagina e l'altra di un libro, ho la sensazione di abitare a soli cento

metri di distanza da te.
Grazie a Costanza Naldi, una compagna (e ora anche collega) ormai di lunga data, alleata di una vita nella ricerca di segnalibri (per me beni palesemente introvabili) nei luoghi più remoti del globo. Grazie per i tuoi consigli, non solo di lettura, ma soprattutto di vita. Grazie per avermi sempre detto con sincerità quello che pensavi ed essere stata presente sempre in questi anni. Sono fiera di essere la tua testimone di nozze!
Grazie a Mariagiulia Rainoni (Raiiiiinoni cit.): sei la mia fonte più genuina di risate. Non vedo l'ora di incontrarci per i nostri periodici "update" per ridere a crepapelle sulle nostre disgrazie (mai su quelle degli altri!). Sei l'unica incosciente con cui potevo fare la pazzia Palazzo Vecchio – Scandicci a piedi per "fare due passi dopo cena". Non vedo l'ora di viverne tante altre insieme (in assenza di piccioni spero)! Penso che la nostra prossima meta sarà la Basilica Santuario di Maria Santissima del Carmine Maggiore (NA), come alternativa economica a Lourdes, che dici?
Grazie a Cristina Ignesti: sono tanto felice che la vita di adulta mi abbia fatto incontrare te. Abbiamo condiviso non solo mete di viaggio indimenticabili come i fiordi norvegesi o New York, ma soprattutto condividiamo passioni e obbiettivi di vita. Le nostre chiacchere quotidiane e update disparati su vita, lavoro, make-up, cucina e gatti mi rallegrano sempre tutte le giornate. Sono tanto felice che tu sia nella mia vita. Non vedo l'ora tu e Francesco possiate venire a vivere vicino a noi così da poterci vedere con maggiore regolarità!
Grazie a Francesca Focardi, nota come Fofo (soprannome che ho inventato io, vorrei precisare anche in questa sede, contrariamente a quanto affermavano malvagiamente i miei nemici 25 anni fa. È una mia proprietà intellettuale che rivendico con ardore. Marchio registrato dal 1999): sei la persona su cui posso sempre contare, l'unica persona a cui non ho mai nascosto niente. Quando sono con te, mi sento a casa. Grazie per dirmi sempre quello che pensi, anche quando fa male. Che per me sei una sorella lo sai, non esistono parole che possano esprimere quanto ti voglia bene. Grazie per la tua amicizia, i tuoi consigli sinceri, le nostre cene a base di sushi e le nostre uscite (che son sempre troppo poche e troppo

corte per aggiornarci come si deve su gatti, cibo, auto e fogli di giornale). Non vedo l'ora di scoprire quali avventure - marine e non - ci attendono! L'unica cosa di cui sono certa è che, ovunque ci porterà il nostro lavoro e le nostre scelte, saremo insieme.

Grazie infine ai miei genitori, che hanno fatto enormi sacrifici per farmi studiare. Ho fatto del mio meglio per rendervi orgogliosi. Grazie per avermi fatto sentire amata e al sicuro. Grazie per avermi lasciato libera di prendere le mie scelte, sin da bambina. Grazie a mio papà Antonio, per il suo ottimismo, qualità di cui purtroppo faccio difetto. Grazie per avermi trasmesso la passione per la storia, per la musica e aver investito tante ore del suo tempo libero per cucinarmi i miei piatti preferiti. Grazie a mia mamma Maria, per avermi reso una donna indipendente e decisa (forse un goccio troppo decisa). Grazie per avermi trasmesso l'amore per la lettura, la passione più grande della mia vita. I nostri momenti insieme a leggere sul divano, condividendo la stessa coperta, sono tra i ricordi più belli della mia infanzia. Sono proprio questi, i ricordi della mia infanzia, i raggi di sole che rischiarono le giornate più cupe strappandomi sempre un sorriso, quando sono triste.
Un ringraziamento doveroso anche alla mia ormai seconda famiglia: Eleonora, Luana, Angelo, zia Mari, zia Angela e zio Patrizio. Grazie per avermi sempre fatta sentire accolta, fin dal primo momento. Grazie per i vostri incoraggiamenti durante questi anni e per tutto quello che avete fatto per noi, aiutandoci in ogni modo possibile. Quando penso alla parola "famiglia", non posso che includervi nella definizione.

Grazie infine a Lorenzo: questi anni insieme sono stati i più belli della mia vita, insieme a quelli della mia infanzia. Nonostante le varie difficoltà e problemi di questi anni, quando penso a te, non riesco che pensare tutte le cose belle che abbiamo vissuto insieme. Grazie per questi anni di studio insieme, sia di università che di dottorato. Non sarebbero stati lo stesso senza di te. Grazie per i nostri viaggi in giro per l'Europa (e a breve per il mondo), i nostri viaggi in macchina in compagnia dello stesso audiolibro,

le nostre gare a chi trovava prima il pezzo del puzzle mancante, le nostre serate sul divano a guardare un film noiosissimo – scelto da te – o un film di animazione divertentissimo – scelto da me. Grazie per la nostra vita insieme in Olanda: la nostra casina a Schiedam – con quelle scale pericolossisime (per chi mi legge: ragazzi, son viva per miracolo), il ramen di Saito, la varietà di papere che popolano i canali, il nostro ristorante al mulino, i tulipani che ci regalavano sempre al supermercato, il nostro parco preferito – dove ci piaceva leggere distesi su un telo ascoltando il suono del vento tra le foglie, la mensa a forma di navicella spaziale di TU Delft, i colori dei quadri di Van Gogh, i film americani sottotitolati in olandese, il nostro supermercato Albert Heijn, la piazza principale di Delft, i mercatini di Haarleem, i ristoranti etnici (quel messicano!) di Rotterdam, le spiagge di Den Haag, i nostri negozi preferiti di Amsterdam, le olie bollen assaggiate a Dordrecht, il giorno del Re e tutti quei dolcetti arancioni limited edition. Grazie per le tue risate, la tua allegria e il tuo entusiasmo verso la vita. Grazie per chiedermi sempre come sia stata la mia giornata, anche quando hai gli occhi socchiusi dal sonno. Grazie per la tua resilienza e la tua perseveranza. Grazie per avere sempre la forza di contrastarmi, so di essere un avversario sempre molto ostinato. Grazie per rimanere sempre in campo, anche quando il gioco si fa duro. Grazie per avermi insegnato che si impara qualcosa sempre, anche quando si pensa di aver perso. Grazie per la tua dolcezza, la tua delicatezza e la tua sensibilità, qualità non comuni, che ti rendono una persona di una empatia unica. Grazie per condividere ogni mio sogno e non veder l'ora di vederlo realizzato con me al tuo fianco. Chiunque ti abbia conosciuto - a parte qualcuno che non ha evidentemente buon gusto - non può che constatare che anima pura e limpida tu sia. Non posso prometterti che la nostra vita sarà sempre facile e senza difficoltà, ma ti prometto che sarà piena di risate e di momenti indimenticabili passati con le nostre famiglie e con i nostri amici. Ma soprattutto, ti prometto che sarà insieme.

Abstract

Combustion–turbine interaction phenomena are attracting ever-growing interest in recent years. In fact, a complex and unsteady flow field, characterized by a high level of turbulence and temperature distortions, usually can be found at the interface plane between the two hot gas path components, especially with the implementation of lean-burn combustors that allow the reduction of NO_x emissions, but at the cost of requiring highly swirled and turbulent flows to stabilize the flame. Such severe conditions at the inlet of the first stage nozzle can have a potential impact on the performance of the component, resulting into a perturbation of the heat transfer, the aerodynamics and the effectiveness of the cooling system. For this reason, a better understanding of the physical processes related to the combustor-turbine interaction nozzle becomes a mandatory step for a reliable the aerothermal design.

The main objective of this work is to study the behaviour of film cooling system and the heat loads on the first stage nozzle in lab-scaled and engine-like conditions.

Firstly, an annular sector rig, made by a non-reactive, trisector combustor simulator and nozzle cascade, where both adiabatic effectiveness and HTC measurements had been carried out, is investigated by performing a systematic computational study by using RANS and SBES. The comparison between numerical predictions and the available experimental results is exploited to assess the capability of advanced scale-resolving methods in the characterization of the mutual combustor-turbine interaction, along with the heat transfer coefficient and film-cooling system behavior. This

evaluation aims thus to assess if such more advanced and more time-consuming methods than RANS, including also turbulence models able to capture the transition, can be more reliably used for a proper prediction of the vane thermal loads.
Then, a fully integrated combustor-nozzle configuration is investigated by using SBES, along with a realistic turbine nozzle cooling system, under realistic engine-like operating conditions. Decoupled RANS/SBES simulations of the stand-alone NGV are also reported to highlight the risks and uncertainties associated with carrying out decoupled simulations. The aim is to evaluate the influence of the combustor's presence under realistic operating conditions and a realistic annular geometry. Then, the focus is shifted to the generation and application of highly representative and reliable boundary conditions at the inlet of the first-stage nozzle in order to enable the separate study of the two components by conducting decoupled simulations. To do so, several SBES decoupled simulations of the stand-alone NGV are carried out by applying two-dimensional unsteady boundary conditions extracted from the fully integrated combustor-NGV SBES simulation. Additionally, the POD technique is applied, considering three different numbers of POD modes, corresponding to a descending level of energy content relative to the total energy of the flow. In this way, the proper coherent structures of turbulent flows are identified and the complexity of the dynamics of a system is reduced, just taking into account the most important modes.
Finally, the research focuses on the prediction of heat loads in engine-like conditions by simulating a single set of uncooled vanes. The main objective of these analyses is to obtain a scaling criterion for the HTC obtained in lab-scaled conditions in order to obtain representative HTC values in engine-like conditions. In fact, when the engine operates in realistic conditions at full speed and full load, direct experimental measurements are not available and therefore the introduction of a scaling criterion becomes necessary.
The present study demonstrates the importance of accurately capture the mutual combustor-turbine interaction, by employing advanced scale-

resolving methods such as SBES calculations, for a reliable aerothermal design of the first stage nozzle also under representative and realistic engine-like operating conditions. To the author's knowledge, a very limited number of studies have been carried out with this kind of EXP-CFD benchmarking, due to the very limited amount of experimental data under representative combustor outflow conditions. In this context, to author's knowledge, this research represents also one of the few study present in literature in studying the impact of the combustor-turbine interaction phenomena on the aerodynamics and thermal fields, including a realistic turbine nozzle cooling system, with realistic inlet conditions representative of the engine marching at full speed and full load.

Contents

Nomenclature

Acronyms

ASC	Axially Staged Combustor
$ACARE$	Advisory Council for Aeronautics Research in Europe
BCs	Boundary Conditions
BL	Boundary Layer
BR	Blowing Ratio
CC	Combustion Chamber
CFD	Computational Fluid Dynamics
CRZ	Central Recirculation Zone
$CTRZ$	Central Turbulent Recirculation Zone
CVP	Counter-rotating Vortex Pair
DAC	Double Annular Combustor
$DDMA$	Data-Driven Modal Analysis
DES	Detached Eddy Simulation
DoE	Design of Experiment
DR	Density Ratio
DFT	Discrete Fourier Transform
EEA	European Environment Agency
EXP	Experiments
$FACTOR$	Full Aerothermal Combustor-Turbine interactiOns Research
$FEET$	First Engine To Test

FTT	Flow Through Time
GE	General Electric
$GEnx$	General Electric next-generation
GMF	Global Market Forecast
GTs	Gas Turbines
HPT	High Pressure Turbine
HS	Hot Streak
HTC	Heat Transfer Coefficient
I	Momentum Ratio
IR	InfraRed
LDI	Lean Direct Injection
LE	Leading Edge
LPP	Lean Premixed Prevaporized
$LOTDF$	Local Overall Temperature Distribution Factor
$LRTDF$	Local Radial Temperature Distribution Factor
$NASA$	National Aeronautics and Space Administration
NGV	Nozzle Guide Vane
OPR	Overall Pressure Ratio
$OTDF$	Overall Temperature Distribution Factor
PA	Passage
PDF	Probability Density Function
$PEEK$	Polyether Ether Ketone
$PERM$	Partially Evaporated and Rapid Mixing
PIV	Particle Image Velocimetry
POD	Proper Orthogonal Decomposition
$PODFS$	Proper Orthogonal Decomposition and Fourier Series
PS	Pressure Side
PSP	Pressure Sensitive Paint
PVC	Processing Vortex Core

$RANS$	Reynolds Averaged Navier-Stokes
RMS	Root Mean Square
ROM	Reduce Order Model
$RPKs$	Revenue Passenger Kilometers
RQL	Rich Quench Lean
$RTDF$	Radial Temperature Distribution Factor
SAS	Scale-Adaptive Simulation
$SBES$	Stress-Blended Eddy Simulation
SGS	Sub-Grid Scale
$SPOD$	Spectral Proper Orthogonal Decomposition
SS	Suction Side
SST	Shear-Stress Transport
$S1N$	First Stage Nozzle
$URANS$	Unsteady Reynolds Averaged Navier-Stokes
$STech$	Smart Technologies
$TAPS$	Twin Annular Premixing Swirler
TE	Trailing Edge
$THTLab$	Laboratory of Technology for High Temperature
TIT	Turbine Inlet Temperature
TNH	Normalized High Pressure Turbine speed
TNL	Normalized Low Pressure turbine speed
VB	Vortex Breakdown
VR	Velocity Ratio

Greeks

α	Local cell volume	$[m^2 \cdot s^{-1}]$
Γ_k	Efficiency function	$[-]$
δ_l^0	Laminar flame front thickness	$[m]$
Δ	Local cell volume	$[m^3]$
ε	Turbulence dissipation rate	$[m^2 s^{-3}]$

η	Adiabatic effectiveness	$[-]$
θ	Non-dimensional vane pitch	$[-]$
λ	Lagrangian Multiplier	$[-]$
μ	Dynamic viscosity	$[Pa \cdot s]$
ρ	Density	$[kg \cdot m^3]$
Σ	Matrix of eigenvalues of the data correlation matrix	$[-]$
σ_r	Eigenvalues of the data correlation matrix	$[-]$
τ_{ij}	sub-grid stress tensor	$[kg \cdot m^{-1} \cdot s^{-2}]$
Φ	Matrix of POD spatial distributions	$[-]$
ϕ_r	Spatial distribution of POD mode	$[-]$
Ψ	Matrix of eigenvectors of the correlation matrix	$[-]$
ψ	Heat loss	$[J \cdot s^{-1}]$
ψ_r	Matrix of eigenvectors of the correlation	$[-]$
ω	Specific dissipation rate	$[s^{-1}]$
$\bar{\dot{\omega}}_c$	Source term progress variable	$[-]$

Letters

a	Strain rate (combustion)	$[s^{-1}]$
c	Progress variable	$[-]$
C	Constant Coefficient	$[-]$
C_{ax}	Axial Chord	$[m]$
C_d	Discharge coefficient	$[-]$
C_p	Pressure Coefficient	$[-]$
c_r	Coefficient (POD)	$[-]$
C_s	Smagorinsky constant	$[-]$
D	Diameter	$[m]$
$D(x,t)$	Original collection of measurements in space and time (POD)	$[-]$
D_0	Time-averaged solution (POD)	$[-]$
$\tilde{D}_k$	k-th POD mode	$[-]$

f_{SBES}	Shielding function SBES	$[-]$
h	height	$[m]$
H	span	$[m]$
l_s	SGS mixing length	$[m]$
l_t	Turbulent lenght scale	$[m]$
k	Thermal conductivity, Turbulent kinetic energy	$[kg \cdot m \cdot s^{-3} \cdot K^{-1}]$,$[m^2 \cdot s^{-2}]$
K	Temporal correlation matrix (POD)	$[-]$
$\dot{m}$	Mass flow rate	$[kg/s]$
$M(x,t)$	Linear Combination of Modes (POD)	$[-]$
Ma	Mach number	$[-]$
n	Flame front normal vector	$[-]$
n_s	Spatial points	$[-]$
n_t	Time points	$[-]$
Nu	Nusselt number	$[-]$
p	Pressure	$[Pa]$
p_{NGV}	Angular NGV-pitch ratio	$[deg]$
Pr	Prandlt number	$[-]$
q	Heat Flux	$[W \cdot m^{-2}]$
r	Radius	$[m]$
Re	Reynolds number	$[-]$
S	Local strain rate magnitude	$[s^{-1}]$
s	Non-dimensional curvilinear abscissa	$[-]$
S_c	Laminar flame speed	$[m \cdot s^{-1}]$
S_t	Turbulent flame speed	$[m \cdot s^{-1}]$
t	Tangential angle	$[deg]$
t_s	Time step	$[s]$
T	Temperature	$[K]$
U, V	Velocity	$[m \cdot s^{-1}]$
$y+$	Dimensionless wall distance	$[-]$
Z	Mixture fraction	$[-]$

Subscripts

ad	Adiabatic
aw	Adiabatic wall
$avg, mean$	Average value
ax	Axial
b	Blade
$c, coolant$	Coolant
D	Diameter
$engine$	Engine-like conditions
g	Gas
$inlet$	Ingress value
lab	Test rig conditions
$local$	Local conditions
$main$	Main Flow
max	Maximum
min	Minimum
nd	Non Dimensional
$nuggets$	Nuggets
$outlet$	Exit value
r	Radial direction
rad	Radial
ref	Reference value
res	Resolved
s	Static Quantity
$scaled$	Scaled value
tan	Tangential
$t, tot, 0$	Total quantity
w	wall
x	Refer to the x-direction
y	Refer to the y-direction
z	Refer to the z-direction
39	Plane 39
40	Plane 40
41	Plane 41

Superscripts

circ	Circumferential
$\star$	Calculated by correlation

Chapter 1

Introduction

Contents

1.1 Evolution of modern gas turbine technology

The introduction of gas turbines (GTs) can date back to the 1930s when a German scientist, Hans von Ohain, and a British engineer, Frank Whittle, carried out two independent studies that lead to the development of gas turbine for aircraft propulsion. Also, the world's first industrial turbine for the power generation became operational, operating at full power for the first time, in 1939 in Neufchateau, Switzerland. Ever since, the ever-increasing gas turbines employment has permitted gas-fired generation to become one of the dominant form of power generation

[1]. As a matter of fact, even if the operating principles are the same of

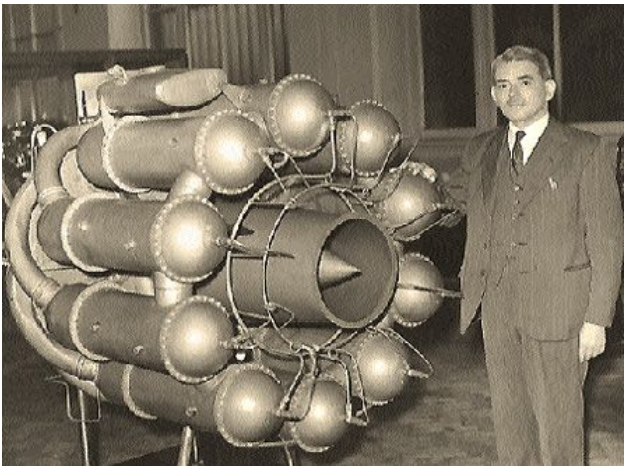

Figure 1.1: Sir Frank Whittle and the birth of the jet engine [1].

the prototype proposed by von Ohain and Whittle, modern gas turbines for both industrial and propulsion applications are nowadays driven by the necessity of improving the engine efficiency and performance [2]. This can be for example realized by increasing components efficiency and the most important cycle design parameters of the engine, like the overall pressure ratio (OPR) and the turbine inlet temperature (TIT), as can be seen in Figure 1.2 and Figure 1.3. Though the increment of these parameters is beneficial to improve the thermal efficiency, unfortunately it also results in drawbacks in terms of NO_x emissions, size and weight of the engine. In fact, as OPR and TIT increase, the compressor exit temperature and pressure are higher and, as a consequence, the required amount of cooling air would increase as well as the NO_x emissions, since they are proportional to the compressor exit temperature and pressure. As a result, the improvement in the thermal efficiency might be annihilated. Moreover, it should be noticed that the increase in TIT could not match with the maximum allowable metal temperature. Looking at Figure

1.3, ever-increasing advances in manufacturing technologies and material properties along with the turbine blade cooling have an increase in TIT from 1280 °F of the von Ohain engine to today's 3200 °F [3].

Despite the aspiration to make the engines more lighter, stronger and efficient has never stopped in the different parts of the world and highly advanced levels have been nowadays reached, still much attention is paid to development of the gas turbine design to meet the proposed emission reduction objectives. As a matter of the fact, in terms of civil air traffic, the Global Market Forecast for Airbus (GMF) shows that the Revenue Passenger Kilometers (RPKs) grew 6.3% in 2016 as compared to 2015 and it is expected that the world air traffic will increase by an average of 4.4%, while in emerging countries like China is forecast to grow at 6.2% per annum [4]. According to the trend that air traffic doubles every 15 years, the world civil aircraft fleet is expected to increase more than twofold by 2031 [4]. The projected explosion in demand will create an inexorable increment of total emissions from aviation sector. To contrast the climate impact of aviation and support the development of a more sustainable civil aviation, the Advisory Council for Aeronautics Research in Europe (ACARE) has set ambitious goals for the year 2050 (see Figure 1.4), that can be summarized as follows [5]:

- Reduction of CO_2 emissions by 75% in reference to a typical engine operating in year 2000;
- Reduction of NO_x emissions by 90% in reference to a typical engine operating in year 2000;
- Reduction of perceived noise emission by 90% in reference to a typical engine operating in year 2000;
- The achievement of emission-free aircraft movements during taxiing;
- Designing and manufacturing air vehicles in order to make them recyclable.

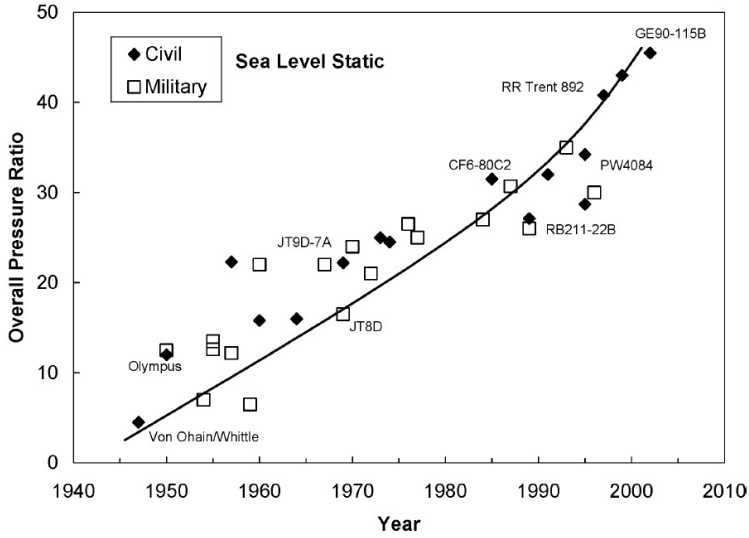

Figure 1.2: Overall pressure ratio (OPR) increase over the years [3].

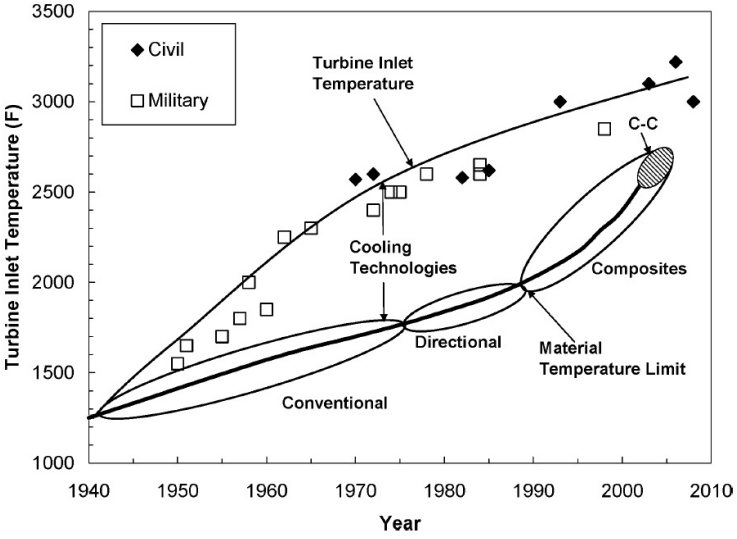

Figure 1.3: Turbine Inlet Temperature (TIT) and blade material temperature limits over the years [3].

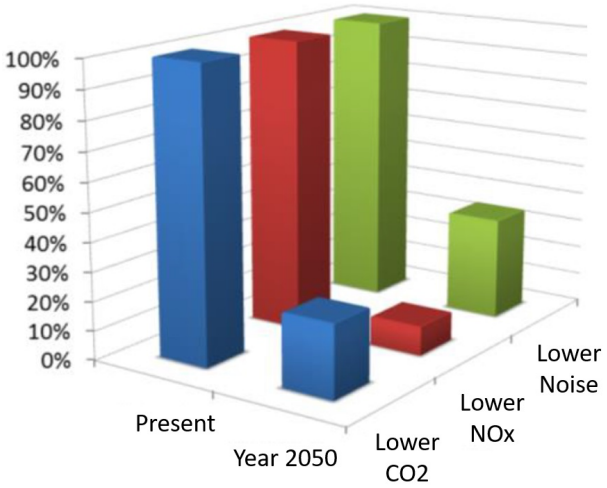

Figure 1.4: The ACARE 2050 objectives for Europe [6].

In the same way, regarding industrial power sector, the European Environment Agency (EEA) has set ambitious goals for the emissions reduction for the year 2030 basing on the 2016 reported emission. This can be summarized as follows [7]:

- Emission reduction of 66-91% for SO_2;
- Emission reduction of 56-82% for dust;
- Emission reduction of 56-82% for NO_x;

Reducing emissions from the power sector would have important positive environmental and human health implications. As already anticipated, over the past decades, the reduction of the emissions has been achieved by improving the engine efficiency. However, it is well known that the increase in OPR and TIT would also result in an increase in the thermal NO_x as well due to the higher temperature in the combustion chamber, if no adaptations are employed. Thus, it is still challenging to meet the ambitious emission reduction objectives that have been proposed. The

increasingly stringent legislation leads so to the necessity of developing innovative engine configurations, that are more efficient, or by employing non-conventional fuels, that are more environmental-friendly in order to contrast the climate impact of aviation and power generation and supporting their sustainability.

1.2 Emissions in gas turbine

Generally, fuels contain oxygen, nitrogen and certain heavy metals, while air, that is the most usual oxidizer, contains large amount of nitrogen. Hence, the combustion process leads to formation of NO_x, CO_x, unburnt hydrocarbons and other obnoxious gases which are released into the atmosphere. In particular, as can be seen from Figure 1.5, the temperature of the flame reveled in the primary zone is one of the most important factor influencing the emissions, especially in terms of CO and NO_x. As a matter of fact, it is quite evident that below 1670 K the production of CO increases significantly while above 1900 K a relevant amount of NO_x is observable, since the most important ones increase exponentially with the temperature, according to the Zeldovich mechanism [9]. Since, as anticipated, elevated values of OPR and TIT are necessary in order to guarantee high thermal efficiency, it is clear that the focus is especially on the right-hand of the Figure 1.5. Moreover, another important factor influencing the pollutant emissions is the air/fuel ratio, as can be seen by Figure 1.6. Also this time, CO and NO_x are characterized by opposite trends [10]: NO_x are significantly produced when air/fuel ratios reach approximately the stoichiometric value, since maximum heat release, corresponding to the highest combustion temperatures, occurs close to this value; on the contrary, CO and unburnt hydrocarbons emissions increase due to incomplete combustion, that occurs at the presence of excessive air (lean mixture) or less air (rich emissions).
The main ways adopted to control emissions are [9]:

- Imposing fuel air ratio away from stoichiometric value. In particular, initiating the combustion process at lean conditions leads to a rele-

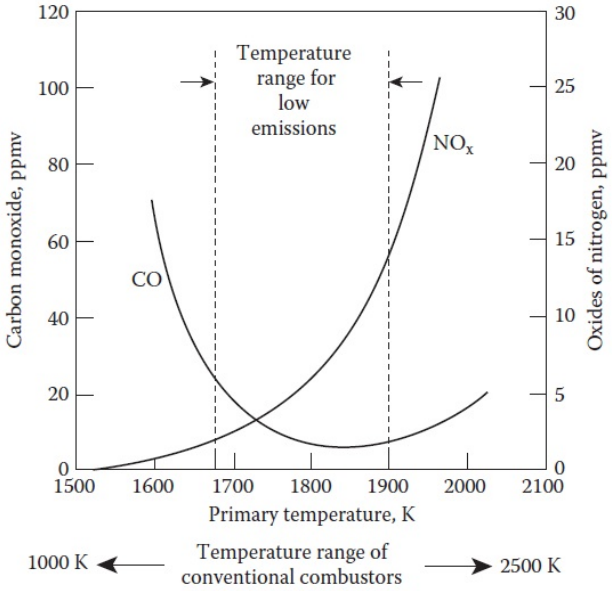

Figure 1.5: Dependence of emissions in terms of NO_x and CO on temperature [8].

vant portion of the air flowing through the dome of the combustion chamber. In this way, the flame temperature that is reached is lower than the one obtained by rich conditions. This results in a reduction of the NO_x emissions, even if such values of air fuel ratio can cause problems in terms of flame stabilization, especially at low power conditions;

- Employing fuel staging at low power conditions by turning off some fuel injectors. In this way, the combustion efficiency is guaranteed at the fuel injectors areas, where the local equivalence ratio is close to the stoichiometric one.

- Employing a good fuel air mixing and fuel atomization to obtain a more homogeneous as possible fuel local fuel air distribution. In

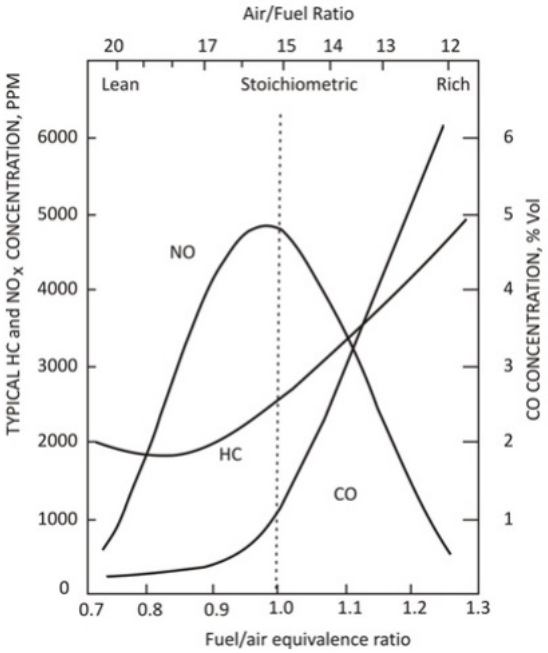

Figure 1.6: Dependence of emissions in terms of NO_x, CO and UHC on air/fuel ratio [8].

this way, a reduced presence of local hot spot due to rich pockets helps to reduce smoke and NO_x emissions;

- Guaranteeing sufficient flow residence time inside the combustion chamber to complete the combustion process and control the CO and unburnt hydrocarbons, in any case taking into account the fact that an excessive residence time results in an equally excessive production of NO_x;

1.3 Aero-engine combustors

In order to be able to apply the measures described above to meet the emission abatement criteria and fulfill the request of more efficient engines, various innovative solutions have been conceived, as anticipated. In particular, especially for the NO_x reduction, two main solutions have been proposed according to Figure 1.6. As a matter of fact, the first option, long considered as the standard procedure, is to adopt high equivalence ratios, as for the Rich-Quench-Lean (RQL) architecture, or to choose equivalence ratios appreciably lower than the unity, as for the lean combustors, the preferred solution in recent years. In the following sections, a brief description of both configurations is reported.

1.3.1 Rich-Quench-Lean combustors

The idea behind the RQL technology is schematically depicted in Figure 1.7 and Figure 1.8. As can be seen, firstly, the combustion process begins in the primary zone a fuel-rich mixture [8]. Typically, ignition occurs at an equivalence ratio ranging from 1.2 to 1.6. An increased equivalence ratio would be more effective in minimizing NO_x, but it has the potential to cause excessive smoke and soot formation [8]. In this way, the stability of the combustion is assured in a wide operation range due to the relevant production of energetic hydrocarbon radical species and hydrogen while, at the same time, the NO_x formation is minimized due to the limited achieved temperature and oxygen concentration [8, 11]. Hence, in the primary zone, the significant amount of CO, hydrogen and hydrocarbon intermediates produced in the primary zone are then oxidized and diluted by admitting a large portion of airflow in the quench section through “dilution holes”. Therefore, in order to limit the NO_x formation, as shown in the bottom route depicted in Figure 1.8, the rich burn mode is very quickly switched to the lean one by rapidly mixing the air with the primary zone effluent. This transition must occur rapidly to avoid the development of near-stoichiometric zones that are prone to high NO_x formation [8]. To further consume CO and unburnt hydrocarbons and to

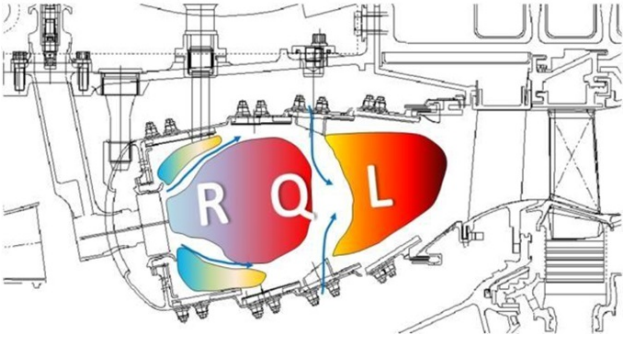

Figure 1.7: Sketch of a Rolls Royce Trent XWB combustor [10, 12].

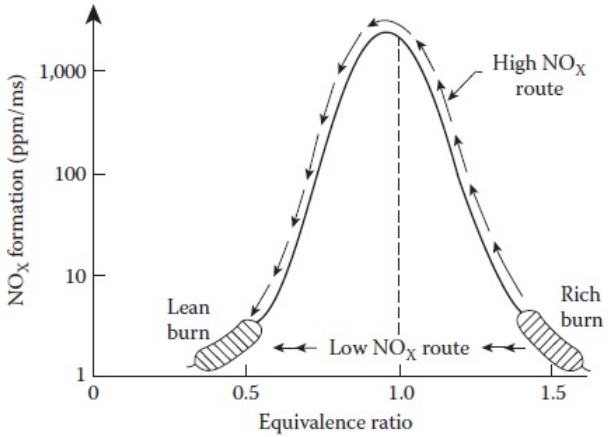

Figure 1.8: RQL working principle schematics and NO_x formation routes [8].

obtain an exhaust at the combustor exit containing a major amount of CO_2, N_2, H_2O and O_2, the combustion process is then followed by the learn burn section [8, 11]. In this way, the distribution of temperature at the exit of the combustion is better controlled. The equivalence ratios that are reached at the lean burn section assume typically values between

0.5 and 0.7 [13].
However, since the mixing between the dilution airflow and the hot efflux gas from the primary zone is not perfect and ideal, some spots with local equivalence ratio equal to the stoichiometric value are generally created, leading to a relevant production of thermal NO_x. Moreover, as a consequence, in order to limit the formation of stoichiometric local regions in the rich primary zone, the secondary airflow for the cooling of the liners should be limited as more as possible. Even if RQL architectures allow to limit the NO_x formation, it has been demonstrated that its concentration generally can not reach values below 30-50 ppm due to their intrinsic characteristics [8, 11]. Moreover, it is important to point out that for RQL combustion to achieve optimal results, the fuel needs to be finely atomized and evenly distributed across the fuel-rich zone. Additionally, the airflow pattern in the primary zone must be configured to avoid the formation of localized flow recirculation zones. Such zones could prolong residence times, leading to an increase in NO_x production [8, 14]. For this reason, in order to meet the ambitious emission reduction objectives that have been proposed, relevant efforts have been required for the development of the lean burn technology, despite more issues are present in terms of reliability and flame stability.

1.3.2 Lean burn combustors

The main idea behind the lean burn technology is let the combustion process occurs at lean conditions, adopting an equivalence ratio between 0.5 and 0.9 and a temperature between 1800 K and 1900 K, according to Figure 1.6. In this way, a trade-off in terms of production of emissions of CO and NO_x is achieved. In order to obtain such conditions, a relevant excess of air is needed in the primary zone, requiring so the employment of a large amount of air. As a consequence, the combustor tends to work close to the flame extinction limit, resulting in non-negligible issues in terms of flame stability. This condition is particularly exacerbated when the combustor operates in off-design conditions. Hence, relevant efforts have been made in order to realize an efficient fuel-air mixing [8].

One of the most employed way to assure the flame stability is the *fuel staging*. Historically, it represents one of the first implementation of the learn burn technology by actively control the injection of air or fuel in different regions of the combustor. In this way, the CO and NO_x production is limited and the flame stability is assured by "activating" and "deactivating" individual or multiple burners depending on the operating condition. In such combustors, two distinct regions can be distinguished: in order to minimize the emissions and guaranteeing a efficient combustion process, the first one is characterized by equivalence ratio lower than the stoichiometric value, but sufficiently high. In this way, the flame stability is achieved also during low power conditions. Moreover, this "primary" zone works as a pilot source of heat at operating conditions characterized by higher power level for the premixed fuel-air mixture, representing the second "main" combustion region. In this way, the engine operates globally in lean conditions. Examples of radially staging strategy in a Double Annular Combustor (DAC) and an axially one in a Axially Staged Combustor (ASC) are represented in Figure 1.9 and 1.10 [8, 10]. In particular, the employment of DAC solution leads to additional complexity on the system, especially in terms of cooling, since a larger dome surface is adopted. Moreover, since the mixing between the primary zone and the main one is not perfect and ideal, some spots with local equivalence ratio equal to the stoichiometric value are generally created, impacting the exit temperature distribution and emissions. Regarding the ASC solution, instead, guarantees an efficient combustion and reliable and rapid ignition in the main region, it however introduces some challenges, especially for the disposition of the main injectors in environment where hot gases are present.

It is important to point out that the "combustion staging" can be also obtained by controlling the equivalence ratio in the "primary" zone by regulating the air flow. However, this solutions leads to major complications in the architecture of the system in order to control large volumes of air, impacting the weight and cost of the entire engine.

Another solution, the Lean Premixed Prevaporized (LPP) has been

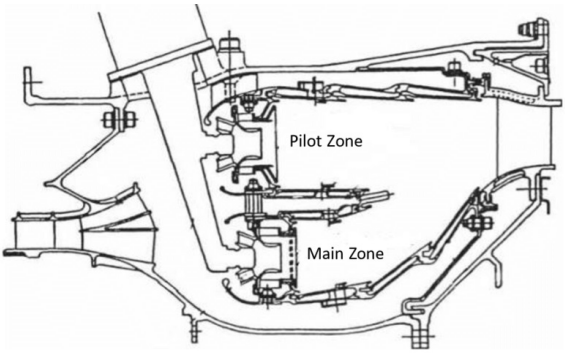

Figure 1.9: Double Annular Combustor cross-section [8].

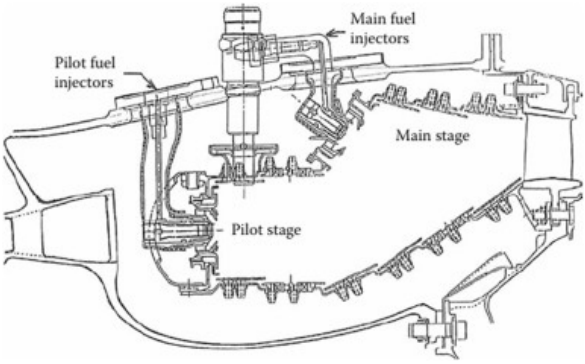

Figure 1.10: Axially Staged Combustor geometry (Pratt & Whitney V2500-A5) [8].

introduced in order to drastically limit the NO_x emissions. This concept provides for the complete atomization of the liquid fuel, which is then mixed with air in a dedicated region, the premixer, in order to obtain a mixing process that is as homogeneous and efficient as possible [8, 11]. In this way, the combustor can operate almost at the lean blowout limit and the temperature of the flame is controlled, avoiding hot spots at stoichiometric equivalence ratio. This has an evident impact on the emissions, especially on the thermal NO_x. However, also CO and unburnt

hydrocarbons emissions are kept under control, thanks to the sufficient long residence time. The principal drawback of this solution, apart from the flame stability problems already mentioned, is the possibility of auto-ignition and/or flashback phenomena inside in the injectors [8].
In order to overcome the latter, it is possible to place a partial evaporation in the inner duct while a rapid mixing is expected inside the combustor. This concept (Partially Evaporated and Rapid Mixing (PERM)) leads to a improved flame stability and to an optimization of the flame location [8, 11].
Another possible solution is represented by the Lean Direct Injection (LDI). This concept provides for a direct injection of the fuel, in a liquid form, inside the lean combustor, which is then rapidly mixed with a relevant amount of air obtained by using generally axial swirlers. So, no premixed ducts are adopted in this case. This solution leads to limit the flashback phenomena and to avoid the stoichiometric hot spot, reducing the NO_x emissions [8]. Moreover, no dilution holes are necessary, since the larger part of the air is injected through the injector, keeping constant the equivalence ration inside the combustor. It is evident that in this case it is mandatory an efficient and rapid mixing between air and fuel should obtained in the region immediately following fuel injection. Hence, the atomization and evaporation play a central role and a particular attention is posed on the injection system. To better control these phenomena, fuel staging is usually adopted by employing a pilot and main nozzle in the injection system. An example of LDI injection is presented by the Twin Annular Premixing Swirler (TAPS), made of a pilot and concentric main stages, as represented in Figure 1.11 [8]. The evolution of RQL combustors to lean combustors leads to a substantial change in the flow field inside the combustor, with consequent different distribution in terms of speed and temperatures at the combustor outlet, thus also impacting the performance of the following first stage nozzle. A comparison between the two technologies is reported in Figure 1.12. The different air flow split distribution consists in the main difference between the two technologies: as a matter of fact, in the RQL combutors, the dilution and coooling flows

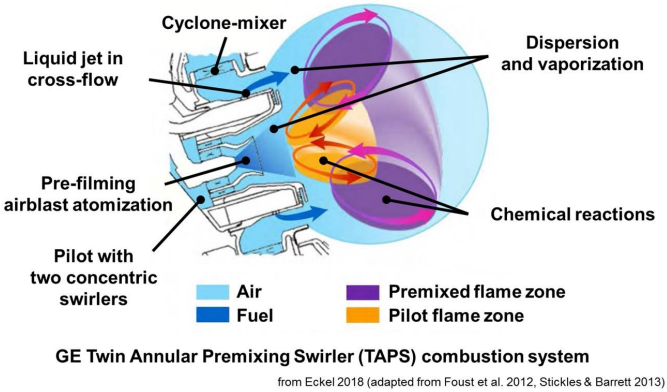

Figure 1.11: Schematic representation of TAPS technology [15].

count for the most of the airflow, up to the 65%-70%, since the primary zone, where rich conditions can be found, requires a limited portion of air; for the lean combustors, instead, the most of the airflow, up to the 70%, is introduced in the primary zone to assure a correct air-fuel mixing [8, 10, 11]. Hence, a different cooling technology is necessary for the liners, since a more limited airflow is available for this purpose. Another important difference is represented by the swirling structures due to the injection system. As a matter of fact, even if they are crucial in both cases to obtain the desired conditions in the primary zone, in the RQL combustors case, characterized in this area by the presence of diffusive flames, the key role is played by the transition from rich to lean conditions, achieved thanks to dilution flows. Hence, these structures are fundamental to assure the desired flow field evolution inside the combustion chamber. On the contrary, for the lean combustors case, as anticipated, the interaction between the main flow and the cooling ones is modest and so the swirling structures assume the role of swirl-stabilizing the combustion process, propagating it without substantial alterations thorough all the combustor [8, 10, 11].

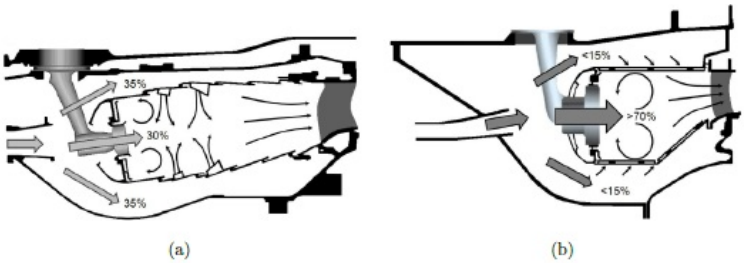

Figure 1.12: Comparison between the air flow split and main flow field for (a) RQL combustor and (b) and lean combustor [16].

1.4 Industrial gas turbine combustors

As the generation of NO_x is greatly influenced by temperature, a clear strategy for decreasing NO_x emissions involves reducing the temperature in the combustion zone. Historically, in the conventional combustors, the control of the emissions is obtained by introducing a heat sink by injecting water or steam in the combustion zone. While this approach is not suitable for aircraft engines, it is a feasible option for large stationary engines, particularly when ample water or steam resources are accessible [8].

At times, water or steam is directly introduced into the flame, either by using a certain number of nozzles positioned at the head end of the component or by employing holes located into the fuel nozzle [8, 17].

Alternatively, water injection can occur before reaching the combustor liner, typically introduced into the airstream that then moves into the combustion zone via the primary air swirler. This approach ensures effective atomization, with smaller droplets carried by the airflow through the swirler into the combustion zone. In contrast, larger droplets collide with the swirler vanes, forming a thin liquid film that undergoes airblast atomization as it flows over the downstream edge of the vane [8, 18].

At the same way, steam be introduced directly into the combustion zone or into air that later enters the combustion area. In certain setups, steam is injected into the air discharged from the compressor. However, this

approach is considered inefficient since only approximately 40% of the steam reaches the combustion zone [8, 17].
Generally speaking, injection of water or steam leads to relevant penalties [8]:

- Relevant capital cost;
- Relevant maintenance cost;
- Relevant cost of water treatment;
- Increase in UHC and CO emissions;
- Increase in fuel consumption;
- Increase in combustion pressure pulsations.

The limitations associated with water and steam injection lead to the development of "dry low-NO_x" (DLN) or "dry low-emissions" (DLE) combustors, that do not need diluent injections to achieve emission targets. Other methods to control the pollutant emission in the conventional combustors are:

- Exhaust gas recirculation: the concept is to inject exhaust gases, previously cooled, to limit the flame temperature in the primary zone. This is a system generally widely used in internal combustion engines. However, this method introduces inevitable complications into the structure of the machine and requires the employment of high quality fuels;
- Active flame temperature control: this control can be obtained by adopting devices that allow direct control of the flame temperature such as fuel staging and variable geometry;

These systems become fully effective when used as control systems in next-generation combustors, the DLN combustors.

1.4.1 Dry Low NO_x combustors

In the design of DLN combustors for stationary gas turbines, there are two major performance criteria to be met. One obvious requirement is that of meeting the emissions goals at base load on both gas and liquid fuels and controlling the variation of emissions levels across the load range of the engine. Equally crucial is the need for optimal system operability, ensuring stable combustion under various operating conditions, a responsive system to handle rapid load changes, acceptable levels of combustion noise, and, if necessary, the ability to transition smoothly between gas and liquid fuel, and vice versa [8].
Dry-Low NO_x combustors utilize a staged architecture featuring a lightly loaded primary zone. This zone generates the necessary temperature increase for low-power engine operation, functioning at equivalence ratios of approximately 0.8. In higher power configurations, its primary function is to serve as a pilot source of heat for the main combustion zone, where a fully premixed fuel-air mixture is supplied. At maximum power conditions, a low equivalence ratio of around 0.6 is maintained in both zones to minimize NO_x and smoke emissions [8, 10].
An example of DLN combustor is the GE DLN combustor, a dual-stage concept intended for use in heavy-duty gas turbines powered by natural gas, but adaptable for liquid fuel operation with the injection of diluents to manage NO_x levels. The core idea of this concept involves implementing two-stage combustion to obtain both low emissions and high operability across the entire load spectrum. Three main zones are present: a primary zone, a secondary zone and a dilution zone. The combustor works in four separate modes [8], represented in Figure 1.13:

- Primary: ignition is achieved by directing fuel through the primary nozzles situated at the leading end of the liner. Primary combustion air is introduced by using primary air holes and swirlers placed around each nozzle. This operating mode is employed for igniting, accelerating, and running the machine at low-power settings, typically up to approximately 40% of its full load.

- Lean-lean: as the engine load rises, fuel is introduced in the secondary zone. This fuel combines with air and subsequently passes through a swirler at the centerbody exit, establishing a swirl-stabilized secondary combustion zone. Both the primary and secondary zones function with low equivalence ratios, leading to the designation of "lean-lean" for this operational mode. This mode can elevate turbine output to base load.

- Secondary: this mode marks a shift between lean-lean and premix modes. The fuel supplied to the primary zone is progressively decreased while concurrently increasing the fuel flow to the secondary zone. Ultimately, the primary flame is extinguished and only the flame in the secondary zone remains.

- Premix: fuel is reinjected via the primary nozzles, and the primary combustion zone, now in a premixed state, is repositioned downstream, where it is ignited by the secondary flame zone. This mode aligns with the lowest levels of pollutant emissions.

DLN combustors aim to eliminate localized high-temperature regions within the flame by mixing the fuel and air upstream of the combustion zone. The introduction of Lean Premixed Prevaporized (LPP) represents a further development in this direction (see 1.3.2) [8]. LPP combustion shows significant promise for achieving extremely low NO_x emissions. Poeschl et al. [20] reported NO_x levels below 10 ppmv, even at flame temperatures exceeding 2000 K. However, several challenging issues persist, with the primary concern being the attainment of complete fuel evaporation and effective mixing of fuel and air within the autoignition delay time, all while mitigating the risks associated with acoustic resonance or flashback.

Since, generally speaking, the lean combustion has been established as the most promising technology to reduce the NO_x emissions, it is therefore necessary to pay particular attention to the flow field that is generated at the outlet of the combustor. As a matter of fact, such conditions can

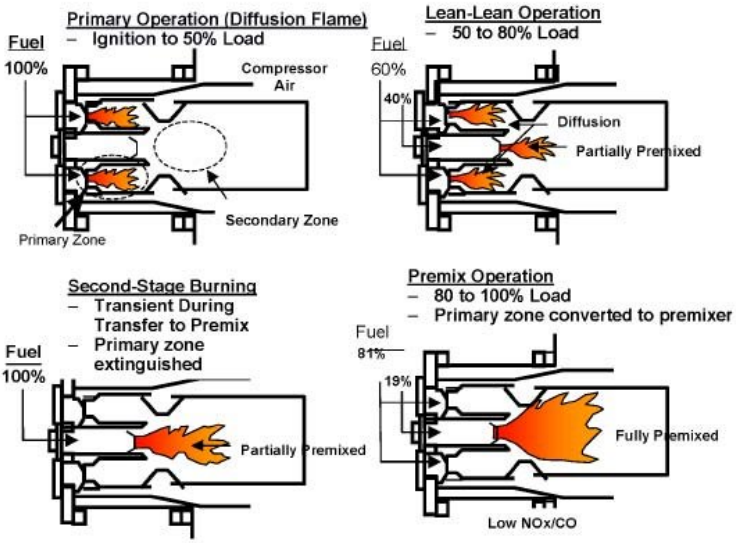

Figure 1.13: GE DLN operating modes [19].

potentially affect the aerodynamic and thermal behavior of the first stage nozzle, remaining also recognizable at the exit of it, possibly impacting the rotor heat load and performance as well. For this reasons, an in-depth analysis of the phenomena related to the combustor-turbine interactions is a mandatory for a robust and reliable aero-thermal design of the first turbine stage.

1.5 Thesis outline and motivation

The thesis work is focused on the numerical study of the combustor-turbine interaction in modern gas turbines. In fact, a complex and unsteady flow field, characterized by a high level of turbulence and temperature distortions, usually can be found at the interface plane between the two hot gas path components, especially with the implementation of lean-burn combustors that allow the reduction of NO_x emissions, but at

the cost of requiring highly swirled and turbulent flows to stabilize the flame. Such severe conditions at the inlet of the first stage nozzle can have a potential impact on the performance of the component, resulting into a perturbation of the heat transfer, the aerodynamics and the effectiveness of the cooling system. For this reason, a better understanding of the physical processes related to the combustor-turbine interaction nozzle have aroused an ever-increasing interest in the recent years, becoming a mandatory step for a reliable the aerothermal design. The main objective of this work is to study the behaviour of film cooling system and the heat loads on the first stage nozzle in lab-scaled and engine-like conditions. To do so, the entire work was carried out by performing coupled and decoupled combustor-turbine CFD simulations by using the commercial code ANSYS Fluent.
The dissertation is organized as follows:

- **Chapter 1** : in this chapter, an introduction to modern gas turbines is reported in order to contextualize the combustor-turbine interaction phenomena.

- **Chapter 2**: in this chapter, an extensive literature review on the combustion-turbine interaction phenomena, including the main combustor outlet flow characteristics and a review of the past researches, is reported.

- **Chapter 3**: in this chapter, an annular sector rig, made by a non-reactive, trisector combustor simulator and nozzle cascade, where both adiabatic effectiveness and HTC measurements had been carried out, is investigated by performing a systematic computational study. The comparison between numerical predictions and the available experimental results is exploited to assess the capability of advanced scale-resolving methods in the characterization of the mutual combustor-turbine interaction, along with the heat transfer coefficient and film-cooling system behavior. This evaluation aims thus to assess if such more advanced and more time-consuming methods, including also turbulence models able to capture the

transition, can be more reliably used for a proper prediction of the vane thermal loads.

- **Chapter 4**: in this chapter a fully integrated combustor-nozzle configuration is investigated by using SBES, along with a realistic turbine nozzle cooling system, under realistic engine-like operating conditions. Decoupled RANS/SBES simulations of the stand-alone NGV are also reported to highlight the risks and uncertainties associated with carrying out decoupled simulations. The aim is to evaluate the influence of the combustor's presence under realistic operating conditions and a realistic annular geometry.

- **Chapter 5**: in this chapter, the focus is on the generation and application of highly representative and reliable boundary conditions at the inlet of the first-stage nozzle in order to enable the separate study of the two components by conducting decoupled simulations. To do so, several SBES decoupled simulations of the stand-alone NGV are carried out by applying two-dimensional unsteady boundary conditions extracted from the fully integrated combustor-NGV SBES simulation. Additionally, the POD technique is applied, considering three different numbers of POD modes, corresponding to a descending level of energy content relative to the global turbulent kinetic energy. In this way, the proper coherent structures of turbulent flows are identified and the complexity of the dynamics of a system is reduced, just taking into account the most important modes.

- **Chapter 6**: in this chapter, the focus is on the prediction of heat loads in engine-like conditions by simulating a single set of uncooled vanes. The main objective of these analyses is to obtain a scaling criterion for the HTC obtained in lab-scaled conditions in order to obtain representative HTC values in engine-like conditions. In fact, when the engine operates in realistic conditions at full speed and full load, direct experimental measurements are not available and therefore the introduction of a scaling criterion becomes necessary.

In the concluding chapter, a summary of the main achievements of this study is provided, along with conclusions and recommendations for future works.

1.6 Publications

- Diurno, T., Tomasello, S. G., Fondelli, T., Andreini, A., Facchini, B., Nettis, L., & Arcangeli, L. (2021, June). Development of a Design Approach for the Optimization of Steam Turbine Exhaust System Performance Through CFD Modelling. In Turbo Expo: Power for Land, Sea, and Air (Vol. 85017, p. V008T22A013). American Society of Mechanical Engineers.

- Tomasello, S.G., Bacci T., Andreini, A., Facchini, B., Cubeda, S., & Andrei, L. (2022, June). Numerical prediction of heat transfer coefficient and adiabatic effectiveness on a nozzle guide vane with representative combustor outflow. In AIP Conference Proceedings. AIP Publishing LLC, 2022.

- Tomasello, S.G., Andreini, A., Meloni, R., Cubeda, S., Andrei L., & Michelassi, V. (2022, June). Numerical study of combustor-turbine interaction by using hybrid RANS-LES approach. In AIP Conference Proceedings. In AIP Publishing LLC, 2022.

- Tomasello, S.G., Bacci T., Andreini, A., Facchini, B., Cubeda, S., & Andrei, L. (2023, June). Numerical prediction of the heat loads on a non reactive test rig for combustor turbine interaction by using hybrid RANS LES approach. In AIP Conference Proceedings. AIP Publishing LLC, 2023.

- Tomasello, S.G., Andreini, A., Meloni, R., Cubeda, S., Andrei L., & Michelassi, V. (2023, June). Analysis of combustor-turbine interaction by using coupled and decoupled scale-resolving simulations under representative operating conditions. In AIP Conference Proceedings. AIP Publishing LLC, 2023.

- Tomasello, S. G., Meloni, R., Andrei, L., & Andreini, A. (2023). Study of Combustor–Turbine Interactions by Performing Coupled and Decoupled Hybrid RANS-LES Simulations under Representative Engine-like Conditions. Energies, 16(14), 5395.

Chapter 2

Literature review on combustion-turbine interaction phenomena

Contents

Given the considerations made in the previous chapter, it is therefore necessary to pay particular attention to the flow field that is generated at the outlet of the modern lean combustors. In particular, the flow field that develops inside the combustor can significantly affects the inlet boundary conditions at the stator and, consequently, its performance and design. Hence, in order to investigate in depth the phenomena related to turbine-combustor interaction, a brief introduction on the combustor is mandatory to better understand the causes for the evident non-uniformities at the stator inlet.

2.1 Flow field characteristics at the combustor outlet

The main flow typical of lean combustor architectures are represented in Figure 2.1. In particular such structures are [10, 11]:

- **Central toroidal recirculation zone (CTRZ)**: Situated in the central area just after the swirler, this flow structure is responsible for the substantial recirculation of gases, extending the duration they stay within the combustor. This extended residence time is essential for stabilizing the combustion process and ensuring its completeness;
- **Vortex breakdown (VB)**: This phenomenon is achieved by expanding the swirling flow in both horizontal directions and towards the inner and outer surfaces of the combustor. It also triggers recirculation along the axis of the swirler, which frequently enhances the Central Turbulent Recirculation Zone (CTRZ), and it interacts with the cooling flow around the liners;
- **Corner recirculation zones (CRZ)**: Located at the corners of the combustion chamber, they promote longer residence times, thereby enhancing the combustion process;
- **Precessing vortex core (PVC)**: A swirling structure rotates around the Central Turbulent Recirculation Zone (CTRZ) with a precessing motion.

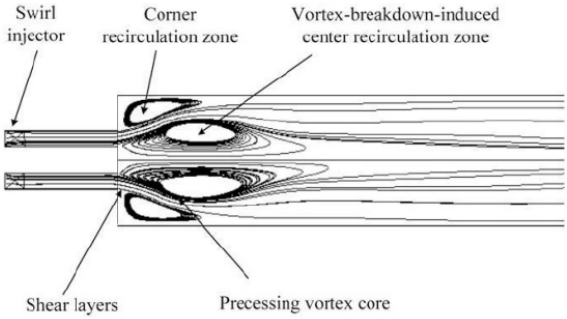

Figure 2.1: The flow patterns within a standard gas turbine combustor equipped with a coaxial injector [21].

In recent years, several researchers have conducted experiments to investigate issues related to combustion instabilities [21] and the interaction between swirling flows and liner cooling methods [22–24]. Berrino et al. [25, 26] focused on studying the flow patterns downstream of an ultra-low NO_x injection system. They discovered that in highly swirling flows, the combustion process, specifically the release of heat, plays a crucial role in stabilizing the flow patterns. Additionally, they observed that unsteady phenomena like the Central Turbulent Recirculation Zone (CTRZ) and Precessing Vortex Core (PVC) were either dampened or diminished when transitioning from non-reacting to reacting conditions using the same injector geometries [27–31]. Therefore, it is important to note that comparing the characteristics of the combustor outlet between reacting and non-reacting cases without any adjustments might lead to variations [32]. In general, the presence of such structures at the combustor exit has significant consequences on the downstream component: the stator. Several studies have highlighted how the Precessing Vortex Core (PVC) manages to maintain many of its characteristics even at considerable distances from the main structures generated by the swirler. In particular, the velocity distribution tends to be highly non-uniform, exhibiting tangential and radial components around the vortex core, interacting with the secondary

flows [33]. As a matter of fact, for aero-engines, the temperature profile in these combustors is entirely different from previous Rich-Quench-Lean (RQL) designs, characterized by the presence of hot spots corresponding to areas where the vortices are present. These hot spots are relatively small regions where the fluid has much higher temperatures compared to the average (see Figure 2.2). Furthermore, an increase in turbulence is observed, with intensity that can exceed 35%, along with larger integral scales [34, 35].

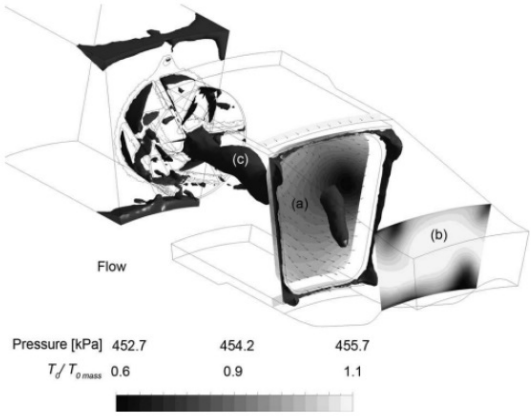

Figure 2.2: (a) Pressure distribution and velocity field; (b) inlet temperature; (c) overlaid with recirculation zone [36].

The interaction with the subsequent stator can only be complex, as the non-uniform temperature and velocity distributions, along with the high turbulence levels, strongly impact the aerodynamic and thermal behavior of the first high-pressure stator. Considering the thermal aspect, it is known in the literature that this factor significantly affects the component's lifetime, as it is responsible for thermal fatigue. As a matter of fact, it has been demonstrated that even small differences in the predicted surface temperature of the stator vanes can drastically reduce their service life

[37]. Furthermore, not all turbine vanes have the same temperature profile and heat transfer characteristics on their surfaces [38]. This variation strictly depends on their relative position to the burner, as shown in the Figure 2.3.

Figure 2.3: Portion including two nozzle guide vanes (NGVs) from a high-pressure turbine in a turbofan engine [38].

Therefore, as a result, modern combustor outlets typically exhibit prominent hot streaks, which possess the following characteristics:

- total temperature non-uniformities;
- residual swirl;
- high turbulence intensity.

2.1.1 Temperature non-uniformities characterization

The temperature flow field at the exit of the combustor is characterized by both radial and circumferential temperature gradients [39, 40], as can

be seen also from Figure 2.4, where the presence of the hot spots is clearly identifiable [41]. Several studies have conducted both experimental and numerical analyses to understand how new lean burn engines alter the temperature profile at the combustor exit. These studies have revealed a common structure, which is obviously a consequence of the swirler geometry, combustion chamber configuration, and film cooling injected through the holes in the liner. For example, recently, Andreini et al. [42] tested different strategies for turbulence modelling, especially Large-Eddy Simulation (LES) and Scale Adaptive Simulations (SAS), benchmarking the numerical results on an experimental test article representative of an aeronautical lean burn combustor cooled by means of effusion. Both LES and SAS simulations, according to the experimental results, evidenced both radial and circumferential temperature non-uniformities at the combustor exit, as can be seen from Figure 2.5. Various parameters have been defined to measure and describe the unevenness of the temperature distribution ("hot streak") at the exit of a combustor [11]. Two coefficients, known as the Overall Temperature Distribution Factor (OTDF) and Radial Temperature Distortion Factor (RTDF), were intro-

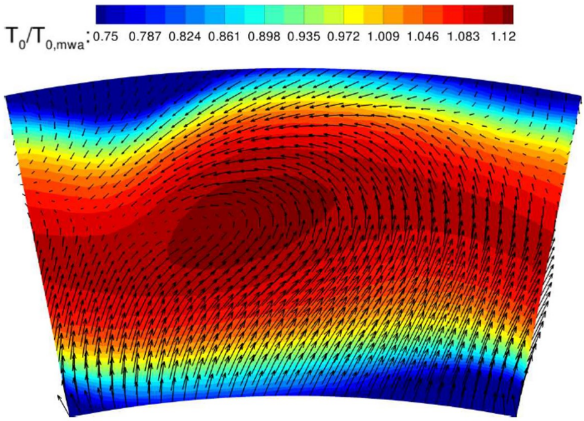

Figure 2.4: Aero-thermal field on the combustor-turbine interface [41].

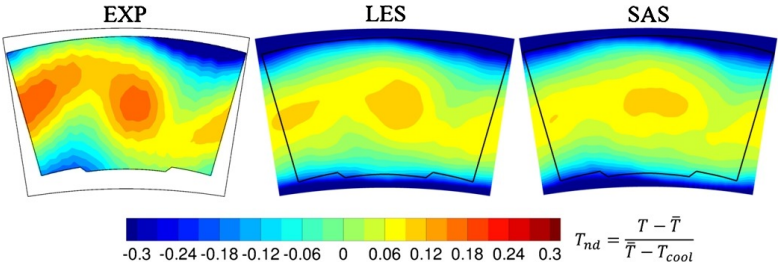

Figure 2.5: Non-dimensional temperature distributions at the combutor exit [42].

duced by Povey and Qureshi [39]. The OTDF compares the maximum temperature with the average temperature across the entire combustor exit section, while the RTDF compares the maximum circumferentially averaged temperature with the average temperature [11].

$$OTDF = \text{PatternFactor} = \frac{T_{40,\,\max} - T_{40,\,\text{mean}}}{\Delta T_{\text{comb}}} \tag{2.1}$$

$$RTDF = \text{ProfileFractor} = \frac{T^{\text{circ}}_{40,\,\max} - T_{40,\,\text{mean}}}{\Delta T_{\text{comb}}} \tag{2.2}$$

where the subscript 40 represents the plane at the exit of the combustor, and ΔT_{comb} denotes the temperature difference between the average temperatures at the combustor exit and inlet. Additionally, one can define the corresponding local parameters (*Local Overall Temperature Distortion Factor* and *Local Radial Temperature Distortion Factor*) if a detailed description of the profile shape is required. In this case, the maximum temperature is replaced with the local temperature at a specific position on the exit plane [11].

$$LOTDF = \frac{T_{40} - T_{40,\,\text{mean}}}{\Delta T_{\text{comb}}} \tag{2.3}$$

$$LRTDF = \frac{T_{40}^{\text{circ}} - T_{40,\text{ mean}}}{\Delta T_{\text{comb}}} \tag{2.4}$$

Nevertheless, in order to minimize the amount of measurements required, it is common practice to analyze the interface between the combustor and the turbine using non-reacting test setups that mimic the flow conditions in real combustors. In this context, alternative definitions of Eq. 2.5 and Eq. 2.6 are typically used to describe the flow at the combustor outlet plane [11, 39]:

$$LOTDF' = \frac{T_{40}}{T_{40,\text{ mean}}} \tag{2.5}$$

$$LRTDF' = \frac{T_{40}^{\text{circ}}}{T_{40,\text{ mean}}} \tag{2.6}$$

or, taking into account the temperature of the cooling flow:

$$LOTDF'' = \frac{T_{40} - T_{40,\text{ mean}}}{T_{40,\text{ mean}} - T_{\text{cool}}} \tag{2.7}$$

$$LRTDF'' = \frac{T_{40}^{\text{circ}} - T_{40,\text{ mean}}}{T_{40,\text{ mean}} - T_{\text{cool}}} \tag{2.8}$$

2.1.2 Residual swirl characterization

Modern combustors with low emissions utilize highly turbulent flows to ensure effective flame stabilization. To achieve a high level of turbulence, specialized systems are installed in the burners. The tangential velocity component plays a crucial role in maintaining swirling motion downstream, extending all the way to the nozzle guide vanes of the high-pressure turbine. As a matter of fact, at the exit of the combustor, it can be observed a highly non-uniform velocity distribution, characterized by high swirl and pitch components, that can be conserved up to the inlet of the following component, the first stage nozzle of the High Pressure Turbine (HPT), as proven both experimentally and numerically [34, 35, 43, 44]. Such severe conditions are particularly exacerbated due to the employment

of the modern gas turbine (GT) combustors, such as the lean burning systems [45]. As a matter of fact, for aero-engines, such systems are indeed characterized by a very compact design, especially compared to the rich-quench-lean (RQL) ones, and by the potential reduction or absence of the dilution holes due to limited portion of air intended for the cooling of the liners. Figure 2.6 illustrates an instance of the remaining swirl present at the combustor exit. The study in question conducted numerical simulations to investigate the effects of inlet flow non-uniformities, specifically the combination of temperature variations and strong swirl, on the high-pressure turbine [46]. Various configurations were analyzed, including baseline setups with either hot-streak or swirl at the inlet, as well as combined cases with both hot-streak and swirl. The simulations also took into account the clocking position of the combustor-nozzle guide vane (NGV) and the direction of the swirl. Qureshi et al. [40] conducted an experimental measurement of the swirl produced in a hot streak simulator. The results were presented as vector plots and distributions of yaw angle at two radial positions, namely 20% and 80% of the radial span. Near the endwalls within this span range, the intensity of the swirl is characterized by both maximum and minimum peaks in the yaw angle. The maximum peak corresponds to approximately 50%, while the minimum peak reaches around -50% [10]. Qureshi et al. [40] conducted a study where they applied a swirl profile to the inlet section of the MT1 high-pressure turbine stage. The effects of this swirl profile were investigated both experimentally and numerically. In their investigation,

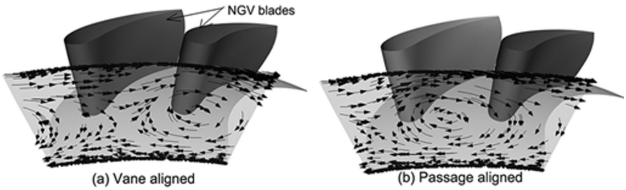

Figure 2.6: Example of residual swirl configuration at the exit of the combustion: (a) vane aligned and (b) passage aligned [46].

they used a ratio of 1 nozzle to 2 swirlers. The results showed that the presence of swirl significantly altered the aerodynamics of the nozzles, leading to noticeable changes in rotor incidence. Specifically, there was an increase in rotor incidence of up to +4% from midspan to the tip and a decrease of -6% near the hub, compared to a case with a uniform inlet flow field [10].

Additionally, both experimental and numerical data revealed that swirling flow had a significant impact on the effectiveness of endwall film cooling. The swirl resulted in a decrease of up to 35% in adiabatic effectiveness of film cooling, while the Nusselt number, which indicates the convective heat transfer, increased by 10-20% [10].

2.1.3 Turbulence intensity characterization

All the studies present in literature agree that an elevated turbulence intensity exists downstream of the combustion chamber, ranging from 20% to 30% at the turbine inlet [34, 47, 48]. However, the specific values of turbulence fluctuations and their length scale have only been recently revealed through recent studies, probably due to the complexity of measuring such fields under realistic conditions. In particular, regarding the turbulence length scale, Radomsky et al. [49] suggested a range spanning from 0.1 to 0.14 times the vane pitch as typical values. In literature, the majority of experimental findings published on this subject have been derived from test setups where turbulence is generated using calibrated grids. However recently, Cha et al. [34, 35] conducted a study that involved experimental and numerical assessments of turbulence at the exit of an RQL combustor. The results showed a turbulence intensity of approximately 30-35% at the interface plane between the combustor and turbine, as observed in both the experimental results, as depicted in the Figure 2.7, and in the large eddy simulation (LES) data [10]. Furthermore, the length scale of turbulence ranged from 15% to 25% of the NGV chord, as can be seen in Figure 2.8. Moreover, in the same study, it has been noted that LES indicates reduction in the turbulent lengthscale by a factor of 2 across the NGV passages. This contradicts the actual experimental

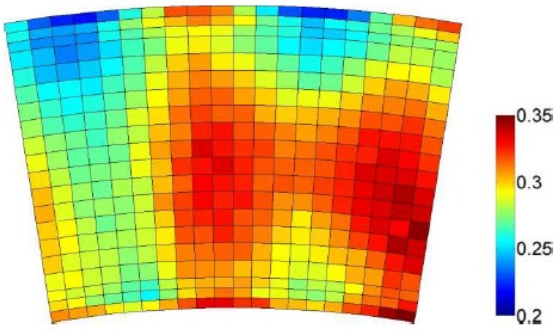

Figure 2.7: Turbulence intensity measured by using Hot Wire Anemometry (HWA) at the exit of the combustor [35].

observations. As a matter of fact, also Radomsky et al. [49] observed experimentally that the turbulence level of the flow at the turbine inlet does not experience significant decay as it passes through the nozzle guide vanes and, instead, it remains relatively high. These contrasting outcomes suggest that accurately characterizing turbulence at the exit of realistic combustors and effectively comparing experimental and numerical data is a challenging undertaking.

2.2 Flow field characteristics in the first stage nozzle

In an axial flow turbine, the initial nozzles called high-pressure nozzle guide vanes (NGVs) play a crucial role. These NGVs direct the airflow onto the turbine buckets, converting pressure into kinetic energy through acceleration, thanks to their converging shape. The design of NGVs must consider various requirements related to aerodynamics, heat transfer, and structural mechanics. While the focus of this work does not include structural mechanics, aerodynamics primarily seeks to minimize pressure losses and maximize efficiency. On the other hand, the heat transfer aspect aims to develop an optimal cooling system that can effectively handle

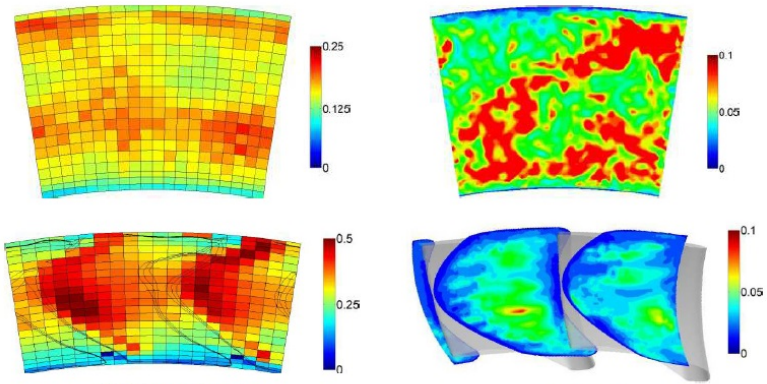

(a) Experiments. (b) LES.

Figure 2.8: Turbulence length scale normalized with to the chord length of the nozzle guide vane (NGV) measured at two locations: the exit of the combustor (top) and the exit of the NGV (bottom) [35].

the prescribed thermal loads and support the NGVs. The evaluation of aerodynamic losses in turbine NGVs typically involves quantifying the total pressure drop across the cascade. However, numerous parameters have been employed for this purpose, often differing in the non-dimensional quantities used to express their values. Ligrani conducted a comprehensive review of many such parameters, with the most frequently utilized ones expressed as follows [10, 50]:

$$c_p' = \frac{\bar{P}_{0,in} - P_{0,out}}{\bar{P}_{0,in} - P_{s,out}} \tag{2.9}$$

$$c_p'' = \frac{\bar{P}_{0,in} - P_{0,out}}{\rho \frac{v_{out}^2}{2}} \tag{2.10}$$

The parameters in the equations correspond to different aspects of the system. The symbol P represents pressure, while the subscripts "in" and "out" indicate the positions at the inlet and outlet of the cascade, respectively. The variable $\rho \frac{v_{out}^2}{2}$ represents the contribution of dynamic

pressure, and the bar symbol signifies the averaging of mass or area at a specific section. By taking averages of $P_{0,out}$, $P_{s,out}$, and $\rho\frac{v_{out}^2}{2}$, an integral quantity can be obtained. The losses in a turbine can be classified into two types: 2D and 3D [51]. The 2D losses pertain to sources of loss that would be observed in a cascade test of a turbine blade row with an infinite span, disregarding any endwall effects. On the other hand, the 3D losses refer to the additional losses that emerge when the turbine stage operates in a practical rotating arrangement. The sources of 2D losses encompass various factors [52]:

- *Blade boundary layers*: the loss experienced in the blade boundary layers can be considered as the dissipation of work due to viscous shear within these layers. Its extent is influenced by the growth of the boundary layer, specifically determined by the pressure distribution along the blade surface and the location of the transition from laminar to turbulent flow. Boundary layer loss commonly constitutes more than 50% of the total 2D loss in subsonic turbines.

- *Trailing Edge Mixing*: the loss attributed to trailing edge mixing occurs when the boundary layers from the suction surface and pressure surface of the blade mix with the surrounding flow behind the trailing edge. This type of loss is notable, usually accounting for approximately 35% of the overall 2D loss in subsonic turbines. In supersonic cases, this loss becomes even more prominent, increasing to around 50%.

- *Flow Separation*: this kind of loss occurs when the boundary layer separates from the surface of the blade, leading to the formation of a significant area with reduced flow kinetic energy downstream. Quantifying this loss is challenging, but in a properly designed turbine, substantial 2D flow separation should not occur, allowing it to be typically disregarded. Separation occurring near the trailing edge is considered as part of the trailing edge mixing loss.

- *Shock Wave*: shock loss arises when the passage of the turbine blade becomes choked, resulting in an exit Mach number exceeding

approximately 0.9. The loss caused by shock waves within the turbine passage is not as substantial as one might anticipate.

The sources of 3D losses can be instead categorized as follows [52]:

- *Tip leakage flows*: tip leakage refers to the flow that occurs from the pressure surface to the suction surface of a turbine blade through the clearance gap. This leakage flow results in a decrease in the work performed by the turbine rotor since the mass flow rate through the blade passage is reduced. It also contributes to a loss in efficiency. The magnitude of tip leakage loss increases significantly with the size of the clearance gap. Typically, a 1% increase in the clearance gap relative to the blade height results in a loss of efficiency ranging from 2-3% [53]. Consequently, tip leakage loss has a more pronounced impact on small turbine stages that feature relatively larger clearance gaps.

- *Endwall (or secondary) flows*: the loss that occurs at the endwalls is a significant and intricate topic that researchers are actively investigating. It includes all the losses that happen on the inner and outer surfaces of the hub and casing, within and outside the rows of blades. Predicting and separating endwall loss is highly challenging, but it generally contributes around 30% of the overall loss in a turbine stage [51]. The movement of the flow near the walls of the turbine's annulus is influenced by secondary flows within the blade passage. These secondary flows are caused by the incoming boundary layers at the endwalls and the turning of the flow within the blade passage. In particular, secondary flows involve additional losses because they deviate from the ideal axisymmetric flow [54]. Langston proposed the fundamental characteristics of secondary flow patterns in nozzle guide vane passages by studying a linear cascade [55]. Although there are variations between annular and linear cascade flow fields, Langston's work is widely regarded as crucial in understanding the fundamental mechanisms applicable to all cascades [56]. The main secondary flow structures are represented

in Figure 2.9 and include the following:

- *Passage vortex*: the presence of boundary layers with lower velocities leads to a flow reversal towards the suction side, resulting in the formation of two opposing vortices near the inner and outer endwalls. These vortices are commonly referred to as passage vortex;
- *Horseshoe vortex*: another factor contributing to the secondary flows is the presence of a horseshoe vortex, which is generated by the pressure gradient resulting from the endwall boundary layer at the stagnation point on the leading edge of the blade. This vortex is then divided into a pressure leg and a suction leg, which are carried inside the passage. The pressure leg is sustained by the flow from the passage's pressure side to the suction side endwall, reinforcing the passage vortex. On the other hand, the suction leg rotates in the opposite direction and is sometimes referred to as the counter vortex [55, 57]. The resulting three-dimensional flow configuration can be observed in Figure 2.9 [58].

- *Coolant flows*: The overall impact needs to be considered in terms of the thermodynamics of the entire gas turbine system. Cooling is implemented to increase the temperature at which the turbine operates, resulting in improved cycle efficiency and work output. However, the cooling process itself introduces a significant amount of irreversibility. Heat transfer from the mainstream flow, the passage of coolant through intricate pathways, and the mixing of the coolant with the mainstream flow all contribute to the creation of entropy. Among these processes, the mixing of the coolant with the mainstream flow has a notable effect on the efficiency of the turbine stage. The coolant is introduced into the blade or vane passages at an angle through holes or slots and possesses different stagnation temperature and pressure compared to the mainstream

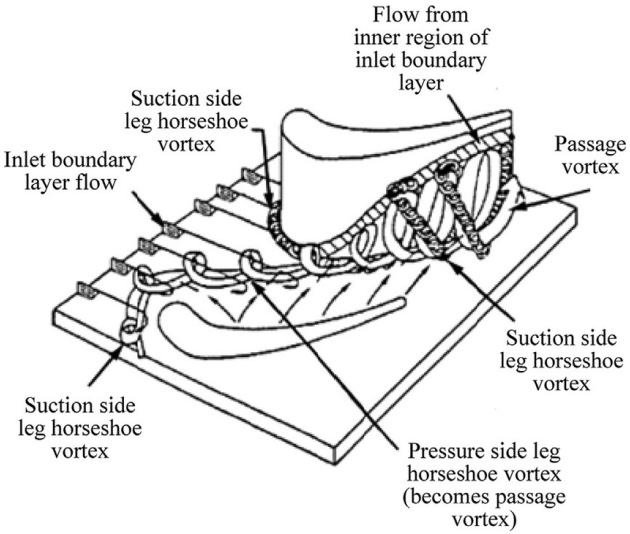

Figure 2.9: Secondary flow vortex model [58].

flow. For high-pressure nozzles or buckets, two types of cooling methods are employed: internal and external cooling. In many cases, the external cooling method is utilized in combination with internal cooling. Specifically, in the case of first stage nozzles, which is the main focus of this study, both cooling schemes are typically employed due to the component's exposure to the highest temperatures within the entire turbine module. Internal cooling often involves the use of impingement inserts and pin-fin arrays, while external cooling is achieved through film cooling. Film cooling entails the flow of air through discrete holes and over the surface of the vane in a thin film-like manner [59]. Figure 2.10 illustrates the manner in which the cooling air is utilized to cool the high-pressure nozzle guide vanes in a modern lean-burn engine. Regarding the film cooling technique, from a design perspective, it is crucial to comprehend how various flow parameters and phenomena affect the behavior of film cooling. Four key factors - blowing ratio (BR), velocity ratio (VR), density

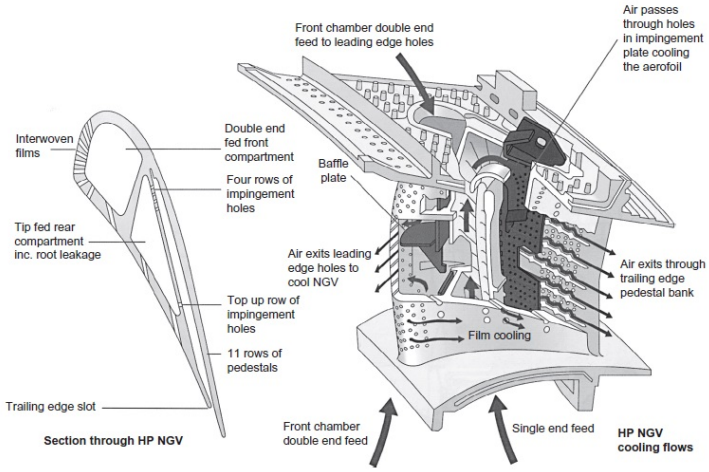

Figure 2.10: The cooling configuration employed for a high-pressure turbine nozzle guide vane in a modern lean-burn engine [52].

ratio (DR) and momentum ratio (I) - which are typically taken into account when assessing the performance of a film-cooling system, include [10, 11]:

$$BR = \frac{(\rho V)_{coolant}}{(\rho V)_{main}} \tag{2.11}$$

$$VR = \frac{(V)_{coolant}}{(V)_{main}} \tag{2.12}$$

$$DR = \frac{(\rho)_{coolant}}{(\rho)_{main}} \tag{2.13}$$

$$I = \frac{(\rho V^2)_{coolant}}{(\rho V^2)_{main}} \tag{2.14}$$

Moreover, according to L'Ecuyer and Soechting [60], the character-

istic regimes of film cooling effectiveness using a flat plate reference geometry have been categorized as follows [10, 11]:

- *Mass addition*: the level of effectiveness increases with the BR due to the higher thermal capacity of the coolant. However, the distribution of effectiveness is not affected by the DR or VR;
- *Mixing*: the distribution of effectiveness is influenced by the BR and DR due to the contrasting effects of increased thermal capacity and increased mixing and penetration of the coolant with the freestream;
- *Penetration*: the distribution of effectiveness is primarily determined by the intricate interplay of excessive coolant penetration and enhanced turbulent diffusivity caused by a high VR.

The aforementioned regimes are defined, based on data from Pedersen et al. [61], who conducted experiments using a flat plate with a single row of holes, 35° injection angle, and a pitch-to-diameter ratio of 3, as follows [10, 11]:

- *Mass addition*: $VR < 0.25$;
- *Mixing*: $0.25 < VR < 0.8$;
- *Penetration*: $VR > 0.8$;

In particular, the cooling system performance can be quantified using the cooling effectiveness defined as:

$$\eta = \frac{T_{0,g} - T_b}{T_{0,g} - T_{0,c}} \tag{2.15}$$

In the given equation, $T_{0,g}$ represents the stagnation temperature of the hot gas stream, T_b denotes the blade metal temperature, and $T_{0,c}$ indicates the coolant stagnation temperature. The parameter η typically has a value of approximately 0.6. Equation 2.15 provides a means to examine how variations in the cooling system impact

the blade metal temperature.

As anticipated, an ideal method for applying coolant onto an airfoil surface would involve introducing a thin layer of coolant through a slot that is angled in a nearly tangential direction to the surface. This approach would ensure a uniform coolant layer that remains attached to the surface. However, the use of long slots would significantly compromise the structural strength of the airfoil, making it impractical. Consequently, coolant is typically introduced through rows of holes, where the effectiveness of the coolant film cooling is influenced by the geometry of the holes and their arrangement. Additionally, several factors related to the coolant and the nature of the mainstream airflow play a crucial role in determining the performance of the coolant film. The most relevant factors include the blowing ratio, density ratio, the turbulence intensity and curvature. When the BR is increased, it leads to two contradictory consequences. On one hand, it enhances the mass-flux of the coolant, which is beneficial. On the other hand, it causes the coolant jets to lift off from the surface and penetrate into the mainstream, which is detrimental. As a result, the film cooling effects generally improve as the blowing ratio increases, until a certain threshold is reached. Beyond this threshold, the ability to provide sufficient coverage decreases due to jet penetration [62], as shown in Figure 2.11. Conversely, an increase in the DR tends to shift this threshold blowing ratio towards higher values. This is because a higher density ratio results in lower jet velocity and reduces the tendency for jet penetration [61]. In this regard, Jose et al. [64] carried out a study focused on investigating numerically the adiabatic film cooling effectiveness on a flat plate test model with cylindrical holes by varying BR and DR. The results showed that the DR has a beneficial impact on the adiabatic effectiveness, especially near the coolant exit. Mainstream turbulence has instead two conflicting effects. Firstly, it enhances the mixing between the coolant and the mainstream airflow, which hampers the effectiveness of film cooling. Secondly,

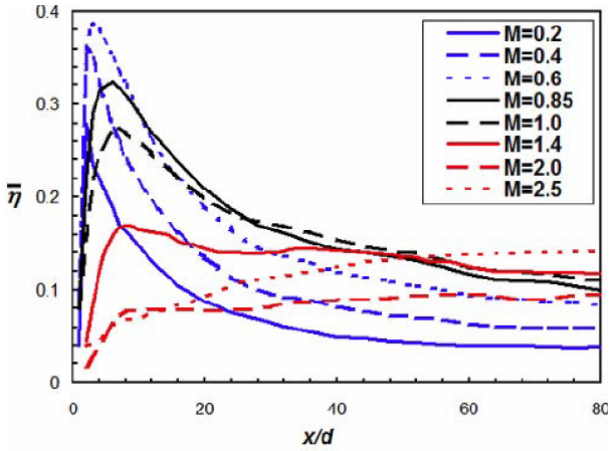

Figure 2.11: Distributions of adiabatic film effectiveness for varying BR as a function of x/d, representing the streamwise distance [63].

it leads to increased lateral spreading of the coolant jets due to greater diffusion. The overall impact of mainstream turbulence is mostly negative when the BR is low, and the coolant jet remains attached to the surface. However, for high blowing ratios where jet lift-off occurs, the detrimental effect becomes less pronounced and can even be beneficial [65]. The relationship between the freestream turbulence level and the laterally averaged effectiveness, expressed as a function of the momentum flux ratio, for a smooth surface and low freestream turbulence is reported as an example in Figure 2.13. Extensive experimental investigations have been conducted to comprehend this phenomenon, resulting in the development of correlations that can predict the adiabatic effectiveness of specific film cooling configurations, especially when flat surfaces are investigated [60, 63]. However, when examining film cooling on vanes and blades, the complexity of the problem intensifies due to the involvement of a greater number of fluid-dynamic and geometric variables. The

curved shapes of the pressure and suction sides of vanes/blades are known to significantly influence film cooling behavior [61, 67, 68]. According to Han et al. [69], it can be concluded that a convex surface is more advantageous for cooling effectiveness at low blowing ratios, whereas a concave surface exhibits superior performance at higher coolant momentum. A concave surface demonstrates improved performance when subjected to higher coolant momentum. In contrast, a convex surface tends to perform better due to the presence of pressure gradients normal to the wall. A concave surface typically exhibits lower coverage compared to a flat plate, while convex surfaces can achieve better coverage due to the same phenomenon but in the opposite direction. In this regard, in 2015 Xingdan et al. [70] conducted experimental tests to examine the film cooling performance at the leading edge region of a turbine blade using Infrared Radiation (IR) thermography and by varying BR. Six different leading edge cooling geometries were designed by varying the radial angle from 35° to 90°. The results indicated that the blowing ratio significantly influenced the cooling effective-

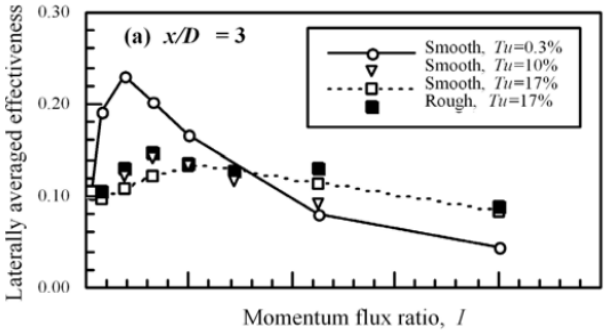

Figure 2.12: The relationship between the freestream turbulence level and the laterally averaged effectiveness, expressed as a function of the momentum flux ratio, for a smooth surface and low freestream turbulence [66].

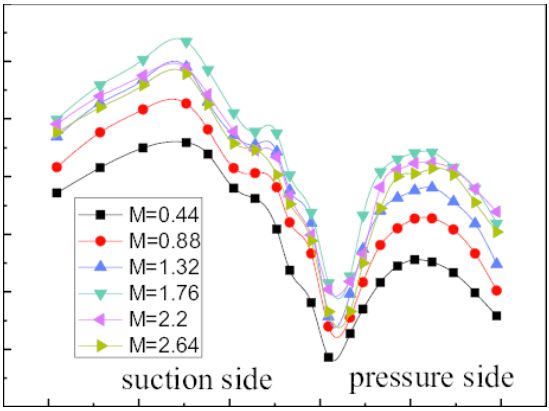

Figure 2.13: Secondary flow vortex model [58].

ness, exhibiting an optimal blowing ratio. The influence of the blowing ratio on the average adiabatic cooling effectiveness along the lateral direction on the test blade surface is reported in Figure 2.13. Additionally, other factors related to the characteristics of the mainstream flow also contribute to the overall performance. These factors include pressure gradients in streamwise direction, how the boundary layer develops and transition phenomena.
Finally, the examination of the physics associated with film cooling also encompasses the interaction between the coolant and the mainstream flow, specifically concerning the generation of vortical structures, referred to as "jet in crossflow" in the literature. These structures are depicted in Figure 2.14. They are outlined below [10]:

- *Jet shear-layer vortices*: caused by the instability of the annular layer, which experiences shear stress and usually separates at the exit of the hole in a ring-shaped manner.
- *Horse-shoe vortex*: formed through a similar mechanism to the flow structures that develop around solid obstacles, this phenomenon can contribute to the lateral dispersion of coolant across the surface;

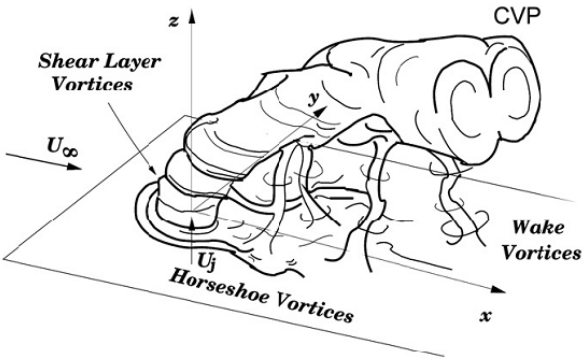

Figure 2.14: Vortical structures created by the interaction of a jet and crossflow [71].

- *Counter-rotating vortex pair (CVP)*: emerging in close proximity to the hole exit, these vortices are both reinforced and redirected as they interact with the crossflow, adopting a distinct kidney-shaped configuration. Although there is no universal consensus on the precise factors contributing to their formation [72, 73], these vortices play a crucial role in the mixing process. They can either facilitate the lateral dispersion of the jet, promoting its spread over the surface, or, in some instances, lead to its lifting, resulting in an adverse outcome;
- *Wake vortices*: arising from the boundary layer separation immediately behind the jet on the surface, these vortices are subsequently lifted by the jet's own motion and carried downstream.

It is important to point out that, when the coolant and the surrounding flow experience turbulent blending at the outlet of the holes, it is advantageous that adjacent jets can combine, forming a layer of coolant further downstream. This effect is dependent on the spacing between the jets and can be intensified by employing

multiple rows of staggered holes [10]. Furthermore, also taking into account more realistic swirled conditions at the stator inlet leads to a sensible alteration of film cooling behavior on the airfoil surface. More information regarding this aspect will be provided in the next sections.

2.3 Combustion-turbine interaction phenomena

From an historical point of view, the combustor and the turbine have been studied separately by distinct teams and with distinct tools and practices, which exchange information through an interface established between the two components. The idea behind such decoupled approach is to assume intrinsically that the performance of the two components is identical whether they are studied separately or coupled. Therefore, the HPT inlet profiles are extracted by a time and tangential average of the CC exit ones to perform Computational Fluid Dynamics (CFD) simulations, while experiments are usually obtained with non engine-representative combustor simulations [74]. Even if the decoupled approach is capable of reducing the overall computational time compared to a CC-HPT nozzle calculation, it is known to provoke potential inaccuracies. For example, studying the combustion chamber and the turbine separated does not allow to take into account the potential effects induced by the vanes on the combustor flow field, which can modify flow quantities upstream the nozzle guide vane (NGV) [75–77]. For this reason, especially when exploring multiple operating conditions, it is not straightforward to enforce the CC exit condition representing the blockage created by the vanes. In the next sections, the main effects that the presence of the first stage stator has on the flow evolving inside the combustor and how, at the same time, the latter impacts the aerothermal behavior of the NGV (Nozzle Guide Vane) will be presented.

2.3.1 Influence of the combustor on the NGV

2.3.1.1 Influence of the residual swirl

As anticipated, the central area of interface plane between combustor and turbine is characterized by high swirl values due to the PVC generated in the combustion chamber and transported by the flow to the exit plane. Such swirled flow can be found also at the exit of the combustor interacts also with the following stator, potentially affecting its aerodynamic and thermal behavior. Generally speaking, the velocity disuniformities can be quantified by looking at the swirl angle (for the tangential ones) and the pitch angle (for the radial ones), which are obtained by normalizing the tangential and radial velocity with the axial velocity, respectively. Regarding the tangential non-uniformities, one of the consequences of swirl is its ability to distort the radial and tangential pressure gradient on the surface of the stator vanes, altering the stagnation line on the leading edge. The different pressure distribution caused by the flow field has been analyzed by Insinna et al. [41] in terms of Mach number on the vane surface. They observed that these effects are significant at the 10% and 90% of the vane height, up to a distance of approximately 40% of the axial chord. Moreover, it has been demonstrated that the clocking position has a considerable impact, especially in the areas near the liner walls, where zones with negative/positive incidence depending on its rotational direction are observable. The different relative positions of the nozzle airfoil with respect to combustor burner axis are reported in Figure 2.15. As a matter of fact, it has been demonstrated that when the combustor is aligned with the leading edge, it often results in a direct impact of the residual swirl on it, leading to more pronounced effects on the distortion of the stagnation line. It has been observed that under this condition, the distortion is greater, significantly affecting the path defined by the cooling flow exiting the holes in those positions. On the other hand, the orientation of the vortex core can reverse the twist of the stagnation line. It is observed that positive swirl values generate areas with positive incidence near the hub, while negative incidence is observed on the shroud,

which has consequences for the migration of coolant on both the leading edge and the suction and pressure sides. Conversely, imposing a negative swirl results in the opposite effect.

The ability of the residual swirl to alter the stagnation line distribution has been demonstrated in various studies. An example is reported in Figure 2.16. Such alteration also disrupts the paths of the cooling fluid, which no longer follow the intended routes and may result in surface areas completely left uncovered. Whang et al. [80] also demonstrated that, depending on the clocking position, the residual swirl can influence the thickness of the boundary layer on the vane, resulting in an alteration of the heat transfer as well. Such effects can also be observed on the combustor liner, on which the cooling holes for lean burn configurations are arranged almost at the combustion chamber exit. Indeed, Werschnik et al. [78] showed that the residual swirl decreases the boundary layer thickness on the liner walls, increasing the mixing of the coolant with the hot main flow, hindering its attachment to the surface and thus inhibiting its effect.

Regarding the radial non-uniformities in terms of velocity, as anticipated, the pitch angle is the parameter that describes the radial migration of

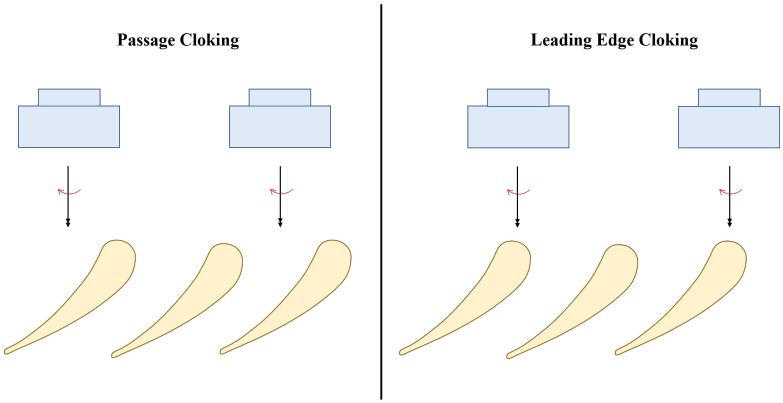

Figure 2.15: Representation of swirler clocking positions (based on [78]).

the flow. It is worth noting that radial migration and subsequent mixing of the cooling with the main hot flow could be significant for both the stator vanes and the cooling of the component casing itself. Zhang et al. [80] have indeed identified a relationship between the distribution of pitch angle along the inner walls and the temperature of the flow that sweeps them. In Figure 2.17, it can be observed that the hub has a higher temperature compared to the shroud, attributing this difference to the higher mixing between the cold flow and the main flow on the wall at low radial positions, which is associated with positive pitch angle values that indicate radial migration of the internal fluid. This phenomenon is not observed along the shroud, where zero pitch angles can be observed.

Moreover, the presence of residual swirled flow has also an impact on the distribution of the secondary flows inside the vane passage. As a matter

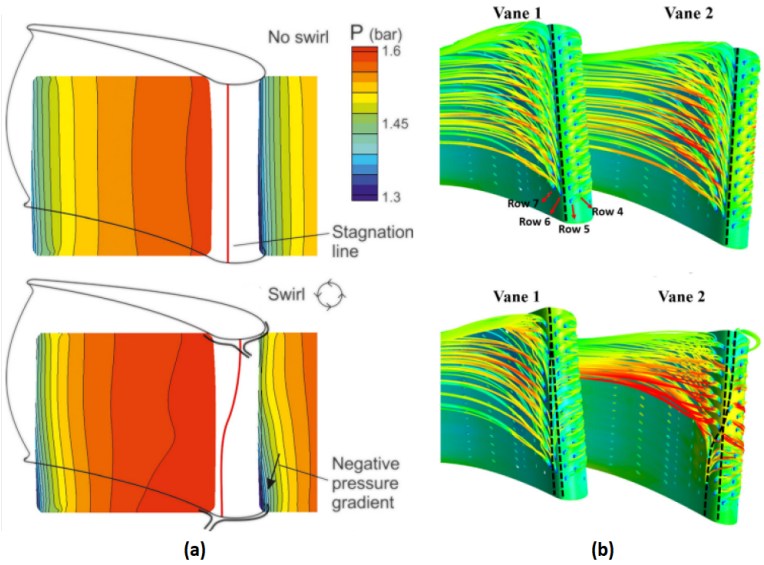

Figure 2.16: a) example of tilting of the stagnation lines due at the residual swirl [79] and b) example of the consequent alteration of the behavior of the cooling system.

of fact, Sharma et al. [58] correlates the horseshoe vortices distribution with the heat transfer on the vane surfaces. In particular, it has been observed that the migration of these vortices and their interaction with the rotating structures generated by the collision between the main flow and the leading edge result in a decrease in the thickness of the boundary layer. This, in turn, increases heat transfer and generates areas with higher temperatures.

2.3.1.2 Influence of the temperature non-uniformities

The effect of temperature distortion on the inlet plane of the stator has consequences on its behavior, particularly in thermal aspects, compared to the uniform case. From an aerodynamic perspective, several investigations [37, 41] have shown that the presence of the hot streak has no significant effects on distribution of the Mach number on the vane surface and on pressure distribution. Consequently, it has been demonstrated [37] that

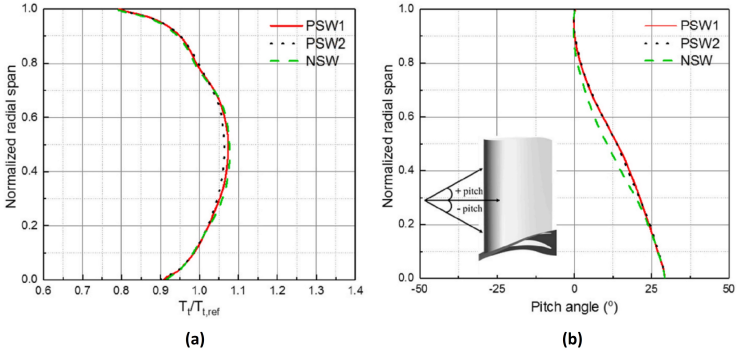

Figure 2.17: Example of radial distribution of a) total temperature and b) pitch angle at the inlet plane of the stator. PSW1, PSW2 and NSW refer to three different configurations studied by Zhang et al. [80]: positive swirler aligned with passage (Case PSW1), positive swirler aligned with leading edge (Case PSW2) and negative swirler aligned with passage (Case NSW).

the hot streak alone appears to have negligible effects on the distribution of the film cooling on the stator surface. In fact, as shown in Figure 2.18, the paths of the fluid jets coming from the cooling holes on the vane surface are not distorted when comparing the case (a), which considers a flow without swirl and uniform temperature at the inlet, to the case (b), where only the hot spot is introduced into the flow. However, other studies have highlighted how the hot streak (HS) affects the BR and DR of the film cooling system. Insinna et al. [41] have demonstrated that the sole effect of the HS can influence these parameters, leading to greater penetration of the cooling flow into the main fluid and worsening the efficiency of the cooling system. The most interesting aspect to examine is the effect of the hot streak on temperature distribution and heat flux on the vane surface since it will impact the turbine's life time. Many studies have shown that the non-uniformity of the temperature profile at the inlet results in a general increase in these values, particularly in the zones where the hot core flow and NGV interact, which strongly depends on the clocking position. As a matter of fact, Insinna et al. [41] also evaluated an average metal temperature increase by over 4% and a higher average heat flux by 19% compared to the case with uniform inlet. Mansouri et al. [81] analyzed how three different shapes of hot streaks, generated by various swirlers, impact the temperature distribution on the surface of the airfoil and how the transport of the hot streak changes, taking into

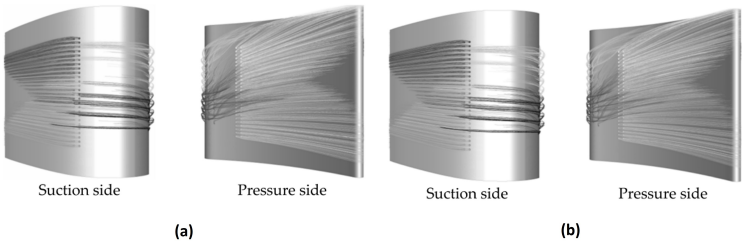

Figure 2.18: Example of streamline pattern of the film cooling by imposing a) uniform inlet in terms of velocity and temperature and b) by taking into account the only presence of the hot streak [37].

account a incoming swirled flow and one characterized by a predominantly axial velocity distribution, as reported in Figure 2.19. Generally speaking, it was observed that the hot streak divides into two segments as it goes through the passage and then recombines downstream. Moreover, the authors demonstrated that the transport of the three different hot streaks across the vane passage strictly depends on the inlet conditions: taking into account a predominantly axial velocity distribution at the inlet, all the three different hot streaks undergo axial migration and experience deformation due to the influence of the vane profile and boundary layer; taking into account a incoming swirled flow instead, all the distributions of hot streaks undergo significant alterations, and their transportation shifts towards a radial direction due to the rotational momentum of the flow. This means that in order to accurately characterize the interaction between the hot temperature distortions coming from the combustor and the NGV, it is essential to also consider the non-uniformities in terms of velocity (residual swirl).

Moreover, in order to understand how the clocking position influences the temperature distribution on vane and the hot streak migration, Koupper et al. [82] carried out an numerical study by means of LES simulations of a 1.5 high pressure turbine stage developed within the European project FACTOR. The authors demonstrated that the hot streak centered

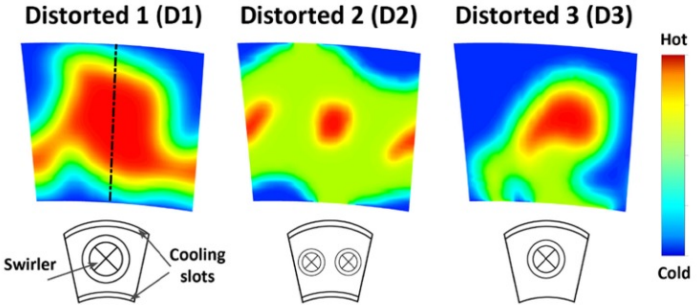

Figure 2.19: Example of three different generated hot-steak maps [81].

on the passage between adjacent two vanes is better preserved, mainly concentrating along the suction side of an airfoil and exhibiting a still visible and hotter core compared to the other studied case (centered on leading edge of the vane), as shown in Figure 2.20. Regarding instead the consequences that the different clocking positions have on the surface temperature distribution of the two analyzed airfoils (see Figure 2.20), the impact of the hot streak centered on the leading edge (Clocking LE) of the first airfoil (NGV1) generates regions with much higher temperatures compared to the corresponding regions in the other case, when the hot streak centered on the passage (Clocking PA). Consequently, NGV1 is 5% hotter than the second airfoil NGV2. On the other hand, in the Clocking PA case, the hot streak itself has a reduced impact on the wall temperature since the hottest flow is located away from the walls. However, a significant migration of coolant flow from the combustor is observed on the pressure side of NGV2. As a result, it has been demonstrated that NGV2 is 2% colder than NGV1.

Regarding instead the impact that the hot steak has on the HTC evaluated on the vane surface, Phan et al. [83] numerically studied the heat transfer performance predictability with uncertainties in the inflow boundary conditions. In particular, the heat transfer coefficient has been studied for two various hot streak configurations. Despite significant differences in the area-averaged heat flux among the investigated hot streak configurations, the surface heat transfer coefficient exhibits only minor changes, except for the case with the highest temperature distortion amplitude and hot streak aligned to the passage center. In fact, it has been demonstrated that under such hot streak conditions, the point at which the laminar-turbulent transition begins on the suction surface is shifted further downstream. Hence, this finding indicates that the clocking position of the hot streak has a notable impact on the point of laminar-turbulent transition and, consequently, on the heat transfer coefficient at high levels of distortion strength. However, its effect is less pronounced at lower levels of distortion amplitude.

Regarding the impact on the film cooling, it has been observed that the

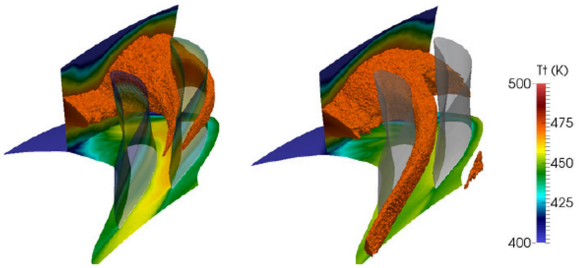

(a) Clocking LE. (b) Clocking PA.

(a)

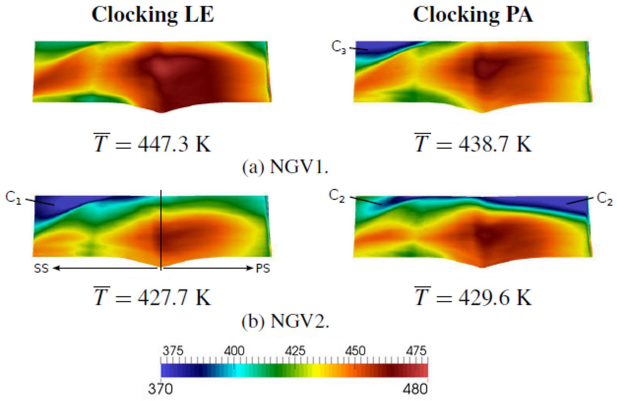

(b)

Figure 2.20: Example of a) contours of hot streak by means of an isosurface coloured by total temperature and b) adiabatic wall temperature distributions on the two vanes of the test case FACTOR depending on the swirler clocking position [82].

hot streak alone is unable to distort the path of the coolant jets exiting the cooling holes. However, when analyzing the adiabatic effectiveness on the blade surface, it is evident that there is a general deterioration [37], especially in areas where the hot streak directly impacts the surface. This is expected, considering that the definition of adiabatic effectiveness takes into account the temperature on the blade surface, and it is clear that this temperature increases when the gas temperature entering the stator is higher.

2.3.1.3 Influence of the turbulence

In certain situations, turbulence intensity can have a significant impact on the flow within the turbine. As a matter of fact, it has been proved an increase in turbulence intensity at the nozzle inlet leads to broader wakes and improved mixing at the nozzle exit [84]. Moreover, some studies have shown that high levels of turbulence at the inlet of the stator stage anticipate the transition of the boundary layer from laminar to turbulent and increase heat transfer on both the pressure side and the suction side of the stator vanes [49, 85]. For example, Bacci et al. [86] analyzed the effect of increased inlet turbulence on the measured heat transfer coefficient (HTC) on the stator surface, as shown in Figure 2.21. They observed a minor increase near the leading edge and the first part of the pressure side, while the largest increases were found in the final part of the pressure side, with significant changes occurring in the suction side in the transition zone. The increase observed at the leading edge and the pressure side was analyzed through LES (Large Eddy Simulation) analysis by Kanani et al. [87]. Although no laminar-to-turbulent transition was detected in the boundary layer, it still exhibited non-steady and three-dimensional flow, with the formation of vortex structures as “stripes” near the leading edge. These structures lose their organization due to the change in curvature of the surface, thereby enhancing heat transfer.
Regarding the interaction between turbulence and hot streak, in literature it has been demonstrated that the mainstream turbulence intensity has minimal influence on the attenuation of hot streaks, since, under mod-

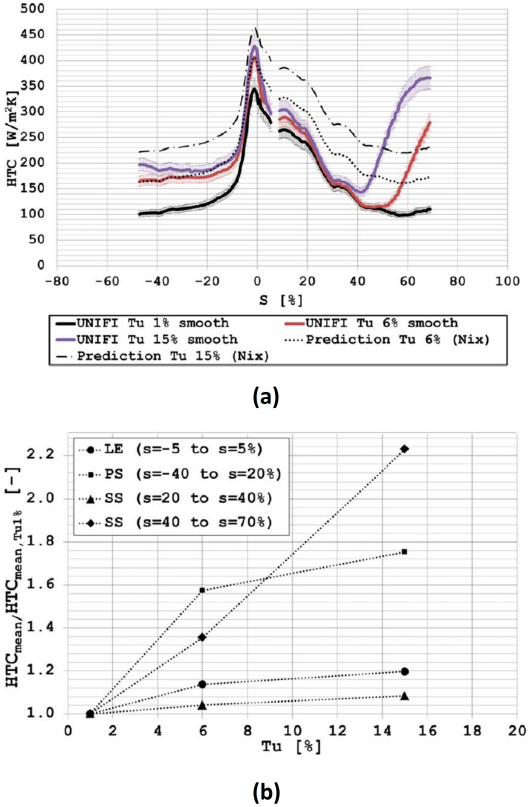

Figure 2.21: Example of a) effect of inlet turbulence intensity on measured HTC as a function of the curvilinear abscissa and b) on measured HTC values averaged on different portions of the profile [86].

erately turbulent conditions, the latters remain more concentrated with higher temperature gradients [88, 89]. However, a suitable combination of nozzle film cooling and high turbulence can reduce the peak temperature of hot streaks by 74%.

As a matter of fact, the effect of turbulence on film cooling is quite complex and depends on other factors such as hole injection angle and BR. Martin

et al. [90] analyzed the behavior of the cooling system by varying the turbulence level of the incoming flow. The study showed that increased turbulence leads to enhanced mixing between the coolant and the main flow, resulting in a decrease in the adiabatic film cooling effectiveness and an increase in heat transfer between the blades and the hot flow. While this occurs at low BRs, at high BRs, increased turbulence levels could have positive effects. This is because the turbulence can result in a beneficial transport of the film cooling, which penetrates into the hot main flow due to the high BR, toward the boundary layer and promote so its adhesion to the wall, as observed in Figure 2.22. In conclusion, generally speaking, increased turbulence has been found to disrupt the coherence of the coolant jets exiting the holes, increasing its mixing with the main flow. This phenomenon can lead to an increase in coolant coverage, albeit with a decrease in the maximum values of adiabatic effectiveness.

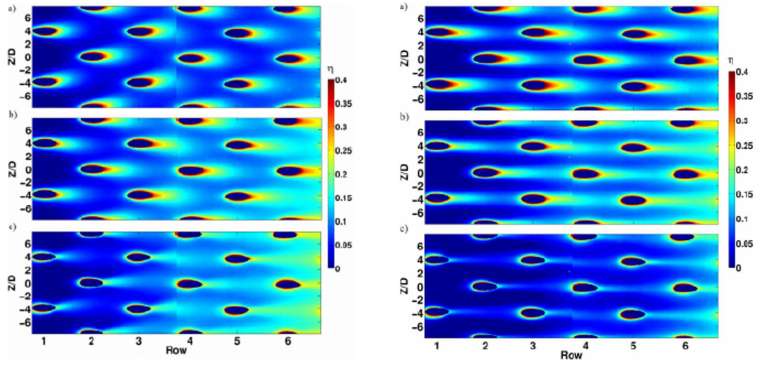

(a) Measured adiabatic effectiveness for DR=1.4, Tu=25 %: a) BR=0.3; b) BR=0.6; c) BR=1.5

(b) Measured adiabatic effectiveness for DR=1.4, Tu=10 %: a) BR=0.3; b) BR=0.6; c) BR=1.5.

Figure 2.22: Example of variations of adiabatic effectiveness as a function of inlet turbulence and BR and DR. [90].

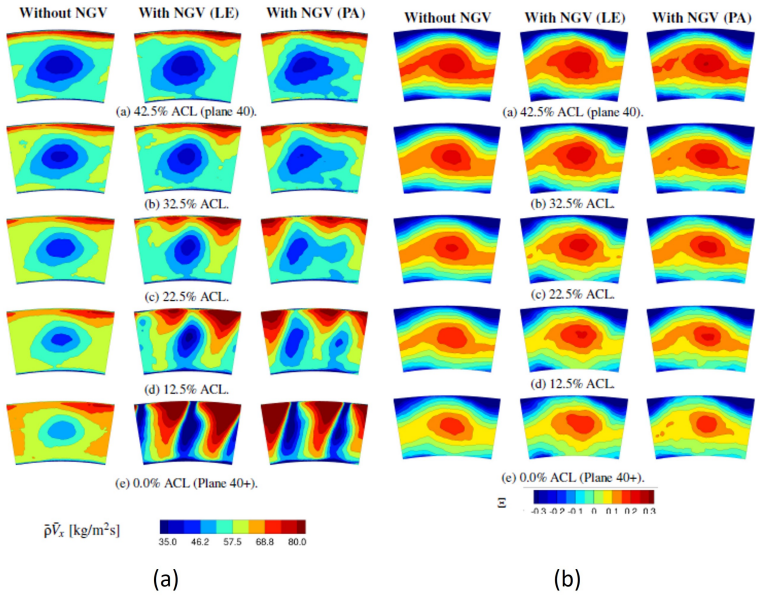

Figure 2.23: Evolution of axial momentum (a) and temperature coefficient (b) across the NGV starting from the inlet plane [82].

2.3.2 Influence of the NGV on the combustor

Concerning the influence of the stator on the combustor, in the context of the European project FACTOR, Koupper et al. [82] has carried out LES numerical simulations of axial combustor equipped with a 1.5 high-pressure turbine stage, representing a lean burn architecture, in order to take into account for the potential effect of the stator on the combustor. The results have highlighted that there is a significant redistribution of the mass flow, expressed as axial momentum ρV_x, as the vanes are approached. As can be seen from Figure 2.23, it can be observed that, up to a distance of approximately 30% of the chord, the differences remain limited. However, as the leading edge is approached, flow accelerations at the passages and decelerations at the vane nose are visible observable.

Such discrepancies are also dependent on two clocking positions of the hot streak relative to the NGVs, as can be still noted in Figure 2.23. These phenomena are also observed in the turbulent kinetic energy values, which tend to increase and concentrate in areas where the vortex core propagates. In this case, the clocking position becomes even more relevant as it has consequences for vortex propagation. The peak values of turbulent kinetic energy when the swirler is aligned with the stator passage can exceed those in the model without vanes by up to 25%. Moreover, as the non-uniformities in axial momentum are much more limited in the tangential direction, there are no substantial differences observed in the temperature distribution, even on planes very close to the LE, as shown in Figure 2.23. However, when the stator is included in the computational domain, there is a higher segregation of the vortex, which concentrates in the central area and reduces its interaction with the cooling mechanism. This results in higher temperatures in those regions.
Similar results have been also observed by Roux et al. [75], who carried out a numerical study on a periodic sector of an actual annular gas turbine, which was either inclusive or exclusive of two NGVs. The findings suggest notable alterations in the flow pattern, particularly towards the back of the combustor, while the primary region largely remains unaffected. Moreover, it is important to point out that apart from the potential influence caused by the existence of the NGVs, the obstruction resulting from the restricted flow passage alters the acoustic environment at the combustor exit [45]. In modern aero-engines, the HP turbine stages typically operate under choked conditions, meaning the sonic throat causes the reflection of acoustic waves to some extent. This can lead to the reflection of the acoustic waves generated by the flame and to the partial transformation of the entropic waves generated by the formation of hotspots within the chamber into acoustic waves. In this case, the propagation can be directed back into the chamber or through the turbine stages. When acoustic waves return to the chamber, they have the potential to interact with the flame, resulting in the occurrence of combustion instabilities. In the most severe scenarios, these instabilities are not adequately suppressed by the

existing technological systems. Instead, they are amplified and ultimately contribute to the deterioration of the combustion chamber [45]. However, this topic will not be explored further, as it is beyond the scope of this work.

2.4 Numerical past studies

Given the information provided earlier, it is essential to conduct a comprehensive analysis of the interactions between the combustor and turbine for a reliable aero-thermal design of the initial turbine stage. To achieve this, employing unsteady fully coupled simulations that encompass both the combustor and the NGV in the computational domain is the most dependable numerical approach [46, 91]. However, performing such simulations presents challenges due to the distinct flow fields in each component, necessitating different spatial and temporal discretization methods. Conversely, studying the combustor and NGV in isolation may lead to significant inaccuracies as the coupling effects between the components are disregarded, impacting the prediction of their respective flow fields [75–77]. Similarly, utilizing the Reynolds Averaged Navier-Stokes (RANS) approach can lead to additional approximations in forecasting the thermal and flow patterns because RANS simulations tend to underpredict the turbulent mixing [92, 93]. Nonetheless, RANS remains advantageous for its ability to control computational cost, making it a historically significant method in investigating combustor-turbine interaction phenomena. In this context, an alternative to RANS, which offers higher reliability, is the Large-Eddy Simulation (LES) [82, 94, 95]. LES has the capability to resolve most of the turbulence scales, leading to high-fidelity solutions [96]. However, due to its demanding spatial and temporal discretization requirements, LES comes with a significantly higher computational cost. Consequently, its usage is often limited to simplified test cases, more suitable for laboratory applications where realistic cooling systems are not incorporated [97]. To address this computational challenge, hybrid RANS-LES turbulence models, such as Scale Adaptive Simulations (SAS) [98]

and Detached Eddy Simulations (DES) [99, 100], have gained prominence in recent studies. For instance, within the FACTOR (Full Aerothermal Combustor-Turbine interactions Research) project, SAS simulations were conducted to study the aero-thermal field on vanes present in a non-reacting test rig of a lean burn annular combustor. By comparing the CFD predictions with experimental results obtained by Bacci et al. [101, 102], Andreini et al. [103] demonstrated that SAS simulations provide better descriptions of the recirculating area inside the combustor compared to RANS. Consequently, SAS improves the prediction of turbulent mixing between the hot main flow from the combustor and the cooling flows [104]. As a matter of fact, Figure 2.24 displays, along with the computational domain employed for the CFD, the relative temperature difference assessed across the experimental domain for both RANS and SAS calculation at the exit of the combustor. As can be seen, RANS significantly overestimates the experimental values in the hot spot and underestimates them in the cold layers. Conversely, SAS provides a more accurate match, with differences staying within 10%. Another alternative to SAS and DES is the Stress-Blended Eddy Simulation (SBES) model, which has gained popularity in recent years. SBES allows modeling of boundary layer regions using the less computationally expensive RANS instead of LES [105]. For example, Verma et al. [106] simulated a coupled combustor-turbine configuration using SBES. The results were then compared to a setup where RANS was used only for the NGV and SBES only for the combustor. The study revealed that the coupled approach is more efficient than the decoupled one, as the latter requires an interactive procedure to converge the co-simulation model.

The application and generation of the most representative and reliable boundary conditions at the inlet of the S1N have assumed an increased importance in studying the combustor-turbine interaction phenomena in the recent years in order to perform decoupled simulations as accurate as possible. As a matter of fact, in the industrial context, assigning the inlet conditions to the first-stage stator, derived from the stand-alone combustor analysis, is obtained in a simplified manner. This simplifica-

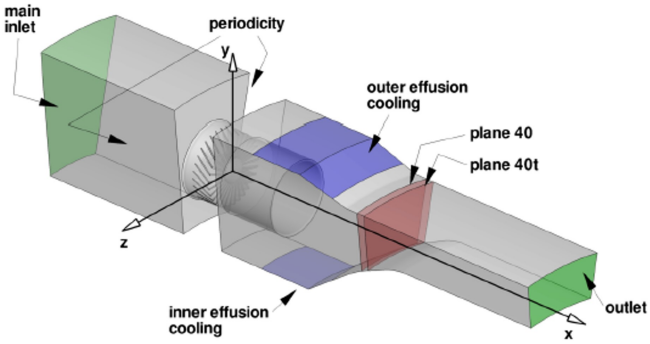

(a)

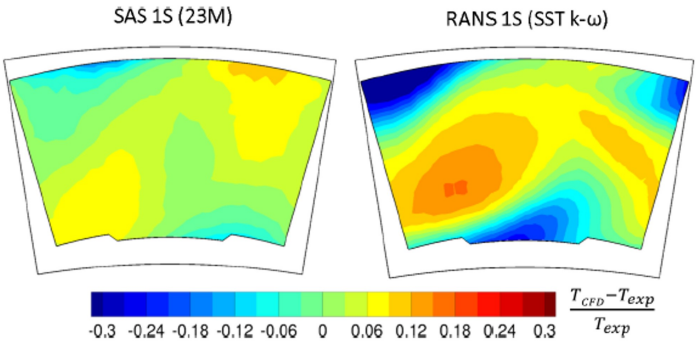

(b)

Figure 2.24: (a) computational periodic domain one sector of the FACTOR test rig and (b) the relative temperature difference assessed across the experimental domain for both RANS and SAS calculation at the exit of the combustor [82].

tion involves averaging the inlet quantities both spatially and temporally, resulting in 1D profiles or even 0D representations. The reason for this approach lies not only in its low complexity but also in the fact that the limited computational power of computers at the time compelled designers to use non-scale-resolving numerical models, based on the steady-state hypothesis. In this context, Duchaine et al. [107] perform a LES simulation of an integrated combustion chamber and the first turbine stage, comparing then the results to LES simulations of the stand-alone turbine stage. As inlet boundary conditions for the turbine stage, two-dimensional mean maps extracted from the fully integrated case have been imposed, without and with three different turbulence injections. The authors demonstrated that, even if the results seem to be quite insensitive to the different turbulent injections, the CFD predictions obtained by simulating the stand-alone first stage are highly impacted by the imposed mean boundary conditions, confirming the importance of employing coupled approach or imposing boundary conditions as realistic as possible. As a matter of fact, in the context of the project FACTOR, Martin et al. [108, 109] generate a database of unsteady inlet boundary conditions under laboratory non-reactive conditions for the isolated NGV. To do so, the data have been recorded at the interface plane between the combustor and nozzle from a fully coupled LES simulations including both components. The data are then post-processed and decomposed using advance methods, such as POD and SPOD in order to assess if such methods can be utilized to partial reconstruct the numerical database. The main objective of such analyses are to assess whether the flow field of the integrated combustor-turbine simulation can be reconstructed in the isolated domain using the aforementioned approach and assess the influence of dominant flow structures on the flow within the vane passage. As a matter of fact, modal decomposition obtained by using POD enables the inclusion or exclusion of various flow features from the inflow data, facilitating the examination of the influence of leading-order features from the combustor on the NGV response. In particular, in this case the PVC vortex is identified as the most dominant flow feature within the

chamber, even though it disintegrates shortly after exiting the confining duct. In order to evaluate the capability of an independent NGV LES to replicate the flow field of the integrated simulation, several unsteady inlet conditions, including one constant condition, are applied to isolated NGV simulations [110]:

- *Case A*: this case represents the fully integrated reference domain, serving as a benchmark for the isolated simulations;
- *Case B*: in this scenario, the complete unsteady dataset acquired from the previous simulation is utilized to generate a fully unsteady inlet boundary condition for the isolated NGV domain;
- *Case C*: all modes from the POD basis, excluding the first ten modes (representative of PVC), are employed as unsteady inlet boundary condition;
- *Case D*: first ten POD modes, representing the PVC and representing of 50% of the total energy, are employed as unsteady inlet boundary condition;
- *Case E*: this case employs the temporally averaged 2D flow field at the inlet of the standalone NGV simulation.

The differences among the four isolated nozzle simulations (Case B, C, D and E) are then examined and compared to the results obtained from the fully integrated simulation (Case A). The authors noted that, despite the PVC being the most energetic structure in the chamber and significantly affecting the flow field in the HPT, the differences in first-order quantities between unsteady cases using all modes without the PVC (Case C) and with the PVC as the inlet signal (Case D) are limited at Plane 40, as can be seen from Figure 2.25. However, including all POD modes is observed to closely resemble the reference case, thus validating the effectiveness of utilizing POD technique to reconstruct the flow field at the exit of combustion chamber. Moreover, looking at flow field inside the vane passage, comparing all cases leads to the conclusion that the HPT domain

is highly sensitive to the flow field provided at its inlet, since PVC has an important contribution to the mixing between the hot and the cold flows through the vanes. This is evident looking the instantaneous temperature distribution at 50% of the span, as represented in Figure 2.26 where it is clear that Case D shows a more unsteady behaviour compared to Case C. Moreover, a time-constant 2D inlet boundary condition, often applied in an industrial context, is found to yield harsher aerothermal conditions than predicted in the case using the fully unsteady flow field, as can be seen from Figure 2.26. In particular, lack of mixing causes even extreme temperature values, especially in the wake of NGV1. Hence, from this analysis, it is event how much is important to employ a representative inlet boundary conditions for the decoupled first stage nozzle. Moreover, the same authors performed further analyses by employing SPOD. Since

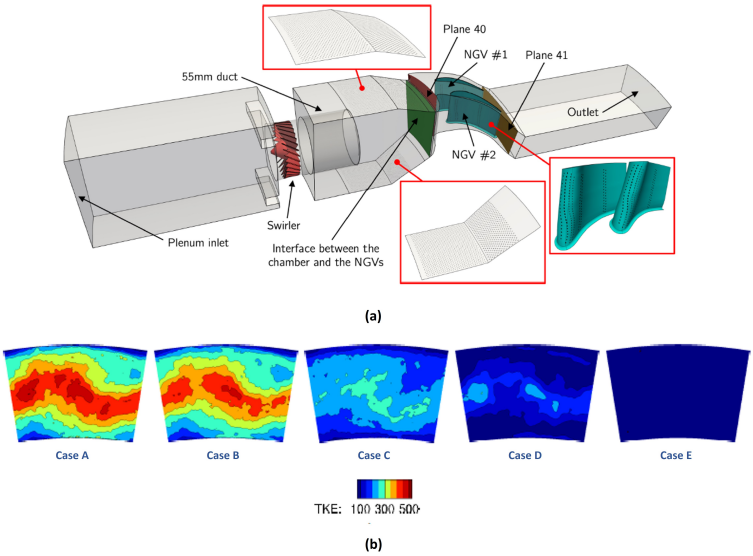

Figure 2.25: (a) computational domain representing the fully integrated FACTOR configuration [108] and (b) the turbulent kinetic energy at Plane 40 for different compared case [110].

partial reconstructions of the initial database can be accomplished using SPOD as per POD, the authors carried out five partial reconstructions, each targeting different levels of total energy [108]:

- *Case F99*: corresponding to a reconstruction that includes 99% of the total energy;
- *Case F90*: corresponding to a reconstruction that includes 90% of the total energy;
- *Case F65*: corresponding to a reconstruction that includes 65% of the total energy;

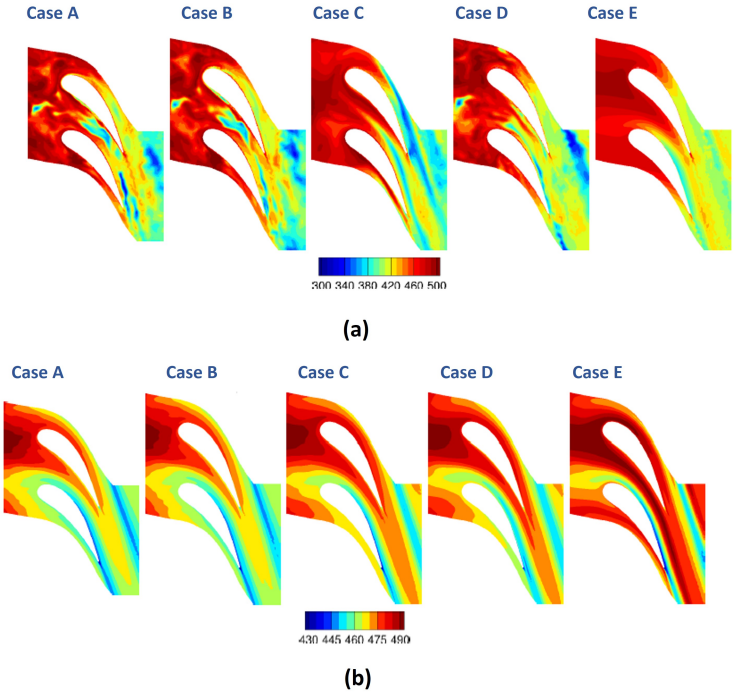

Figure 2.26: (a) instantaneous temperature and (b) time-averaged at 50% of the span [110].

- *Case F20*: corresponding to a reconstruction that includes 20% of the total energy;
- *Case F10*: corresponding to a reconstruction that includes 10% of the total energy;

These five cases listed above, obtained by using SPOD technique, are compared hence with the integrated simulation, assumed as reference, and with four other scenarios that employ instead conventional methods [108]:

- *Case S0*: 0D quantities are prescribed at the inlet. These values are obtained by spatially and temporally averaging the ones obtained from the integrated simulation;
- *Case T0*: as Case S0, with the addition of velocity RMS that are randomly generated and added to create turbulent activity (synthetic turbulent injection);
- *Case S2*: 2D maps are imposed as inlet boundary conditions, obtained by time-averaging the database;
- *Case T2*: as Case S2, with the addition of 2D maps for velocity RMS that are then used to randomly generate local turbulent activity at the inflow (synthetic turbulent injection). The 2D maps of velocity RMS are obtained from a only time-average the data recorded in the integrated simulation.

From the results [108], the authors observed that using SPOD, preserving a significant portion of total turbulent energy (at least 65%), leads to numerical predictions closely match the integrated reference simulation, while standard boundary conditions, employing 0D quantities or 2D maps with or without synthetic turbulence injection, fail to capture the coupling between the combustion chamber and the turbine. As a matter of fact, the application of standard boundary conditions consistently results in insufficient temperature fluctuations due to the limitations of the turbulence injection method used. Moreover, Figure 2.27 represents, along

with the computational domain used for the analyses, the mean adiabatic temperature contours at the vane number two for different compared case, aiming to analyze the thermal behavior of the vane. With the exception of the S2 case, the contours in the other cases exhibit close similarities. As a matter of fact, in the S2 case, the temperature at the leading edge is considerably overestimated due to the lack of turbulent mixing introduced by the boundary condition making sure that the hot spot generated by the chamber remains undissipated between the entry plane and vane LE. Comparatively, cases F90 and F65 do not show any significant differences when compared to the reference integrated simulation. Recently, also Grȕndler et al. [111] present a method to prescribe unsteady inlet boundary conditions by using Proper Orthogonal Decomposition and Fourier Series (PODFS) in order to preserve a realistic level of turbulence and unsteadiness at the stator inlet. Subsequently, such method has been employed to study a turbine case [112]. To do so, the data collected at the outlet of the stand-alone combustor simulation are employed to generate PODFS boundary conditions for a simplified high pressure turbine stand-alone stator studied by using a scale-resolving simulation performed in CFX. Then, the present simulation is contrasted with other simulations that adopt steady-state boundary conditions, aiming to illustrate how the unsteadiness in the inlet boundary condition impacts both the aerodynamic and thermal performance of the turbine. While the aerodynamics display only slight sensitivity to the approach used for applying the inlet

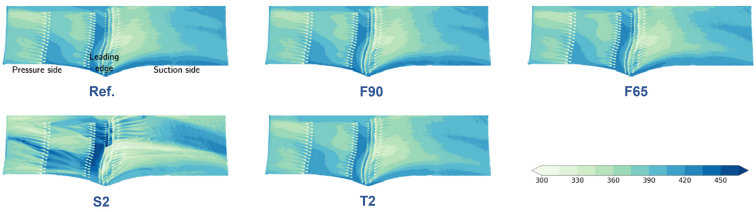

Figure 2.27: Mean adiabatic temperature contours at the vane number two for different compared case [108].

boundary conditions, it has been demonstrated that the thermal behavior of the vanes is significantly influenced by the way combustor unsteadiness is modeled.
In conclusion, the prediction and modeling as accurate as possible of the combustor outlet conditions assumed an increased importance in studying combustor–turbine interaction phenomena in recent years. Moreover, it is particularly important try to impose time-varying boundary conditions at the inlet of the first stage nozzle taking into account the effect of the unsteadiness provides more reliable and accurate results in terms of 2D quantity distributions at the outlet plane.

2.5 Proper Orthogonal Decomposition

In this section, the fundamental principles that are the basis for the analyses reported in Chapter 5 are presented. Here, the explanation of the advanced data-driven technique called Proper Orthogonal Decomposition (POD) is reported. In particular, POD proves to be a valuable tool for extracting maximum information from extensive datasets, particularly in identifying coherent structures within turbulent flows. These structures are often complex, providing valuable insights into their interactions and contributions to the occurrence of specific phenomena.
The Data-Driven Modal Analysis (DDMA) is an area of the data analysis which focuses on the discrete decomposing of a dataset into a linear combination of modes $M_j(x_i, t_k)$, characterized by their own temporal structures, depending on the values of the modes assumed at the point x_i during the different temporal instants, and by their own spatial structures, depending on the values of the modes assumed at the instant t_k in the different spacial points, as shown in Figure 2.28.
The DDMA can be employed for several applications:

- *filtering/data compression*: in case of a large dataset, it could be necessary to filter or compress the data by eliminating low-importance modes, associated to background noise. This type of data-processing is usually employed for CFD simulations and PIV

images;

- *pattern recognition*: the spatial distribution proper of a mode is strongly associated to the coherent structures that characterize the turbulent flows. For this reason, DDMA is a useful technical of post-processing for experimental activities and CFD analyses as well;

- *model order reduction (Reduce Order Model, ROM)*: in order to analyze the overall dynamics of a system, DDMA can be successfully employed to obtain a simplified model, by taking into account just the leading modes to generate a basis into which projecting the problem. In this way, it is possible to reduce the complexity of the problem and therefore the computational effort as well;

Looking at Figure 2.28, the data matrix $D(x_i, t_k) = D[i,k] \in \mathbb{R}^{n_s \times n_t}$ to be decomposed, associated to the complete dataset, can be generally assumed as:

$$D(x_i, t_k) = \begin{bmatrix} d_1[1] & \dots & d_k[1] & \dots & d_{n_t}[1] \\ \vdots & \vdots & \vdots & \vdots & \vdots \\ d_1[n_s] & \dots & d_k[n_s] & \dots & d_{n_t}[n_s] \end{bmatrix} \tag{2.16}$$

Assuming $n_s >> n_t$, as it is common for CFD and experimental applications, the aim of the DDMA is therefore to decompose the dataset in n_t modes. In particular, the matrix is generally obtained by recording the

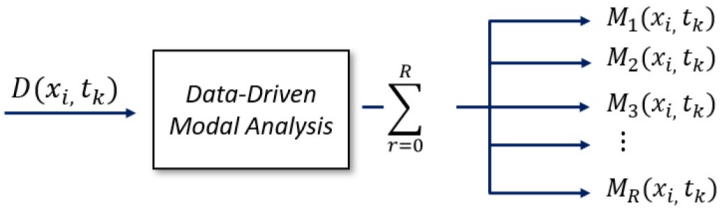

Figure 2.28: Schematic representation of data-driven modal analysis.

temporal and spatial evolution of several quantities and each "snapshot", which for a CFD application can be for example a plane placed in the computational domain, is here placed in each column of the matrix. Hence, the spatial distribution can be read by looking at the columns, while the temporal one is represented by the rows.
After performing a normalization, the matrix can be analyzed by two different but equivalent point of view, the temporal view:

$$D(x_i, t_k) = \sum_{r=1}^{R} c_r[i]\psi_r[k] = \sum_{r=1}^{R} \sigma_r \phi_r[i]\psi_r[k] \tag{2.17}$$

And the spatial one:

$$D(x_i, t_k) = \sum_{r=1}^{R} c_r[k]\phi_r[i] = \sum_{r=1}^{R} \sigma_r \psi_r[k]\phi_r[i] \tag{2.18}$$

where:

- σ_r are the eigenvalues of the data correlation matrix (that will be introduced later) and they can be associated to the energy content of each mode, representing so the weight in reproducing the global dynamics of the system. They represent the amplitude of each mode.

- ψ_r are the eigenvectors of the data correlation matrix and can be associated to the temporal evolution of each mode. As a matter of fact, the frequency content related to each POD mode can be obtained by carrying out a FFT of these terms.

- ϕ_r identify the distribution in space of each POD mode, providing thus useful information regarding the coherent structures that characterize the turbulent flows.

Therefore, from the temporal point of view, each snapshot can be represented by a linear combination of the temporal bases ψ_r, while the

coefficients of this combination c_r change depending on the spatial location of the point considered, associated to the term ϕ_r. In the same way, from a spatial point of view, each snapshot can indeed be represented by a linear combination of the spatial bases ϕ_r, while the coefficients of this combination c_r change depending on the differnt temporal instant of the point considered, associated to the term ϕ_r. So, it is clear that if ϕ_r and ψ_r represent an orhtogonal basis, they are coupled and not indipendent from each other. To semplify the problem, in order to directly associate σ_r to the amplitude of the POD mode, the temporal and the spatial bases are often assumed of unitary lenght ($||\psi_r|| = ||\phi_r|| = 1$). In this way, the decomposition of Eq. 5.1 or 5.2 becomes a matrix factorization of the form [113, 114]:

$$D = \sum^{R=rank(D)} \sigma_r \phi_r \psi_r^T \tag{2.19}$$

It is important to point out that a data matrix of rank n_t, still supposing $n_s >> n_t$, is a full rank matrix, so no approximation is obtained. Otherwise, a the rank is less than n_t, as usual practice for fluid mechanics applications, leads to a reconstructed matrix that represents an approximation of the original one.
The Eq. 5.3 can be also expressed in a more compact form:

$$D = \Phi \Sigma \Psi^T \tag{2.20}$$

where:

$$\Phi = \begin{bmatrix} \phi_1[i] & \phi_2[i] & \dots & \phi_R[i] \\ \vdots & \vdots & \vdots & \vdots \end{bmatrix} \tag{2.21}$$

$$\Sigma = \begin{bmatrix} \sigma_1 & 0 & 0 \\ 0 & \ddots & 0 \\ 0 & 0 & \sigma_R \end{bmatrix} \tag{2.22}$$

$$\Psi = \begin{bmatrix} \psi_1[k] & \psi_2[k] & \dots & \psi_R[k] \\ \vdots & \vdots & \vdots & \vdots \end{bmatrix} \tag{2.23}$$

As anticipated, since Φ and Ψ are made of orthonormal column vectors and represent bases of unitary length ($\Psi^T = \Psi^{-1}$ and $\Phi^T = \Phi^{-1}$) and Σ is a diagonal matrix, it is not possible to simultaneously and independently select Φ and Ψ. Considering the rank R, that corresponds to the number of modes, of the matrix D, the reconstructed matrix that represents an approximation of the original one D can be expressed as follows:

$$\tilde{D} = \tilde{\Phi}\tilde{\Sigma}\tilde{\Psi^T} \tag{2.24}$$

In particular, Ψ can be obtained in different way, depending on the decomposition technique selected. Assuming Ψ as orthogonal, it is possible to demonstrate that the following expression is true:

$$D(\Psi^T)^{-1} = \Phi\Sigma = C \tag{2.25}$$

If each column resulting from the product $\Phi\Sigma = C$ is normalized and the spatial basis is made by unitary length elements, it is possible to compute σ as follows:

$$\sigma_r = ||C_r|| = ||\phi_r\sigma_r|| \tag{2.26}$$

Then, once the Σ matrix is inverted, Φ can be also calculated as follows:

$$\Phi = D(\Psi^T)^{-1}\Sigma^{-1} \tag{2.27}$$

As already anticipated, Ψ can be obtained in different way, depending on the decomposition technique selected. The Proper Orthogonal Decomposition (POD or PCA) is one of the several DDMA techniques, firstly introduced by Lumley et al. [115] and now widely employed for the CFD applications. It is a energy-based decomposition which aims to approximate the original data as efficient as possible, minimizing the error from the approximation of the data using only the first R modes.

These R modes are associated to the highest energy content, that in this way is maximized. The dominant dynamics of the physical phenomenon under study is then captured, starting from the original solution $D(x_i, t_k)$, recreating a subspace of reduced size with an orthonormal basis. Hence, starting from 5.3, an approximation matrix of rank R from the original data set can be expressed as follows:

$$D = \Phi\Sigma\Psi^T \rightarrow \Phi = D\Psi\Sigma^{-1} \rightarrow D = D\Psi\Psi^T \rightarrow \tilde{D} = D\tilde{\Psi}\tilde{\Psi}^T \tag{2.28}$$

where $\Psi \in \mathbb{R}^{n_t \times n_t}$ and $\tilde{\Psi} \in \mathbb{R}^{R \times n_t}$. Since Ψ is an unitary matrix and so an orthonormal basis, from Eq. 2.28 $D = D$ is obtained. In the same way, the projection matrix, $\tilde{\Psi}\tilde{\Psi}^T$ can not be identified by an identity and so it leads to the approximation matrix $\tilde{D}$. In particular, in the POD analysis, the temporal basis is selected in order to obtain the optimal ("optimal temporal basis") as the one that minimize the error in the approximation process of the matrix D into matrix $\tilde{D}$. The optimization problem can be solved in two different but equivalent ways, so by minimizing the error:

$$\min\left(||D - \tilde{D}||_2\right) = \min\left(||D - D\tilde{\Psi}_1\tilde{\Psi}_1^T||_2\right) \tag{2.29}$$

or by maximizing the energy content:

$$\max\left(\sigma_1\right) = \max\left(||\Phi_1\sigma_1||_2\right) = \max\left(||D\tilde{\Psi}_1||\right) \tag{2.30}$$

and defining as constraints that the basis Ψ is made of elements orthornomal to each other:

$$\langle\psi, \psi\rangle = \psi^T\psi = 1 \tag{2.31}$$

By solving the problem according to the energy content maximization 2.30, employing the Lagrange multipliers methods leads to the necessity of introducing an auxiliary function $\mathcal{L}$ as follows:

$$\mathcal{L} = \left\{(D\psi)^\dagger(D\psi)\right\} + \lambda\left\{1 - \psi^\dagger\psi\right\} \tag{2.32}$$

where the first term represents the maximization object, while the second one the constraint and λ is the Lagrange multiplier. To resolve the constrained optimization problem, the Eq. 2.32 is derived ad set equal to zero:

$$\frac{\partial \mathcal{L}}{\partial \psi} = (D^{\dagger} D)\psi - \lambda\psi = 0 \tag{2.33}$$

where, since D is the known staring data matrix, ψ is the unknown quantity to be determined. From Eq. 2.33, it possible to conclude:

$$(D^{\dagger} D)\psi = \lambda\psi \tag{2.34}$$

The problem is so reduced to an eigenvalue problem, indicating that the optimal temporal basis must be the eigenvector of the matrix $K = D^{\dagger} D$, defined as the "temporal correlation matrix", with eigenvalue λ. In particular, K assumes such name because it includes the correlations between the different considered snapshots. The eigenvalue problem just described can be thus solved by determining the eigenvalues λ and the related eigenvectors starting form Eq. 2.23. It is also important to notice that a different POD method can be obtained by applying the same procedure described above computing firstly the spatial basis Φ.
As a matter of fact, it is worth to recall that the POD decomposition just described relies on two assumptions previously made (see Eq. 5.3):

- Φ and Ψ are made of orthonormal column vectors and represent bases of unitary length ($\Psi^T = \Psi^{-1}$ and $\Phi^T = \Phi^{-1}$);

- Σ is a diagonal matrix;

A priori, it is not known if such hypotheses will be met and can be verified only by carrying out the POD procedure. To do so, it is possible to combine the expression of matrix K with the Eq. 5.3:

$$K = D^T D = (\phi\Sigma\psi^T)^T)(\phi\Sigma\psi^T) = \psi\Sigma\phi^T\phi\Sigma\psi^T \tag{2.35}$$

Being K a symmetric matrix, it also diagonalizable. Representing Ψ the eigenvectors of the matrix, it is possible hence to express K as:

$$K = \psi \Lambda \psi^T \tag{2.36}$$

From Eq. 2.35 and 2.36, it is possible to conclude:

$$\Lambda = \Sigma \phi^T \phi \Sigma \tag{2.37}$$

Since Λ is an eigenvalue matrix, it is for definition a diagonal matrix, then $\phi^T \phi = I$ is true. Therefore, it results in:

$$\Lambda = \Sigma^2 \tag{2.38}$$

In this way, the previous assumptions have been demonstrated.
The POD procedure, as anticipated, was firstly introduced by Lumley [115] for CFD applications focusing exclusively on the spatial distribution of the modes (spatial POD). The Snapshot-POD methods, introduced by Sirovinch [116, 117], that correlates the spatial and temporal evolution of the modes, is instead the one employed in this work since the hypothesis $n_s >> n_t$ is verified, as for the most of the CFD investigations. The procedure for the Snapshot POD has been implemented in Matlab as follows:

- Firstly, the matrix K is computed as:

$$K = D^T D$$

- Secondly, the eigendecompositon of matrix K is performed by obtaining:

$$K = \Psi_P \Lambda_P \Psi_P^T$$

- Thirdly, the spatial POD modes and the amplitude coefficients of

the modes are computed as follows:

$$\Sigma_P = \sqrt{\Lambda_P}$$

$$\Phi_P = D\Psi_P\Sigma_P^{-1}$$

Chapter 3

Numerical prediction of the heat loads on a non reactive test rig

Contents

As anticipated in the previous chapter, the utilization of lean-premix combustors in modern gas turbines offers a means to decrease NO_x emissions by controlling the temperature of the flame. However, achieving this comes at the cost of introducing highly turbulent and uneven flow patterns that are essential for stabilizing the flame. This complex swirling flow, characterized by noticeable temperature variations, brings about changes in the aerodynamics and heat transfer within the initial high-pressure turbine stator. These changes have the potential to negatively impact the engine's longevity and efficiency.

From a computational standpoint, researchers have explored the interaction between the combustor and turbine using conventional turbulence modeling techniques, which are commonly employed during the design phase. However, more advanced scale-resolving methods have demonstrated greater reliability, having been rigorously validated against a variety of experimental results.

On the experimental front, there is a scarcity of data concerning film-cooling adiabatic effectiveness and heat transfer coefficient (HTC) measurements on the external surface of the nozzle guide vanes, especially when exposed to the representative outflow conditions from the combustor. The presence of significant temperature distortions makes conducting such measurements exceedingly challenging. As a result, there is limited existing literature that assesses these approaches in relation to this particular aspect.

The scope of the present work is to illustrate the comparison between numerical and experimental results relatively to the film-cooling adiabatic effectiveness and the external HTC over the airfoil surface, which are of major importance in the design of HPT nozzle guide vanes. To do so, an experimental test case with a combustor simulator and a nozzle cascade, where both adiabatic effectiveness and HTC measurements were carried out, is investigated. In particular, coupled and decoupled RANS and SBES simulations are carried out on both trisector and periodic one-sector configurations. Film-cooled nozzles are obviously employed for the adiabatic effectiveness test, whereas a non-cooled NGV doublet, with the same

airfoil profile of the former, is adopted for predicting the external HTC. The main objective of the analysis is to exploit the comparison between numerical predictions and experimental results to assess the capability of traditional modeling approaches in the characterization of both adiabatic effectiveness and heat transfer coefficient. This evaluation represents an effective means to assess if conventional/industrial approaches can be reliably used, when representative and highly unsteady combustor outflows are considered, or advanced and more time-consuming methods, including also turbulence models able to capture the transition, shall be adopted.

3.1 STech test rig overview

As part of the STech (Smart Technologies) initiative, a jointly funded project involving Regione Toscana and led by the turbomachinery company Baker Hughes, an experimental non-reactive test rig was constructed at the Technologies for High Temperature (THT) laboratory located at the University of Florence, Italy. The configuration of this setup, depicted in Figure 3.1, comprises realistic components from a heavy-duty gas turbine provided by Baker Hughes. Specifically, as illustrated schematically in Figure 3.1, the setup includes three authentic lean-premix burners and an actual film-cooled first-stage nozzle arrangement with three passages (referred to as a trisector geometry). It is important to mention that the swirlers are shaded in gray to safeguard Baker Hughes' proprietary information. As depicted in figure, the primary airflow is introduced into the combustion chamber through three lean-premixed burners. Adjacent to the exit region of these burners, cylindrical ducts were incorporated to ensure the presence of a realistic swirling flow at the interface plane between the combustor and the turbine. This step proved necessary during the initial phases of the project, due to the fact that the rig operates under non-reactive conditions, a methodology also employed in related studies with similar objectives [36, 118]. Depending on the specific test conditions, the primary airflow can undergo a rise in temperature via an

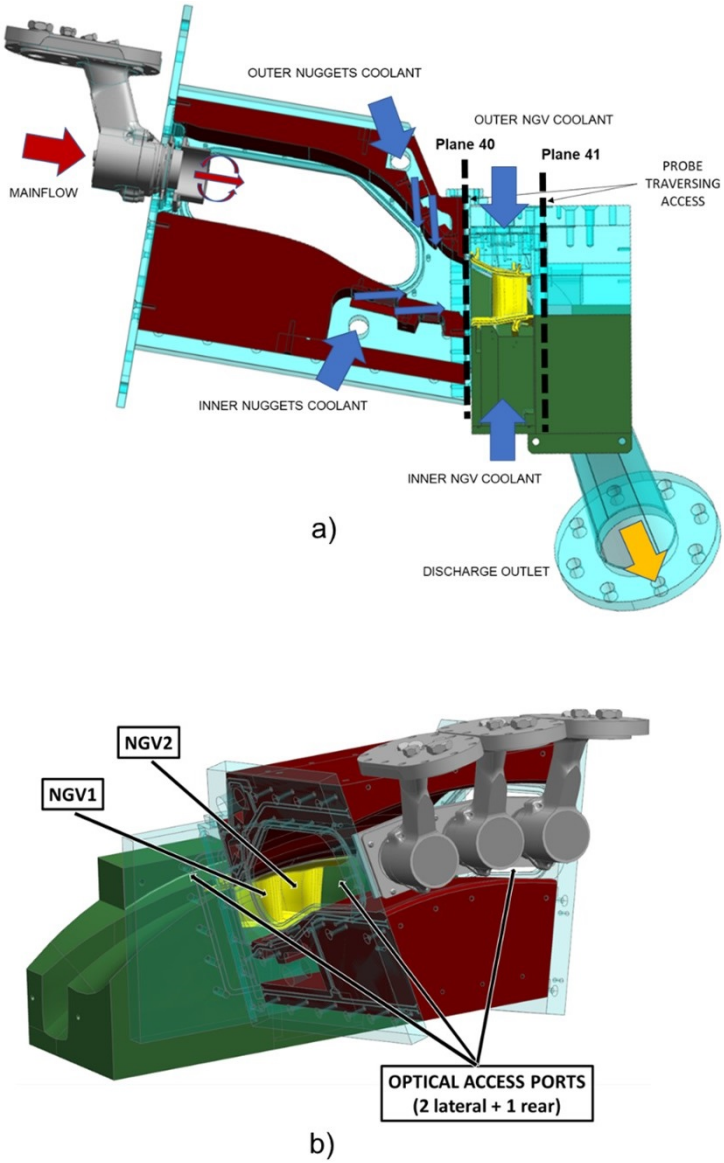

*Figure 3.1: (**a**) Test rig 3D layout and (**b**) optical access details* ***(©2024 Baker Hughes Company—All rights reserved)***.

electric heater positioned upstream of the swirlers.
Furthermore, in addition to simulating high-swirl characteristics representative of the combustor, the flow pattern at the entrance of the turbine can also be influenced by introducing temperature-distorting liner cooling nuggets. These nuggets (two on the outer surface and two on the inner surface) utilize a 2D slot-cooling mechanism and are positioned towards the end of the combustion chamber. They are supplied with ambient air.
The assembly of nozzle guide vanes (NGV) comprises a cascade of two vanes and three passages. This module underwent design in the project's early stages [119] using a design of experiments (DoE) approach facilitated by CFD. In this process, the sidewalls were constructed to mimic the desired conditions for a periodic simulation on the central vane passage, bearing in mind the non-1:1 correspondence between the actual components of the swirler and the nozzle.
The rig is equipped with access points for inserting probes to perform measurements across the nozzle cascade. These measurements are carried out at both Plane 40 and Plane 41 (refer to Figure 3.1). Additionally, three optical access ports are present, as illustrated in the same figure. The two lateral ports are used to alternately explore the front section of the PS of NGV2 or the LE and front section of the SS of NGV1. The rear port is dedicated to the final segment of the SS of NGV1.
Regarding the experimental procedures, which are extensively explained in separate works [120, 121] and are not the focus of the current thesis, a series of test campaigns were conducted. These campaigns aimed to provide a comprehensive understanding of the aerothermal conditions and turbulence intensity in the inlet and outlet regions of the NGV. This was achieved using a five-hole-probe and hot wire anemometry for traversing measurements. Additionally, measurements were performed on the surface of the NGV to characterize two key parameters: the adiabatic effectiveness produced by the film-cooling system and the external heat transfer coefficient. This was done on a solid vane airfoil, meaning it lacked film-cooling holes.
To determine the adiabatic effectiveness, the Pressure Sensitive Paint

(PSP) technique was employed. This technique utilized the analogy between heat and mass transfer and involved tracing an oxygen-free gas, used to feed the film-cooling flows. The PSP technique not only facilitated the evaluation of adiabatic effectiveness but also enabled the assessment of pressure distribution on the airfoils, allowing the measurement of vane loads. On the other hand, the measurement of heat transfer coefficients (HTC) and adiabatic wall temperatures involved a transient thermal approach. In this approach, the temperature rise on the vane surface was monitored using an infrared (IR) camera following a rapid temperature change induced by activating a fast heater within the swirling flow. For the evaluation of adiabatic effectiveness, film-cooled nozzles were employed. For the measurement of external heat transfer coefficients, a non-cooled NGV doublet was used. This non-cooled NGV doublet had the same airfoil profile as the film-cooled one but was made of a material with low thermal diffusivity and high-temperature resistance, specifically polyether ether ketone (PEEK). Detailed information about the methodologies, post-processing techniques, and accuracy assessments for both approaches can be found in references [121] and [120]. The experimental setup used glass windows for PSP measurements, while sapphire windows were necessary for capturing images with the IR camera, allowing for the derivation of HTC and adiabatic wall temperatures in the case of the non film-cooled configuration.

The operational parameters of the test rig used for stationary probe traversing assessments on Plane 40 and 41 were established based on the reference nominal conditions [119]. These nominal conditions were adjusted from real engine settings to maintain the Mach number, although achieving consistent Reynolds number similarity was not feasible due to limitations of the facility. Despite this, the rig managed to replicate conditions that are representative of secondary flows and pressure loss mechanisms, albeit with a slight reduction in heat transfer rates. Notably, specialized operating conditions were employed for the PSP and HTC tests, as outlined in Table 3.1, owing to limitations associated with the measurement techniques.

Specifically, for the PSP tests, all flows had to be maintained at room temperature. Swirler temperature variations did not significantly affect the aerodynamic field, and using CO_2 for film-cooling flows helped achieve a turbine temperature ratio similar to the design point (approximately 1.5). As a result, PSP outcomes are expected to effectively reflect the adiabatic effectiveness generated under design point conditions. The uncertainty in PSP measurements remained relatively low, generally within 10% for lower adiabatic effectiveness values (around 0.2) and 2% for higher ones (greater than 0.8).
In contrast, for HTC tests, the mainstream temperature was elevated to the nominal value (533.15 K), while cooling flows were maintained at ambient temperature. It is important to acknowledge that, due to the metallic composition of most rig components, some heat conduction effects were unavoidable. This led to a minor temperature rise in the cooling flow temperature, as documented in Table 3.1. However, these effects did not undermine the integrity or representativeness of the testing procedure.
The conditions employed for numerical simulations were meticulously chosen to closely resemble the experimental setup. These conditions differed between the runs performed to predict adiabatic effectiveness and HTC outcomes, as previously described. Notably, it should be emphasized

Table 3.1: Operating conditions STech test rig.

	PSP test	**HTC test**
Combustion chamber		
Rem @ Plane 40 [-]	1.65E+05	1.17E+05
Mam @ Plane 40 [-]	0.074	0.074
Swirler temperature [K]	300	533.15
Nuggets flow temperature [K]	300	325
Swirler-nuggets flow split [%]	85-15	85-15
Turbine		
NGV throat Mach number [-]	0.79	0.67
Film-cooling temperature [K]	300	-
Film/Plane 40 mass flow ratio [%]	13.6	-

that HTC tests were conducted under transient conditions, resulting in a slightly greater temperature decrease across the chamber compared to steady tests or CFD predictions. The estimated experimental uncertainty was within $\pm 13\%$ for heat transfer coefficient measurements and $\pm 3K$ for adiabatic wall temperature measurements.

3.2 HTC prediction: RANS trisector simulation

As anticipated, firstly, a comparison between numerical and experimental results relatively to the external HTC over the airfoil surface is reported, since this aspect is of major importance in the design of HPT nozzle guide vanes. To do so, the full combustor-cascade integrated domain, including two vanes and three passages, is simulated by employing RANS method in order to assess if conventional/industrial approaches can be reliably used when representative and highly unsteady combustor outflows are considered, or advanced and more time-consuming methods shall be adopted.

3.2.1 Numerical setup

The simulations were conducted utilizing ANSYS CFX v19.4 software. The chosen approach involved a pressure-based algorithm with Rhie-Chow pressure-velocity coupling. Consistent with guidelines outlined by the software developers [122], the equations were discretized using the "high resolution" scheme. Turbulence was accounted for using the $k-\omega$ SST model developed by Menter [123]. To ensure a smooth transition between wall-function and wall-integration application, an automated near-wall treatment was employed. This transition was determined based on the local $y+$ value, not always able to be maintained below 1 due to geometric and computational constraints.

The simulation domain corresponds to the one depicted in Figure 3.2. The computational grid utilized was a hybrid unstructured grid, as illustrated in Figure 3.3, and it was generated using ANSYS Meshing. This grid consists of 14 layers of prismatic elements and is filled with tetrahedral

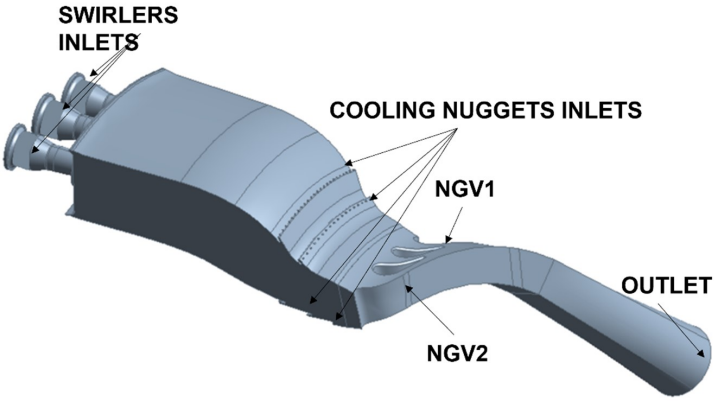

Figure 3.2: Computational domain of trisector combustor+nozzles rig ***(©2024 Baker Hughes Company—All rights reserved).***

elements. The total number of elements in the mesh is 99 millions. Within the injectors, a characteristic size of 1.5 mm was employed, which was then reduced to 1 mm in the region downstream of the swirlers where refinement is applied. Throughout the blade surface, the $y+$ value remains below 5, ensuring proper mesh resolution. This mesh sizing approach aligns with the methodology used in analyzing a similar configuration [124].

At all inlet sections, the mass flow boundary conditions were established based on experimental data, and static pressure was enforced at the outlet of the computational domain. Additionally, the correct expansion ratio across the NGV cascade was managed by comparing the static pressure at predetermined positions on the outer endwall with measurements from pressure probes. The surfaces of all walls were treated as smooth and non-slip.

As anticipated, replicating the exact HTC test case was unfeasible due to the transient nature of the method. Attempting to simulate this "long" 20-second experiment through CFD would be unworkable due to time constraints and the considerable resource demands. This is primarily

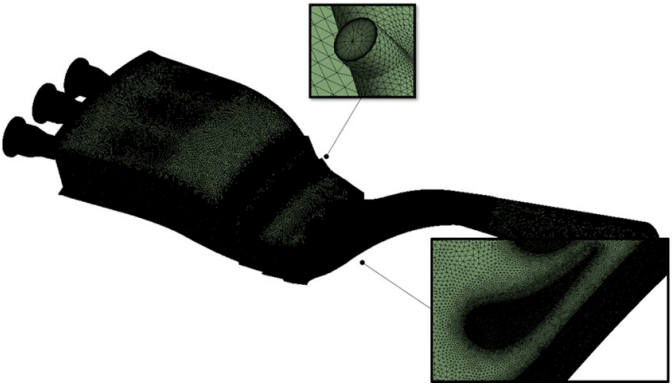

Figure 3.3: Computational grid of the three-sector combustor+nozzles domain ***(©2024 Baker Hughes Company—All rights reserved)****.*

because a very small time step would be necessary to maintain an appropriate Courant number, particularly in the swirling area and especially within the nozzles. The high acceleration of the flow in these regions would require an even finer mesh, further complicating the computational demands.

For this reason and according to the purpose of this activity, the heat transfer coefficient was determined using the conventional two-point technique, a common approach for heat transfer computations in gas turbines. This approach involves conducting two consecutive simulation runs:

- The first is adiabatic, from which the adiabatic wall temperature (T_{aw}) on the airfoils surface is retrieved;
- The second is then carried out by imposing a specified wall temperature, equal to T_{aw} detracted by an arbitrary ΔT (150 K in this case), which determines a wall heat flux $\dot{q}$.

Eventually, the HTC is evaluated at any location as per the following expression:

$$HTC = \frac{\dot{q}}{T_{aw} - T_w} = \frac{\dot{q}}{\Delta T} \tag{3.1}$$

3.2.2 Verification of boundary conditions

Before displaying the comparison between experimental results and numerical predictions of heat transfer coefficient on the surface of the airfoils, it is important to validate that the primary flow field parameters at the interface between the combustor and turbine, as estimated by CFD simulations, align with the measurements. In Figure 3.4, the left-hand column presents the measurements acquired through a five-hole probe traversing Plane 40 under warm operating conditions (design point or equivalently for the HTC test). On the corresponding right-hand column, the aerothermal field parameters obtained through CFD are illustrated.

In particular, the swirl, pitch, dimensionless total temperature and pressure fields are shown in sequence on each row of the figure. Note that on the x-axis of the plots is the t/p_{NGV}, i.e. the tangential-angle to the angular NGV-pitch ratio, whereas on the y-axis the normalized NGV height h/H (or span) is reported. Swirl, pitch and $T_{t,nd}$ are defined as follows:

$$swirl = \arctan\left(\frac{V_{tan}}{V_{ax}}\right) \tag{3.2}$$

$$pitch = \arctan\left(\frac{V_{rad}}{V_{ax}}\right) \tag{3.3}$$

$$T_{t,nd} = \frac{T_t - T_{nuggets}}{T_{max} - T_{nuggets}} \tag{3.4}$$

where T_{max} refers to the maximum temperature on Plane 40, the interface plane between combustor and stator. The comparison presented at Plane 40 demonstrates a satisfactory alignment with the experimental data maps. This alignment is particularly strong in relation to the swirl, total temperature, and pressure distribution. However, a noticeable difference remains apparent in the distribution of pitch. It is noteworthy to emphasize the agreement in the swirl, as this parameter significantly influences the propagation of the hot streak through the stator. Furthermore, it

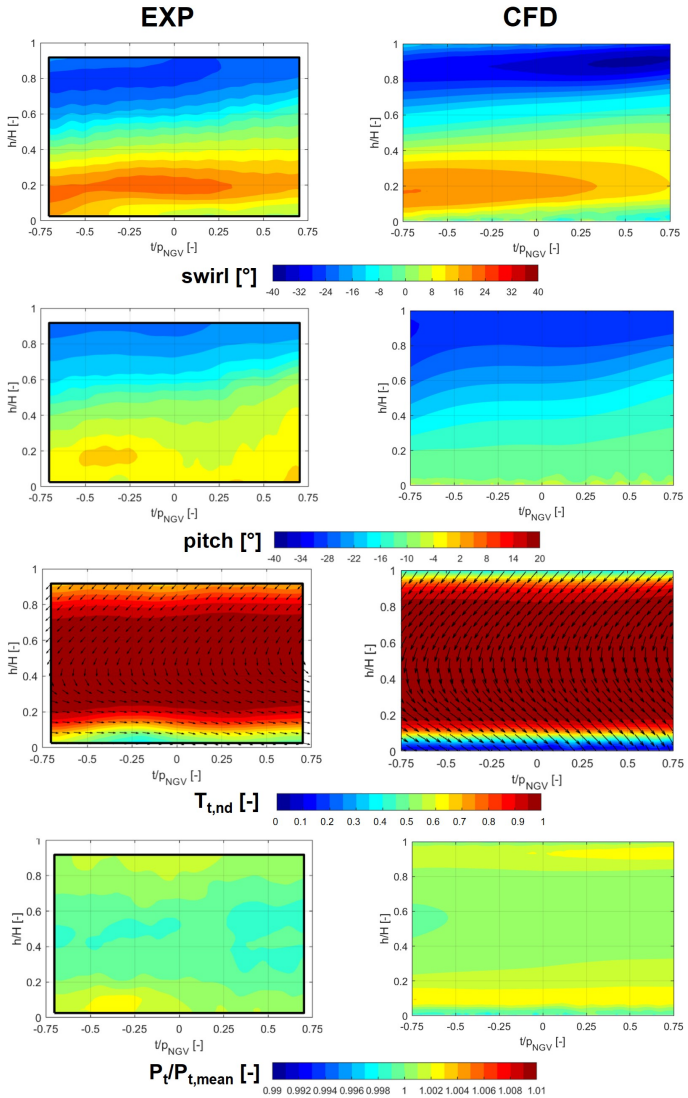

Figure 3.4: Five-hole probe and CFD contours at Plane 40 (RANS trisector) ***(©2024 Baker Hughes Company—All rights reserved).***

plays a crucial role in modifying the flow that interacts with the nozzles, thereby potentially influencing both the distribution of HTC.
The validation of accurate boundary conditions also encompassed, as previously indicated, an assessment of the pressure distribution on the outer endwall at Plane 41, where pressure measurement points are situated. In Figure 3.5, a comparison is provided between the actual experimental measurements and the values predicted through CFD. Additionally, a representation of the shape of the rig section is included to provide clearer insight into the positioning of the pressure measurement points.

The pressure distribution achieved through CFD closely approximates

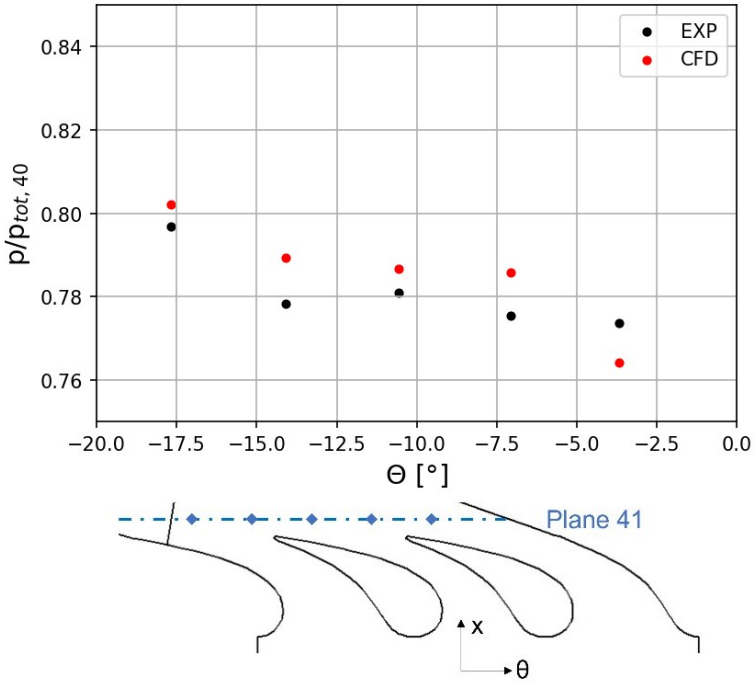

Figure 3.5: Pressure distribution on the outer endwall of Plane 41, at the NGV outlet (RANS trisector) ***(©2024 Baker Hughes Company—All rights reserved).***

the experimental data, although there is a slight tendency for overestimation at all pressure taps positions, except for the rightmost one. In this particular location, the CFD model represents some overexpansion, which is not observed in the measurements. More accurate results can be pursued by improving the match with experimental data at the combustor-turbine interface as well as across the vane passage via the use of more advanced CFD modelling.
The comparison can then be extended to the blade load curves at a certain span section of the airfoil, which, per the mid-span, is reported in Figure 3.6. The data from the experiments indicate notable measurement noise, primarily coming from the measurement technique's limited sensitivity to pressure measurements [119]. However, when concentrating on the central vane passage, specifically the SS of NGV1 and the PS of NGV2, the CFD results exhibit a satisfactory match with the measurements. It is worth noting that this alignment aligns with the initial design intent.

3.2.3 HTC and adiabatic wall temperature

The assessment of the heat transfer coefficient, both measured and numerically evaluated, is illustrated in Figure 3.7. Results are reported separately for the three optical setups, used in the experimental survey for investigating a sufficient part of the surfaces, and superimposed to the vane model; corresponding images were created for the numerical results. Specifically, the first setup was employed to capture the front section of the pressure side of NGV2, while the second and third frames encompassed the leading edge region and the terminal section of the suction side of NGV1, respectively. Importantly, it should be emphasized that the reported HTC values are normalized, utilizing the maximum HTC at the LE of the airfoil as a reference (HTC_{ref}).

Examining the experimental maps reveals that the highest HTC is located on the airfoil's LE at approximately 0.25 span fraction, slightly leaning towards the PS in frame 1. Focusing on frame 2, it becomes evident that the actual stagnation line (continuous) diverges in a "twist"

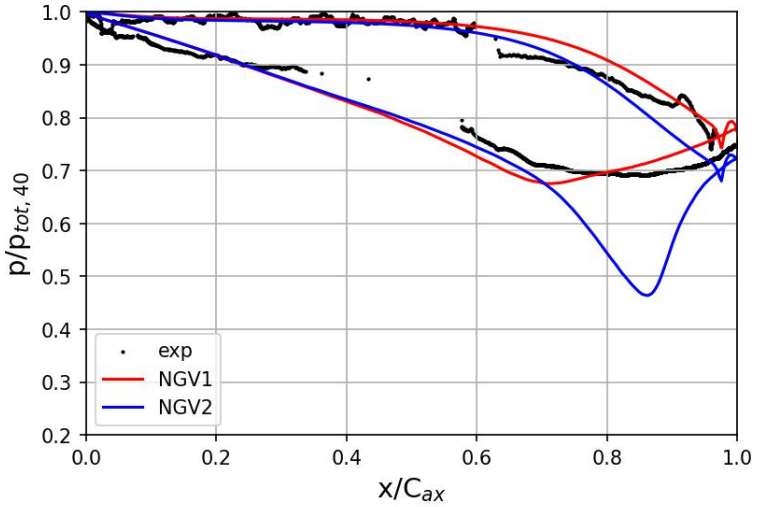

Figure 3.6: Nozzles pressure load (RANS trisector) ***(©2024 Baker Hughes Company—All rights reserved).***

manner compared to the geometrically defined one (dashed), a deviation attributed to the influence of the superimposed inlet swirl.

Indeed, referring to Figure 3.4, it is observed that the lower portion of the LE region experiences a greater flow incidence (positive swirl angle), while the opposite is true for the upper half (negative swirl angle). This condition leads to a higher HTC value on the lower span half compared to the higher span half, consistent with findings in prior studies [125, 126].

Now moving to frame 1, HTC is observed to gradually decrease and subsequently increase as the flow accelerates toward the throat section. Additionally, there is a reduction in HTC near both the inner and outer endwalls where flow velocities are lower. Regarding CFD results, they exhibit qualitative similarities to the measurements but fail in achieving a satisfactory quantitative alignment, as indicated by the colorbar variation between experimental and CFD results.

Indeed, a similar twisted stagnation line is noticeable on the airfoil's

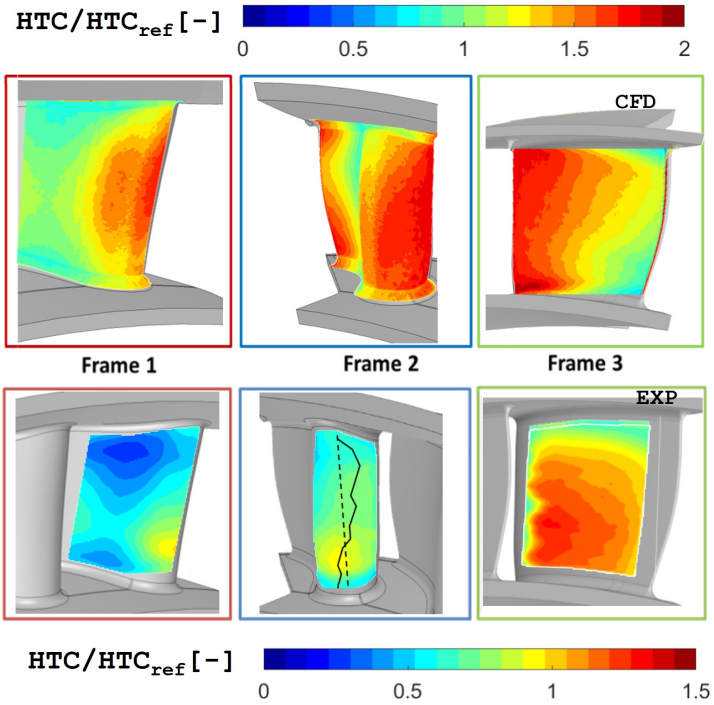

Figure 3.7: Heat Transfer Coefficient (RANS trisector) ***(©2024 Baker Hughes Company—All rights reserved).***

LE in the CFD results. However, it fails to exhibit the corresponding higher/lower HTC values in the lower/higher span half region, which significantly contradicts the experimental maps. Additionally, CFD reveals a gradual reduction and subsequent increase in HTC on the PS surface, with lower HTC zones near the inner and outer endwalls. Although there is some agreement, the radial gradient is underestimated compared to measurements. It is worth noting that the numerical results for frames 1 and 2 clearly indicate a non-perfectly periodic behavior of the flow field between the two airfoils, in contrast to what was observed in the experimental setup.

Conversely, the two airfoils do not exhibit identical HTC at the nose. As emphasized earlier, CFD significantly overestimates quantitative values on the LE and PS. In contrast, the predicted values align more closely on the TE of the SS in frame 3, after the transition. However, the predicted pattern diverges notably, with CFD indicating higher HTC values in the inner part of this surface, contrary to the experimental observations where higher values are generally measured in the outer part.
To delve further into the analysis, the HTC 1D profiles extracted at 25%, 50% and 75% of the span for both experiments and CFD are compared to correlations applicable for a flat plate (Figure 3.8). This comparison specifically focuses the analysis on the PS and the SS. In particular, the predominant correlation employed for laminar flow over a flat plate with constant velocity and temperature involves solving the energy differential equation of the boundary layer. Within the Prandtl number range of 0.5-15, this results in [127]:

$$Nu_x = 0.332 \cdot Pr^{1/3} \cdot Re^{1/2} \tag{3.5}$$

where in the vane setup, the term x signifies the longitudinal coordinate, which corresponds to the curvilinear abscissa s. Regarding turbulent flows, there are primarily two approaches employed to establish a corresponding relation. The first approach involves utilizing the Reynolds analogy, resulting in the following [128]:

$$Nu_x = 0.0288 \cdot Pr^{1/3} \cdot Re^{4/5} \tag{3.6}$$

The alternative correlation was formulated by [127] through the application of a law of the wall approach to approximate the solution of the energy equation, resulting in:

$$Nu_x = 0.0287 \cdot Pr^{0.6} \cdot Re^{4/5} \tag{3.7}$$

Hence, as can be seen from Figure 3.8, it is clear that, despite the elevated levels of turbulence at the inlet, the experimental data show a strong impact of the BL transition on the airfoil, presenting laminar HTC values,

according to Eq. 3.5, on PS and SS, until the transitions occurs. On the contrary, CFD yields fully turbulent HTC values, consistent with the turbulence model employed, which does not account for transition phenomena, assuming values much closer to those predicted by the correlations reported in Eq. 3.6 and Eq. 3.7. Unfortunately, this is a further indicator of the inaccuracy of the present numerical technique. For this reason, further analyses will be conducted in order to improve the prediction of HTC.
Similar to Figure 3.7, Figure 3.9 reports the contours of non-dimensionalized adiabatic wall temperature ($T_{aw,nd}$) according to the following equation:

$$T_{aw,nd} = \frac{T_{aw} - T_{nuggets}}{T_{max} - T_{nuggets}} \tag{3.8}$$

The highest adiabatic wall temperature is observed in proximity to the midspan, slightly shifted radially inward. The hot streak near the midspan and the cold "trails" at both inner and outer radii follows a pattern consistent with that observed at Plane 40 up to the airfoil leading edge, maintaining coherence along the SS surface. However, a slight more relevant temperature decrease occurs on the PS, where flows tend to detach, thus facilitating mixing. Examining the CFD outcomes, the adiabatic wall temperature patterns are accurately reproduced, particularly on the PS and LE surfaces. Nonetheless, notable distinctions arise when examining the SS, where the hot streak appears to become narrower as it progresses downstream, a contrast not observed in the experimental results.

3.3 HTC prediction: periodic one-sector RANS/S-BES simulations

In order improve HTC prediction, further analyses are conducted on the nozzles under warm operating conditions (design point). To do so, coupled/decoupled RANS/SBES simulations are carried out on periodic domain. Initially, following conventional industrial design practices, a periodic stand-alone NGV configuration is established to assess the HTC on the vane surface. This involved conducting RANS fully-turbulent

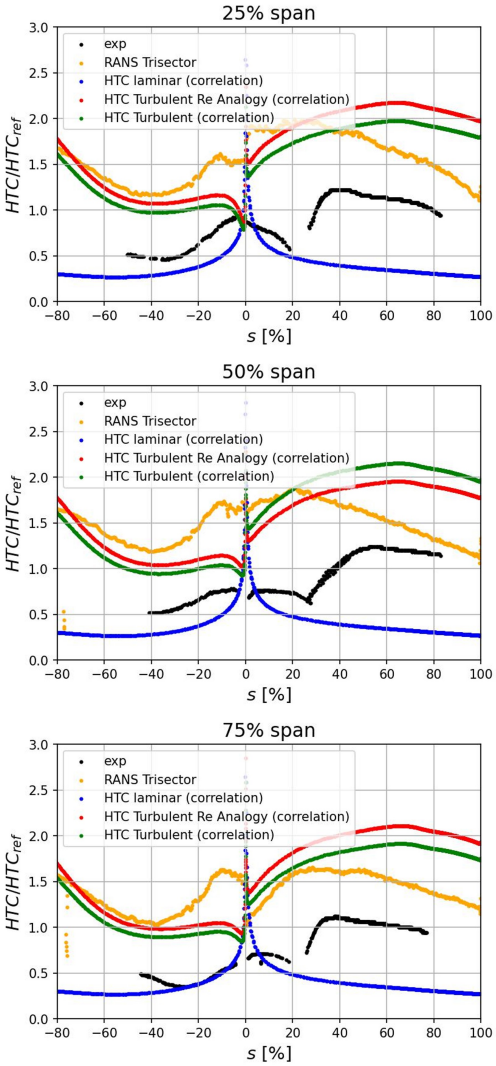

Figure 3.8: Heat Transfer Coefficient on the NGV surface at the 25%, 50% and 75% of the span for the experiments and RANS trisector calculation. The results are then compared to flat plate correlations. It is reported the SS of NGV1 ($s > 0$) and the PS of NGV2 ($s < 0$), according to the experiments. ***(©2024 Baker Hughes Company—All rights reserved).***

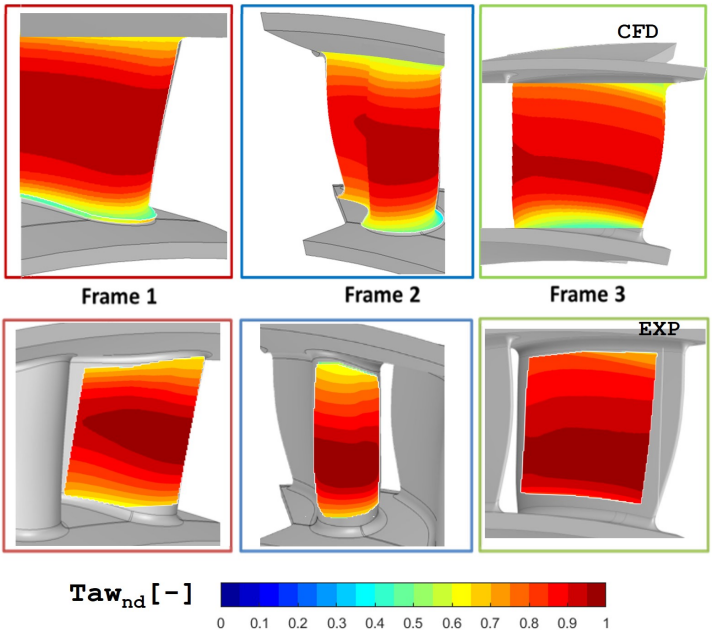

Figure 3.9: Adiabatic wall temperature (RANS trisector) ***(©2024 Baker Hughes Company—All rights reserved).***

simulation and utilizing 1D profiles from experiments as inlet boundary conditions (RANS input EXP SST). Subsequently, a fully integrated combustor-stator periodic domain is explored through SBES (SBES integrated SST). For information about SBES approach please see 4.1.3. Unsteady data obtained from this simulation are then extracted and stored in order to generate realistic unsteady inlet boundary conditions for the non cooled NGV configuration. As a matter of fact, the NGV is studied by employing both RANS (RANS input SBES SST and RANS input SBES Transition SST) and SBES (SBES input SBES Transition SST) simulations along with the $k-\omega$ SST and Transition SST to model the turbulence effects. Finally, numerical results were compared to exper-

imental data to assess discrepancies between various CFD approaches. The comparison between numerical predictions and the available experimental results was exploited to assess the capability of advanced scale resolving methods in the characterization of the mutual combustor turbine interaction, along with the heat transfer coefficient behavior. This evaluation aims thus to assess if such more advanced and more time consuming methods, including also turbulence models able to capture the transition, can be more reliably used for a proper prediction of the vane thermal loads.

3.3.1 Computational domains, mesh resolution and numerical setup

3.3.1.1 Combustor-NGV coupled case

The computational domain utilized for the SBES Integrated SST investigation is depicted in Figure 3.10. Thus, the computational study is conducted through SBES simulation, aiming to control computational cost by utilizing RANS to model boundary layer regions, which is certainly less computationally demanding than LES. Furthermore, the Dynamic Smagorinsky Sub-Grid Scale (SGS) closure is applied to the resolved regions, while the $k-\omega$ SST model is chosen for the under-resolved ones. Mass flow boundary conditions are set at the entrance sections of swirlers and nuggets, by averaging preliminary experimental data. Meanwhile, static pressure is applied at the outlet of the domain based on initial considerations and available experimental information. All walls are treated as smooth and no slip surfaces. The hybrid unstructured computational grid, depicted in Figure 3.11, is created using ANSYS Fluent Meshing. It comprises 40 million polyhedral elements and includes 14 prismatic layers. The chosen mesh configuration aims to maintain a $y+$ value below 1 across all NGV surfaces and, within the LES-modeled zones, to resolve at least 80% of the turbulent kinetic energy. In order to verify this statement, the contour plot depicted in Figure 3.12 illustrates the computed values of Pope's criterion on the cross section of the domain. Moving in the

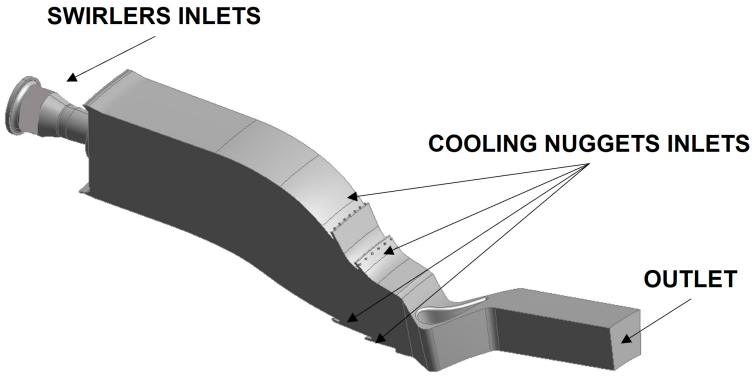

Figure 3.10: CFD Periodidc domain including both CC and NGV ***(©2024 Baker Hughes Company—All rights reserved).***

flow direction, the criterion's value is notably higher than 0.9 inside the combustor and remains above 0.8 within the nozzle, indicating that the requirement to resolve at least 80% of the turbulent kinetic energy has been successfully met. The areas close to the wall, where the RANS model is applied, show values below this threshold. Notably, on the suction side of the airfoil, where the solution is handled with RANS, there is an observable thickening of the boundary layer.

The numerical simulations, including the ones where only the stator is simulated, are conducted using the commercial software Ansys Fluent v21.1, which employs a fully compressible approach and a coupled scheme for pressure-velocity coupling within the 3D Navier-Stokes solver. Furthermore, a second-order accurate scheme is utilized for discretization in both time and space. The time step is set to approximately 10^{-6} seconds to control the value of the convective CFL number.

3.3.1.2 NGV stand alone cases

The computational region utilized for the stand alone stator analyses is derived from the larger domain including both the combustor and

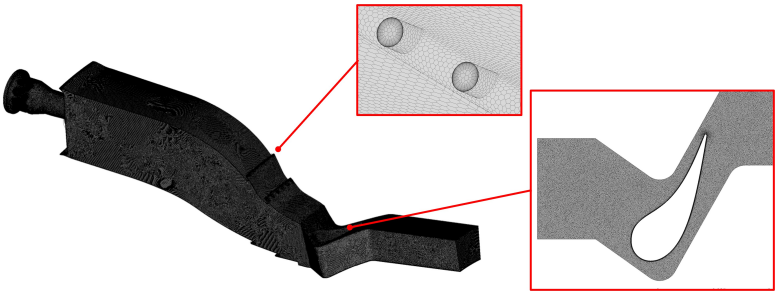

Figure 3.11: Computational grid of the combustor+nozzle periodic domain ***(©2024 Baker Hughes Company—All rights reserved)****.*

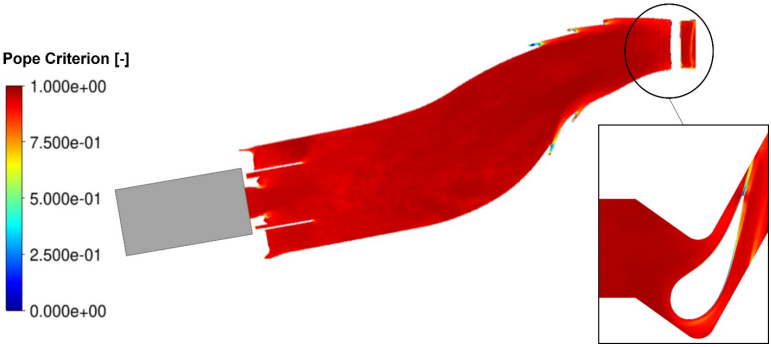

Figure 3.12: Pope's criterion ***(©2024 Baker Hughes Company—All rights reserved)****.*

stator, with the inlet set at Plane 40. Regarding mesh refinement, the number of cells for the standalone NGV setup is approximately 10 million, composed of polyhedral elements with 20 prismatic layers. The grid is generated also in this case by using ANSYS Fluent Meshing. In addition, the numerical simulations of the stator stand alone case share the same features in terms of general setup.

As previously mentioned, an initial step involved conducting a RANS simulation (RANS input EXP) of the periodic NGV. This is accomplished by utilizing 1D profiles obtained from experimental data as the inlet bound-

ary conditions. Specifically, at the stator inlet, the prescribed boundary conditions encompassed total pressure and total temperature 1D profiles, as well as flow direction specified in terms of cylindrical components. To account for turbulence effects, the $k-\omega$ SST model is applied. Turbulence intensity and turbulent length scale 1D profiles are included in accordance with experimental findings. The purpose of this simulation is to establish a baseline solution, reflecting conventional industrial practices, against which the subsequent approaches could be compared to evaluate their enhancements.

Furthermore, to facilitate additional investigations on the nozzle, supplementary RANS and SBES simulations for the isolated periodic stator are conducted (RANS input SBES SST and RANS input SBES Transition SST, SBES input SBES SST). To carry out these simulations, as previously mentioned, two-dimensional unsteady boundary conditions are extracted from the interface plane shared by the two components in the SBES simulation of the fully integrated CC NGV. These conditions were then applied at the inlet of the stand-alone stator. In the case of RANS, the 2D maps assigned at the inlet corresponded to the time-averaged solution, whereas for the SBES simulation, a series of instantaneous maps are employed. This approach allowed for a direct comparison between RANS and SBES methodologies utilizing the same inlet conditions, differing primarily in their intrinsic nature (i.e., time-averaged vs. time-varying). In order to obtain a balance between maintaining a manageable database size and achieving a satisfactory temporal discretization, data are stored at intervals of 0.005 ms during a 45-ms timeframe. This timeframe covered 3 FTT of the combustor coupled with the stator, which is roughly equivalent to 45 FTT of the isolated NGV domain. However, a limited subset of the database corresponding to 15 ms (equivalent to 15 stator FTT) is utilized for generating the inlet boundary conditions for the nozzle simulation. This approach allowed for a reduction in the computational effort required by the SBES simulation, while simultaneously ensuring statistical numerical convergence. Specifically, the time period used for time averaging in the fully integrated configuration (SBES integrated

SST) was based on approximately 3 FTT of the combustor coupled with the stator, whereas for the isolated NGV domain, it was about 15 FTT. Regarding the inlet conditions, within each data collection instance, parameters such as mass flow (ρu_x, ρu_y, ρu_z), velocity components (u_x, u_y, u_z), total temperature, and turbulence characteristics are recorded for every node on the mesh situated at plane 40. This plane corresponds to the interface between the combustor and the stator, as anticipated. Therefore, mass flow in terms of mass flux, along with the flow directions, and total temperature are prescribed at the inlet of the stator, along with the turbulent quantities previously extracted. Also in this case, for all the stand alone NGV simulations, all walls were treated as smooth and no slip surfaces.

Regarding the conditions at the outlet, static pressure is enforced at the domain's exit. Furthermore, to maintain an appropriate expansion ratio across the NGV cascade, the distribution of static pressure on the airfoil surface is compared to experimental data.

Regarding turbulence considerations, turbulence effects are taken into account in the RANS simulations using both the $k-\omega$ SST model and the Transition SST model. In the case of decoupled SBES simulation, the Transition SST model is chosen for regions with lower resolution, while the Dynamic Smagorinsky (SGS) closure is used for the resolved regions, as for the coupled calculation.

Key parameters pertaining to the configuration of the CFD simulations are outlined in Table 3.2. As already mentioned, in relation to predicting HTC values on the vane surfaces, replicating the exact experimental conditions was not feasible due to constraints linked to the transient approach applied in the experiments. In reality, reproducing the experimental timeframe of approximately 20 seconds would be impractical in terms of resource and time requirements. Consequently, in alignment with the objectives of these numerical investigations, HTC is determined through a two-step simulation process, involving two runs characterized by different wall heat fluxes, $\dot{q}_w$. Subsequently, HTC is calculated by applying a linear regression based on the conventional $T_w - \dot{q}$ regression method for

each point on the vane surfaces. The resulting HTC values consequently represent the angular coefficient within the subsequent equation:

$$\dot{q} = HTC(T_{aw} - T_w) \tag{3.9}$$

Meanwhile, the adiabatic wall temperature is obtained by assuming a zero heat flux. To enhance clarity regarding the process, a visual illustration is provided in Figure 3.13. To validate the accuracy of this methodology, an initial analysis was undertaken involving three separate simulations, each with distinct imposed heat flux values. This investigation confirmed that the resultant wall temperature values align on a consistent linear trend.

Table 3.2: Summary of the main parameters regarding the setup of the CFD simulations. ***(©2024 Baker Hughes Company - All rights reserved).***

CFD Simulation	**Domain**	**Inlet BCs**	**Turbulence**
RANS input EXP SST	NGV	1D profiles from EXP	$k-\omega$ SST
SBES Integrated SST	CC+NGV	Mass flow inlets from EXP	Dynamic-Smagorinsky SGS + $k-\omega$ SST
RANS input SBES SST	NGV	2D time averaged maps from SBES integrated	$k-\omega$ SST
RANS input SBES Transition SST	NGV	2D time averaged maps from SBES integrated	Transition SST
SBES input SBES Transition SST	NGV	Set of instantaneous 2D maps from SBES integrated	Dynamic-Smagorinsky SGS + Transition SST

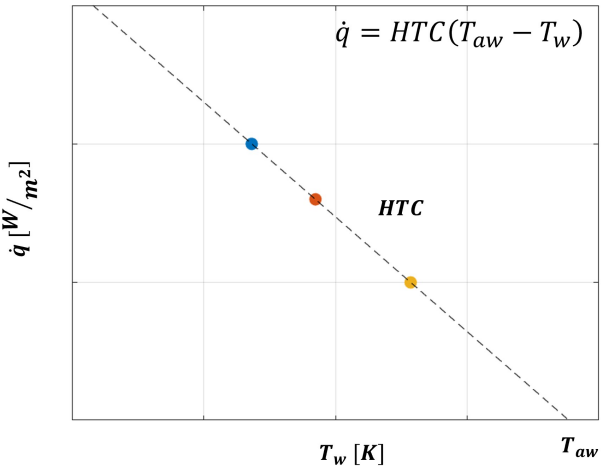

Figure 3.13: Example of the $T_w - \dot{q}$ regression approach applied at one point of the grid of the NGV surface. Each colored point corresponds to a run with a specified different heat flux. ***(©2024 Baker Hughes Company—All rights reserved)****.*

3.3.2 Combustor exit conditions

Before delving into the disparities between numerical outcomes and experimental data concerning the heat transfer coefficient on the vane surfaces, it is crucial to initially compare the principal aerothermal variables at plane 40 also in this case. This step aims to ensure that the CFD demonstrates satisfactory correspondence with the experimental findings. Figure 3.14 illustrates this comparison, encompassing parameters such as swirl and pitch angles, non-dimensional total temperature, and total pressure, as previously done for the RANS trisector under warm operating conditions (design point or equivalently for the HTC test). Specifically, the left side presents the experimental outcomes, while the CFD predictions are displayed on the right. Concerning all the results reported in the Figure 3.14, it must be pointed out that:

- EXP results are measurements output and they are used, in their 1D

tangentially averaged form, as input for the first RANS simulation (RANS input EXP SST);

- CFD results are the time average predictions from the SBES simulation in the fully integrated CC NGV configuration (SBES Integrated SST);
- The time-averaged outcome of the SBES Integrated SST simulation serves as the input for the subsequent pair of RANS simulations (RANS input SBES SST and RANS input SBES Transition SST);
- The time varying dataset obtained in runtime from the SBES Integrated SST case is employed as the input for the SBES simulation of the isolated stator (SBES input SBES Transition SST).

As done previously, in order to better understand the maps, it is also important to point out that the t/p_{NGV}, corresponding to the tangential angle to the angular NGV pitch ratio, is reported on the x axis of each plot, while the normalized NGV height h/H (or span) is on the y axis. Swirl, pitch are defined according to Eq. 3.2 and Eq. 3.3, while $T_{t,nd}$ is defined according to Eq. 3.4. For experimental results, the maximum T evaluation is made over the only central sector ($-0.5 < t/p < 0.5$), for coherence with respect to CFD results.
In general, the experimental findings point out the significance of the analyzed test scenario, as they reveal a distinct radial temperature distribution within a notable level of swirling. Regarding the contours, the current comparison at the interface plane displays a satisfactory agreement with the measurements. In reality, the swirl distribution closely resembles that of the two cases. Similarly, the pitch distribution exhibits a qualitatively similar pattern, even though some differences are observable. This holds true for the temperature maps as well. The vector field that overlays these maps serves to summarize the aero-field behaviour on this plane, highlighting the presence of a counterclockwise rotating structure. However, its closure (upward motion) on the maps' right side is hindered by the overall inward movement influenced by the combustion chamber's

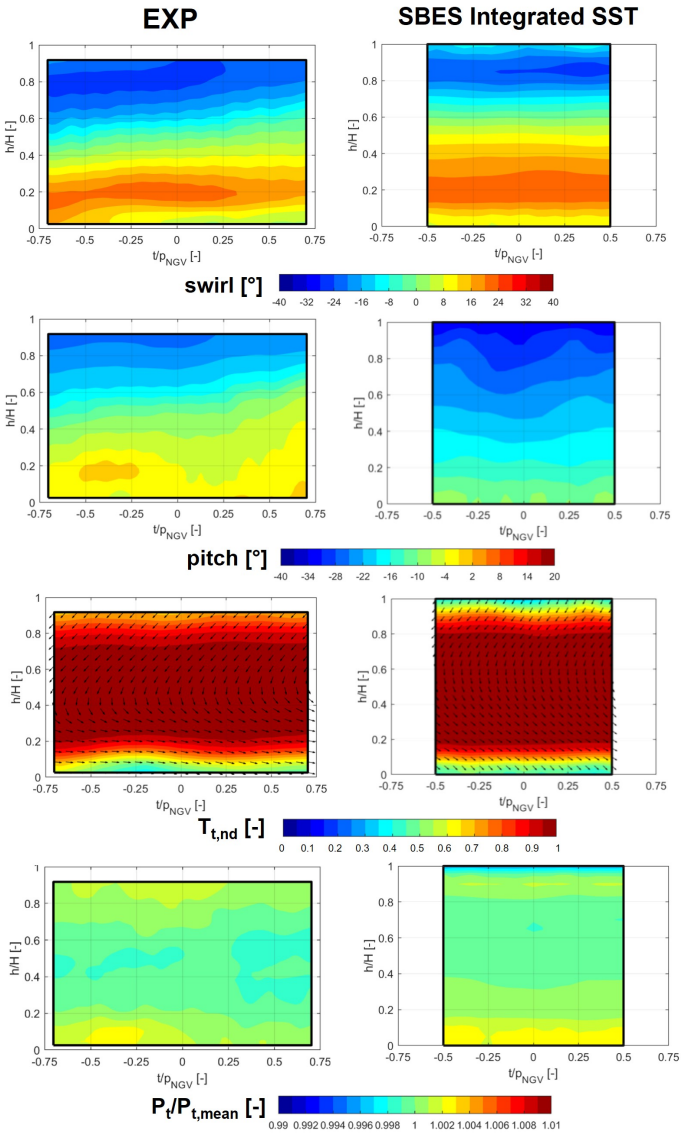

Figure 3.14: Experimental and CFD contours at Plane 40 ***(©2024 Baker Hughes Company—All rights reserved).***

shape. This same pattern holds true for both experimental and CFD results.

Enhancing the quantitative evaluation of the comparison involves the extraction of 1D profiles that are tangentially averaged from the maps. These profiles are presented in Figure 3.15, alongside turbulence intensity.

Similar observations apply to the linear plots. Although the general

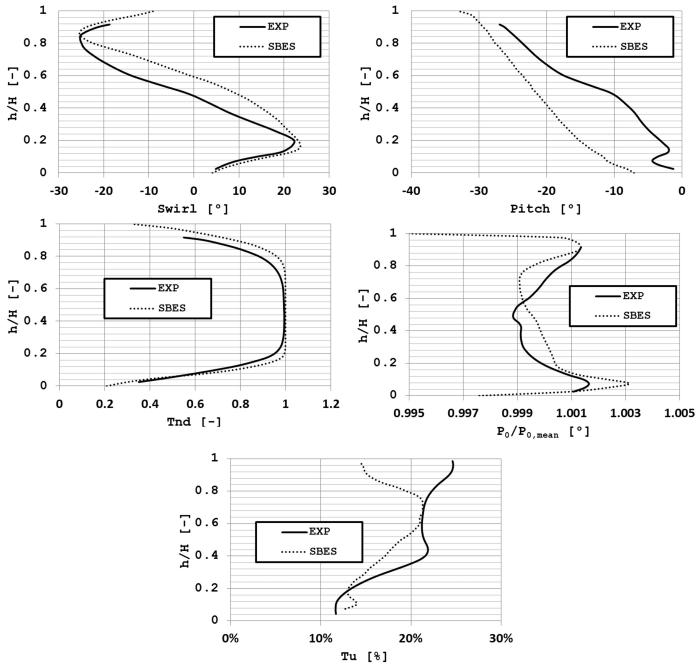

Figure 3.15: 1D tangentially averaged profiles on Plane 40 ***(©2024 Baker Hughes Company—All rights reserved)****.*

distribution is largely analogous, there are certain quantitative disparities that can be emphasized. The CFD results accurately replicate the maximum and minimum values of the swirl angle, despite positioning the center of the swirling structure (i.e., Swirl=0°) at a greater radial extent. This same observation holds true for the pressure and turbulence

profiles as well. While the CFD results indicate similar overall values, the positions of the minimum and maximum points – denoting the core of swirling for pressure and turbulence respectively – are situated at higher h/H values in comparison to the experimental data. Concerning $T_{t,nd}$, the experimental outcomes reveal a slightly more pronounced profile peak. This implies that the numerical method underestimates the turbulent mixing between the heated core and the colder layers.
In spite of the discrepancies highlighted earlier, the CFD outcomes demonstrate a satisfying level of accuracy in replicating the overall aerothermal pattern at the inlet of the NGV cascade. Once inlet BCs have been described, and before moving to NGV results, it is important to check the pressure load on the NGV surface. This alignment is established by adjusting the outlet pressure, which serves as a boundary condition for the CFD simulations.
The pressure loads obtained on the NGV surface at 50% span are depicted in Figure 3.16 for all numerical simulations, allowing for a comparison with experimental results from PSP measurements. Experimental loads are presented for NGV1, for SS results, and for NGV2, for PS results, as these surfaces demarcate the central passage. It is evident that the pressure distribution across all simulations closely aligns with the experimental curves, presenting a satisfactory correspondence. This outcome represents a reliable verification that the same aero-behaviour is achieved.

3.3.3 HTC and adiabatic wall temperature

The heat transfer coefficient, as measured during the experimental campaign and predicted through numerical CFD simulations, is depicted in Figure 3.17. Results are reported separately for the three optical setups, used in the experimental survey for investigating a sufficient part of the surfaces, and superimposed to the vane model; corresponding images are then created for the numerical results. Specifically, the first setup was employed to capture the front section of the pressure side of NGV2, while the second and third frames encompassed the leading edge region and the final

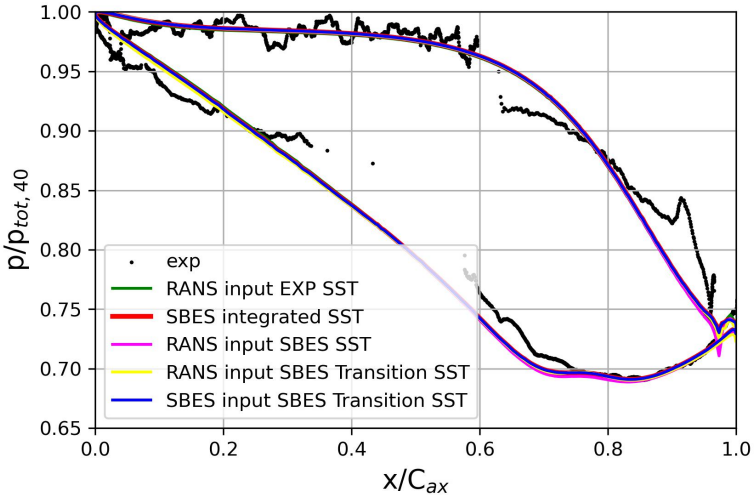

Figure 3.16: NGV pressure load at midspan ***(©2024 Baker Hughes Company—All rights reserved).***

section of the suction side of NGV1, respectively. Importantly, it should be emphasized that the reported HTC values are normalized, utilizing the maximum HTC at the LE of the airfoil as a reference (HTC_{ref}). This reference value remains equal for both the experimental and numerical plots.

While a description of the observed pattern is available in the experimental study [120] and the previous sections, once again it is valuable to provide briefly the same significant details here. Specifically, as already anticipated in the last section, focusing on the experimental findings, it becomes apparent that the HTC value is situated at the lower half of the LE, approximately around 25% of the span (as depicted in frame 2). This peak value is slightly skewed toward the pressure side (frame 1). According to references [125, 126], the rationale behind the greater HTC values in this region can be understood by considering the distribution of swirl angles (as shown in Figure 3.14): the lower portion of the LE

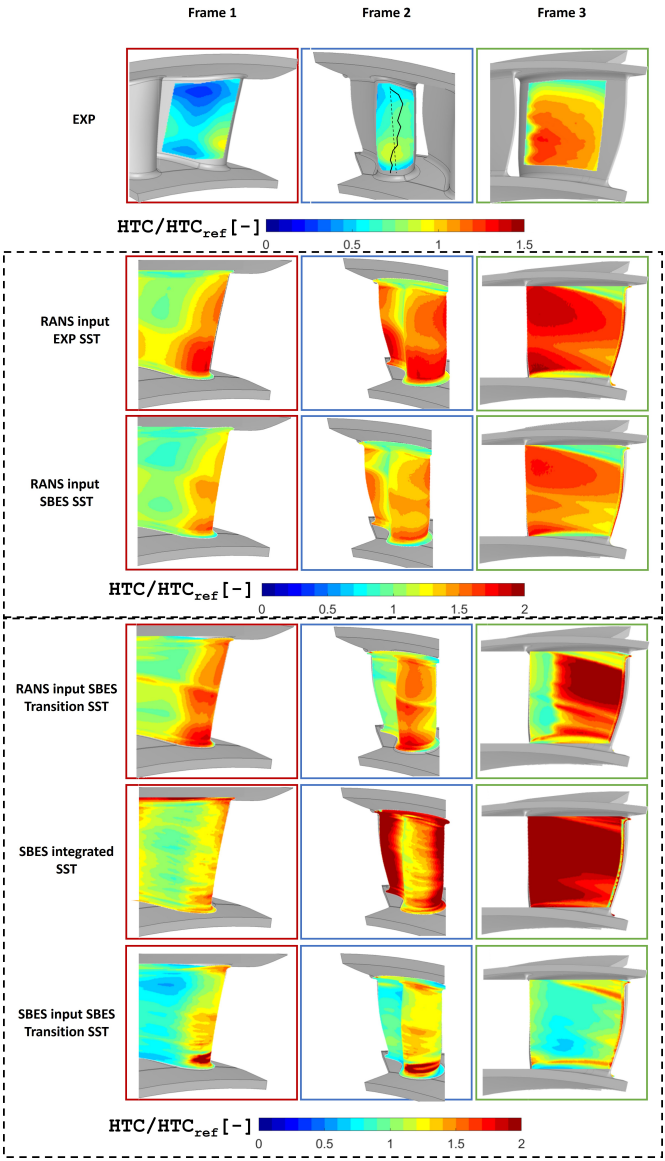

Figure 3.17: Heat transfer coefficient maps ***(©2024 Baker Hughes Company—All rights reserved)***.

exhibits positive swirl angle values, resulting in a greater flow incidence. Conversely, the higher span values display negative swirl angles. Consequently, the highly swirling flow at the NGV inlet causes a rotation of the stagnation line (depicted as a continuous line) in relation to the geometric reference (illustrated as a dashed line), which can be observed in Frame 2. Looking at the PS (frame 1), a gradual reduction in HTC becomes evident, accompanied by the presence of two distinct areas characterized by lower HTC values. Additionally, as anticipated, a reaugment of HTC is observable at the throat section where flow velocities increase.
Moreover, focusing on the SS (frame 3), higher values of HTC than the PS and LE are observable, especially after the transition occurs.
Focusing now on the HTC predictions from the numerical simulations, there are substantial variations in the outcomes based on the CFD models applied (RANS or SBES) as well as the chosen turbulence model ($k-\omega$ SST model and Transition SST model). Note that for the RANS input EXP SST and RANS input SBES SST it was necessary to increase the colorbar range to fit the significantly higher calculated values of HTC. To facilitate a more comprehensive discussion of the findings, the normalized HTC profiles across the vane surfaces are also extracted. These profiles are extracted at three different locations along the span – specifically at the 25%, 50%, and 75%. These profiles are generated for all the numerical simulations as well as the experimental data, and their representation is presented in Figure 3.18. To detail the outcomes in a more comprehensive manner, both Figure 3.17 and Figure 3.18 will be collectively analyzed in the upcoming sections. This analysis aims to provide a detailed comparison between the experimental results and the CFD outcomes from both qualitative and quantitative standpoints.

In particular, a notable discrepancy can be observed when examining the outcomes of the first RANS simulation (RANS input EXP SST) in terms of absolute values and trends as well. The HTC values predicted by the numerical simulations are markedly higher compared to the measured values, often exceeding them by a factor of over 2. Regarding the pattern, the numerical results effectively capture the qualitative aspects of the

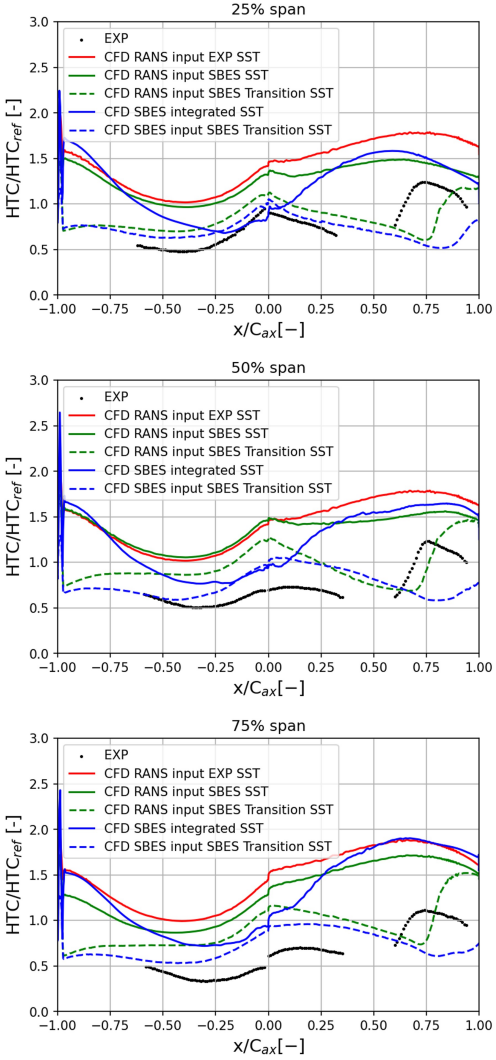

Figure 3.18: Heat transfer coefficient profiles at 25%, 50% and 75% of the span ***(©2024 Baker Hughes Company—All rights reserved)***.

twisted HTC distribution at the LE location. However, this accuracy diminishes in the SS area, where an elevated HTC zone is identified near the outer endwall. Similar results, with minor quantitative improvements, emerge from analyzing the maps and 1D plots produced by the RANS input SBES SST case, where similar patterns can be observed. The main differences can be attributed to the different boundary conditions at the NGV inlet (1D profiles vs 2D maps) that can influence the actual incidence distribution.

Shifting focus to the outcomes derived from the RANS input SBES Transition SST, there is an enhancement in the quantitative assessment both at the LE and in correspondence to the laminar regions of the PS and SS. This improvement is attributed to the introduction of the transition model. Nonetheless, when examining the SS region (frame 3), it becomes evident that the transition occurs later compared to the experimental observations. This delay is also noticeable from the 1D plots.

Regarding the SBES Integrated SST case, in which a fully turbulent simulation was conducted (using the $k-\omega$ SST model for the under-resolved regions), the outcomes demonstrate a closer alignment with experimental data. However, it is worth noting that, generally speaking, the HTC is still overpredicted. More specifically, when considering the quantitative 1D profiles, the comparison displays enhancement at the LE region. However, as the analysis extends beyond this region, the HTC is notably overestimated due to the adoption of the fully turbulent approach. This discrepancy arises in contrast to the laminar trend observed in the experimental results. Furthermore, the predicted pattern depicted in the 2D maps demonstrates a relatively uniform distribution across the span at the LE. However, this prediction fails to account for the non-uniformities observed in the experimental data, making the quantitative comparison acceptable only at a span of 25%, as evident in the corresponding line plot. Substantial differences in the revealed pattern are also noticeable on the PS and SS, indicating a lack of improvement over the results obtained from the RANS simulations, when assessed from a qualitative point of view.

Shifting the focus to the HTC predictions derived from the SBES input SBES Transition SST case, a greater resemblance to the experimental data becomes evident. Indeed, the HTC values undergo a substantial reduction, particularly along the PS, where the closest similarities to the experiments can be reached, notably at the 25% span position. In regard to the LE, even if the overall quantitative values are quite similar to the ones from the SBES Integrated SST case, the predicted pattern improves, with a better reproduction of the twisted shape of maximum HTC and inner outer differences. A comparable observation holds true for the PS distribution, where the low HTC region proximate to the outer endwall is distinctly recognizable. This results in the best overall matching of the quantitative profiles at the different spans. Nevertheless, certain quantitative disparities remain, particularly at the 75% span position. More substantial discrepancies can be noted by looking at the SS at frame 3, where the model fails to predict the turbulent transition. This behavior is evident through the 1D profiles across all span values. This demonstrates that the transition with high free stream turbulence remains a complex phenomenon to model but that, however, an improving of HTC prediction can be obtained by adopting the Transition SST model along with the SBES modelling. According to Figure 3.8, the experimental data show a strong impact of the BL transition on the airfoil.

Furthermore, in order to accentuate the disparities with the experimental data, the ratio between each CFD simulation and experimental HTC values is presented in Table 3.3. This comparison is reported at both the LE and the PS for three different span values. These ratios are specifically calculated utilizing the mean HTC values on the LE ($-0.1 < x/C_{ax} < 0.1$) and the PS ($-0.4 < x/C_{ax} < -0.1$). It is notable that the findings related to the SS are omitted due to the limitations within the CFD simulations, which appear to inadequately capture the HTC distribution within this region, as mentioned earlier.

As evident in Table 3.3, generally speaking, the utilization of SBES methodology tends to decrease the relative deviations from experimental data, consequently improving the match on both surfaces.

Moreover, generally speaking, also the employment of 2D maps instead of the conventional 1D profiles has a beneficial impact on the HTC distributions, as can be seen by comparing the results of RANS input EXP SST and RANS input SBES SST.
In conclusion, it becomes evident that providing reliable 2D boundary conditions at the inlet of the NGV, achieved by resolving the combustor's flow field through SBES, yields an overarching enhancement in the outcomes. Additionally, incorporating a transition model into RANS simulations (RANS input SBES Transition SST) brings about a substantial enhancement in predicting HTC on both the LE and the laminar portions of the PS and SS. Nonetheless, certain disparities still persist, particularly in regions where the transition occurs. Furthermore, the employment of SBES modeling demonstrates an further employment in outcomes compared to RANS cases, particularly evident on the LE. This effect is accentuated when combining SBES with a turbulence model capable of capturing transition phenomena to study the NGV. In this context, an improvement in HTC distributions through 2D maps is also observed. However, despite these advancements, noticeable discrepancies are still present, thus demonstrating that the transition with high free stream turbulence remains a complex phenomenon to model. However the results are supposed to improve further if particular attention is paid in employing such turbulence models by improving their application also to SBES calculations.

Similarly to the HTC maps presented earlier, Figure 3.19 displays 2D representations of the adiabatic wall temperature along the airfoil. The adiabatic wall temperature is normalized using Eq. 3.8. The maximum value of adiabatic wall temperature is assessed across the entire measured area and corresponds to the LE. The temperature contours resulting from the experiments exhibit an almost uniform radial distribution. Specifically, the highest temperature value is typically located approximately around the midspan of the airfoil, but slightly closer to the inner radial position. This particular temperature distribution, with a hot region near the midspan and colder regions towards the endwalls, is directly

influenced by the total temperature distribution found at Plane 40 (refer to Figure 3.15). Interestingly, the hot streak around the midspan remains coherent along both the SS and PS surfaces, although it experiences a more significant reduction on the latter.
Examining the CFD outcomes, it is observed that the behavior of adiabatic wall temperature is accurately captured, particularly on the PS and LE surfaces. However, significant disparities emerge when looking

Table 3.3: CFD/EXP ratio in terms of HTC for both the LE and PS and for three different values of the span. These ratios have been evaluated by respectively using the average value of HTC on the LE $(-0.1 < x/C_{ax} < 0.1)$ *and the PS* $(-0.4 < x/C_{ax} < -0.1)$ *for each CFD simulation and the experiments.. **(©2024 Baker Hughes Company - All rights reserved)**.*

CFD Simulation	25% span	50% span	75% span
	Leading Edge		
RANS input EXP SST	1.58	2.02	2.67
RANS input SBES SST	1.47	2.06	2.39
RANS input SBES Transition SST	1.21	1.75	2.06
SBES Integrated SST	**0.96**	**1.34**	1.77
SBES input SBES Transition SST	1.08	1.41	**1.64**
	Pressure Side		
RANS input EXP SST	1.80	2.03	2.98
RANS input SBES SST	1.69	2.09	2.65
RANS input SBES Transition SST	1.35	1.74	2.19
SBES Integrated SST	**1.14**	1.41	2.02
SBES input SBES Transition SST	1.18	**1.32**	**1.71**

at the SS surface, where the hot streak appears to become thinner as it progresses downstream, unlike what is observed in the experiments. While assessing the exact cause of this inconsistency is challenging, it can be suggested that CFD may be underestimating turbulence dissipation in this region, thereby overestimating turbulent mixing and, consequently, the HTC, as indicated by previous findings. Furthermore, when analyzing the maps generated by RANS input EXP SST, the hot streak around the midspan seems to be less extended compared to both the other CFD results and the experimental observations. This primary distinction can likely be attributed to differences in the boundary conditions at the inlet of the NGV, where 1D profiles were prescribed. Nevertheless, generally speaking, the 2D maps derived from CFD show remarkable similarity to one another, even on the SS surface, where, as mentioned earlier, the most significant disparities with the experimental results become apparent. In conclusion, even if the CFD is able to capture well the trend related to the temperature distribution on the vane, differences with respect to the experiments are still visible, especially on the SS, where there is a greater drop than the experiments in the numerical results.

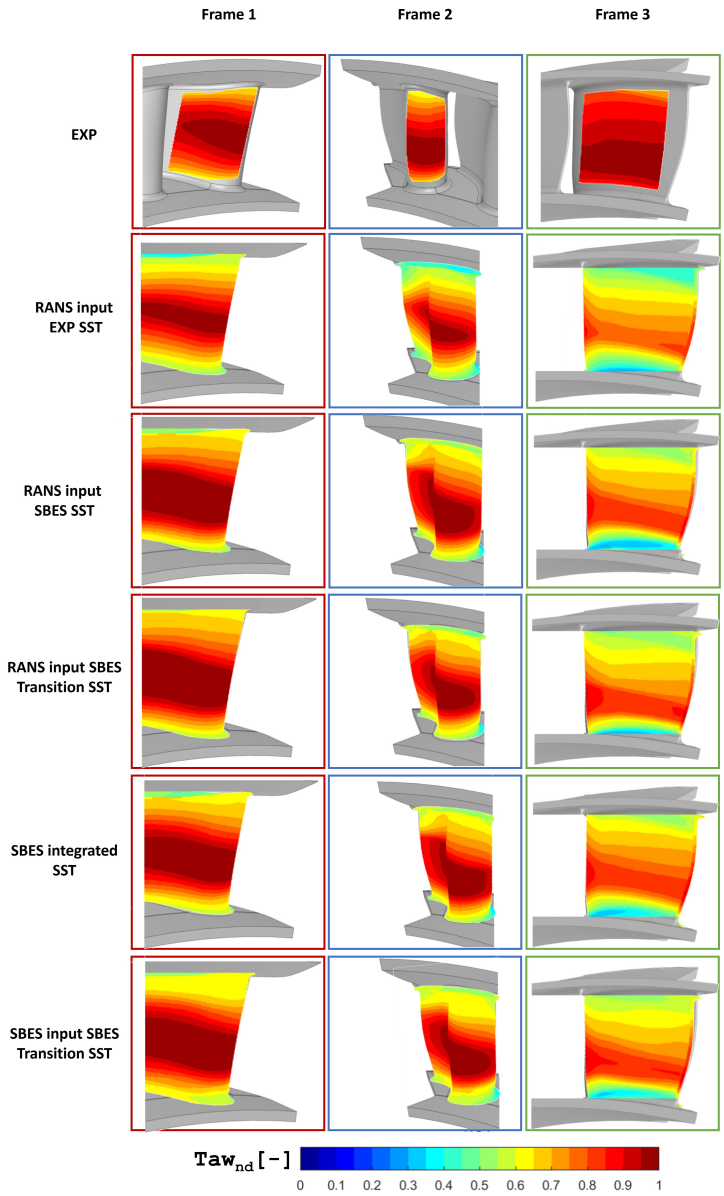

Figure 3.19: Adiabatic wall temperature maps ***(©2024 Baker Hughes Company—All rights reserved)****.*

3.4 Adiabatic effectiveness prediction: periodic one-sector SBES simulation

After demonstrating the improvements achieved using an SBES approach compared to conventional RANS for predicting HTC, the objective is to quantify these improvements while also describing the behavior of the film cooling system. To do so, a SBES simulation is performed on the one-sector periodic configuration, as previously done for the prediction of HTC, aiming to keep the computational costs manageable.

3.4.1 Numerical setup

The computational domain employed for the calculation is reported in Figure 3.20. According to previous calculations, the Dynamic Smagorinsky Sub-Grid Scale (SGS) closure is applied to the resolved regions, while the $k-\omega$ SST model is chosen for the under-resolved ones.

Mass flow boundary conditions are set at the inlet sections of swirlers and nuggets, by leveraging preliminary experimental data from the PSP testing campaign. It is important to point out that the inlet sections of swirlers and nuggets are fed by air. Meanwhile, static pressure is applied at the outlet of the domain based on initial considerations and available

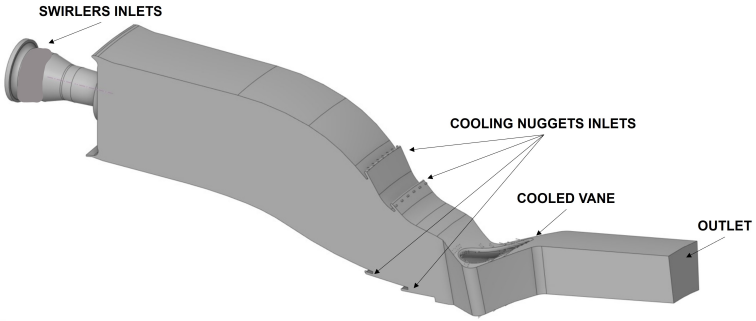

Figure 3.20: CFD Periodidc domain including both CC and cooled NGV ***(©2024 Baker Hughes Company—All rights reserved).***

experimental information from the PSP tests. Moreover, mass flow inlet-type boundary condition is used for each film cooling hole inlet within the domain and a flow network is used to predict the injection mass flow rates. Film cooling holes are simulated by extending the computational domain into the cooling channel. This approach is used to improve the accuracy of cooling flow prediction, avoiding the use of boundary conditions directly applied as patches on the airfoil surface. Probably, the pressure-inlet boundary condition type is deemed more suitable for the inlets of the NGV than the mass flow rate adopted in the current study. However, due to the simplification of the cooling jets' geometry to reduce the overall cell count and the unavailability of numerical data for the total pressure at specific locations, the decision is made to retain the total cooling flow rate as it is. All film cooling holes are fed by CO_2, according the experimental procedure: in this way, the adiabatic effectiveness can be evaluated by looking at the mass fraction of CO_2. All walls are treated as smooth and no slip surfaces. The hybrid unstructured computational grid, depicted in Figure 3.21, is created using ANSYS Fluent Meshing. It comprises 50 million polyhedral elements and includes 12 prismatic layers. The chosen mesh configuration aims to maintain a $y+$ value below 1 across all NGV surfaces and, within the LES-modeled zones, to resolve at least 80% of the turbulent kinetic energy. Unfortunately, all the meshed film cooling holes can not be shown, due to proprietary reasons. In order to verify this statement, the contour plot depicted in Figure 3.22 illustrates the computed values of Pope's criterion on the cross section of the domain. Moving in the flow direction, the criterion's value is notably higher than 0.9 inside the combustor and remains above 0.8 within the nozzle, indicating that the requirement to resolve at least 80% of the turbulent kinetic energy is successfully met. The areas close to the wall, where the RANS model is applied, show values below this threshold. Notably, on the suction side of the airfoil, where the solution is handled with RANS, there is an observable thickening of the boundary layer.

According to the previous analyses, the numerical simulation is conducted

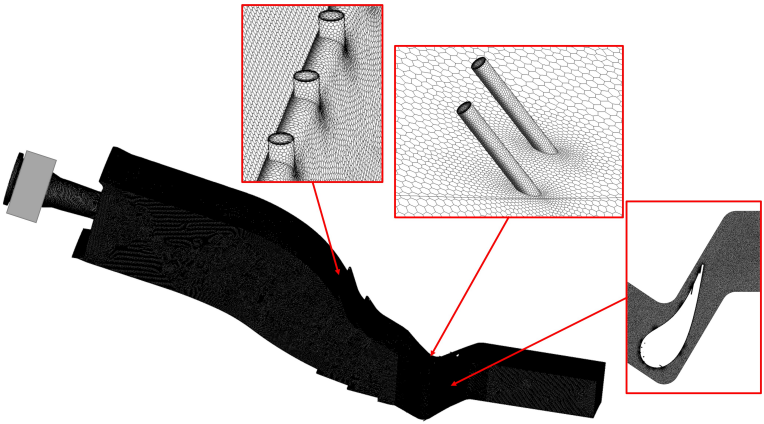

Figure 3.21: Computational grid of the combustor+cooled nozzle periodic domain ***(©2024 Baker Hughes Company—All rights reserved)****.*

using the commercial software Ansys Fluent v21.1, which employs a fully compressible approach and a coupled scheme for pressure-velocity coupling within the 3D Navier-Stokes solver. Furthermore, a second-order accurate scheme is utilized for discretization in both time and space. The time step is set to approximately 10^{-6} seconds to control the value of the convective CFL number.

3.4.2 Verification of boundary conditions

Once again, before displaying the comparison between experimental results and numerical predictions of adiabatic effectiveness on the surface of the airfoils, it is important to validate that the primary flow field parameters at the interface between the combustor and turbine, as estimated by CFD simulation, align with the measurements performed during the PSP testing campaign. In Figure 3.23, the left-hand column presents the measurements acquired through a five-hole probe traversing Plane 40 under PSP operating conditions. On the corresponding right-hand column, the aerothermal field parameters obtained through CFD are

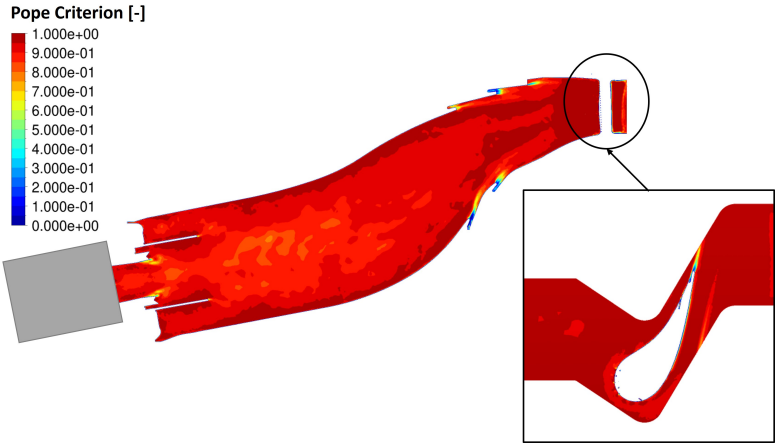

Figure 3.22: Pope's criterion (PSP operating conditions) ***(©2024 Baker Hughes Company—All rights reserved)****.*

illustrated.

In particular, the swirl, pitch, Mach number and dimensionless total pressure fields are shown in sequence on each row of the figure. Note that on the x-axis of the plots is the t/p_{NGV}, i.e. the tangential-angle to the angular NGV-pitch ratio, whereas on the y-axis the normalized NGV height h/H (or span) is reported. Swirl, pitch are defined according to Eq. 3.2 and Eq. 3.3. Regarding the contours, the current comparison at the interface plane displays a satisfactory agreement with the measurements. In reality, the swirl, Mach number and dimensionless total pressure distributions closely resemble that ones from experiments. Similarly, the pitch distribution exhibits a qualitatively similar pattern, even though some differences are observable. Enhancing the quantitative evaluation of the comparison involves the extraction of 1D profiles that are tangentially averaged from the maps. These profiles are presented in Figure 3.24. As per their name, PSP can be first of all employed to retrieve the pressure distribution over the given tested surface. Thus, CFD results can be benchmarked against experimental measurements as shown in Figure 3.25.

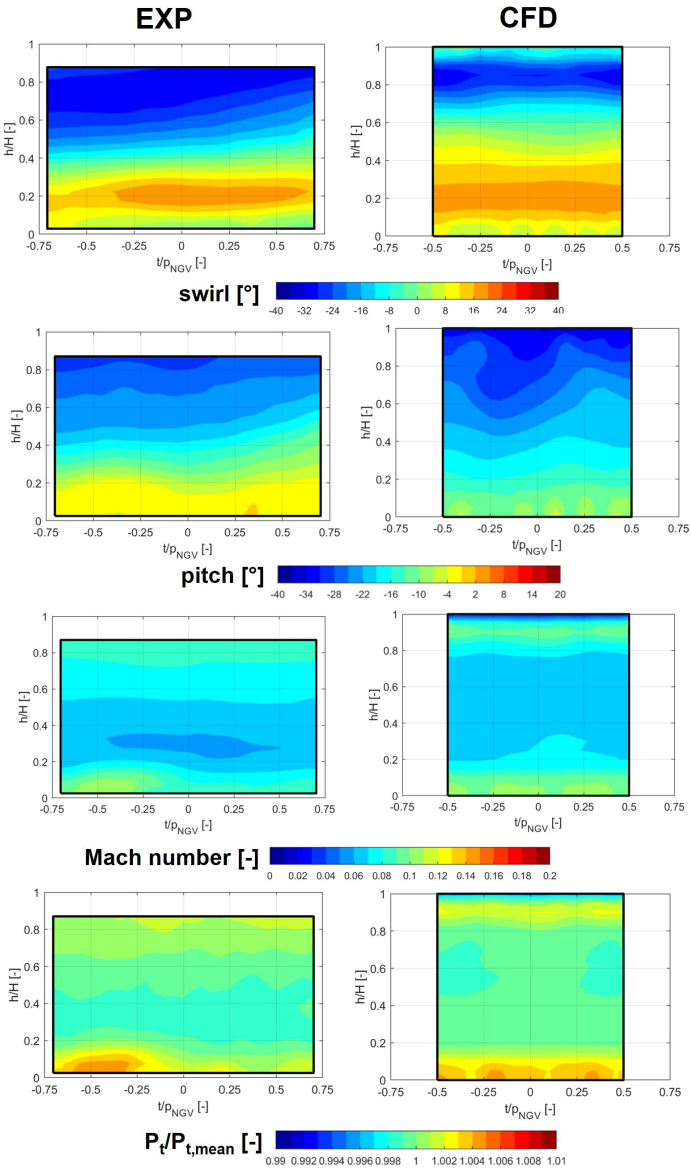

Figure 3.23: Five-hole probe and CFD contours at Plane 40 (PSP operating conditions) ***(©2024 Baker Hughes Company—All rights reserved).***

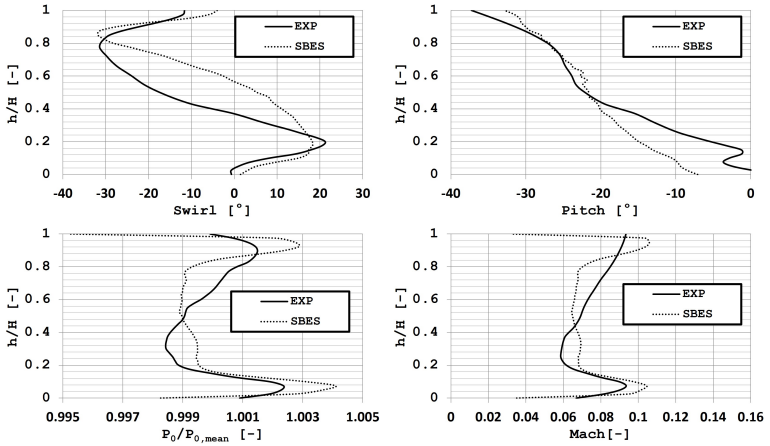

Figure 3.24: 1D tangentially averaged profiles on Plane 40 (PSP operating conditions) ***(©2024 Baker Hughes Company—All rights reserved).***

In both cases, the pressure distribution is fairly uniform in the first part of the PS (frame 1), while on the SS (frame 2 and 3) the pressure gradient is more pronounced, especially where the throat section is crossed. The comparison can then be extended to the blade load curves at a certain span section of the airfoil, which, per the mid-span, is reported in Figure 3.26. The data from the experiments indicate notable measurement noise, primarily coming from the measurement technique's limited sensitivity to pressure measurements [119]. Experimental loads are presented for NGV1, for SS results, and for NGV2, for PS results, as these surfaces demarcate the central passage. In this case, the experiments were carried out by employing cooled NGV doublet. Also in this case, it is evident that the pressure distribution predicted by the SBES calculation closely aligns with the experimental curves, presenting a satisfactory correspondence. This outcome represents a reliable verification that the same aero-behaviour is achieved.

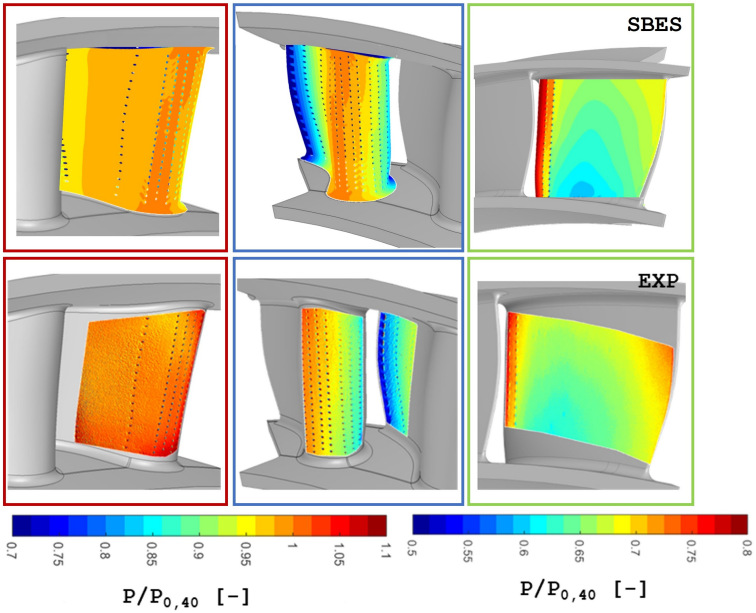

Figure 3.25: Nozzles pressure distribution (PSP experiments vs CFD ***(©2024 Baker Hughes Company—All rights reserved)****.*

3.4.3 Adiabatic effectiveness

As already anticipated, PSP technique serves as an efficient method for assessing the adiabatic effectiveness of film cooling, functioning as a concentration detector. When it comes to film-cooled nozzles, the adiabatic effectiveness stands out as a crucial gauge of the cooling system's performance, evaluating its capacity to adequately cover and safeguard the surface of the nozzles. Figure 3.27 presents a comparison between numerical predictions and experimental results for the three reference frames, corresponding to the optical accesses, as already presented for the HTC results. The frame reference remains so consistent with Figure 3.7 and Figure 3.17. Analyzing each frame individually provides more in-depth

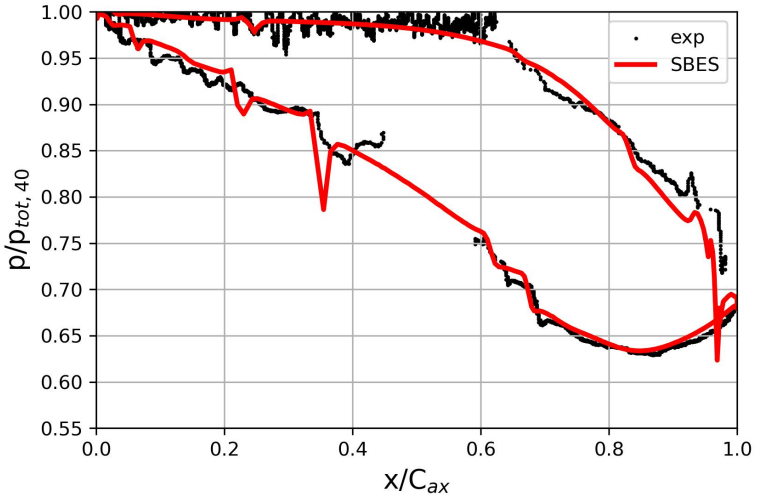

Figure 3.26: NGV pressure load at midspan (cooled NGV) ***(©2024 Baker Hughes Company—All rights reserved).***

insights and considerations. It is important to point out that, in order to quantify the improvements of using more advanced CFD modelling technique as SBES instead on RANS, the results coming from a RANS performed on the trisector domain is also included. Such calculation was performed by Baker Hughes and the main result were kindly shared in order to facilitate this comparison. The calculation was performed using ANSYS CFX v19.4 with all equations are discretized with the "high resolution" scheme. Turbulence is modelled using the $k-\omega$ SST model. The main difference with the one-sector SBES is that for the trisector RANS trisector the internal cooling system of the tested vane was meshed and resolved bringing the total mesh elements number to about $169 \cdot 10^6$ of tetrahedral elements. Another noteworthy difference between the two simulations is that the trisector RANS uses only air (ideal gas) as working fluid, while the one-sector SBES employs CO_2 to model the coolant, according the experimental procedure. Hence, for the trisector RANS, to

track film cooling concentration, a passive scalar was introduced, assigning a value equal to 1 at the inlets of the internal channels and 0 at the combustor outlet flow; in this way it was possible to retrieve adiabatic effectiveness values, based on concentration measurements, as it is done by PSP, capitalizing on heat and mass transfer analogy.

Looking at Figure 3.27 and starting from the LE region (frame 2), the experimental map depicts a non-straight stagnation line, since two

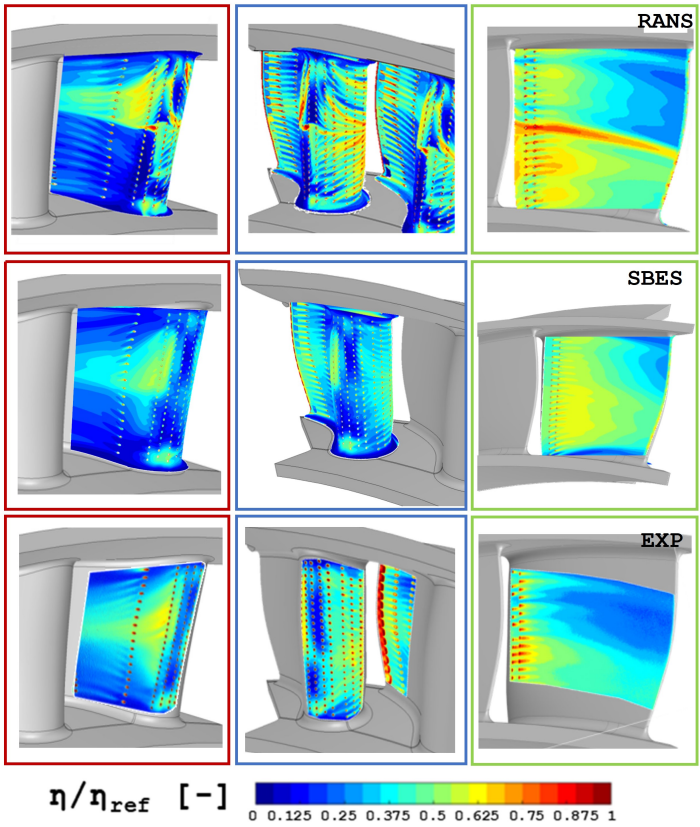

Figure 3.27: Film-cooling adiabatic effectiveness ***(©2024 Baker Hughes Company—All rights reserved).***

low effectiveness areas are spotted. This phenomenon, induced by the highly-swirled impacting flow, is partly captured by trisector RANS, where coolant traces appearing slightly more isolated compared to the experimental map. Additionally, measurements suggest that the stagnation line's position shifts slightly more downstream on the SS than predicted by the trisector RANS. Looking instead to the contours of one-sector periodic SBES, it is instead evident that this comes closer to the experimental data, although the coolant coverage appears slightly lower in the remaining zones of the LE.

Subsequently, generally speaking, the PS (frame 1) and SS (frame 3) exhibit diametrically opposed behaviors. Specifically, owing to the swirled structure of the main flow, improved film coverage is observed in the upper half of the PS and the lower half of the SS. Looking at the trisector RANS, the most effective protection is achieved near the midspan, where the coolant traces appear more pronounced, likely influenced by the low-pressure core of the main flow. This behaviour can be attributed to the RANS modelling, since it is known how its associated strong underprediction of the turbulent mixing can lead to a different distribution of the adiabatic effectiveness along the vane compared to the experimental data, leaving areas of the vane locally unprotected (such as the lower half of the PS) while overpredicting the effectiveness in others (such as the higher half of the PS), according to [104, 129]. As a matter of fact, the one-sector SBES predicts a distribution much more similar to the experimental data, providing a more homogeneous coolant distribution on the SS while still maintaining the correct alternation between areas with higher and lower coverage due to the highly-swirled impacting flow. In addition, even on the PS, the coolant distribution is more faithful to the experimental data, capturing the "triangular-shape" distribution characteristic of the experiments. This is in contrast to the trisector RANS, which instead predicts two distinctly separated areas of high and low coolant coverage, as for the SS.

To have a further and more quantitative appreciation of the differences between experiments and RANS/SBES predictions line plots of the film-

cooling adiabatic effectiveness are reported in Figure 3.28. Figure 3.28 shows an extraction at a given axial location on the NGV PS and SS surfaces, with profiles of the normalized adiabatic effectiveness (x-axes) along with the nozzle span (y-axes).

Such comparison on the PS surface highlights how the trisector RANS predicts a net separation of coolant distribution between the higher and lower half, which is induced by the swirled inflow but is not as sharp in the experimental measurements. On the other hand, on the SS the comparison holds on a more restricted portion of the surface due to accessibility constraints. Despite this fact, numerical and experimental values are comparable on the higher span-fraction, while an intense accumulation of coolant is predicted by the trisector RANS, which however and as mentioned is in line with previous literature findings. Some higher coolant presence and hence less mixing is also predicted on the lower span-fraction, which in both trisector RANS and measureaments is however specular to the distribution on the pressure side as dictated by the impacting swirling flow.

Looking at the one-sector SBES plots, it is evident that CFD resembles the experimental data, improving significantly the prediction compared to RANS. Even on the SS, it can be observed that, in terms of trend, the radial distribution of adiabatic effectiveness closely resembles the experimental data, unlike the RANS. However, the curve is shifted towards higher values of adiabatic effectiveness. This can be explained by the fact that the film cooling system in the SBES simulation was simplified by extending the computational domain into the cooling channels. This approach is used to improve the accuracy of cooling flow prediction, avoiding the use of boundary conditions directly applied as patches on the airfoil surface. This causes the film cooling jets to be fed in an “ideal” manner, without distortions. In reality, these effects would result in a lower average velocity at the hole inlet, reducing the actual BR and causing less penetration of the jets. Furthermore, in addition to this simplification, possible errors or inaccuracies can be also present due to the necessity of using a flow network for predicting injection mass flow rates imposed as

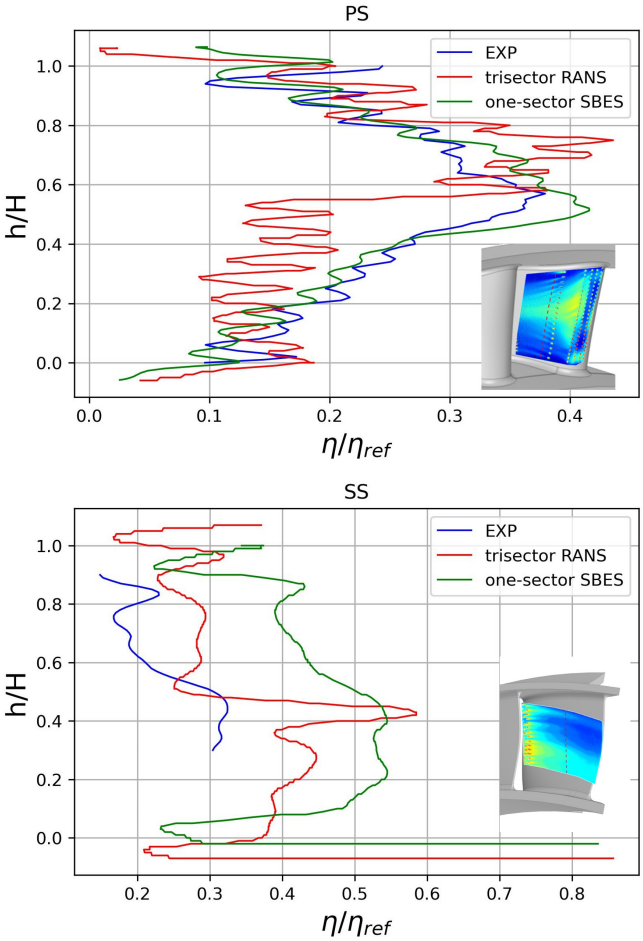

Figure 3.28: Film cooling normalized adiabatic effectiveness extracted at a given axial position on the PS and SS surfaces ***(©2024 Baker Hughes Company—All rights reserved)***.

inlet boundary conditions to all film-cooling holes. The RANS simulation, although in a simplified and averaged manner, takes more into account the presence of such non-uniformities, as the entire cooling system was represented and meshed. Such complexity could not be replicated in the SBES case due to prohibitive computational costs. Analyzing the VR on the PS and SS, both cases yield values indicative of a penetrative regime ($VR > 0.8$), according to Pedersen et al. [61], although the values on the SS are lower, justifying the higher values of adiabatic effectiveness in this area. Unfortunately, further analyses were not possible due to a lack of additional information related to experimental data and the RANS simulation.
However, in conclusion, it can be stated that one-sector SBES simulation is satisfactorily replicating the coolant alternate spread on the higher/lower half of the PS/SS due to the main flow swirling structure, leading to a significant improvement compared to RANS overcoming its limitations. However, there would be still a margin of improvement if it were possible to reproduce and mesh the entire cooling system. A more comprehensive discussion on the RANS simulations previously conducted on a trisector cooled configuration can be found in [10].

3.5 Concluding remarks

This chapter describes an experimental test case with a combustor simulator and a nozzle cascade, where both adiabatic effectiveness and HTC measurements were carried out, together with comparative numerical simulations. In order to firstly study the HTC, a RANS calculation of the trisector combustor-cascade integrated domain is performed. The objective was to judge the capability of traditional RANS modeling approaches in characterizing heat transfer. For what regards the HTC results, derived via transient IR measurements on the rig, its distribution on the airfoil surface is strictly dictated by the inlet swirl profile, which not only induces a twisted stagnation line on the airfoil LE but also implies a non-uniform radial distribution on both pressure and suction sides. RANS modelling

returns only qualitatively comparable results as compared to test data, although it fails to provide an acceptable quantitative assessment which results in high discrepancies.
Then, in accordance with the standard industrial design practice, a periodic stand-alone NGV configuration was created in order to evaluate HTC on the vane surface by performing RANS simulations and by using 1D profiles from the experiments as inlet boundary conditions (RANS input EXP SST). Then, a fully integrated combustor-stator periodic domain was investigated by performing a SBES simulation (SBES integrated SST). From this run, a set of unsteady data were extracted and stored to generate realistic unsteady inlet boundary conditions to further investigate the non-cooled NGV configuration in a decoupled way by performing RANS (RANS input SBES SST and RANS input SBES Transition SST) and SBES (SBES input SBES Transition SST) simulations as well. Eventually, numerical results were compared to the experiments in order to evaluate the discrepancies between different CFD approaches. This evaluation aims thus to assess if such more advanced and more time-consuming methods, including also turbulence models able to capture the transition, can be more reliably used for a proper prediction of the vane thermal loads.
For what regards the HTC, experimentally obtained by using transient IR measurements on the rig, it emerged that its distribution on the airfoil surfaces is strictly dependent on the swirl distribution that can be found at the inlet of the NGV, which induces indeed an evident twisting of the stagnation line on the LE influencing thus the HTC distribution on the PS and SS as well. Looking at the CFD results, especially focusing on the RANS input EXP SST case, that represents the standard industrial practice to evaluate heat loads, evident differences emerged. It was also noted that the employment of 2D maps instead of the conventional 1D profiles leads to a global improvement of the results (RANS input EXP SST vs RANS input SBES SST). Therefore, it can be concluded that providing reliable boundary conditions at the NGV inlet by solving the flow field of the combustor by using a SBES (SBES integrated SST) improves considerably the results. Moreover, the introduction of the

transition model for the RANS (RANS input SBES Transition SST) leads to a significant improvement in the prediction of the HTC on both LE as well as in the laminar parts of PS and SS, even if some discrepancies are still evident, especially where the transition occurs. Moreover, it was also demonstrated that the employment of the SBES modelling leads to a further improvement in results compared to RANS cases, especially on LE. This is especially true by using SBES jointly with a turbulence model able to capture the transition phenomena to study the NGV (SBES input SBES Transition SST). However, some important differences are still evident, especially on the SS, where the transition seems not to occur. These discrepancies can be attributed to the fact that, despite the elevated levels of turbulence at the inlet, the experimental data show a strong impact of the BL transition on the airfoil. The transition with high free stream turbulence in fact, remains a complex phenomenon to model.
As far as the author' knowledge is concerned, the present work represents one of the first attempt for the estimation of HTC, under the presence of high swirled and temperature distorted flow at the inlet of the stator, by using different CFD approaches to be benchmarked with the experiments. After demonstrating the improvements achieved using an SBES approach compared to conventional RANS for predicting HTC, the objective is to quantify these improvements while also describing the behavior of the film cooling system. To do so, a SBES simulation is performed on the one-sector periodic configuration, as previously done for the prediction of HTC, aiming to keep the computational costs manageable.
Moreover, in order to quantify the improvements of using more advanced CFD modelling technique as SBES instead of RANS, the results coming from a RANS performed on the trisector domain is also included. Such calculation was performed by Baker Hughes and the main result were kindly shared in order to facilitate this comparison.
Looking at the results, under representative combustor outflow conditions, it can be stated that one-sector SBES simulation is satisfactorily replicating the coolant alternate spread on the higher/lower half of the PS/SS due to the main flow swirling structure, leading to a significant improvement

compared to RANS overcoming its limitations. However, there would be still a margin of improvement if it were possible to reproduce and mesh the entire cooling system.

Chapter 4

Analysis of combustor-turbine interaction in an industrial turbine under representative engine-like conditions

Contents

In recent years, there has been a growing interest in understanding the interaction between combustion and turbine phenomena. The combustor's strong unsteady and three-dimensional flow field typically extends up to the first-stage nozzle, potentially influencing its design and affecting its aerodynamics and cooling system efficiency. These effects are even more pronounced when lean-burn combustors are used, as they require high turbulence levels for flame stabilization, leading to increased temperature and velocity distortions at the first-stage nozzle inlet. While it is known that the most comprehensive approach to studying combustor-turbine interaction is by simulating both components together, performing coupled simulations remains challenging, especially in an industrial context. As a result, the generation and application of highly representative and reliable boundary conditions at the inlet of the first-stage nozzle (S1N) have become increasingly important. This enables the separate study of the two components by conducting decoupled simulations.

In this chapter, the objective is to compare fully integrated combustor-stator SBES simulation with isolated stator simulations, whose computational domain is obtained by an extraction from the one including both components. Hence, to assess the risks and uncertainties associated with conducting decoupled simulations, scale-resolving simulations are performed to ensure a accurate resolution of most flow structures while keeping computational costs low.

To do so, a fully integrated combustor-nozzle configuration is therefore firstly investigated, along with a realistic turbine nozzle cooling system, under realistic engine-like operating conditions. Subsequently, the obtained results are compared with those from a separate SBES simulation focusing solely on the first stage nozzle. For this particular case, time-varying inlet boundary conditions are derived from an SBES of the standalone combustor, where the nozzle was replaced with a discharge convergent maintaining the Mach number of the NGV and ensuring a consistent throat area. Furthermore, in an effort to evaluate discrepancies between various CFD approaches, the outcomes of the corresponding preliminary RANS S1N simulations are also presented, employing both one-dimensional pro-

files, as per standard design practice, and two-dimensional maps from the time-averaged solution of the precursor SBES of the standalone combustor as inlet boundary conditions. Therefore, the focus of this study is on comparing and analyzing numerical SBES simulations of an integrated combustor-NGV configuration and isolated NGV RANS and SBES simulations. The aim is to evaluate the influence of the combustor's presence under realistic operating conditions and a realistic annular geometry.

4.1 Overall setup

In the next sections, the overall characteristics in terms of computational model and setup that all the simulations carried out in engine-like conditions share will be reported. The main differences between one simulation and another, which will be limited to the decoupled simulations of the stand-alone nozzle, will be explained and indicated on the basis of the specific case under examination.

4.1.1 Computational model

4.1.1.1 Combustor-S1N case

The numerical analysis is carried out on a specific part of the annular combustor of a heavy-duty gas turbine provided by Baker Hughes, which is shown in Figure 4.1 (see also Figure 4.5). Unfortunately, the number of swirlers and first-stage nozzles (S1N) have a prime relationship with each other and, due to computational limitations, it is not feasible to simulate the entire annular ring. Therefore, to address this, the geometry of the S1N is slightly altered to fit within a single sector of the combustion arrangement. The modifications involve stretching the geometry while maintaining the same pitch-chord ratio and throat area as the original design. This ensures that the numerical model accurately represents the real stator despite the adjustments made for computational efficiency. The combustor model begins at the compressor discharge chamber, which is positioned upstream of the premixer (not shown in Figure 4.1). Including this component in the model is crucial for accurately representing flow

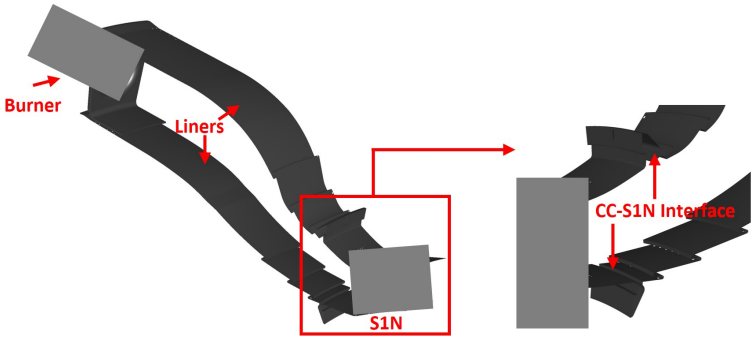

Figure 4.1: Single sector geometry with detailed view of the simplified first-stage nozzle and platforms. Details regarding the swirler and the cooling system are not visible due to Baker Hughes disclosure policy reasons. ***(©2024 Baker Hughes Company—All rights reserved).***

fluctuations at the burner entrance. The burner itself is simulated in detail, encompassing all aspects of the counter-rotating swirler [130]. Within the swirler, the primary fuel is injected to create the premixed mixture, and there is an additional pilot fuel line responsible for stabilizing the flame in the primary zone of the dome.

In the investigation of the interaction between the combustion chamber and the first stage nozzle, special attention is given to the interface plane (plane 39.5). This plane is strategically positioned to account for the leakage arising from the leaf seals, as reported in Figure 4.2. Including such flows in the study is crucial since they predominantly contribute to temperature distortions both along the streamwise and spanwise directions at the interface plane. Moreover, in the same figure, also the locations of four different cross sections orthogonal to the axis of the machine upstream of the p39.5 plane (plane P1, plane P2, plane P3 and Plane P4) are reported. These sections, along with plane 39.5, will be employed for the following analyses of this study. However, when it comes to circumferential temperature distortions, a remarkably uniform distribution is observed at plane 39.5. This phenomenon can be attributed

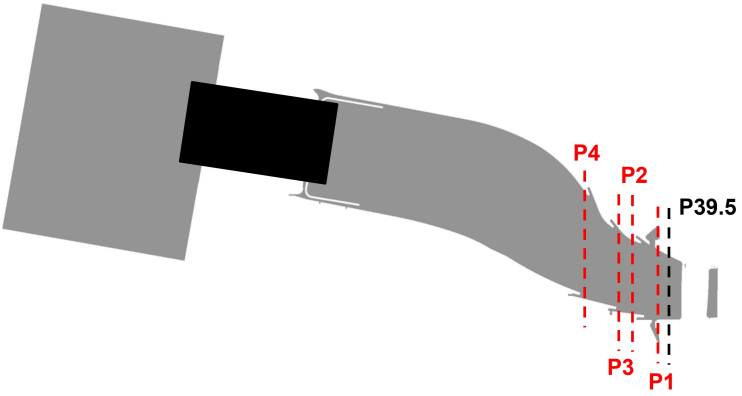

Figure 4.2: Representation of the interface plane between combustor and first stage nozzle, known as plane 39.5, and four planes (P1, P2, P3, P4) orthogonal to the machine axis in the coupled computational domain. Details regarding the swirler are removed for Baker Hughes disclosure policy reasons ***(©2024 Baker Hughes Company—All rights reserved)***.

to the long residence time characterizing this industrial combustor. As a result, analyzing different swirler-to-S1N clocking positions becomes unnecessary in this context.

In this study, the fuel composition is simplified, assuming pure methane. Although this assumption may not cover the entire range of natural gas compositions, it serves as a suitable representation, as methane can be considered a typical component of natural gas, which may contain higher hydrocarbons ($C2+$) as well as inert elements. As anticipated, the liners of the combustor incorporate cooling holes at all sections. For instance, Figure 4.1 illustrates the presence of film cooling in the final part of the liners near the cavities. Looking at the S1N more closely, the model includes all the cooling flows not only of the vane but also of the outer and inner platforms. Such flows have to be included not just to investigate the solution related to the platforms but also to understand their interaction with the cooling flows of the airfoil and with the flow coming out from

the cavities. Regarding the cooling of the stator, the number of holes on both sides of the airfoil is preserved if compared to the real design, while the position is slightly different as a consequence of the above mentioned scaling of the geometry. Mass flow inlet-type boundary condition is used for each inlet within the domain and a flow network is used to predict the injection mass flow rates. Film cooling holes are simulated by extending the computational domain into the cooling channel. This approach is used to improve the accuracy of cooling flow prediction, avoiding the use of boundary conditions directly applied as patches on the airfoil surface. The primary objective is to investigate the interaction between the film cooling jets and the main hot flow from the combustor. To achieve this goal, the pressure-inlet boundary condition type is deemed more suitable for the inlets of the S1N than the mass flow rate adopted in the current study. However, due to the simplification of the cooling jets' geometry to reduce the overall cell count and the unavailability of numerical data for the total pressure at specific locations, the decision is made to retain the total cooling flow rate as it is. Regarding the NGV outlet boundary condition, a standard pressure outlet condition is applied at the outlet as a 1D radial profile. The pressure drop associated with the flow expansion in the stator is enforced in the outlet boundary condition, and these conditions are based on the ISO base load of the engine, which is being studied. The same 1D radial pressure profile is also shared by all the stand-alone S1N simulations, both RANS and SBES, here presented. Moreover, two passive scalars are introduced in order to track film cooling concentration coming from the film cooling holes placed on the vane surface and from the two-dimensional slots cooling placed on the liner of the combustor (cooling nuggets). The final mesh consists of 81 million polyhedral elements. This high element count is a result of an extremely refined resolution applied in the combustor, particularly in the primary zone, the burner, and at the fuel inlets [131]. Additionally, the mesh inside the first-stage nozzle (S1N) is also highly refined. Furthermore, to maintain accuracy in the boundary layer, 14 prism layers are generated at the walls, aiming to achieve a y^+ value of 1. Figure 4.3 displays the mesh in the primary zone and inside

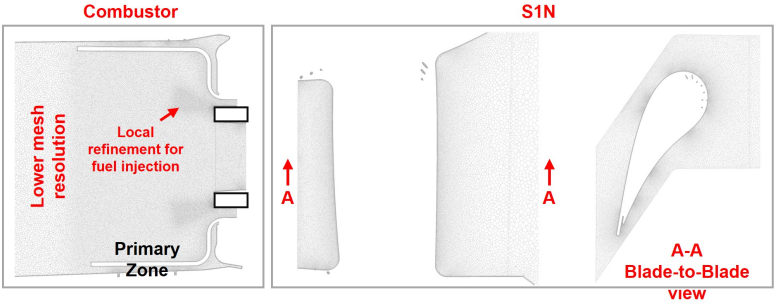

Figure 4.3: Mesh resolution inside the primary zone of the combustor ***(left)*** *and the first-stage nozzle* ***(right)*** ***(©2024 Baker Hughes Company—All rights reserved)***.

the first-stage nozzle, offering a longitudinal view of the combustor's middle plane. Additionally, a blade-to-blade section is provided to better illustrate the mesh resolution in the stator. To validate the adequacy of this mesh resolution, the assessment involves computing Pope's criterion [132]. Following a rigorous procedure, this criterion should be evaluated solely in the flow core, away from the walls where the large-eddy simulation (LES) is carried out. The calculation of Pope's criterion is as follows:

$$\frac{k_{res}}{k_{res} + k_{sgs}} \tag{4.1}$$

with k_{res} the resolved part of the turbulent kinetic energy spectrum and k_{sgs} the modeled one evaluated through the SGS viscosity:

$$k_{sgs} = \left(\frac{\mu_{sgs}}{\rho l_{sgs}}\right)^2 = \left(\frac{\mu_{sgs}}{\rho C_s \Delta}\right)^2 \tag{4.2}$$

For further details on the conservation and turbulence equations related to the numerical model employed in this study, additional information can be found in [105, 122]. The contour plot depicted in Figure 4.4 illustrates the computed values of Pope's criterion on the stator. Moving in the flow direction, the criterion's value is notably higher than 0.9 inside the

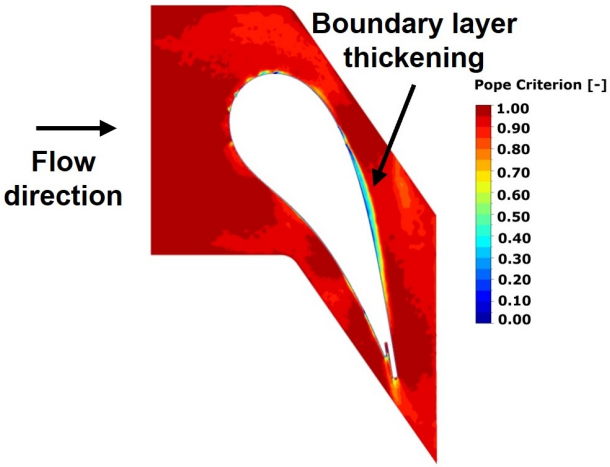

Figure 4.4: Pope's criterion visualized on the S1N ***(©2024 Baker Hughes Company—All rights reserved).***

combustor and remains above 0.8 within the nozzle, indicating that the requirement to resolve at least 80% of the turbulent kinetic energy is successfully met. The areas close to the wall, where the RANS model is applied, show values below this threshold. Notably, on the suction side of the airfoil, where the solution is handled with RANS, there is an observable thickening of the boundary layer.

4.1.1.2 S1N cases

The S1N stand-alone numerical grid precisely matches the mesh of this component in the integrated configuration. This alignment is achieved by implementing a cutting plane at plane 39.5 to isolate the stator, which corresponds to the component's inlet. The resulting mesh for the isolated S1N consists of approximately 20 million polyhedral elements, including 14 prismatic layers. Furthermore, the SBES numerical calculations for the S1N stand-alone case share identical characteristics and overall setup with the integrated configuration, as represented in Figure 4.5. Further

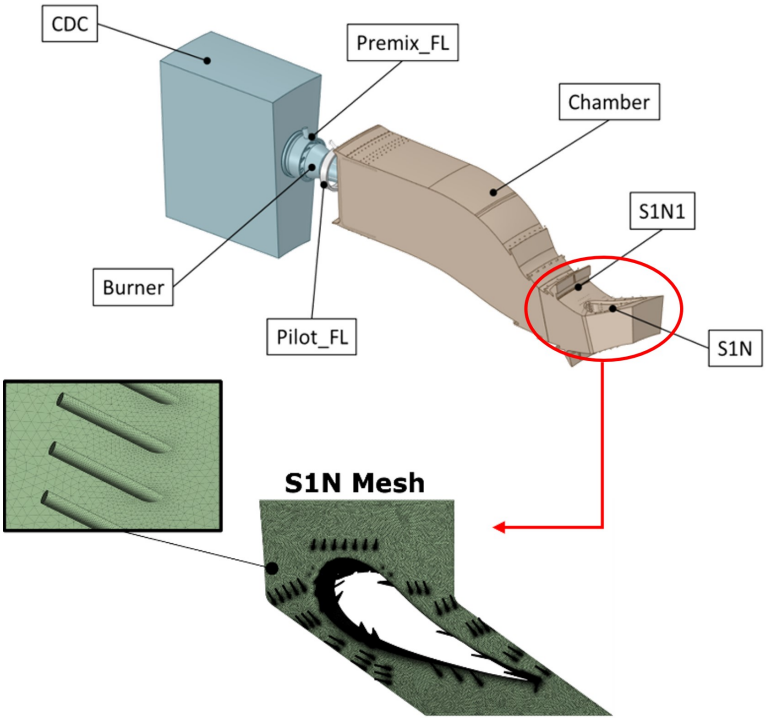

Figure 4.5: CFD domain of the integrated model along with a detail of the S1N mesh. For periodicity reasons, the computational studyis limited to one-cup of the annular combustion system. ***(©2024 Baker Hughes Company—All rights reserved).***

details about the boundary conditions and the turbulence model will be provided in the next sections and chapters depending on the case of study.

4.1.2 Combustion model

The combustion model relies on the transport equation of the progress variable (c). The source term in this equation is determined using the

formulation of the turbulent flame speed (S_t) as presented in [133]:

$$\bar{\dot{\omega}}_c = \rho_u S_t |\nabla \tilde{c}| \tag{4.3}$$

with ρ_u the density of the unburned mixture. The term S_t can be determined according to Equation (4.4):

$$S_t = u_{\Delta}^{'3/4} S_c^{1/2} \alpha^{-1/4} (C_S \Delta)^{1/4} \tag{4.4}$$

where $u_{\Delta}^{'}$ and $(C_S\Delta)$ are, in the LES framework, the sub-grid-scale (SGS) fluctuation and the length scale, respectively, while α is the thermal diffusivity, and S_c is the laminar flame speed in the original formulation of this combustion model. In this study, the laminar flame speed is substituted with the consumption speed of the mixture [134, 135]. The major advantage of using the consumption speed lies in its ability to incorporate both the effects of strain rate (a) and heat loss (ψ) into the turbulent combustion model. This approach enables the consideration of non-equilibrium effects, resulting in improved predictions of emissions, particularly CO [136, 137], and better handling of flame extinction [138]. By leveraging the instantaneous solution and not considering the curvature contribution, which can be negligible for high Karlovitz numbers, the strain rate can be computed as follows:

$$a = (\delta_{i,j} - n_i n_j) \frac{\partial u_i}{\partial x_j} \tag{4.5}$$

with n being the flame front normal vector and $\left(\frac{\partial u_i}{\partial x_j}\right)$ the velocity gradient. In the LES context, the grid-filtered contribution can be expressed according to Equation (4.6):

$$\tilde{a}_{res} = (\delta_{i,j} - n_i \tilde{n}_j) \frac{\partial \tilde{u}_i}{\partial x_j} \tag{4.6}$$

while the SGS-grid term, that quantifies the interaction between the flame front and the modeled vortexes, is calculated as follows:

$$\tilde{a}_{sgs} = \Gamma_k \frac{\sqrt{k_{sgs}}}{\Delta} \tag{4.7}$$

where k_{sgs} is the SGS-turbulent kinetic energy and Δ is the grid size. The efficiency function Γ_k is utilized to model the SGS interaction, following the approach by Meneveau et al. [139]. The mathematical formulation for the efficiency function is summarized in Eq. (4.8), and its primary components are presented in Eq.s (4.9) and (4.10):

$$\log_{10} \Gamma_k = -\frac{1}{s+0.4} e^{-(s+0.4)} + (1 - e^{-(s+0.4)})(s\sigma - 0.11) \tag{4.8}$$

$$s = \log_{10}\left(\frac{\Delta}{\delta_l^0}\right) \tag{4.9}$$

$$\sigma = \frac{2}{3}\left(1 - \frac{1}{2}\exp\left[-\left(\frac{u'_\Delta}{S_c}\right)^{1/3}\right]\right) \tag{4.10}$$

with δ_l^0 the laminar flame front thickness. This formulation indicates that the flame front can only be affected or "wrinkled" by vortexes whose characteristic size is at least 0.4 times the laminar flame thickness. Turbulent eddies that are smaller than this critical size are not capable of penetrating or causing any alteration to the flame front.

The enthalpy deficit resulting from heat loss effects is determined by comparing the actual cell-based temperature to the adiabatic temperature that the cell would have under the same conditions of the mixture fraction Z, progress variable, and their respective variances. During each time step of the LES, the corresponding consumption speed value for a cell can be extracted from a pre-computed table. This table is accessed based on the local values of the mixture fraction, strain rate, and heat loss, which are determined using the equations described earlier. The table is constructed by conducting multiple one-dimensional premixed flame simulations using

Cantera [140]. In these simulations, each parameter combination (Z, a, ψ) is varied independently. Within Cantera, the strain rate is progressively increased, leading to higher velocities of the opposing jets (one carrying fresh mixture and the other carrying combustion products). Additionally, to simulate the enthalpy deficit, the temperature of the combustion products is lowered. By independently varying these quantities through three "for" loops, a 4-dimensional table S_c (Z, a, ψ) is created. Both Cantera and the CFD simulations utilize the GRI-3.0 [141] as the chosen chemistry set. Furthermore, they employ identical operating conditions in terms of operating pressure, oxidizer temperature, and pure methane as the fuel.

Figure 4.6 illustrates a consumption speed map with respect to the parameters $a - \psi$ (a) and $Z - a$ under adiabatic conditions (b). Figure 4.6a is particularly valuable for understanding the impact of strain in the presence of heat loss. Even when heat loss is relatively weak, an increase in the strain rate leads to a rapid decline in the consumption speed, ultimately resulting in flame extinction ($S_c \approx 0$). Conversely, as adiabatic conditions are approached, the 1D flame extinguishes for significantly higher values of a (approximately a >> 7,000 1/s).

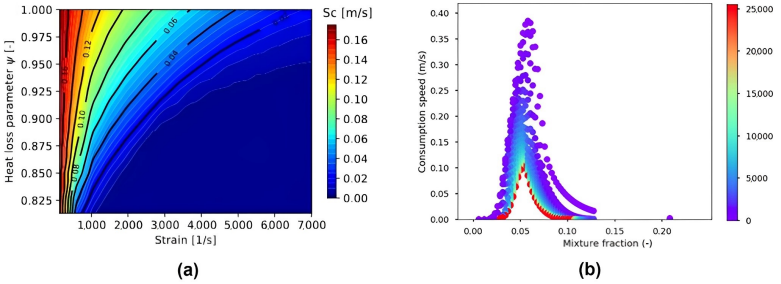

*Figure 4.6: (**a**) $S_c(a, \psi)$,(**b**) $S_c(Z, a)$. Image provided by Baker Hughes.* ***(©2024 Baker Hughes Company—All rights reserved).***

4.1.3 Turbulence model

The entire computational campaign is conducted using the commercial software Ansys Fluent v21.1, which employs a 3D Navier–Stokes solver. Regarding the numerical schemes, all equations, including the time step advancements, are treated at a second-order level. Additionally, a coupled scheme is utilized for the pressure–velocity coupling. For the fully-integrated combustor-turbine simulation, the chosen turbulent model is the SBES. This model allows the utilization of the RANS approach near the boundary layer while employing LES in the core of the flow, where the turbulent SGS modeling is handled using the dynamic-Smagorinsky algorithm. For the stand-alone S1N simulations, both SBES and standard RANS approach are employed, depending on the case of study, as will specified in the next sections. As anticipated, the Stress-Blended Eddy Simulation (SBES), a hybrid RANS/LES method [105, 122], is predominantly utilized for conducting the simulations. This model falls under the category of DES (Detached Eddy Simulation) methods, where wall stresses are computed using a RANS approach, while regions experiencing significant separations and unguided flows are addressed using a LES approach. Under this approach, the $k-\omega$ SST model [123, 142] is applied to solve near-wall regions, while the flow field is modeled using an LES approach in the freestream regions. The transition from RANS to LES characteristics is managed internally through a blending function [143], which determines the sub-grid stress tensor in the SBES approach. To model the sub-grid stresses in the LES portion, the Dynamic-Smagorinsky model [143] is employed. This numerical approach enables the efficient management of turbulence models based on the characteristics of the local flow field. It enhances the solution quality compared to a purely RANS simulation while also reducing the computational workload required for boundary layer modeling, which would be necessary in a pure LES simulation. The transition between RANS and LES behaviors is exclusively governed by a blending (or shielding) function, denoted as f_{SBES}, defined

as follows:

$$\tau_{ij}^{SBES} = f_{SBES} \cdot \tau_{ij}^{RANS} + (1 - f_{SBES}) \cdot \tau_{ij}^{SBES} \tag{4.11}$$

where τ_{ij}^{SBES} and τ_{ij}^{RANS} represent, respectively, the LES and RANS parts of the sub-grid stress tensor. As already anticipated, the sub-grid stress in the RANS portion is represented using the $k-\omega$ SST model [123, 142]. On the other hand, the sub-grid stress tensor in the LES section is determined using the Dynamic-Smagorinsky model [143] for closure. In this method, the eddy viscosity is determined based on the resolved strain rate $\bar{S}$, which is calculated as follows:

$$\mu_t = \rho L_s^2 |\bar{S}| \tag{4.12}$$

where $\bar{S}$ represents the symmetric component of the velocity tensor gradient squared, excluding the trace:

$$|\bar{S}| = 2\sqrt{\bar{S_{ij}}\bar{S_{ij}}} \tag{4.13}$$

while L_s denotes the characteristic SGS mixing length, which is defined as:

$$L_s = \min(kd, C_s, V^{1/3}) \tag{4.14}$$

In this definition, several factors are compared, as the the Kolmogorov constant k, including the distance of each cell from the nearest wall (d), the cell volume (V), and the Smagorinsky constant (C_s), which is dependent on the resolved turbulent scales.
Moreover, regarding the temporal discretization, the selection of the time step size is determined based on the flow velocity at the throat of the S1N, where the Mach number reaches a significantly high value above 0.8. For this reason, the time step size has been set to $1.5 \cdot 10^{-6} s$. Furthermore, the time step is constrained not to exceed a value of 3 for the Courant number in this specific section.

4.1.4 Operating conditions

All the simulations are performed according to realistic engine-like operating conditions, corresponding to a condition of full speed and load for the engine during the FEET campaign. The most interesting information regarding the operating conditions are summarized in Table 4.1. While keeping the fire temperature at design value, the pilot/premix fuel ratio is chosen in order to limit the NO15 emission below 15ppmv. Moreover, as can be observed, the C2+ and the inert content are kept limited for the fuel composition.

Table 4.1: Summary of the main parameters about the operating conditions taken as reference for all calculations here presented. ***(©2024 Baker Hughes Company - All rights reserved)****.*

Test point conditions		
Fuel Composition [% vol.]	**CH4**	87
	C2+	7.5
	Inert	5.5
Pilot/Premix fuel ratio [-]	0.36	
Ambient Temperature [°C]	6	
Firing Temperature	Design Value	
TNH, TNL [%]	100	

4.2 Boundary conditions for stand-alone S1N simulations

The computational domain for the stand-alone S1N cases was derived by extracting it from the one that includes both components. For more information, see 4.1.1.2. As anticipated, firstly, three different simulations are carried out, imposing boundary conditions with a different level of accuracy and reliability. In order to obtain the most representative and realistic boundary conditions as possible at the S1N inlet, two-dimensional

time-varying boundary conditions are applied to maintain the high residual swirled flow, characterized by elevated turbulence and temperature distortions, at the outlet of the combustion chamber. These conditions are obtained by extracting instantaneous data from the interface plane between the two components in a precursor SBES of the isolated combustor (SBES CC), provided by Baker Hughes, carried out at the same test point. During this simulation, the S1N was excluded and the nozzle was replaced with a discharge axisymmetric convergent that preserved the Mach number of the NGV while ensuring the same throat area. For instance, Figure 4.7 shows a representation of the instantaneous total temperature at the S1N inlet at time t_1 and at time $t_2 = t_1 + 100t_s$, where t_s is the time step employed for the SBES simulations (see 4.1.1.1).

To achieve an adequate temporal discretization while maintaining a

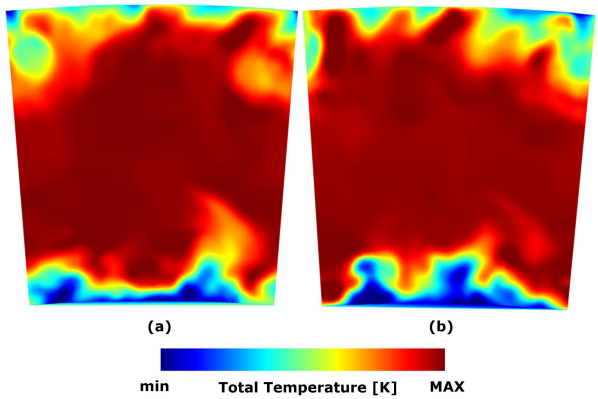

Figure 4.7: Visualization of two different instantaneous of total temperature recorded at the interface plane between combustor and turbine at ***(a)*** *the instant* t_1 *and* ***(b)*** *the instant* $t_2 = t_1 + 100t_s$*.*

manageable database size, the data were saved at intervals of 0.015 ms over a time span of 45 ms. This period covers approximately 3 FTT (Flow Through Time) of the isolated-combustor and 45 FTT of the isolated-NGV

domain. However, to reduce the computational cost of the isolated S1N simulation, only a portion of the database corresponding to 7.5 ms (7.5 FTT of the isolated-S1N) was used, as the stand-alone stator exhibits a reduced FTT.

Data related to mass flow (ρu_x, ρu_y, ρu_z), velocity (u_x, u_y, u_z), total temperature, turbulence parameters, progress variable, mixture fraction, and a passive scalar to track film cooling concentration from the nuggets were collected at each node of the mesh forming the interface plane. Consequently, the mass flow, expressed as mass flux, as well as flow directions and total temperature, were imposed at the inlet of the S1N, along with the remaining quantities that were extracted. Consistent with the integrated combustor-S1N case, mass flow rates and total temperature were imposed at the cooling holes on the vane surface. Regarding the outlet boundary conditions, all the simulations utilized the same radial static pressure profile, ensuring consistency in this aspect.

Furthermore, to evaluate discrepancies among various CFD approaches, the outcomes of the corresponding preliminary RANS S1N simulations are also included in this analysis, where turbulence effects are modeled using the $k-\omega$ SST turbulence model. For this RANS simulations, 1D profiles and 2D maps are utilized as inlet boundary conditions, obtained from the available SBES of the stand-alone combustor, representing the time-averaged solution of the unsteady boundary conditions prescribed at the S1N SBES inlet. It is worth noting that the use of 2D maps as boundary conditions for a RANS simulation represents a progressive step compared to the standard industrial practice typically employed, especially during the design phase, where simple radial profiles are usually imposed. In summary, the key parameters pertaining to the setup of all CFD simulations here are presented in Table 4.2:

Table 4.2: Summary of the key parameters for setting up the CFD simulations here presented ***(©2024 Baker Hughes Company - All rights reserved).***

CFD Simulation	CFD Domain	Inlet BCs
SBES CC+S1N	CC+S1N	mass flow inlets
SBES S1N (BCs from CC)	S1N	set of instantaneous 2D maps from SBES CC
RANS S1N 2D maps (BCs from CC)	S1N	time-averaged 2D maps from SBES CC
RANS S1N 1D profiles (BCs from CC)	S1N	time-averaged 2D maps from SBES CC

4.3 Analysis of the plane 39.5 conditions

In order to highlight the discrepancies between carrying out coupled and decoupled simulations, an analysis of the plane 39.5 conditions is firstly reported, focusing on the quantities that show the most relevant features. As anticipated, the plane 39.5, visible at Figure 4.2, corresponds to the interface between the two components.

Consequently, Figure 4.8 illustrates the two-dimensional maps and tangential averaged profiles of the axial velocity at the S1N inlet. The data on the left are derived from the integrated combustor-stator SBES simulation, whereas the data on the right are obtained from a precursor SBES simulation of the stand-alone combustor, fully provided by Baker Hughes. It is crucial to note that the latter data serve as the prescribed maps for the RANS S1N simulations, representing the time-averaged solution of the time-varying maps applied to the SBES stand-alone stator simulation, as anticipated. By looking at the axial velocity plot extracted from the integrated SBES simulation, it is noticeable that the presence of the LE of the NGV clearly affects the velocity distribution by creating a non-negligible blockage effect. As a matter of fact, the deceleration observed in the central part of the reported cross section is countered by a noticeable acceleration around the LE. This pattern leads to a more

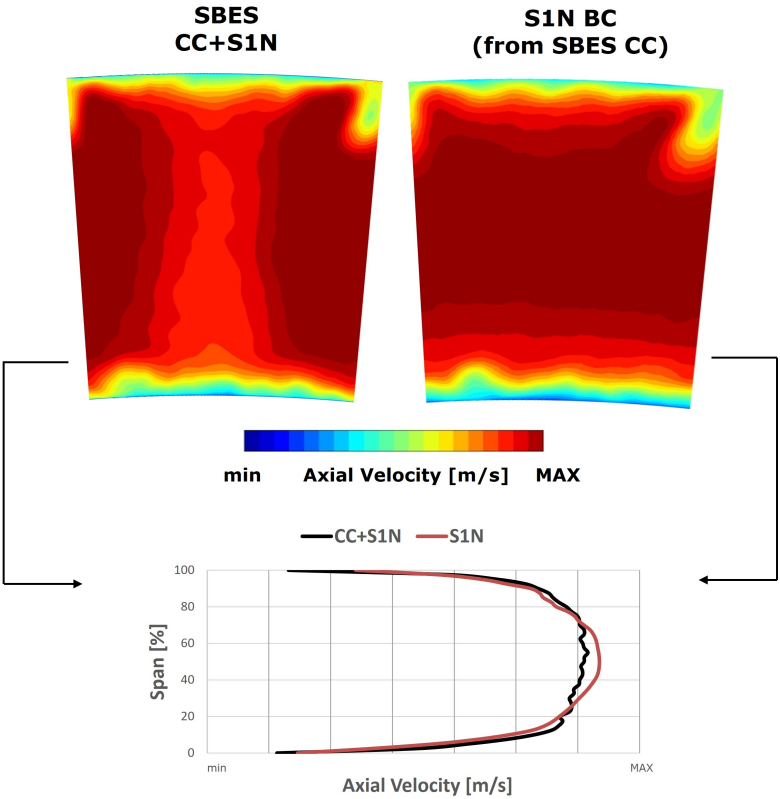

Figure 4.8: Time-averaged axial velocity from the coupled SBES case (SBES CC+S1N) ***(right)*** *and the corresponding time-averaged solution from the SBES CC* ***(left)*** *at plane 39.5, imposed as inlet boundary conditions for the S1N RANS calculations. Therefore, the latter refer also to the time-average solution of the unsteady boundary conditions prescribed at the SBES S1N (BCs from CC) inlet* ***(©2024 Baker Hughes Company—All rights reserved)****.*

pronounced circumferentially-averaged profile in the coupled simulation for the central portion of the cross section, roughly spanning from 20% to 70% of the span.

The availability of an integrated SBES calculation allows also to extend the analysis to other interesting quantities at the interface plane, such as the swirl and the pitch angles. Consequently, given the observed differences in terms of axial velocity, to gain deeper insights into the variations observed at plane 39.5 when using decoupled or coupled simulations, a comparative analysis of swirl and pitch angles is presented in Figure 5.4. These angles are defined as follows:

$$swirl = \arctan\left(\frac{V_{tan}}{V_{ax}}\right) \tag{4.15}$$

$$pitch = \arctan\left(\frac{V_{rad}}{V_{ax}}\right) \tag{4.16}$$

The comparison presented reveals noticeable disparities in swirl distribution between the two cases, primarily due to the NGV's presence. The time-averaged swirl obtained from the SBES of the stand-alone combustor exhibits higher absolute values and maintains a more uniform distribution around the circumference compared to the coupled SBES simulation. As a result, this behavior leads to a steeper 1D profile, particularly in the span range of 20% to 80%.

On the other hand, the pitch distribution does not exhibit significant differences between the two cases. However, it is worth noting that the data extracted from the time-averaged solution of the SBE CC slightly indicates lower values, especially from the hub to approximately 50% of the span, as demonstrated in the corresponding 1D radial profile.

In order to deepen further the analysis at plane 39.5 and gain a better understanding of the differences, especially concerning the swirl angle, Figure 4.10 and Figure 4.11 illustrate the evolution of the pitch and swirl angles before reaching plane 39.5 for both the integrated SBES calculation and the precursor SBES of the stand-alone combustor. These angles are depicted on a midplane section at four different cross sections perpendicular to the axis of the machine upstream of the plane 39.5 (see Figure 4.2). Additionally, the azimuthal profiles obtained by averaging

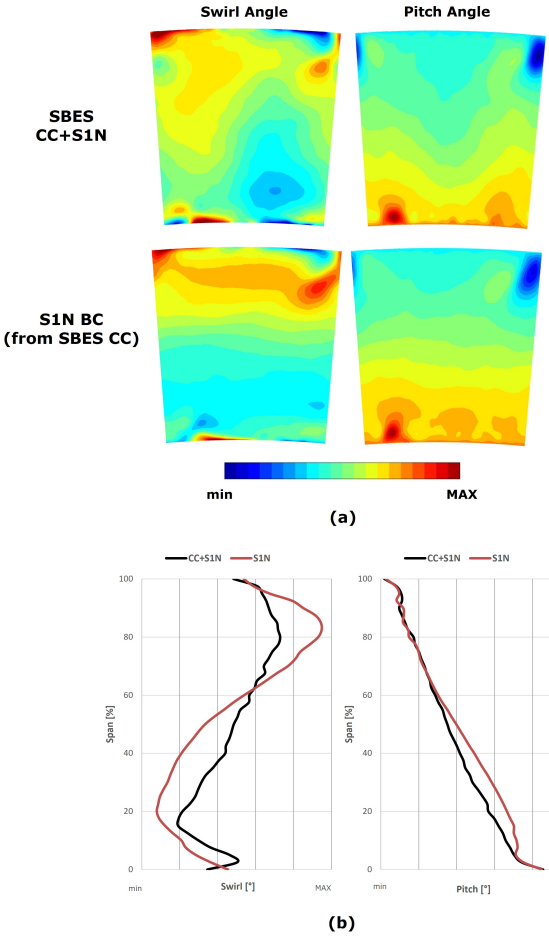

Figure 4.9: Time-averaged swirl and pitch angles from the coupled SBES case (SBES CC+S1N) ***(top)*** *and the corresponding time-averaged solution from the provided SBES CC* ***(bottom)*** *at plane 39.5, imposed as inlet boundary conditions for the S1N RANS calculations. Therefore, the latter refer also to the time-average solution of the unsteady boundary conditions prescribed at the SBES S1N (BCs from CC) inlet.* .

the 2D contours are provided.

Specifically, P1 is situated just before the leaf seals. Figure 4.10 shows that the distribution of the pitch angle along the axial direction remains consistent and highly similar between the two cases. As one moves upstream from plane 39.5, the minor discrepancies previously observed on the interface plane between the two components seem to gradually diminish. This behavior is also evident in the corresponding radial 1D profiles, indicating that the blockage effect associated with the presence of the stator is progressively weakening, as expected.

However, upon examining Figure 4.11 and analyzing the swirl angle distribution from the SBES simulation, it becomes evident that the nozzle's presence continues to have an impact even as one moves considerably upstream of the nozzle's LE. In fact, the 2D contours display significant differences along the tangential direction when moving from P1 to P4. Moreover, upon inspecting the one-dimensional profiles on all the investigated planes, noticeable disparities in both the minimum and maximum swirl values are apparent between the two cases. This confirms that, despite the combustor's considerable axial extension, ensuring a prolonged residence time within the combustion chamber, the nozzle's presence continues to influence the velocity field of the combustor, even when the analysis is moved sufficiently upstream from the selected interface plane between the CC) and the NGV.

In conclusion, it is essential to thoroughly analyze these differences as they can potentially affect the aero-thermal characteristics of the flow at the interface between the CC and the NGV. The key finding of this analysis is that the axial position chosen for the nozzle inlet, aimed at decoupling the two components for separate analysis, could significantly influence the solution due to the considerable blockage effect of the NGV on the velocity field. Thus, careful consideration of the nozzle's axial position is crucial for accurate simulations and a comprehensive understanding of the flow behavior in the CC and NGV regions.

Moreover, thanks to the availabily of a coupled SBES, it becomes possible to expand the investigation of the plane 39.5 to encompass important

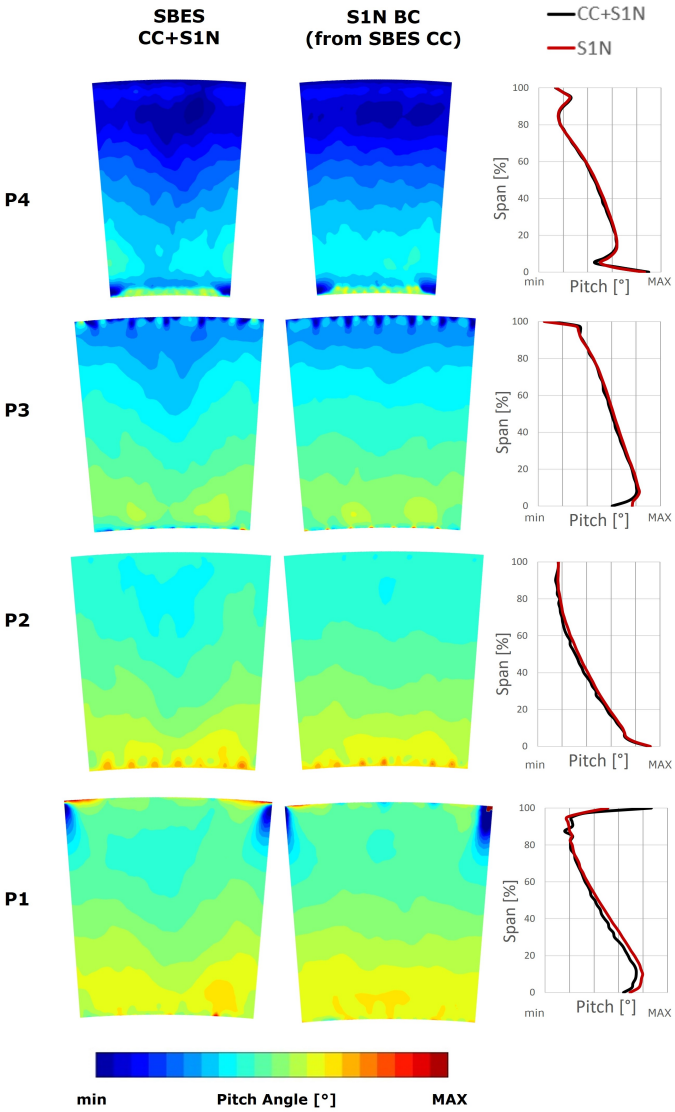

Figure 4.10: Analysis of the pitch angle on four planes (P1, P2, P3, P4) orthogonal to the machine axis derived from the coupled SBES (Top) and the SBES CC (Bottom) case. ***(©2024 Baker Hughes Company—All rights reserved).***

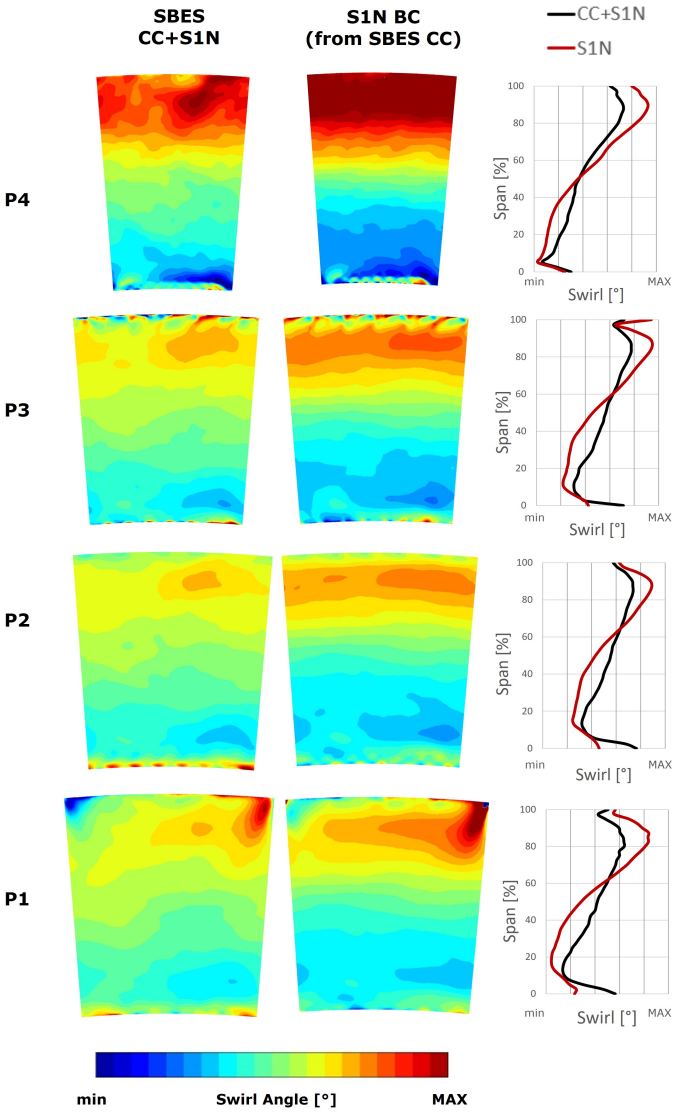

Figure 4.11: Analysis of the swirl angle on four planes (P1, P2, P3, P4) orthogonal to the machine axis derived from the coupled SBES (Top) and the SBES CC (Bottom) case. ***(©2024 Baker Hughes Company—All rights reserved).***

parameters related to turbulent flow characteristics. Specifically, the turbulent length scale, calculated using Eq. 4.17, is now taken into consideration as a key factor in the analysis since it represents a significant quantity that governs turbulence decay:

$$l_t \propto \frac{k^{3/2}}{\varepsilon} \tag{4.17}$$

In the RANS formulation, the turbulent kinetic energy k, turbulent dissipation rate ε, and turbulence frequency ω are directly available. However, in the SBES approach, these parameters must be derived from the solution. The resolved turbulent kinetic energy is computed using the time-averaged values of the instantaneous velocity components. On the other hand, the sub-grid scale contribution is determined using Eq. 4.18, which is derived from the subgrid scale model:

$$k_{sgs} = \frac{(0.18\Delta^{1/3} \cdot S)^2}{0.3} \tag{4.18}$$

where Δ represents the local cell volume while S is the local strain rate magnitude. The turbulent dissipation rate, which solely operates at the sub-grid scale within the LES-resolved portion of the solution, is computed as follows:

$$\varepsilon_{sgs} = \frac{\mu_{eff}}{\rho}(\frac{\partial u_i}{\partial x_j})^2 \tag{4.19}$$

Figure 4.12 presents the turbulent length scale data for both SBES CC+S1N and RANS S1N 2D maps (BCs from CC) simulations on five planes (P39.5, P5, P6, P7, P8) perpendicular to the machine axis, along with the 1D profiles obtained by averaging the 2D plots azimuthally. As RANS simulation, RANS simulation S1N 2D maps (BCs from CC) was selected, considered as representative of what happens in a RANS simulation. At plane P39.5, the radial profile of the turbulent length scale obtained from SBES CC+S1N closely resembles the one extracted from the RANS simulation. Notably, it is interesting to observe that in the SBES results of the stand-alone combustor, which served as the basis

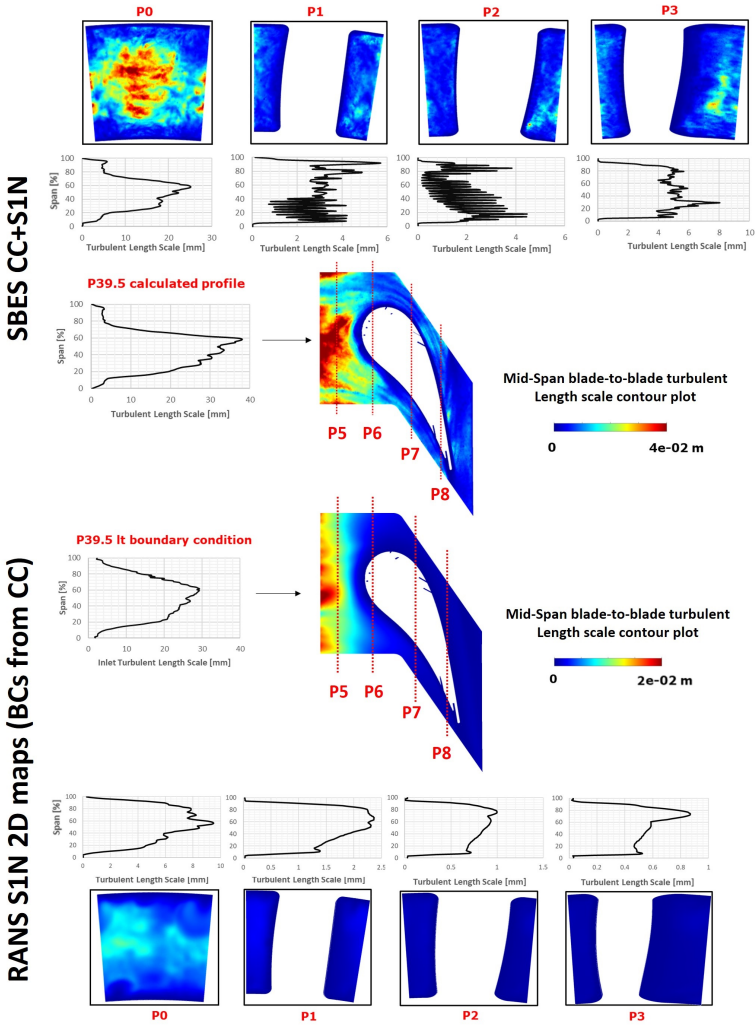

Figure 4.12: Analysis of the turbulent length scale on five planes (P39.5, P5, P6, P7, P8) orthogonal to the machine axis derived from the SBES CC+S1N (Top) and the RANS S1N 2D maps (BCs from CC) (Bottom) case. In the latter case, a sharp decreasing of l_t is present right downstream the p39.5 location ***(©2024 Baker Hughes Company—All rights reserved)***.

for deriving the inlet boundary conditions for the RANS simulation, the maximum turbulent length scale value reaches around 30 mm at 60% of the span. In contrast, in the SBES CC+S1N case, the peak occurs at the same span position but with a higher amplitude. This discrepancy indicates that the set of boundary conditions employed for the S1N stand-alone calculations is accurate, further supported by the alignment between the two simulations at plane P39.5.

More importantly Figure 4.12 illustrates the variation of the turbulent length scale within the NGV for the two suggested approaches. This parameter is presented on a blade-to-blade surface situated at 50% of the radial span and at four distinct cross sections downstream of the p39.5 plane. Specifically, plane P5 is positioned between the p39.5 and the LE of the blade, while P7 is located at the throat section.

The primary outcome of the analysis is that, despite the similarity of turbulent length scale l_t at plane p39.5, which imposes the inlet boundary condition, the RANS simulation exhibits a much more rapid decay, evident even at P0. At this location, the peak of the turbulent length scale reduces to approximately 10 mm, three times smaller than the characteristic size at the inlet. As the flow progresses downstream through the vane, l_t undergoes a gradual reduction due to flow expansion and the consequent turbulence strain.

In contrast, the profiles predicted by the SBES CC+S1N case display a notable decay of the turbulent length scale only within the first stage nozzle, influenced by the favorable pressure gradient. Prior to reaching the LE, l_t experiences a mild reduction where the pressure gradient begins to take effect. Inside the vane, the minimum value of l_t (approximately 3 mm) is reached at the P7 location, coinciding with the maximum flow velocity. To comprehend the reasons for these differences, the circumferentially averaged radial profiles of the turbulent dissipation rate at P5 are examined, as reported in Figure 4.13. Examining the behavior away from the walls, it is evident that the turbulent dissipation rate calculated by the RANS simulation significantly overestimates the value obtained from Eq. 4.19. Two-equation models are known to exhibit a

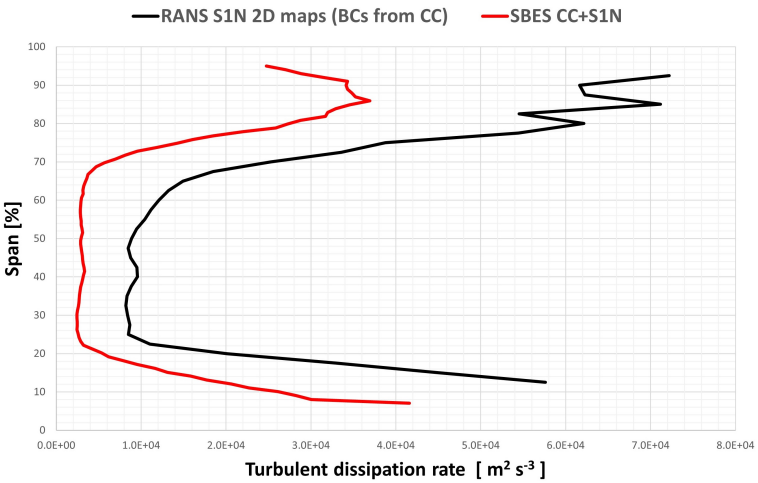

Figure 4.13: Turbulent dissipation rate along the span at P5 location: the RANS is affected by a higher dissipation, producing a fast decay of the turbulence and leading to a lower characteristic length scale ***(©2024 Baker Hughes Company—All rights reserved)****.*

tendency for excessive turbulence decay, particularly when the integral length scale is imposed based on LES/SBES data. As a matter of fact, in the LES-resolved regions, wide range of scales are resolved and any energy dissipation to the large values of l_t are associated, but only to the smaller scales that are modelled separately. On the other hand, RANS struggles to differentiate the various contributions across an extensive range of turbulent length scales and, as a consequence, overestimates turbulence decay. Furthermore, Figure 4.12 illustrates that l_t values at P39.5 are comparable to the NGV pitch at midspan, making a simple RANS model inadequate for accurately modeling the impact of macro-scale turbulence on the mean flow field. In contrast, the SBES model, relying on a pure LES solution in the core of the flow, proves to be more precise than steady-state RANS solutions. Therefore, when employing RANS, one can anticipate a significant underestimation of the interaction between the

turbulent structures of the main flow and the film cooling of the vane. A detailed analysis of this phenomenon will be conducted in the following sections.

4.4 Airfoil loads along the vane

To enhance the comparison between coupled and decoupled simulations, vane loads expressed as isentropic Mach numbers are presented in Figure 4.14. The data is reported at 25%, 50%, and 75% of the span for both the coupled SBES calculation and the companion RANS and SBES simulations of the isolated-S1N cases. The isentropic Mach distributions obtained from the RANS and SBES calculations for the isolated stator closely match the one predicted by the integrated SBES simulation, demonstrating a highly satisfactory agreement. This observation also indicates that the inlet boundary conditions at the NGV inlet were correctly applied for the isolated-S1N cases, leading to accurate predictions of the aero-thermal field development in correspondence of the stator.

4.5 Normalized temperature distributions along the vane

Contrary to what happens with the airfoil loads, significant disparities between the numerical calculations are evident when examining the prediction of the static temperature distribution along the stator. Figure 4.15 and Figure 4.16 illustrate the normalized static temperature distribution over the vane surface, including the endwalls, for all numerical calculations here reported. Not all the cooling system is visible due to Baker Hughes disclosure policy reasons. As can be seen, the distributions are quite different between the four cases. In particular, by looking at the LE, it can be noted that the static temperature distribution predicted by both RANS simulations is strongly non-uniform. As a matter of fact, a significant portion of the vane remains exposed, without coverage. Furthermore, the stagnation line appears notably straight in this scenario. However,

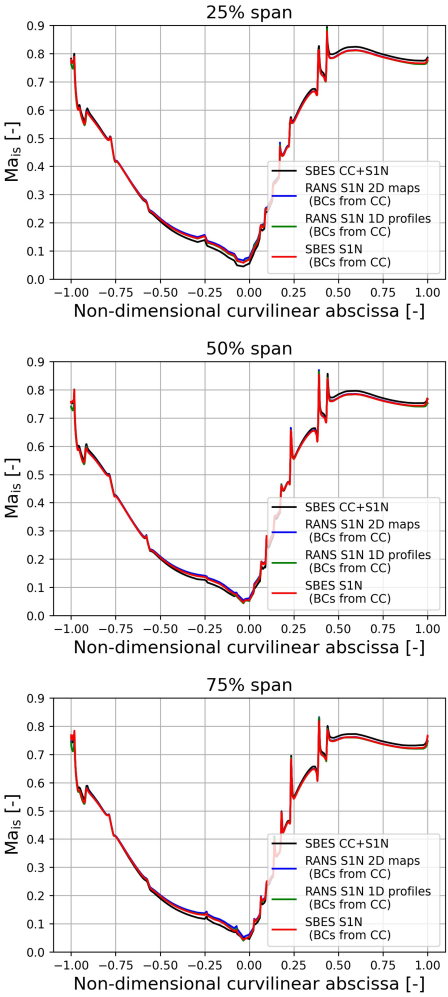

Figure 4.14: Vane loads in terms of isentropic Mach Number on the NGV surface at the 25%, 50% and 75% of the span. The isentropic Mach number is reported as a function of the non-dimensional curvilinear abscissa, where $x = 0$ corresponds to the leading edge of the NGV, $x = -1$ is the trailing edge pressure side and $x = 1$ is the trailing edge suction side ***(©2024 Baker Hughes Company—All rights reserved)***.

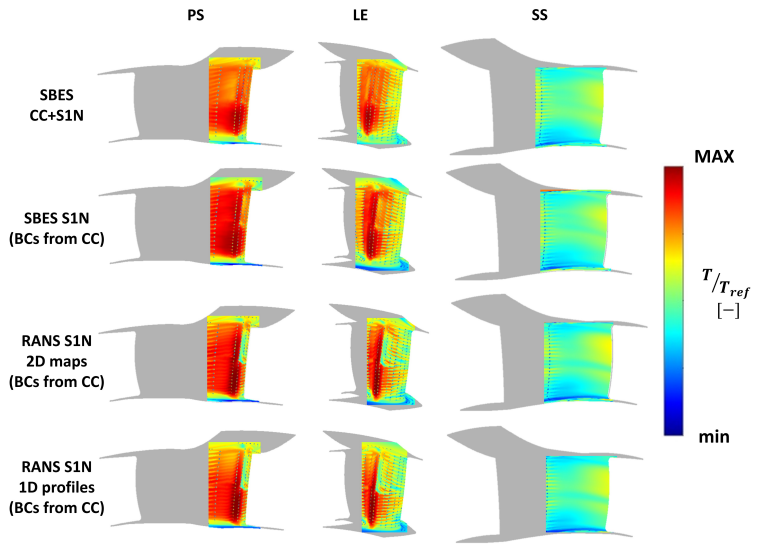

Figure 4.15: Time-averaged normalized temperature distribution on the NGV surfaces for all the simulations here reported ***(©2024 Baker Hughes Company—All rights reserved)****.*

when examining the SBES NGV-isolated case, the results exhibit a closer agreement with those from the integrated case compared to the RANS cases. Despite this improvement, the accurate representation of the stagnation line behavior remains a challenge in this simulation as well. This discrepancy can be attributed to the variations in the time-averaged swirl angle distribution at the NGV inlet for the isolated-stator simulations. The distorted position of the stagnation line is effectively captured only by the coupled SBES simulation, which provides better coverage of the vane's LE, particularly at the extreme span values.

Moreover, concerning the SS surface as well as the inner and outer platforms, the normalized static temperature distribution for the four simulations displays a considerable resemblance. Nonetheless, it is noticeable that the RANS scenario tends to predict a less even distribution, particu-

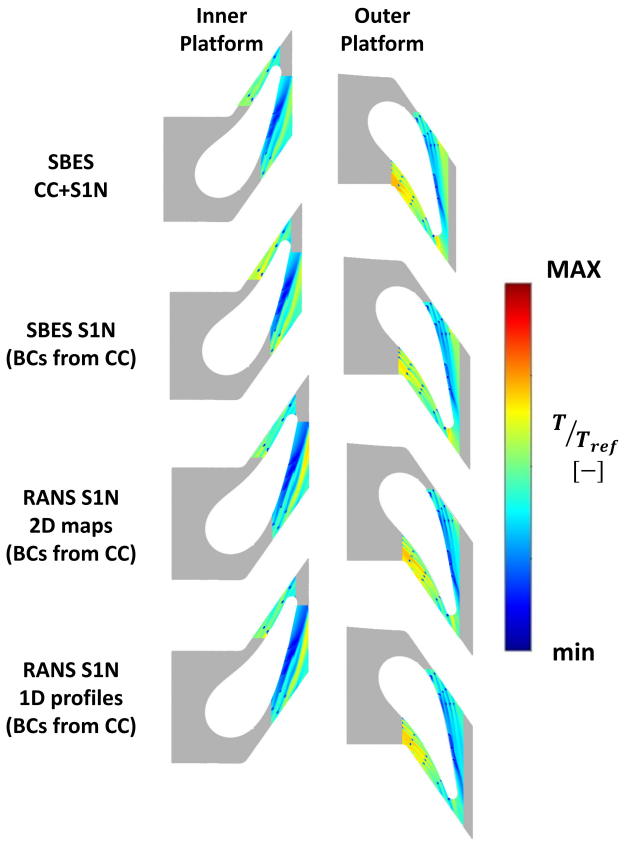

Figure 4.16: Time-averaged normalized temperature distribution on NGV inner and outer platforms for all the simulations here reported ***(©2024 Baker Hughes Company—All rights reserved)****.*

larly when compared to the companion SBES simulation. As previously mentioned, this tendency can be linked to a significant underestimation of turbulent mixing inherent to the RANS approach. This leads to a limited interaction between the high-temperature swirling primary flow emerging from the combustion chamber and the cooling flows within the vane.

Relatively to this same aspect, the different swirled impacting flow outcoming from the combustor also influences the jet-spreading distribution on the PS of the NGV, as can be deducted from the static temperature distribution. In fact, both the RANS S1N 2D maps and SBES S1N simulations of the isolated-NGV case reveal a uniformly spread radial pattern throughout the length of the vane. Conversely, the coupled SBES simulation forecasts a distinct non-uniform distribution, emphasizing more effective coverage in the upper half of the PS. Consequently, the coolant tends to be drawn toward the midsection of the airfoil's span, while the hub and tip areas receive comparatively less coverage. The same reasoning can also be applied by looking at the contours related to the RANS S1N 1D profiles simulation. The only exception is on the upper half of the PS, where a greater decrease in temperature is expected, due to a greater presence of film cooling, compared to the companion RANS S1N 2D maps and SBES S1N simulations. This could be explained, by a slight local variation of swirl conditions for the simulation RANS S1N 1D profiles, where tangentially averaged 1D profiles on plane 39.5 are prescribed as inlet boundary conditions.

As far as the endwalls are concerned, the static temperature distributions are very similar between the four simulations (see Figure 4.16). However, slight differences can be highlighted on the inner platform, where both RANS simulations predict a greater temperature peak on the SS, compared to the two SBES. This behavior can be attributed, as previously discussed, to the different prediction of turbulent mixing in the case of the RANS approach. Similar observations, albeit on a smaller scale, can be made by observing the outer endwall, especially on the SS, where the RANS simulations predict a greater persistence of the film cooling.

The same phenomena observed for the 2D maps can be also noted by the 1D radial profiles. In order to go into more details about the temperature distribution, the 1D profiles of the normalized wall temperature over the vane are presented in Figure 4.17 as a function of the non-dimensional curvilinear abscissa. Specifically, noticeable discrepancies are evident at the 50% and 75% of the span. The predictions of the isolated-stator simu-

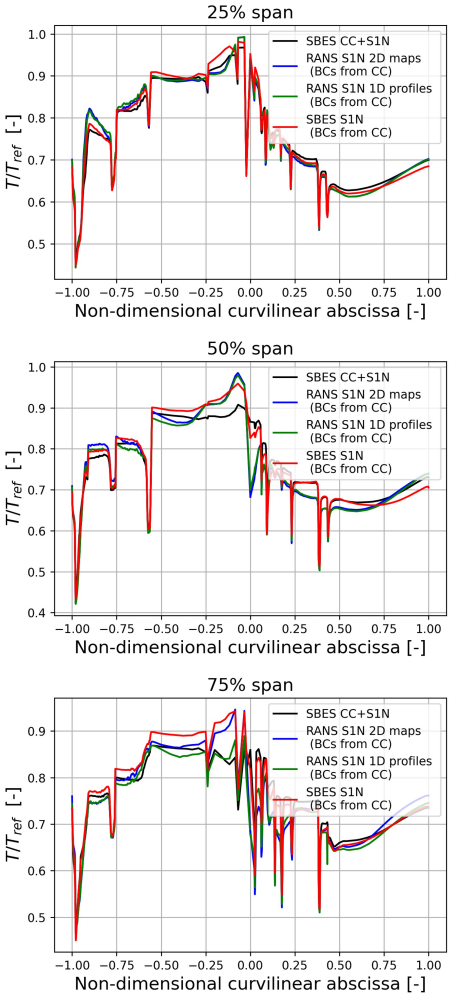

Figure 4.17: Normalized temperature on the NGV surface at 25%, 50% and 75% of the span for all the simulations. It is reported as a function of the non-dimensional curvilinear abscissa, where $x = 0$ corresponds to the leading edge of the NGV, $x = -1$ is the trailing edge pressure side and $x = 1$ is the trailing edge suction side ***(©2024 Baker Hughes Company—All rights reserved)***.

lations notably deviate from those of the coupled SBES case, particularly on the PS where the adiabatic effectiveness is underestimated, with the only exception at 75% for the RANS S1N 1D profiles case as anticipated. However, generally speaking, both RANS simulations, as anticipated, tends to yield higher adiabatic effectiveness values, or equivalently lower static temperature values, compared to its counterpart SBES simulation of the isolated-S1N configuration due to its inadequate modeling of turbulence mixing. However, even when introducing unsteadiness by imposing time-varying boundary conditions at the inlet of the SBES S1N, effectively utilizing the most accurate boundary conditions achievable from an SBES simulation of the isolated combustion chamber, this adjustment is insufficient to achieve a perfect match with the static temperature results obtained from a coupled SBES simulation. This underscores the fact that the presence of the combustor chamber does indeed exert a notable influence on the solution under realistic operational conditions and within a realistic annular geometry.

4.6 Analysis of the plane outlet conditions

To illustrate the disparities arising from conducting both coupled and decoupled simulations, an examination of conditions at the outlet plane is presented, focusing particularly on quantities exhibiting significant features. This is crucial as the outlet conditions from S1N could potentially impact the performance, durability, and design of the subsequent rotor. In Figure 4.18 and Figure 4.19, two-dimensional maps and tangentially averaged profiles of swirl and pitch angles, as defined by Eq. 4.15 and 4.16, respectively, are depicted at the S1N outlet for all four simulations. The upper portion displays data extracted from the integrated combustor-stator SBES simulation, while the middle and lower sections show data obtained from the RANS and SBES simulations of the standalone S1N, respectively. It is evident that swirl and pitch distributions show considerable similarity across the four simulations. This observation implies the accurate application of boundary conditions at the NGV inlet for all

isolated-S1N cases, leading to an accurate prediction of the aero-thermal field that develops around the stator. However, despite the consistent trends, certain discrepancies are still noticeable, particularly when examining the pitch angle extracted from the isolated-stator simulations. These calculations do not perfectly align with the data from the coupled SBES case, particularly in the wake region. This discrepancy is most pronounced in the corresponding 1D radial profile, particularly from the 50% to 80% of the span. Nonetheless, conducting an SBES simulation specifically to study NGV behavior enables a better alignment with the pitch distribution trend. A similar rationale can also be extended to the swirl angle, particularly in the vicinity of the hub region, where the most significant deviation from the coupled-SBES solution can be observed, primarily up to approximately 20% of the span. Furthermore, Figure 4.20 presents contours of normalized total temperature extracted at the outlet plane for all the simulations. Total temperature values are normalized according to following equation:

$$T_{t,nd} = \frac{T_t - T_{min}}{T_{max} - T_{min}} \tag{4.20}$$

As anticipated, the contours exhibit a remarkably similar pattern, although there are minor disparities confined to the regions adjacent to the endwalls. In the isolated-S1N RANS simulations, these areas display lower total temperature values, which corresponds to the more extensive regions influenced by the cooling flow. This observation once again confirms the pronounced underestimation of turbulent mixing inherent in the RANS modeling, thereby affecting the interaction between the primary hot flow and the cooling flows. In summary, upon analyzing the outlet plane, overall, only slight variations between the isolated-S1N simulations and the fully integrated counterpart are discernible. However, it is important to point out that including the effect of the unsteadiness by imposing time-varying boundary conditions at the inlet of the S1N seems to provide more reliable and accurate results in terms of 2D quantities distribution, taking as reference the coupled-SBES simulation here presented.

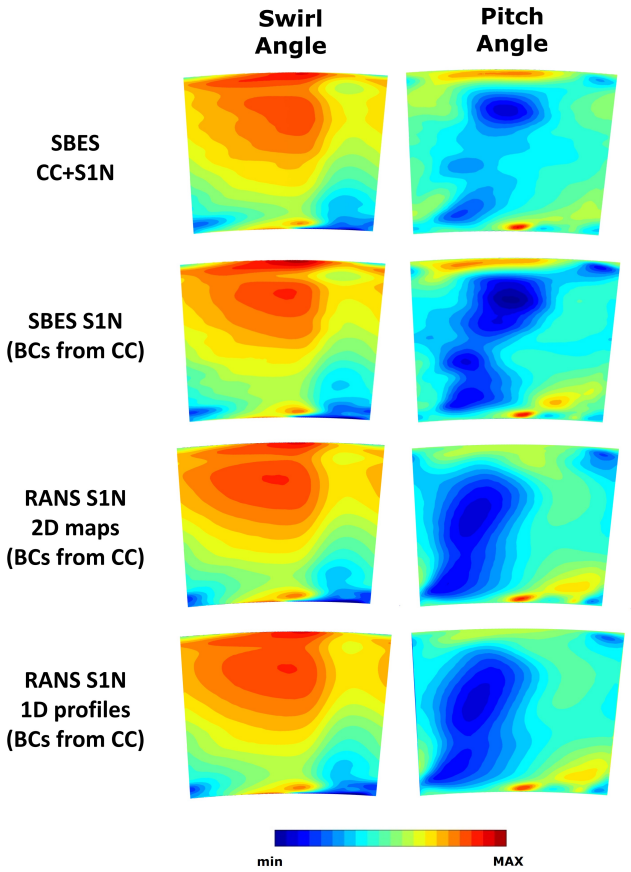

Figure 4.18: Time-averaged swirl and pitch angles in terms of 2D maps extracted from the outlet plane of the S1N stator for all the simulations here reported ***(©2024 Baker Hughes Company—All rights reserved)***.

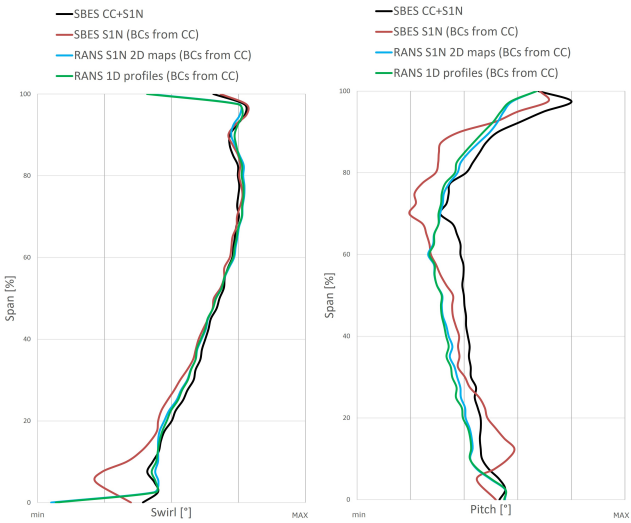

Figure 4.19: Time-averaged swirl and pitch angles in terms of 1D tangentially averaged profiles extracted from the outlet plane of the S1N stator for all the simulations here reported ***(©2024 Baker Hughes Company—All rights reserved)****.*

4.7 Concluding remarks

In conclusion, in this chapter, a numerical study was carried out to examine the interaction between a combustion chamber and a first stage stator under realistic operational conditions and annular geometry. Additionally, the investigation includes a realistic turbine nozzle cooling system to analyze how coolant flows respond to the interaction with the primary hot flow originating from the combustion chamber. To investigate these phenomena, firstly a fully integrated configuration was analyzed encompassing both the combustor and the NGV, utilizing SBES approach. Subsequently, the results from this computation were compared with outcomes from simulations focusing solely on the isolated NGV. In the latter case, the stator was initially simulated using a RANS approach, following established industrial practice. Eventually, a SBES calculation

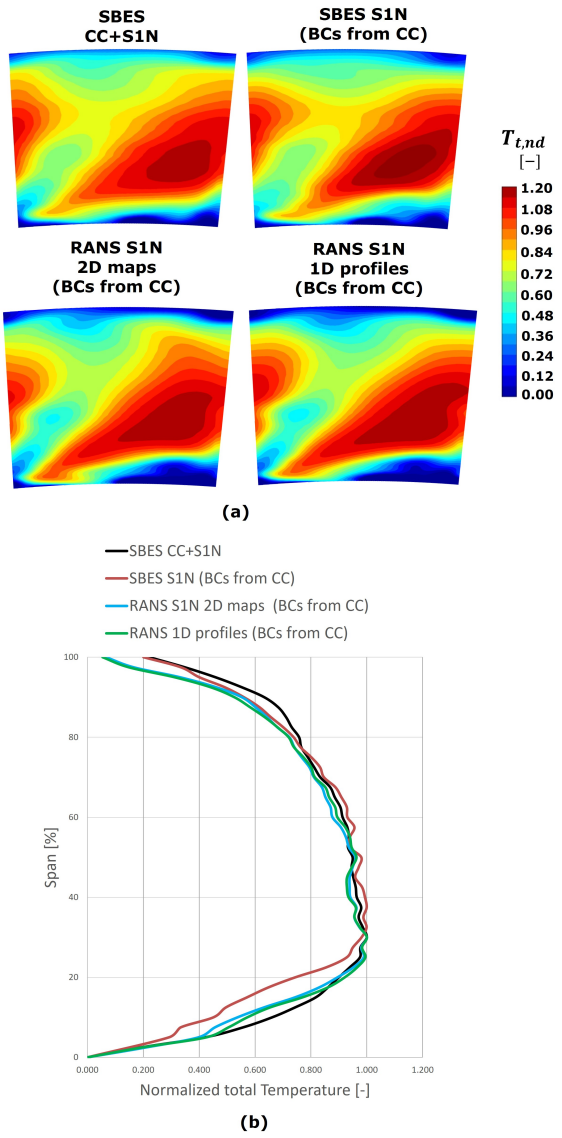

Figure 4.20: Time-averaged normalized total temperature in terms of (a) 2D maps and (b) 1D circumferentially-averaged profiles extracted from the outlet plane of the S1N stator for all the simulations here reported

was performed. For this specific SBES calculation, in order to establish representative and realistic conditions at the inlet of S1N, two-dimensional time-varying boundary conditions were imposed. These conditions were derived by extracting instantaneous data sets from the corresponding interface plane between the two components, obtained from a available SBES of the isolated combustor at the same testing point. Conversely, for the RANS simulations, 2D maps and 1D circumferentially-averaged profiles derived from the available SBES of the combustor were employed as inlet boundary conditions. These maps correspond to the time-averaged solution of the unsteady boundary conditions set at the S1N SBES inlet. Firstly, an assessment of the disparities between coupled and decoupled simulations was carried out by examining conditions at plane 39.5. This plane indicates the interface between the two components under exam. Notable distinctions were identified, particularly in terms of the axial velocity distribution extracted from the coupled SBES calculation and the preliminary SBES conducted on the stand-alone combustor. Due to the stator's LE, the presence of this obstruction introduced modifications in the velocity distribution within the coupled SBES scenario compared to the decoupled one. This phenomenon also manifested in the distribution of swirl and pitch angles on the same plane. While the differences in terms of pitch were not substantial, more significant deviations related to the swirl angle were evident in both trend and absolute values.

To further deepen and enhance the analysis at plane 39.5, especially with regard to the swirl angle variations, the evolution of pitch and swirl angles was examined at four distinct cross-sections orthogonal to the machine's axis upstream of the p39.5 plane. This investigation validated that, despite the extensive axial extent of the combustor, which resulted in a prolonged residence time within the combustion chamber, the presence of the nozzle also imparted an effect on the velocity field of the combustor. This influence persisted even when the analysis was conducted significantly upstream from the chosen interface plane between the CC and the NGV. Additionally, although the initial resemblance in terms of turbulent length scale existed between a decoupled RANS simulation (RANS 2D maps)

and the coupled SBES one at plane 39.5, it was observed that the l_t parameter in the RANS case demonstrates a considerably more rapid decay. This phenomenon was evident when analyzing four distinct cross-sections downstream of the p39.5 plane. This distinctive behavior could be attributed to the higher turbulent dissipation rate inherent in the RANS calculation, which became apparent even prior to reaching the leading edge (plane P5). Consequently, this led to an accelerated diminishment of turbulence, which influenced also the interaction between the primary flow and film cooling.

The different imposed boundary conditions at the nozzle inlet between the integrated SBES calculation and the stand-alone stator ones had also a not negligible impact on the normalized static temperature prediction on the vane surface. In general, it was observed that the RANS simulations tended to exhibit higher adiabatic effectiveness values compared to the companion SBES simulation of the isolated-S1N configuration, as expected due to the RANS model's underestimation of turbulence mixing. Nevertheless, even when introducing the effects of unsteadiness by imposing time-varying boundary conditions at the SBES S1N inlet, thus employing the most optimal boundary condition set achievable from an SBES simulation of the isolated combustion chamber, this adjustment did not completely align the static temperature outcomes with those from the coupled SBES simulation. This phenomenon became particularly apparent when observing the PS distribution and the behavior of the stagnation line on the LE. The distinctive position of the stagnation line was accurately captured only by the coupled SBES simulation, leaving only a limited portion of the LE uncovered, especially at the lowest and highest values of span.

Furthermore, in order to highlight the disparities arising from conducting coupled and decoupled simulations, an examination of outlet plane conditions was presented, focusing on the distribution of normalized total temperature, as well as swirl and pitch angles. This analysis was crucial due to the potential impact of the S1N outlet conditions on the subsequent rotor's performance, longevity, and design. Upon analyzing the outlet

plane conditions, overall, only minor distinctions between the isolated-S1N simulations and the fully integrated configuration were observable. However, it is important to point out that including the effect of the unsteadiness by imposing time-varying boundary conditions at the inlet of the S1N seems to provide more reliable and accurate results in terms of 2D quantities distribution, taking as reference the coupled-SBES simulation here presented.

In conclusion, the key finding from this analysis is that the choice of the axial position for the nozzle inlet, aimed at decoupling the two components to individually examine the nozzle, can also impact the solution due to the significant blockage effect of the NGV on the velocity field. This underscores that the presence of the combustion chamber indeed exerts a substantial influence on the solution even under realistic operational conditions and realistic annular geometry. This holds true even when employing advanced CFD approaches to study the NGV in an isolated manner.

As next step of this study the application of two-dimensional unsteady boundary conditions derived from the fully integrated combustor-NGV SBES simulation will be employed in the next chapter. This approach aims to more precisely identify the distinctions that arise when utilizing boundary conditions obtained from a decoupled simulation of the stand-alone combustor, as was carried out in the current investigation.

Chapter 5

Study of generation of reliable inlet boundary conditions to perform NGV decoupled simulations

Contents

As anticipated in the previous chapter, the generation and application of highly representative and reliable boundary conditions at the inlet of the first-stage nozzle have become increasingly important since this enables the separate study of the two components by conducting decoupled simulations. In this chapter, the objective is to compare fully integrated combustor-stator SBES simulation with isolated stator SBES simulations, whose the computational domain is obtained by an extraction from the one including both components.

To achieve this, the unsteady inlet conditions applied at the stator were recorded during the fully integrated SBES simulation and then reconstructed at the interface plane between the two components. The recorded snapshots were utilized to recreate the most realistic and representative unsteady boundary conditions as possible, without requiring any further post-processing steps.

Additionally, the POD technique was applied, considering three different numbers of POD modes (30, 10, 5). Each mode corresponds to a descending level of energy content (80%, 50%, 30%) relative to the total energy of the flow. This type of post-processing technique can be successfully used in order to identify the proper coherent structures of turbulent flows, which are associated with the spatial distribution of each mode, and to reduce the complexity of the dynamics of a system, just taking into account the most important modes. Finally a comparison was made with a stand-alone stator SBES simulation, where time-averaged 2D maps extracted from the time-averaged solution of the fully-integrated SBES simulation were imposed.

Therefore, all the simulations of the isolated stator were conducted with the objective of assessing whether the flow field obtained is comparable to that of the integrated simulation, which serves as the reference case, allowing more realistic results to be obtained rather than imposing time-averaged 2D maps, as per standard design practice.

5.1 Reminders and application of POD for the study of Combustor-Turbine Interaction

First, some basic elements of the POD technique will be recalled here to help better understand the text. For more information and a more in-depth explanation, see chapter 2. POD technique belongs to the category of DDMA techniques. The primary goal of these methods is to break down an initial dataset into a set of linear combinations of modes. Each mode exhibits a distinct temporal pattern based on its values at different time points and a spatial pattern based on its values at various spatial positions. These techniques are useful for identifying coherent structures within turbulent flows. These structures correspond to the spatial distribution of each mode and can simplify system dynamics by focusing on the most significant modes. Specifically, POD is an energy-based decomposition method designed to approximate the original dataset, represented as the matrix $D(x,t)$. It achieves this approximation by utilizing only the initial n_t modes. Typically, the number of spatial points n_s significantly exceeds the number of time points n_t, a common scenario in CFD applications. By doing so, the energy content can be maximized, as these key modes account for the highest energy levels. In the context of the snapshot method, the matrix $D(x,t)$ is generated by capturing the temporal and spatial variations of selected quantities at a specified location. This location is often a plane situated within a point of interest in the computational domain, as demonstrated in this study. Each column of the matrix represents a "snapshot", and analyzing these columns offers insight into the spatial distribution. Conversely, observing the rows of the matrix reveals information about the temporal evolution [113, 114]:

$$D(x,t) = \begin{bmatrix} d_{11} & \dots & d_{1k} & \dots & d_{1n_t} \\ \vdots & \vdots & \vdots & \ddots & \vdots \\ d_{n_s1} & \dots & d_{n_sk} & \dots & d_{n_sn_t} \end{bmatrix} \tag{5.1}$$

Specifically, the POD method enables the breakdown of the original collection of measurements $D(x,t)$ into a linear composition of orthogonal bases known as POD modes $\tilde{D}$. These modes possess distinct energy levels denoted as σ_k, which solely depend on time functions $\psi^T(t)$ and spatial functions $\phi_k(x)$ [113, 114]:

$$D(x,t) = \sum_k \phi_k(x) a_k(t) = \sum_k \phi_k(x) \sigma_k \psi^T(t) = \sum_k \tilde{D}_k \tag{5.2}$$

Consequently, it becomes feasible to depict solely the varying component of the phenomenon under exam. The variables presented in Eq. 5.2 can be calculated by simplifying the original issue into an eigenvalue problem associated with the matrix K, referred to as the "temporal correlation matrix". This matrix encompasses correlations among distinct snapshots, which are outlined as follows [113, 114]:

$$K = D^T D \tag{5.3}$$

While maintaining the assumption of a significantly larger number of spatial points compared to time points ($n_s >> n_t$), it is noteworthy that it is feasible to choose a reduced count of POD modes $\tilde{n} < n_t$ that adequately capture the essence of the phenomenon. This approach introduces an approximation of the original matrix, characterized by a certain level of error. Regardless of the quantity of modes under consideration, the impact of a given k-th mode, represented as $\tilde{D}k = \phi k(x)\sigma_k\psi_k^T(t)$, can be singled out using Eq. 5.2. To evaluate the influence of a particular mode $\tilde{D_k}$, it is possible to algebraically combine it with the time-averaged field of the relevant parameter, as depicted in Figure 5.1. This approach enables the assessment of how the specific mode being studied modifies the mean field, thereby influencing the overall behavior of the aerothermal field.

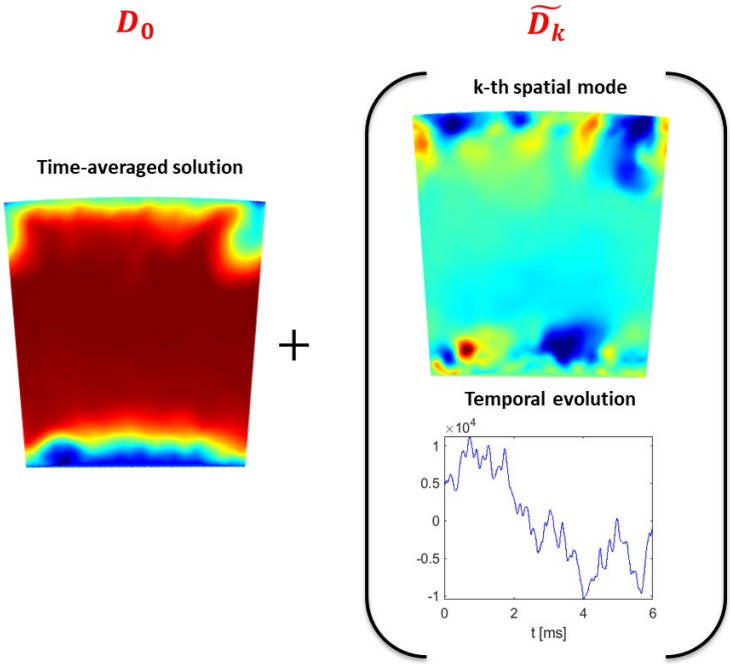

Figure 5.1: Schematic representation of data-driven modal analysis ***(©2024 Baker Hughes Company - All rights reserved).***

5.2 Boundary conditions

To perform realistic simulations of the stand-alone combustor and to account for the significant turbulence and temperature distortions characteristic of the combustor's outlet, a set of two-dimensional time-varying boundary conditions is imposed. To accomplish this, a collection of instantaneous quantities is extracted from the integrated SBES simulation at the interface plane p395, situated between the combustor and the turbine. This is the main difference compared to the previously presented case, where the snapshots were extracted from a SBES simulation of the isolated combustor. The data are saved at regular intervals of 0.015 ms

over a 25 ms duration, encompassing nearly two FTT of the isolated combustor and 25 FTT of the isolated NGV domains. This approach ensures a satisfactory temporal discretization while controlling the data size. However, only a subset of the recorded data has been utilized to generate the unsteady boundary conditions for the stator-only model. Specifically, a portion corresponding to approximately 6 ms (equivalent to 6 FTT of the isolated S1N) is selected for the boundary conditions generation. This decision is influenced by the reduced FTT characteristic of the stand-alone stator, allowing for more manageable computational efforts. The selected interface plane consists of 22,172 nodes. For instance, Figure 5.2 depicts the instantaneous total temperature at the S1N inlet for two instances, t_1 and $t_2 = t_1 + 100t_s$, with t_s representing the adopted time step. Each snapshot contains data related to mass flow (ρu_x, ρu_y, ρu_z), velocity (u_x, u_y, u_z), total temperature, turbulence quantities, mixture fraction, and progress variable. Additionally, a passive scalar

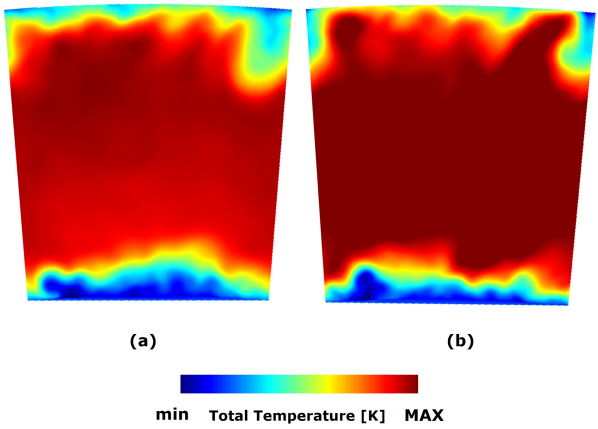

Figure 5.2: Visualization of two different instantaneous of total temperature recorded at the interface plane between combustor and turbine at ***(a)*** *the instant* t_1 *and* ***(b)*** *the instant* $t_2 = t_1 + 100t_s$*.*

is incorporated to monitor the concentration of film cooling from the nuggets. Regarding the inlet boundary conditions, in all S1N stand-alone simulations, mass flow in terms of mass flux, along with flow directions, and total temperature are prescribed at the S1N inlet, along with the previously extracted turbulent quantities. The outlet conditions are imposed by using the same static pressure profile from the integrated SBES calculation at the domain's outlet.

- Firstly, the collected snapshots are utilized to generate unsteady boundary conditions that aim to replicate the flow as realistically and accurately as possible, without requiring any additional post-processing operations.
- Subsequently, the POD technique is applied, considering three distinct number of POD modes:
  - The first thirty POD modes, accounting for approximately 80% of the energy compared to the fully integrated SBES simulation (used as a reference), are identified and applied at the S1N inlet.
  - The first ten POD modes are identified and enforced at the S1N inlet, collectively representing approximately 50% of the total energy.
  - The first five POD modes are identified and enforced at the S1N inlet, collectively representing approximately 30% of the total energy.
- Lastly, an additional SBES analysis is included in this study, wherein two-dimensional maps are used as inlet boundary conditions. These maps are obtained by time-averaging the unsteady boundary conditions prescribed in the previously described S1N SBES calculations, where POD was not applied. This simulation represents the standard industrial practice when conducting an unsteady SBES calculation.

In summary, the key parameters pertaining to the setup of all CFD simulations are presented in Table 5.1:

Table 5.1: Summary of the main parameters about the setup of the CFD simulations ***(©2024 Baker Hughes Company - All rights reserved)****.*

CFD Simulation	CFD Domain	Inlet BCs
SBES CC+S1N	CC+S1N	mass flow inlets
SBES S1N	S1N	set of instantaenous 2D maps from SBES CC+S1N
SBES S1N 30POD	S1N	set of instantaenous 2D maps from SBES CC+S1N (first 30 POD modes)
SBES S1N 10POD	S1N	set of instantaenous 2D maps from SBES CC+S1N (first 10 POD modes)
SBES S1N 5POD	S1N	set of instantaenous 2D maps from SBES CC+S1N (first 5 POD modes)
SBES S1N timeavg	S1N	time-averaged 2D maps from SBES CC+S1N

5.3 Analysis of the application of time-varying boundary conditions at S1N inlet

Firstly, before applying the POD technique, the focus lies on the ability of time-varying boundary conditions of reconstructing the flow field at the interface plane between combustor and turbine proper of the integrated simulation. To do so, RMS U_x, RMS U_y, RMS U_z and RMS T_t are presented in Figure 5.3 for SBES S1N and S1N timeavg calculations, then comparing them with SBES CC+S1N, selected as reference. Observing the RMS values for U_x, U_y, and U_z, it becomes evident that the results obtained from SBES S1N are in close agreement with those from SBES CC+S1N. This provides strong evidence that the time-varying boundary conditions effectively replicate the turbulence kinetic energy at the stator inlet, in contrast to the constant boundary conditions used in SBES timeavg. Similar conclusions can be drawn when

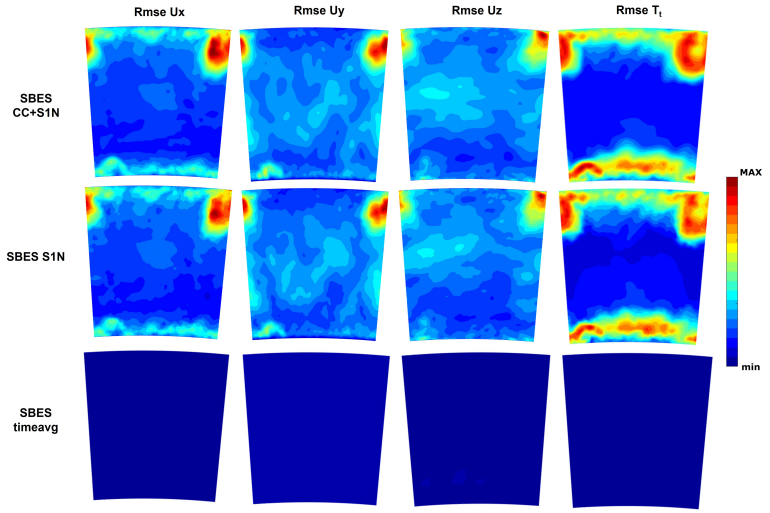

Figure 5.3: RMS U_x, RMS U_y, RMS U_z and RMS T_t for the SBES CC+S1N, SBES S1N and SBES timeavg calculations at plane 39.5.

examining the RMS values for T_t. Consequently, it can be inferred that the described approach of applying time-varying boundary conditions successfully reproduces the fluctuations of velocity and temperature fields characteristic of the integrated simulation. To quantify the similarities between SBES CC+S1N and SBES S1N, the velocity components and their respective RMS values, along with the normalized total temperature and its RMS values, are presented in Table 5.2. These values are obtained by performing spatial averaging at plane 39.5. The total temperature is normalized as follows:

$$T_{t,nd} = \frac{T_t - T_{min}}{T_{max} - T_{min}} \tag{5.4}$$

The results demonstrate that the relative discrepancies between SBES S1N and the reference case SBES CC+S1N are below 5% for all the evaluated variables, except for U_z. Since the obtained quantities are

strictly related to the imposed inlet boundary conditions for the SBES S1N case, these findings reinforce the notion that the applied set of boundary conditions for SBES S1N can realistically and accurately replicate the flow field characteristics observed in SBES CC+S1N, providing a representative representation of the simulation.

Table 5.2: Averaged values performed at plane 39.5 for the three velocity components and the respective RMS, normalized total temperature and the total temperature RMS are reported for SBES CC+S1N and SBES S1N. The relative differences between the two cases are also included. .

	SBES CC+S1N	**SBES S1N**	**Relative Difference [%]**
U [m/s]	59.848	60.466	1.032%
RMS U [m/s]	12.596	12.226	-2.941%
Ux [m/s]	56.186	56.788	1.072%
RMS U_x [m/s]	6.176	6.081	-1.527%
Uy [m/s]	-17.417	-17.673	1.471%
RMS U_y [m/s]	6.614	6.518	-1.447%
Uz [m/s]	-3.543	-3.246	-8.390%
RMS U_z [m/s]	8.430	8.027	-4.774%
$T_{t,nd}$ [-]	0.852	0.849	-0.397%
RMS T_t [K]	0.861	0.849	-1.489%

Additionally, it is essential to highlight that the inlet boundary conditions for the selected simulations share the same averaged values. As previously mentioned, the inlet boundary conditions for SBES timeavg are obtained by averaging the unsteady boundary conditions used in the S1N SBES calculation over time. To provide a clearer comparison, the three simulations are further assessed by examining the distributions of normalized total temperature, swirl, and pitch angles at the S1N inlet. These quantities are defined as follows:

$$swirl = \arctan\left(\frac{V_{tan}}{V_{ax}}\right) \tag{5.5}$$

$$pitch = \arctan\left(\frac{V_{rad}}{V_{ax}}\right) \tag{5.6}$$

As observed in Figure 5.4, the contours exhibit a remarkably similar behavior, as expected.

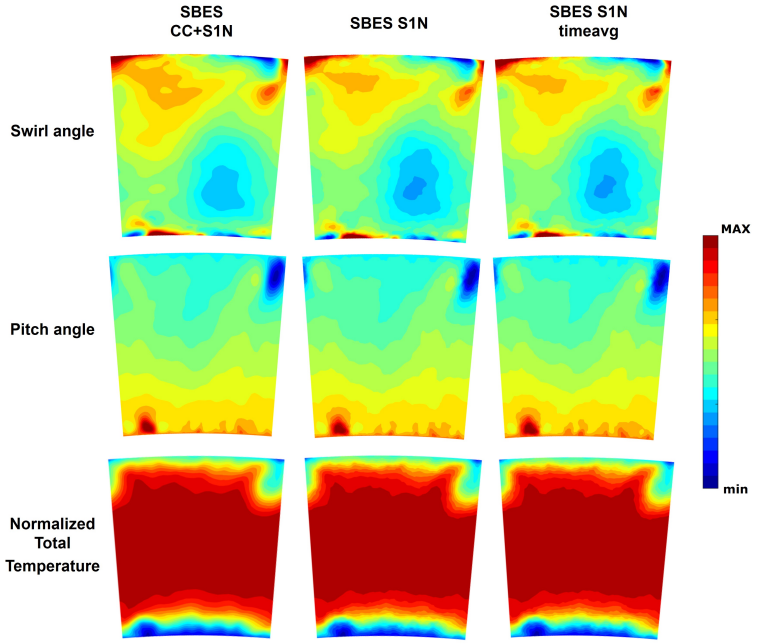

Figure 5.4: Time-averaged normalized total temperature, swirl and pitch angles from the SBES CC+S1N, SBES S1N and SBES timeavg at plane 39.5.

5.4 POD sensitivity analysis

As anticipated, data were collected at intervals of 0.015 ms, resulting in a series of snapshots spanning 25 ms. However, to manage computational resources efficiently, only a reduced number of snapshots were considered when calculating the truncated correlation matrix. In this context, a sensitivity analysis for determining the number of snapshots is presented, following a similar approach as described in a prior study by Meloni et al. [144]. Looking at Figure 5.5, the analysis assesses the energy content contribution and dominant frequency of the first three modes of ρu_x on plane 39.5, which serves as the prescribed inlet boundary condition for the S1N simulations. It is evident that the energy contribution of the first three modes does not vary significantly, ranging from 400 to 450 snapshots. These modes contribute to approximately 11%, 6%, and 5% of the total energy for the first, second, and third modes, respectively.

The findings related to the dominant frequency are presented in Figure 5.6. Notably, when considering more than 350 snapshots, both the first

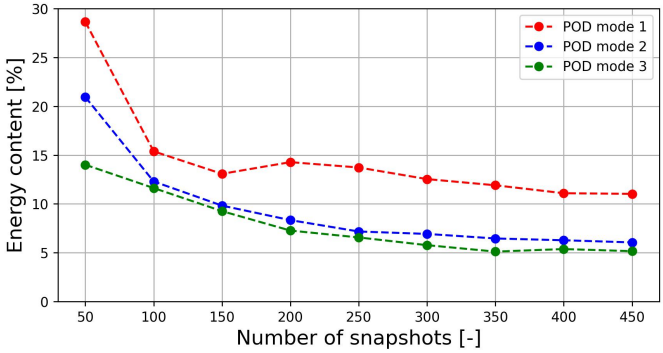

Figure 5.5: Energy content with respect to the total for the first three modes of ρu_x calculated at the interface plane between combustor and S1N by varying the total number of snapshots.

and second modes exhibit constant dominant frequencies of approximately 166.7 Hz. Similarly, the third mode displays a similar trend, albeit with slightly more noticeable variations in dominant frequency between 350 and 400 snapshots. Consequently, for subsequent calculations, 400 snapshots are chosen as the optimal number.

As previously mentioned, the POD analysis allows to determine the energy content contribution of each mode, providing valuable insights into the key modes that capture the overall dynamics of the flow. Figure 5.7 illustrates the characteristics of each mode, including their amplitudes and energy contributions. Notably, the first five modes significantly contribute to the flow dynamics, while the energy content of subsequent modes diminishes gradually. This observation suggests that the first five modes may be sufficient to capture the essential coherent structures of the aerothermal field. Specifically, the first mode serves as the principal mode, accounting for 11% of the energy content. In total, the first five modes collectively represent 30% of the total energy of the flow.

5.5 Interpretation of the POD modes

In order to gain a deeper insight into the coherent patterns that the POD modes can reveal, Figure 5.8 presents essential information concerning ρu_x, showing both spatial and temporal evolution for the first three coherent structures. For brevity, this analysis focuses solely on the first three POD modes. To provide a more precise assessment, the minimum and maximum distortions of the ρu_x field are also presented and compared to the time-averaged field. For this purpose, each POD mode is added algebraically to the time-averaged solution, which is obtained for all the collected time history. Upon observing the time-averaged field, a relevant blockage effect is evident owing to the presence of the leading edge of the following first stage stator. As observed from the previous analyses, this effect leads to a pronounced deceleration in this particular region, which is distinctly observable in the central area of plane 39.5. The presence of a significant acceleration around the leading edge clearly

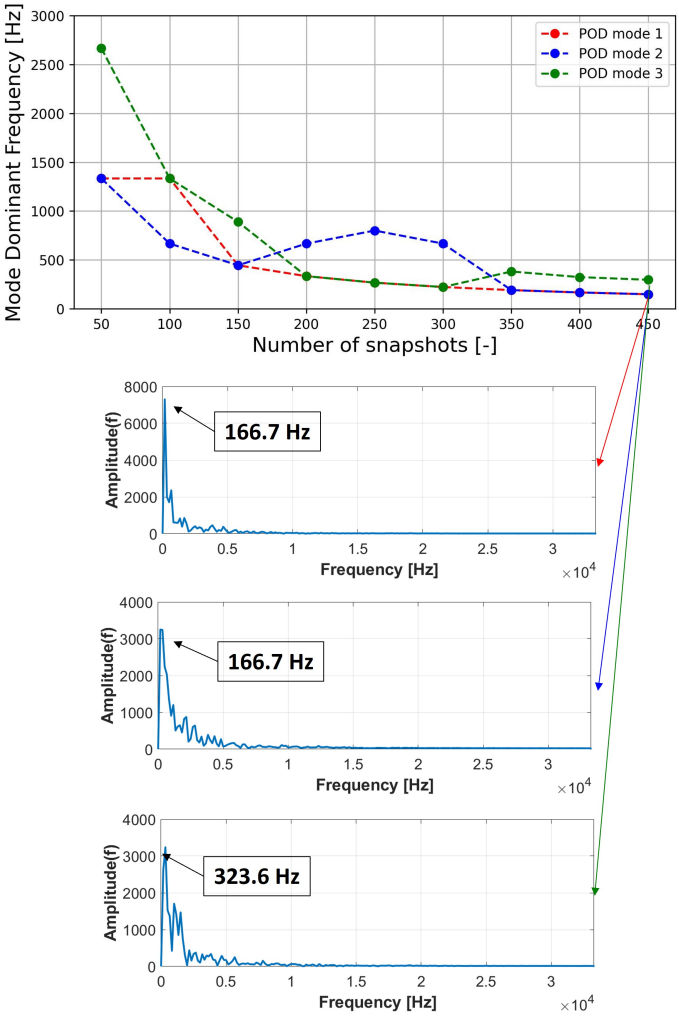

Figure 5.6: Dominant peak frequency for the first three modes of ρu_x calculated at the interface plane between combustor and S1N by varying the total number of snapshots.

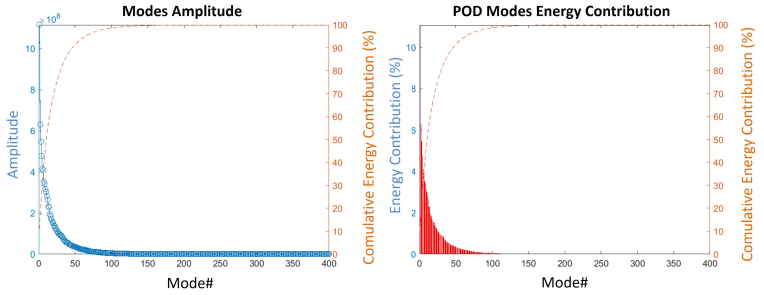

Figure 5.7: On the left, the amplitude of each mode is reported as function of the mode number, while on the right, the energy contribution of each mode is represented. In the right axis the cumulate of energy contribution is plotted.

offsets the deceleration observed in the region. The fluctuations in the flow field captured by the POD modes are primarily confined to the endwalls, particularly in areas where the cooling flow comes from the nuggets. As expected, the central region of plane 39.5, where the blockage phenomenon is highlighted, remains preserved. In this specific area, the minimum and maximum flow distortions exhibit limited expansions and contractions, which are consistently balanced by local accelerations and decelerations around the LE, ensuring an overall conservation of the average total mass flow. Regarding the endwalls, all considered POD modes exhibit more noticeable fluctuations, highlighting that higher levels of turbulence and flow unsteadiness are primarily concentrated in these regions due to the presence of the outgoing flow from the nugget. This phenomenon is further evident when examining the 2D contours of RMS U_x, RMS U_y, and RMS U_z at plane 39.5, as shown in Figure 5.3, which represent the three components of turbulent kinetic energy. Similarly, Figure 5.9 presents the most relevant information concerning the normalized total temperature, as defined in Eq. 5.4, displaying both spatial and temporal evolution for the first three coherent structures. Once again, to provide a more precise assessment, the minimum and maximum distortions of the

$T_{t,nd}$ field are reported with respect to the time-averaged field.
As observed in the time-averaged solution, the $T_{t,nd}$ distribution at the S1N inlet plane exhibits remarkable homogeneity, with minimal circumferential distortions. This behavior is attributed to the extended residence time within the combustion chamber. Consequently, further analysis concerning different relative swirler-to-S1N clocking positions becomes unnecessary, as anticipated in the previous chapter. Similarly to the ρu_x component, the first three POD modes, which represent the most energetic ones, introduce significant fluctuations in the distribution of the normalized total temperature, particularly near the endwalls. Furthermore, by examining the minimum and maximum distortions, it becomes evident that the hot gases experience notable expansion and contraction, leading to substantial variations in the mean total temperature at the central region of plane 39.5. These variations can be quantified by a maximum deviation of approximately 10%.

5.6 Analysis of the plane inlet conditions

In order to better compare the decoupled simulations with the coupled one, Figure 5.10 shows the total temperature RMS distribution for all the decoupled simulations and for the coupled simulation, taken as a reference, at plane 39.5. Since, as anticipated, the boundary conditions observable at the inlet are equal in terms of average values, as also demonstrated in the Figure 5.4, the comparisons on this plane are limited to the RMS values. For the sake of brevity, the comparisons are limited to the total temperature RMS, by way of example, being in any case also representative of the other quantities. As can be seen, as already noted, most of the fluctuations are noticeable at the endwalls, in correspondence to the coolant flow leaving the nuggets. In this case, as can be seen, the observable values of the decoupled simulations fall rather close to those of the SBES CC+S1N simulation, with the exception, as already noted, of the SBES S1N timeavg simulation. In general, it can be observed that as the number of POD modes considered decreases, the RMS values become

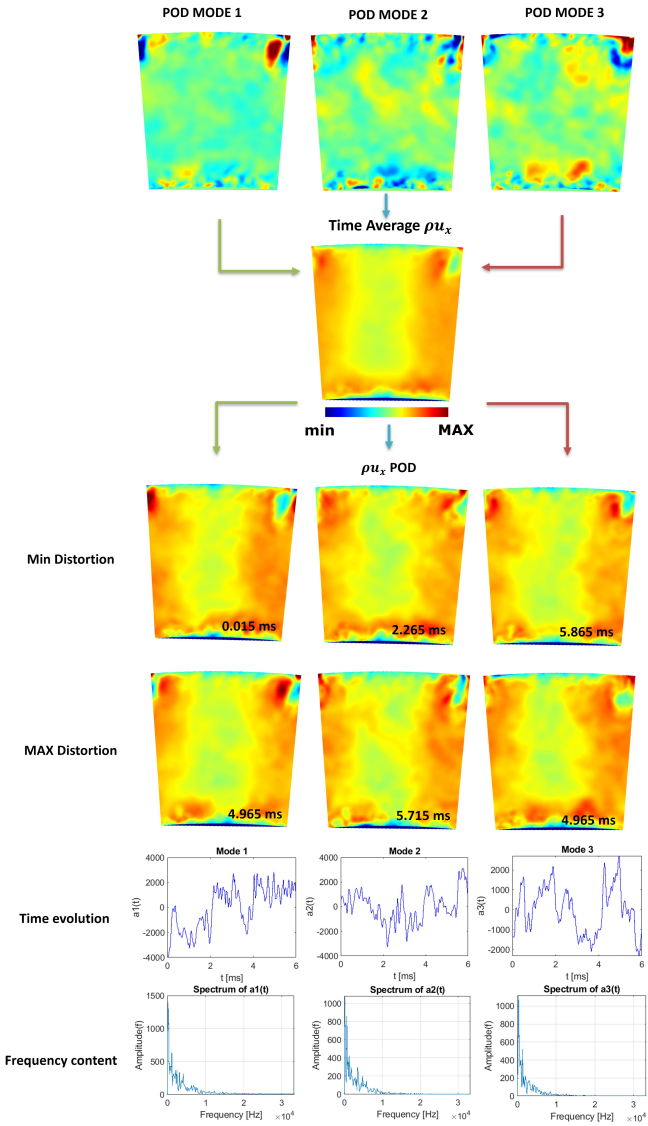

Figure 5.8: Representation of the first three modes of ρu_x and their interaction with the time-averaged field. To better quantify the results, the minimum and maximum distortions of the ρu_x field is reported with respect to the time-averaged field.

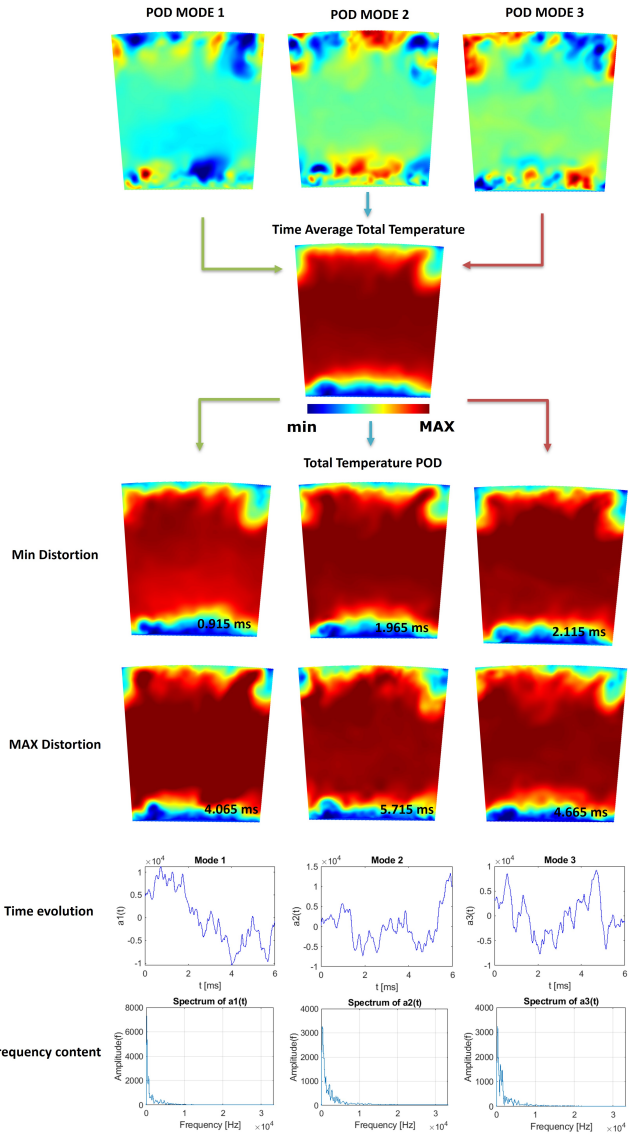

Figure 5.9: Representation of the first three modes of normalized total temperature and their interaction with the time-averaged field. To better quantify the results, the minimum and maximum distortions of the normalized total temperature field is reported with respect to the time-averaged field.

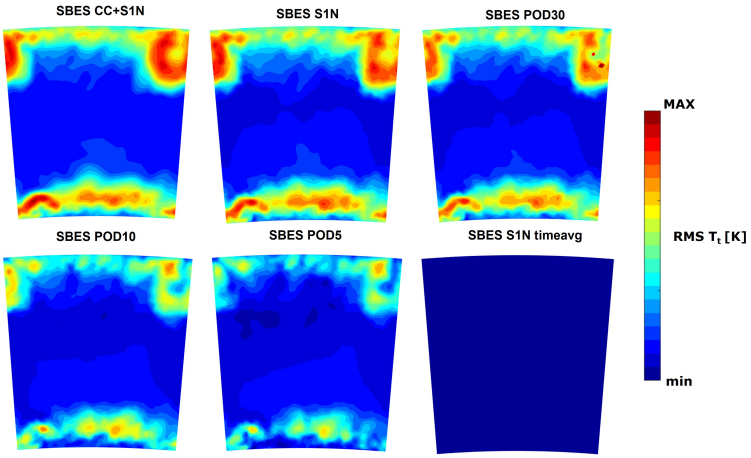

Figure 5.10: Representation of RMS total temperature for all the SBES calculations at plane 39.5. ***(©2024 Baker Hughes Company—All rights reserved).***

increasingly lower, as can be well observed above all from the SBES S1N 5POD simulation. This can be explained by the fact that, although the first five POD modes are the most important in order to reconstruct the dynamics of the system, the first thirty modes are representative of about 80% of the energy, while the first five ones of 30%. In order to understand how this may impact the nozzle aero-thermal field and its performance, further analyses on the vane are needed, which will be presented in the next section.

5.7 Airfoil loads and normalized temperature distributions along the vane

To facilitate a more comprehensive comparison between the decoupled simulations and the coupled one, Figure 5.11 displays the vane loads represented by the isentropic Mach number at three span locations (25%, 50%, and 75%). The isentropic Mach number is presented as a function of

the non-dimensional curvilinear abscissa, where negative values correspond to the pressure side, and positive values correspond to the suction side. Upon examining the figure, it is evident that the isentropic Mach number distributions from all the decoupled simulations closely align with the results obtained from the SBES CC+S1N calculation. This observation validates the correctness of the boundary conditions applied at the S1N inlet for all the decoupled cases and affirms their ability to accurately capture the S1N aero-thermal field. However, in contrast, significant disparities between the numerical calculations are evident when examining the prediction of the static temperature distribution along the stator. Figure 5.12 illustrates the normalized static temperature distribution over the vane surface for all SBES calculations. Figure 5.13 instead represents the normalized static temperature distribution over the endwalls for all SBES calculations. Focusing first on the SBES S1N timeavg and SBES S1N cases, noticeable discrepancies are observed between the two. The 2D maps clearly show that the SBES S1N case closely resembles the initial case SBES CC+S1N, both on the LE and on the PS and SS. On the contrary, when applying averaged and constant conditions over time to the stator inlet, significant errors arise in the prediction of the wall temperature distribution. Specifically, on the PS, there is a considerable overestimation of the wall temperature on the lower part and a similar but less pronounced behavior is observed on the upper part. As for the SS, the differences are less prominent, although around 50% of the span, a more extensive coverage by the coolant is evident, leading to a less uniform temperature distribution compared to SBES CC+S1N. The most significant differences are observed on the LE, where the wall temperature predicted by SBES S1N timeavg shows high non-uniformity. It is evident that a considerable portion of the LE is left completely uncovered by the cooling system, and around 50% of the span, the temperature prediction is notably underestimated.

Moreover, in order to better quantify the differences between the simulations, Figure 5.14 shows the relative differences, in terms of normalized temperature distribution, between SBES S1N (in red) and SBES S1N

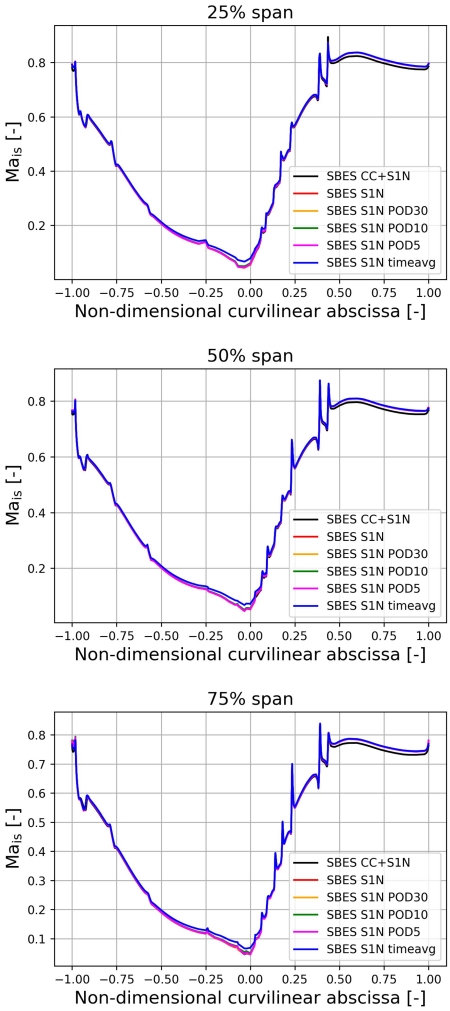

Figure 5.11: Isentropic Mach number on the NGV surface at the 25%, 50% and 75% of the span for all the SBES calculations. It is plotted as a function of the non-dimensional curvilinear abscissa, where x=0 corresponds to the leading edge of the NGV, x=-1 is the trailing edge pressure side and x=1 is the trailing edge suction side.

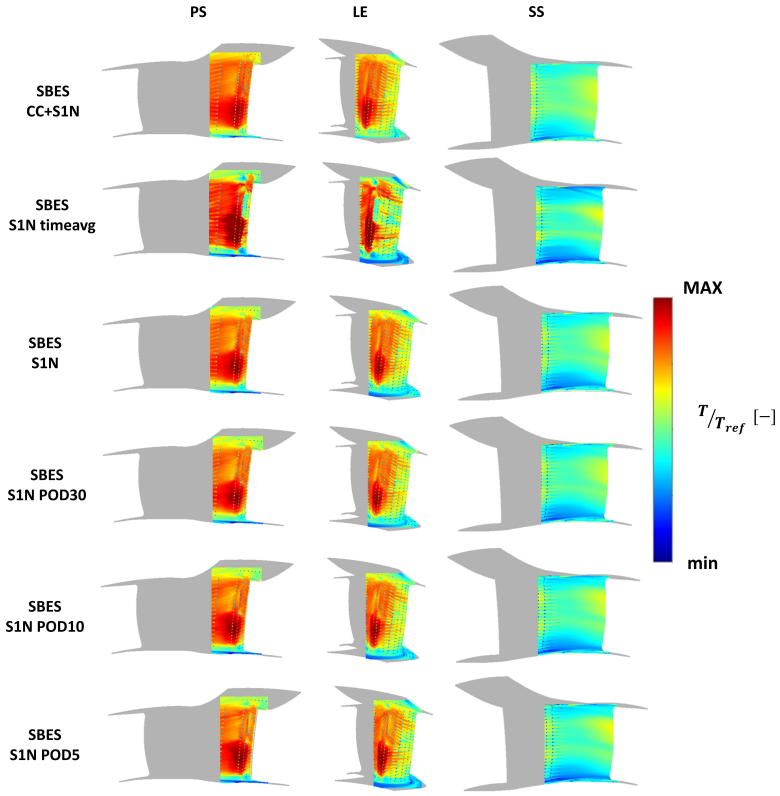

Figure 5.12: Time-averaged normalized temperature distribution on the NGV surfaces for the SBES CC+S1N simulation (Top) compared against all the S1N stand-alone simulations. ***(©2024 Baker Hughes Company - All rights reserved)***

timeavg (in blue) with respect to the temperature profile of the case SBES CC+S1N (in black) at 25%, 50%, and 75% of the span. As observed, the SBES S1N case consistently exhibits relative errors within 5% for all span values considered, except for certain points on PS around the TE, where the slot cooling system is present. Consequently, SBES S1N demonstrates a temperature distribution quite similar to the reference

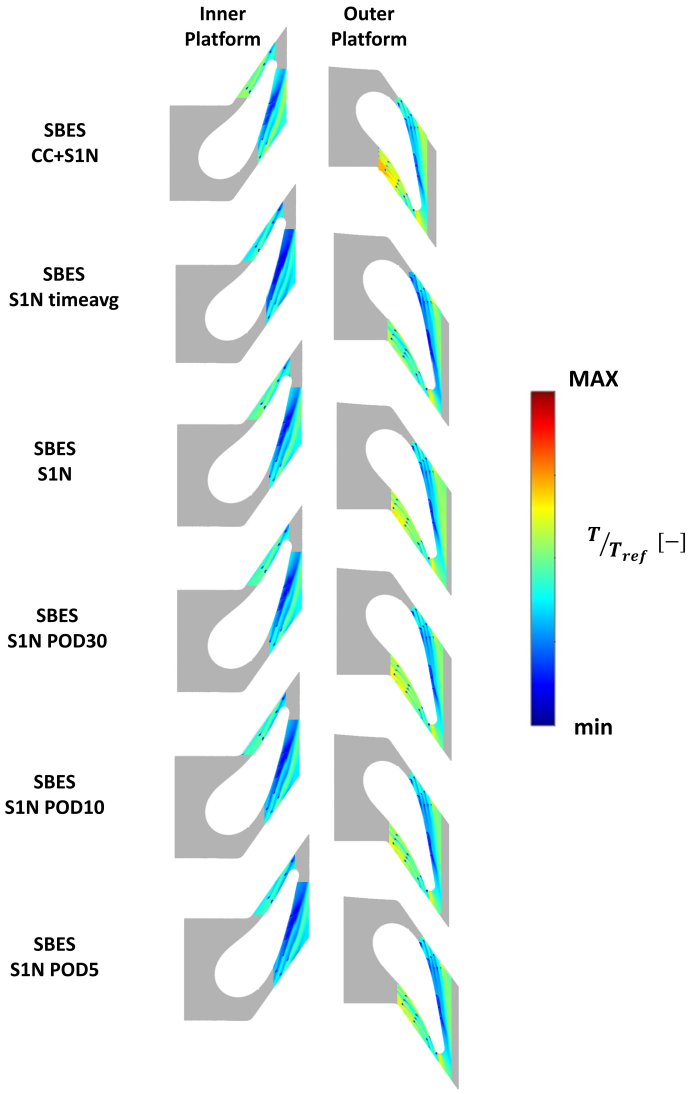

Figure 5.13: Time-averaged normalized temperature distribution on the endwalls for the SBES CC+S1N simulation (Top) compared against all the S1N stand-alone simulations.

case SBES CC+S1N across all span values. However, for the SBES S1N timeavg simulation, differences persist consistently for all three span values. Specifically, the most significant deviation occurs around the LE, where the wall temperature exhibits extreme non-uniformity, resulting in relative error peaks of approximately 10%, 20%, and 25% at 25%, 50%, and 75% of the span, respectively. Notably, at 50% of the span, an overestimation of the temperature on the PS side of the LE is evident, as evident also from the 2D maps. Conversely, on the SS, a significant temperature underestimation is observed, corresponding to the non-homogeneous contour temperature highlighted in the respective 2D map. A similar trend is also evident at 75% of the span, where an underestimated prediction of the wall temperature is noticeable on the PS, particularly for a curvilinear abscissa greater than -0.5. In conclusion, applying constant and time-averaged conditions results in considerable inaccuracies in predicting the temperature distribution on the vane, especially around the LE, despite using average values consistent with SBES CC+S1N and SBES S1N. This further emphasizes the necessity of generating realistic and representative conditions for conducting decoupled simulations of the S1N alone. Shifting now the focus to the 2D maps obtained from applying the POD technique with different mode selections, namely the first 30 modes (SBES S1N POD30), the first 10 modes (SBES S1N POD10), and the first 5 modes (SBES S1N POD5), it possible to observe that the contours in all cases closely resemble those obtained from the fully integrated simulation. This similarity is also observed in the inner and outer platforms (see Figure 5.13), where a good match is evident in comparison to SBES CC+S1N. However, upon closer examination of the contours, particularly on the PS and LE, a slight increase in wall temperature non-uniformity can be observed when considering fewer POD modes. This behavior can be attributed to the fact that fewer POD modes correspond to a lower energy content being considered at the stator inlet. Similar trends are also evident in the 1D radial profiles. In order to go into more details about the temperature distribution, the 1D profiles of the normalized wall temperature over the vane are presented in Figure 5.15, depicting

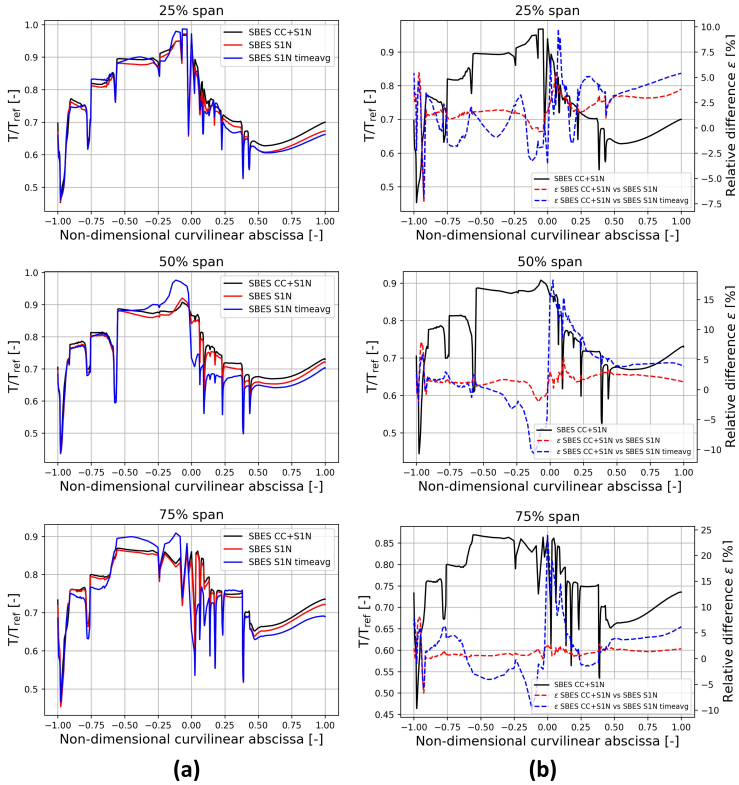

Figure 5.14: Normalized temperature on the NGV surface at 25%, 50%, and 75% of the span for the SBES CC+S1N simulation compared against SBES S1N and SBES S1N timeavg. It is plotted as a function of the non-dimensional curvilinear abscissa, where x *= 0 corresponds to the leading edge of the NGV,* x *= −1 is the trailing edge pressure side, and* x *= 1 is the trailing edge suction side.* .

the results for SBES CC+S1N, SBES S1N POD30, SBES S1N POD10, and SBES S1N POD5 calculations, as a function of the non-dimensional curvilinear abscissa. As observed, the wall temperature predictions from all simulations align closely with the SBES CC+S1N case, indicating a highly satisfactory match. This observation suggests that the application of the POD technique yields favorable results, successfully identifying the main coherent structures that significantly influence the system's dynamics. This further confirms that the POD technique is effective in characterizing phenomena related to combustor-turbine interactions.

5.8 Analysis of the plane outlet conditions

To emphasize the distinctions between a fully integrated simulation and decoupled ones, an analysis of the outlet plane conditions is provided, as they can significantly impact the lifetime and performance of the subsequent rotor. Firstly, Figures 5.16 and 5.17 present two-dimensional maps of the pitch and swirl angle, defined by Equations (5.5) and (5.6), respectively, at the stator outlet for all the simulations. It can be observed that both swirl and pitch distributions exhibit comparability among all the SBES simulations, affirming the accuracy of the set of inlet boundary conditions applied in the decoupled simulations. The swirl and pitch distributions of the stand-alone S1N simulations closely resemble those of the fully integrated ones. However, despite the general trends being comparable, some discrepancies still exist, particularly in the wake region. Specifically, examining the contours of S1N SBES timeavg, it becomes evident that the pitch distribution does not perfectly match the data from the fully integrated SBES simulation. The SBES timeavg predicts a more intense and non-uniform distribution, especially from 70% of the span, where a region characterized by higher pitch values is uniquely found in this case. A similar observation can be made when examining Figure 5.18, which displays the corresponding 1D radial profile, especially from 50% to 70% of the span. Furthermore, all the decoupled simulations exhibit a slight overestimation of the pitch angle, approximately around

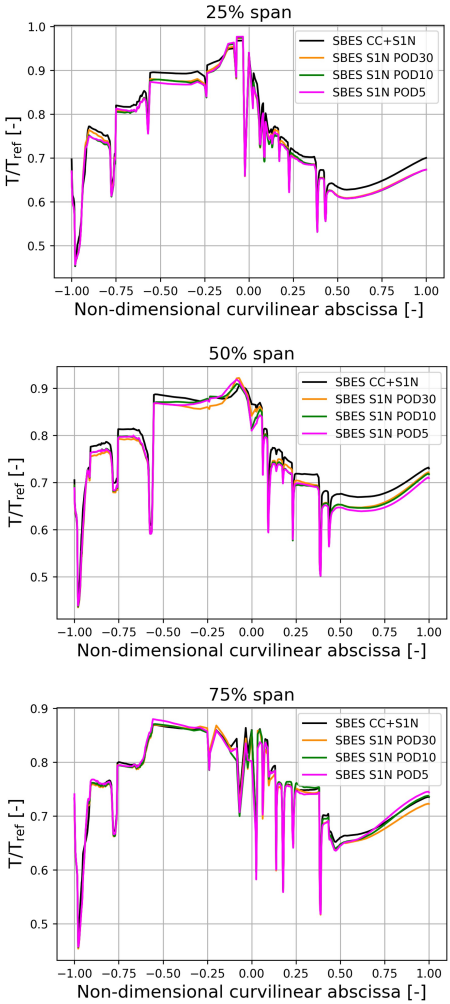

Figure 5.15: Normalized temperature on the NGV surface at 25%, 50% and 75% of the span for the SBES CC+S1N simulation compared against SBES S1N POD30, SBES S1N POD10, and SBES S1N POD5. It is plotted as a function of the non-dimensional curvilinear abscissa, where x *= 0 corresponds to the leading edge of the NGV,* x *= −1 is the trailing edge pressure side, and* x *= 1 is the trailing edge suction side.* ***(©2024 Baker Hughes Company—All rights reserved).***

10% of the span. A similar observation can also be extended to the swirl angle. In this case as well, applying time-averaged boundary conditions at the stator inlet leads to a more intense and non-uniform distribution, as depicted in Figure 5.17. This discrepancy results in a less consistent swirl distribution between 70% and 90% of the span, as evident from Figure 5.18, where the corresponding 1D radial profiles are presented for all the simulations. Additionally, in this case, especially near the hub region, approximately up to 10% of the span, a deviation from the coupled SBES solution is observed. Nonetheless, overall, in all the simulations, particularly those where time-varying boundary conditions are applied, the pitch and swirl angle distributions closely align with the coupled simulation, resulting in a highly satisfactory match. Additionally, the contours of the normalized total temperature, as defined by Equation 5.4, obtained at the outlet plane are displayed in Figure 5.19 for all the SBES simulations. It can be observed that all the 2D maps exhibit a very similar distribution, particularly for all the stand-alone S1N SBES calculations, with the exception of SBES S1N timeavg. Similar to the pitch and swirl angles, in this case as well, the 2D contour of SBES S1N timeavg displays a more distorted distribution, especially in the wake region, from 60% of the span. Nevertheless, these discrepancies are not as pronounced when examining the averaged 1D radial profiles, as presented in Figure 5.18. In conclusion, the analysis of the outlet plane reveals that, overall, only minor differences exist between the stand-alone S1N SBES calculations and the fully integrated simulation, with the exception of the SBES S1N timeavg calculation. Consequently, when considering the SBES CC+S1N case as the reference, imposing time-varying boundary conditions at the inlet of the S1N, accounting for unsteadiness, yields more reliable and precise results in terms of 2D quantity distributions at the outlet plane. This observation extends to the SBES S1N simulations that utilized the POD technique (SBES S1N 30POD, SBES S1N 10POD, and SBES S1N 5POD), indicating that including only the first five POD modes, corresponding to 30% of the total energy, produces satisfactory and accurate results.

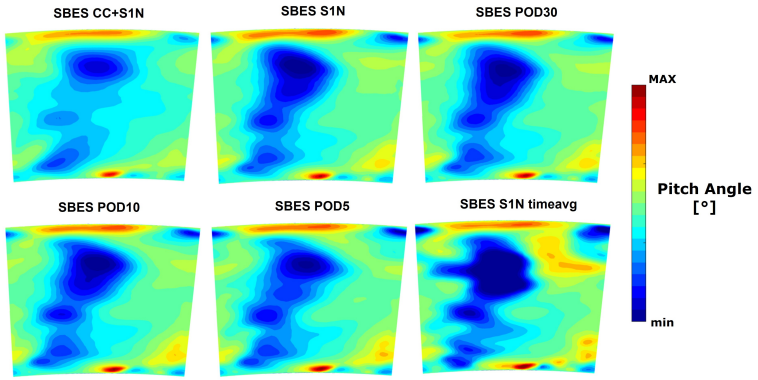

Figure 5.16: Time-averaged pitch angle for all the SBES simulations extracted from the outlet plane of the S1N stator ***(©2024 Baker Hughes Company—All rights reserved)****.*

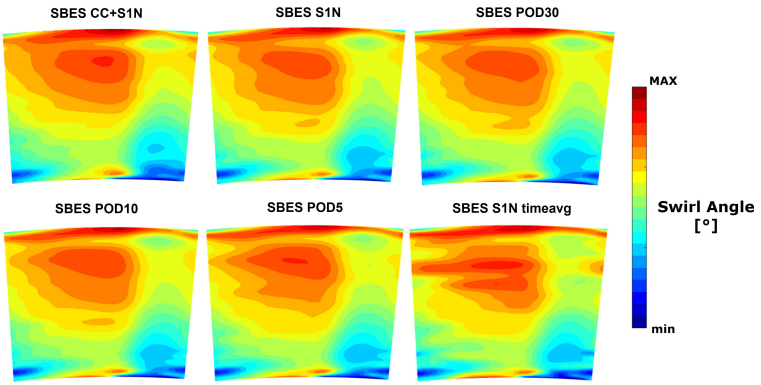

Figure 5.17: Time-averaged swirl angle for all the SBES simulations extracted from the outlet plane of the S1N stator ***(©2024 Baker Hughes Company—All rights reserved)****.*

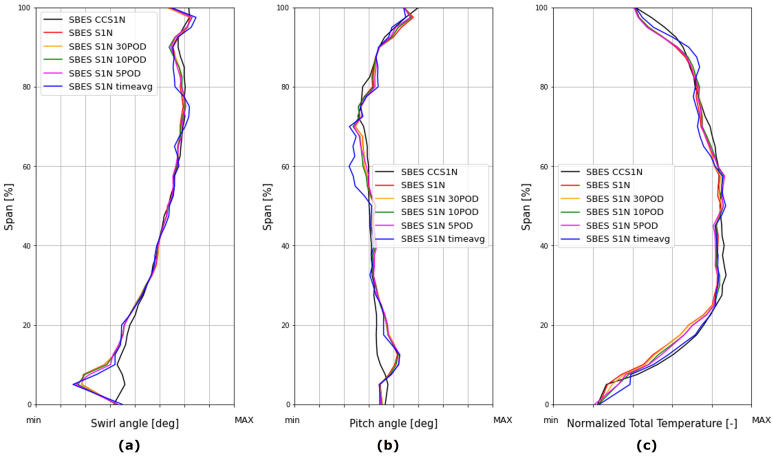

*Figure 5.18: Time-averaged (**a**) swirl angle, (**b**) pitch angle, and (**c**) normalized total temperature circumference-averaged 1D profiles for all the SBES simulations extracted from the outlet plane of the S1N stator* ***(©2024 Baker Hughes Company—All rights reserved)***.

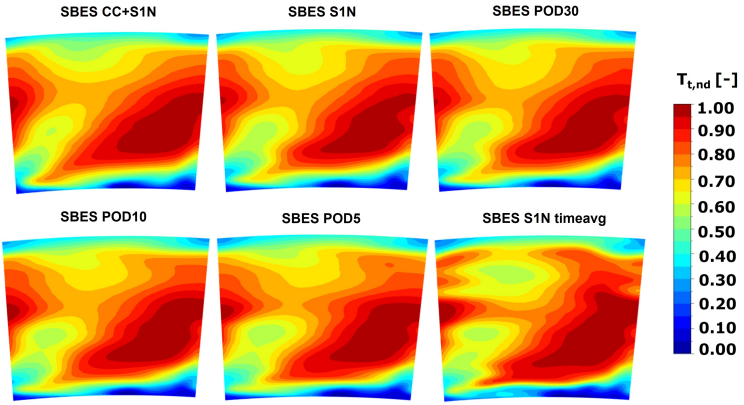

Figure 5.19: Time-averaged normalized total temperature for all the SBES simulations extracted from the outlet plane of the S1N stator ***(©2024 Baker Hughes Company—All rights reserved)***.

5.9 Concluding remarks

In summary, the primary objective of this study is to compare simulations of a fully integrated combustor-stator system (referred to as SBES CC+S1N) with simulations of an isolated stator component. The fully unsteady inlet condition of the stator was recorded and reconstructed at the interface plane between the two components from the fully integrated SBES. To create more accurate and representative unsteady boundary conditions, the recorded snapshots were firstly employed without any additional post-processing (referred to as SBES S1N simulation). Then, the proper orthogonal decomposition (POD) technique was applied taking into account three different numbers of POD modes (30, 10, and 5), corresponding to decreasing levels of energy content (80%, 50%, and 30%) relative to the overall energy of the flow (referred to as SBES S1N POD30, SBES S1N POD10, and SBES S1N POD5) at the interface plane between the two components. This type of post-processing technique can be successfully used in order to identify the proper coherent structures of turbulent flows that are associated with the spatial distribution of each mode, and to reduce the complexity of the dynamics of a system, just taking into account the most important modes. The obtained results were then compared with an SBES simulation of the stand-alone stator, which was carried out by imposing time-averaged 2D maps extracted at plane 39.5 from the fully integrated SBES simulation (referred to as SBES S1N timeavg simulation). These simulations were conducted under realistic operating conditions and geometry to investigate the interaction between the combustor and the first-stage nozzle. Additionally, the interaction between the main hot flow from the combustor and the cooling flows by including a realistic turbine nozzle cooling system was studied. Consequently, all SBES simulations of the isolated stator aimed to determine whether the obtained flow field inside the stator passage vane is comparable to that of the integrated simulation, which serves as a reference. Hence, all the SBES simulations of the isolated stator were performed with the aim of determining whether the flow field obtained is comparable

with that of the integrated simulation, assumed as a reference, allowing more realistic results to be obtained rather than imposing time-averaged 2D maps, as per standard design practice.

Firstly, the focus lies on the ability of time-varying boundary conditions to reconstruct the flow field at the interface plane between the combustor and turbine compared to the integrated simulation. To accomplish this, the RMS values of U_x, U_y, U_z, and T_t for both S1N SBES and S1N time-averaged calculations are compared with SBES CC+S1N ones, which serve as reference point. Upon examining the results, it becomes evident that the employed time-varying boundary conditions successfully replicate the turbulence kinetic energy at the stator inlet, in contrast to the outcome when constant boundary conditions (SBES timeavg) are employed.

Next, following the presentation of a sensitivity analysis regarding the determination of the number of snapshots, the application of POD technique was undertaken, considering three distinct numbers of POD modes. To gain a deeper understanding of the coherent structures that can be discerned through the POD modes, the most relevant information about the ρu_x and normalized total temperature in terms of both spatial and temporal modes for the first three coherent structures were studied. Moreover, alongside revealing a significant blockage effect resulting from the stator's presence, the contours indicated that greater levels of turbulence and flow unsteadiness predominantly localized in these areas, attributable to the outflow from the nuggets.

To facilitate a more effective comparison between the decoupled simulations and the integrated one, the distribution of RMS total temperature is examinated for all the decoupled simulations, focusing on the interface plane between the combustor and turbine. The findings reveal that as the number of considered POD modes decreases, the RMS values exhibit a corresponding decrease. This trend is particularly evident in the SBES S1N 5POD simulation, as expected.

Furthermore, when examining the 2D distribution of normalized static temperature across the vane surface for all SBES calculations, it becomes

evident that the isolated S1N simulations, where unsteady boundary conditions are employed, closely resemble the SBES CC+S1N simulation. This similarity is observed on both the LE and the PS as well as the SS. In contrast, when average and constant conditions over time are applied to the stator inlet, noticeable discrepancies arise in predicting the wall temperature distribution, particularly on the PS and LE.

Subsequently, an examination of the conditions at the outlet plane is presented, with a specific emphasis on pitch and swirl angles along with the normalized total temperature. In this instance, the findings indicate that the distributions are consistent across all the SBES simulations, affirming the accuracy of the applied set of inlet boundary conditions for all the decoupled simulations. Nonetheless, while the overall trends exhibit similarity, certain disparities can still be detected, particularly in the wake region, as observed in the S1N SBES timeavg simulation.

In conclusion, it can be asserted that, when comparing with a coupled simulation as the benchmark, the imposition of time-varying boundary conditions at the inlet of the S1N, accounting for the impact of unsteadiness, yields more reliable and accurate results concerning the distribution of 2D quantities at the outlet plane. This observation also applies to the SBES S1N simulations that incorporated the POD technique (SBES S1N 30POD, SBES S1N 10POD, and SBES S1N 5POD). Notably, the application of only the initial five POD modes, which constitute 30% of the total energy, results in satisfactorily accurate outcomes.

Chapter 6

Numerical prediction of the heat transfer coefficient under engine-like conditions

Contents

As anticipated in the previous chapters, innovation in the field of gas turbines, driven by the pursuit of maximizing efficiency and minimizing pollutants, led to the development of new types of combustors, known as lean burn combustors. However, these components introduce distortions in the thermo-fluid dynamic characteristics of the outgoing flow, resulting in thermal challenges in downstream components, particularly in the first stage stator. Therefore, studying these distortions and their effects on the NGV is of fundamental importance as it allows manufacturers to make

necessary modifications to ensure a long service life.

In this chapter, a section of a Baker Hughes heavy-duty gas turbine, already presented in the previous chapters, comprising a single set of uncooled vanes, will be analyzed through numerical simulations with the objective of assessing the heat transfer coefficient under engine-like conditions. Two different numerical models, RANS and SBES, will be used to evaluate potential improvements in employing scale-resolved model with respect to the traditional RANS as per standard design practice. Inlet flow conditions to the first stage nozzle were set as time-averaged 2D maps and time-varying 2D maps for RANS and SBES simulations, respectively. This is in accordance to the procedure that was employed for the cooled vanes configuration, as already discussed (see chapter 4). These conditions were derived from two different SBES calculations: the first one was conducted on the integrated geometry comprising the combustor and downstream stator while the other one was performed on the stand-alone combustor (see chapters 4 and 5). This choice was made for two reasons: first, to provide a measure of HTC under realistic operational conditions, including pressure, temperature, and turbulence typical of engine operation, and second, to analyze the validity of the commonly used approach in studying such components, which tends to use inlet conditions to the stator derived from the combustor analysis alone, without considering the mutual combustor-turbine interaction.

Finally, the objective is to obtain a scaling criterion for the HTC in lab-scaled conditions in order to provide representative HTC values in engine-like conditions. In fact, when the engine operates in realistic conditions at full speed and full load, direct experimental measurements are not available and therefore the introduction of a scaling criterion becomes necessary. In particular, the scaling process is applied to the HTC obtained by performing numerical simulation in lab-scaled condition (SBES Integrated SST, see chapter 3) and the results are then compared to the ones obtained by performing the CFD calculations under engine-like conditions above described and reported in this chapter. In order to carry out such scaling process, the HTC values obtained in lab-scaled conditions

are scaled by extracting significant quantities in the prediction of heat exchange, such as the Reynolds number and the Prandtl number, only at the inlet and outlet of the stator, as average quantities. In conclusion, in this way, it is possible to obtain a relationship such that it allows to scale the HTC, obtained in test rig conditions, as standard practice, into a representative HTC in full speed and full load engine-like conditions, where typically there are no experimental measurements available.

6.1 HTC prediction in engine-like conditions

6.1.1 Numerical setup

In accordance with what has already been done for the previous analyses in engine-like conditions, the computational domain used is similar to what has already been described in the previous simulations conducted on the isolated nozzle (see chapters 4 and 5), with the only difference that the cooling system on the vane is excluded. In fact, the vane is simulated as uncooled for the purpose of calculating the HTC, as per industrial design practice, and in accordance with what was done in the experiments in non-reactive conditions, as described in the chapter 3. In particular, the cell count regarding just the stand-alone uncooled stator is approximately 2.5 million of polyhedral elements and it was designed in order to keep the y+ value below 1 all over the vane surface. The computational domain and the mesh that were utilized for all the calculations reported in this chapter are reported in Figure 6.1.

For the numerical prediction of the HTC in engine-like conditions, two different numerical models, RANS and SBES, are employed. As anticipated, the inlet boundary conditions for the uncooled S1N are the really same already used for the analyses of the cooled vanes and so they were derived from two different SBES calculations: the first one was conducted on the integrated geometry comprising the combustor and downstream stator while the other one was performed on the stand-alone combustor (see chapters 4 and 5). In particular, time-averaged 2D maps and time-varying 2D maps were set for RANS and SBES simulations,

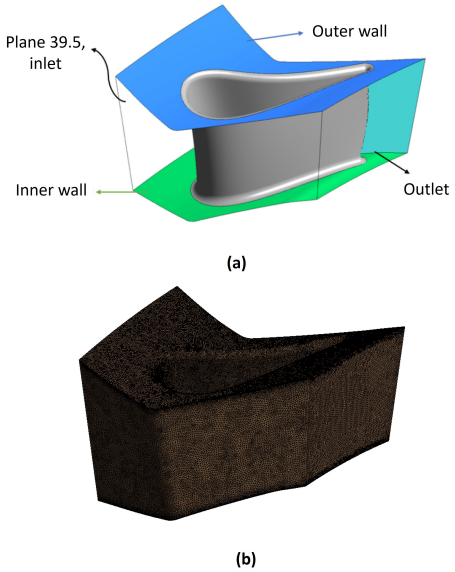

Figure 6.1: (a) CFD domain of the uncooled periodic vane along with (b) a detail of the mesh. ***(©2024 Baker Hughes Company—All rights reserved).***

respectively, as already discussed for the cooled vanes configuration. For more information regarding the inlet boundary conditions, see chapter 4. Regarding the outlet boundary conditions, all the simulations utilized the same radial static pressure profile, which however differs from the one used for the cooled S1N simulations in order to obtain the same vane load, despite the lack of incoming flow rate from the film cooling slots.
To enhance the comparison between coupled simulation, taken as reference, and decoupled uncooled ones, vane loads expressed as isentropic Mach numbers are presented in Figure 6.2 for the RANS and SBES cases in which the boundary conditions were extracted from the SBES CC+S1N simulation, as an example. In fact, these curves are also representative for the RANS and SBES simulations in which the boundary conditions

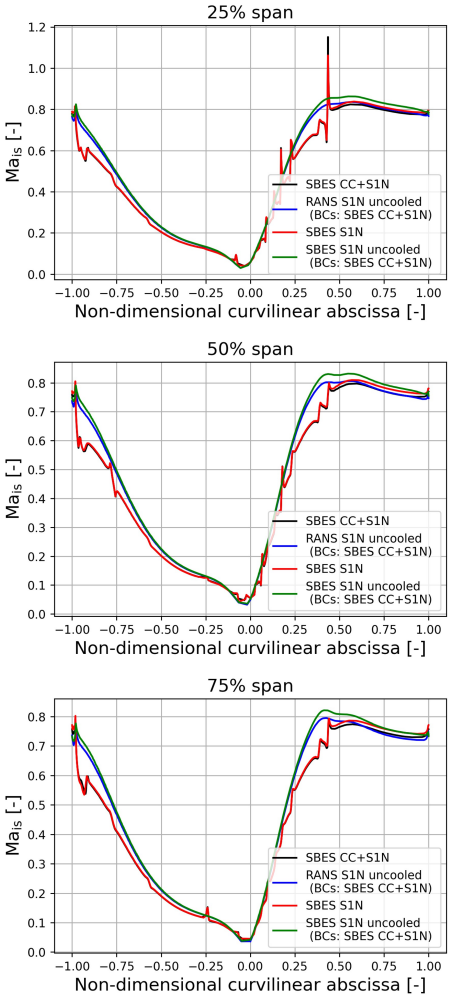

Figure 6.2: Vane loads in terms of isentropic Mach Number on the NGV surface at the 25%, 50% and 75% of the span. The isentropic Mach number is reported as a function of the non-dimensional curvilinear abscissa, where $x = 0$ corresponds to the leading edge of the NGV, $x = -1$ is the trailing edge pressure side and $x = 1$ is the trailing edge suction side .

at the nozzle inlet are extracted from SBES CC and are therefore not reported for brevity. The data is reported at 25%, 50%, and 75% of the span for all the considered simulations. In addition to the vane load of the SBES CC+S1N simulation, the one referring to the SBES S1N simulation is also reported, described in the previous chapter 5, where the cooled nozzle is studied in a decoupled way. The isentropic Mach distributions obtained from the RANS and SBES calculations for the isolated uncooled stator closely match the one predicted by the integrated SBES simulation, demonstrating a highly satisfactory agreement.
More information regarding the turbulence effects and the numerical setup of all the RANS and SBES simulations can be found in chapter 4, since all the calculations share the same features of the already described cooled S1N analyses.
In summary, the key parameters referred to the setup of all CFD simulations are presented in Table 6.1:

Table 6.1: Summary of the main parameters about the setup of the CFD simulations ***(©2024 Baker Hughes Company - All rights reserved)****.*

CFD simulation	**CFD modelling**	**Inlet BCs**
RANS uncooled (BCs: SBES CC+S1N)	RANS	time-averaged 2D maps from SBES CC+S1N
RANS uncooled (BCs: SBES CC)	RANS	time-averaged 2D maps from SBES CC
SBES uncooled (BCs: SBES CC+S1N)	SBES	set of instantaneous 2D maps from SBES CC+S1N
SBES uncooled (BCs: SBES CC)	SBES	set of instantaneous 2D maps from SBES CC

6.1.1.1 HTC numerical prediction procedure

In accordance with what has already been done previously for the numerical prediction of the HTC in lab-scaled conditions, for all the CFD simulations HTC was determined through a two-step simulation process, involving two runs characterized by different imposed wall heat fluxes, $\dot{q}$. Subsequently, HTC was calculated by applying a linear regression based on the conventional $T_w - \dot{q}$ regression method for each point on the vane surfaces. The resulting HTC values consequently represent the angular coefficient within the subsequent equation:

$$\dot{q} = HTC(T_{aw} - T_w) \tag{6.1}$$

Meanwhile, the adiabatic wall temperature is obtained by assuming a zero heat flux. To enhance clarity regarding the process, a visual illustration is provided in Figure 6.3. To validate the accuracy of this methodology, an initial analysis was undertaken involving five separate RANS simulations, each with distinct imposed heat flux values. This investigation confirmed that the resultant wall temperature values align on a consistent linear trend.

6.1.2 HTC results

The heat transfer coefficient predicted numerically by the CFD simulations in which the boundary conditions at the nozzle inlet are extracted from SBES CC+S1N is reported in Figure 6.4.
In this way, it is possible to make some considerations on the differences introduced by the different numerical models. As a matter of fact, generally speaking, it is possible to observe an overestimation of the HTC in the RANS simulation with respect to the companion SBES. This phenomenon has been already observed in chapter 3, where the HTC has been predicted in lab-scaled conditions and compared with experiments. This evident overestimation due to the RANS modelling is particularly true on the LE and on the SS, where the HTC reaches its peak value, especially on the most convex part of the SS, where the highest speeds

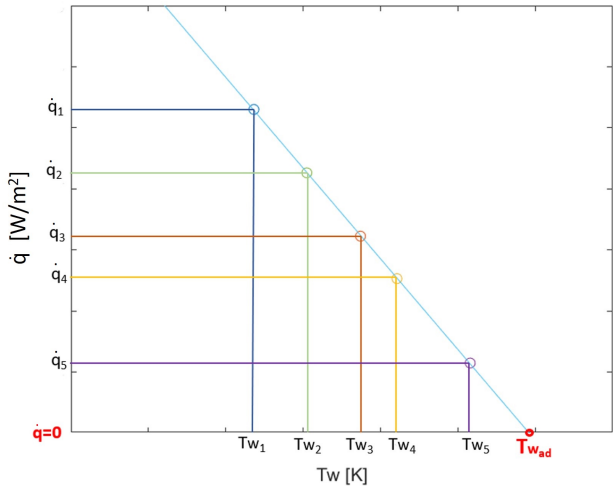

Figure 6.3: Example of the $T_w - \dot{q}$ regression approach applied at one point of the grid of the NGV surface. Each colored point corresponds to a run with a different fixed heat flux. ***(©2024 Baker Hughes Company—All rights reserved).***

are reached. The same considerations can be also made looking at the 1D profiles of HTC, as reported in Figure 6.4, extracted at the 25%, 50% and 75% of the span as a function of the non-dimensional curvilinear abscissa. However, despite the clear discrepancies especially in terms of absolute values between the two modelling, it is important to point out that some similarities can be still noted between the simulations in terms of distribution: at the LE, all the simulations indeed predict a minimum in HTC, even if its position is delayed downstream along the PS for the RANS case. The heat transfer coefficient predicted numerically by the CFD simulations in which the boundary conditions at the nozzle inlet are extracted from SBES CC is instead reported in Figure 6.6. In the same way, the 1D profiles of HTC extracted at the 25%, 50% and 75% of the span as a function of the non-dimensional curvilinear abscissa are represented in Figure 6.7. As can be clearly seen, by comparing these results with the ones obtained for the case in which the boundary

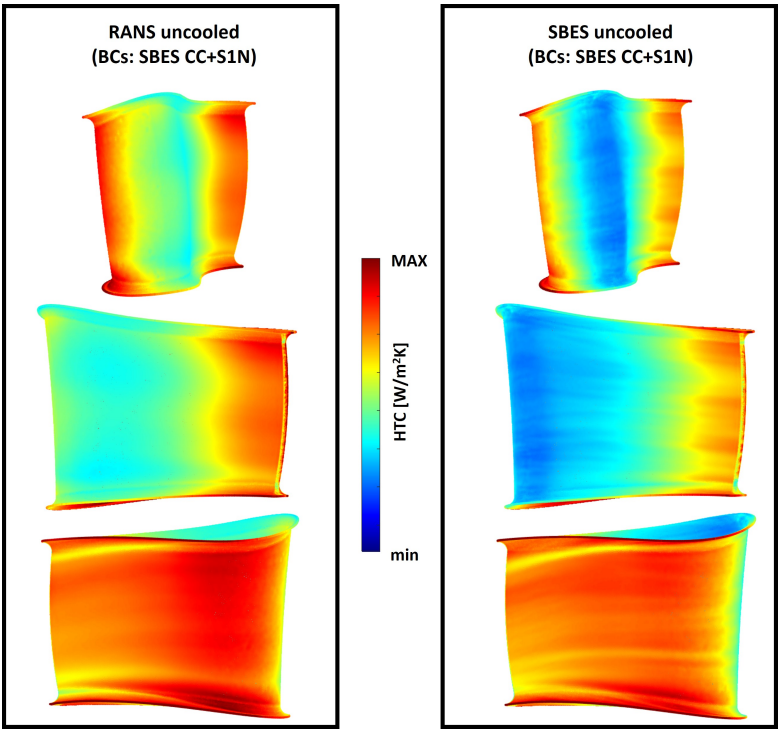

Figure 6.4: Heat transfer coefficient maps for the CFD simulations in which the boundary conditions at the nozzle inlet are extracted from SBES CC+S1N ***(©2024 Baker Hughes Company—All rights reserved)***.

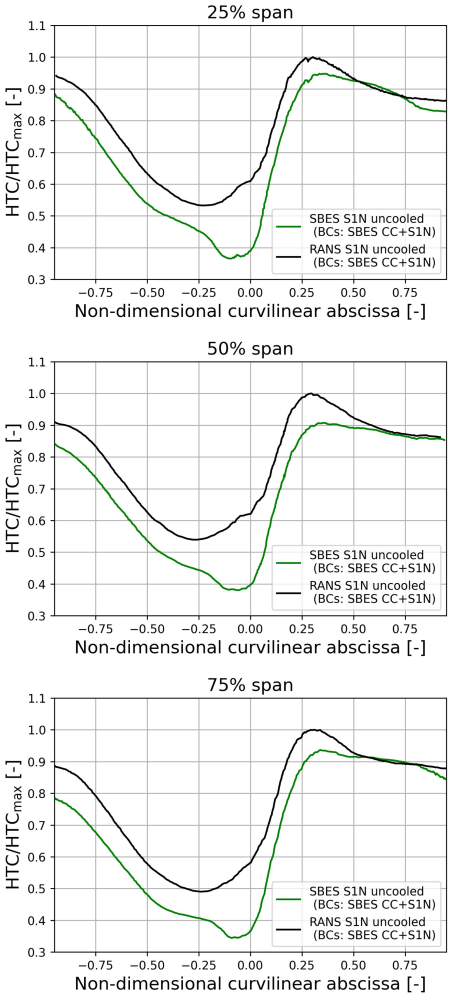

Figure 6.5: Heat Transfer Coefficient profiles at 25%, 50% and 75% of the span for RANS and SBES simulations in which the boundary conditions at the nozzle inlet are extracted from SBES CC+S1N ***(©2024 Baker Hughes Company—All rights reserved)***.

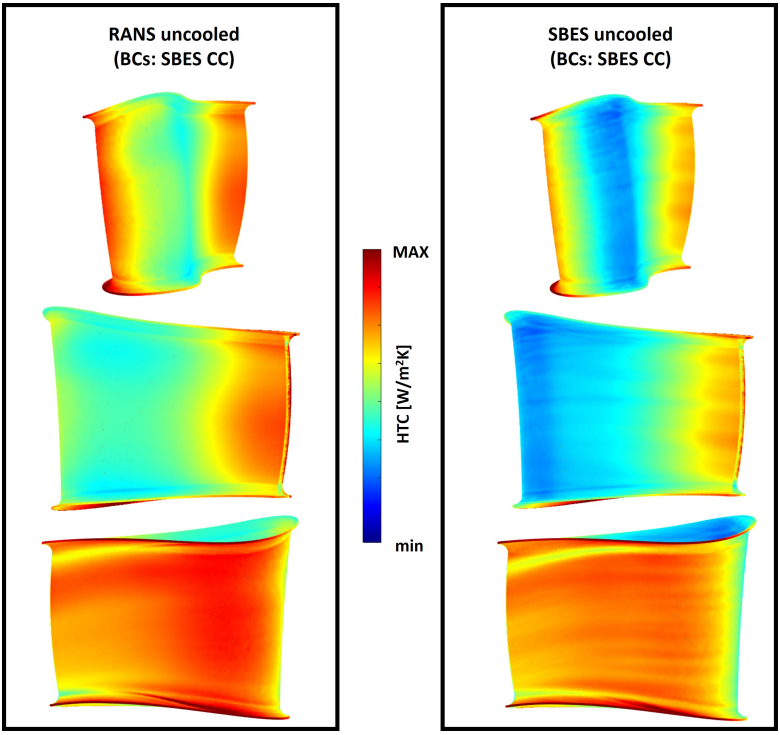

Figure 6.6: Heat transfer coefficient maps for CFD simulations in which the boundary conditions at the nozzle inlet are extracted from SBES CC ***(©2024 Baker Hughes Company—All rights reserved).***

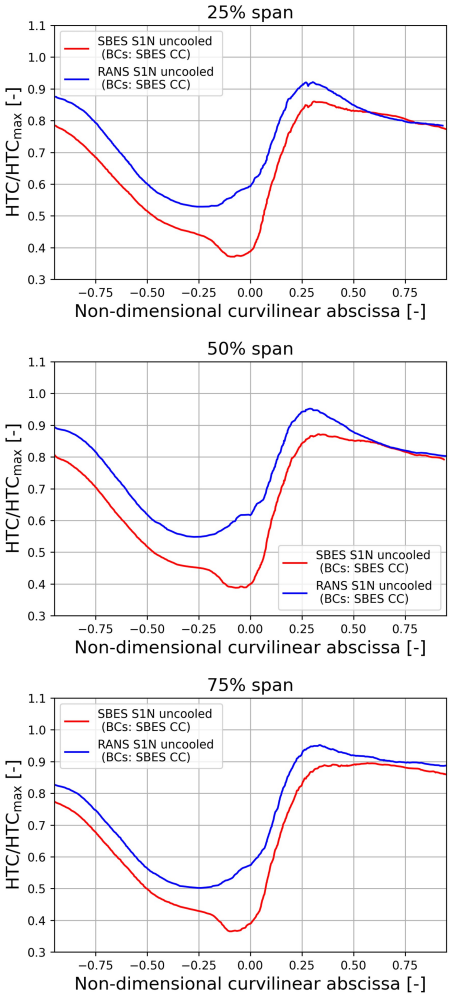

Figure 6.7: Heat Transfer Coefficient profiles at 25%, 50% and 75% of the span for RANS and SBES simulations in which the boundary conditions at the nozzle inlet are extracted from SBES CC ***(©2024 Baker Hughes Company—All rights reserved)****.*

conditions at the nozzle inlet are extracted from SBES CC+S1N, no relevant differences can be found, contrary to what was observed in the cooled simulations. In fact, if in the prediction of the behaviour of the cooling system it was highlighted how the different boundary conditions coming from an SBES CC or SBES CC+S1N simulation had a significant impact on the temperature distribution on the vane and therefore on the mixing between the hot main flow and the cold coolant, in this case, the different boundary conditions imposed have a very limited impact in predicting the HTC on an uncooled vane. Such observations can be confirmed by looking at the extracted 1D HTC profiles at the 25%, 50% and 75% of the span, where the SBES uncooled (BCs: SBES CC+S1N) and SBES uncooled (BCs: SBES CC) are compared. In fact, looking at the Figure 6.8, it is clear that the two simulations give very similar results to each other, with more discrepancies occurring around the LE, where the different incidence conditions at the inlet have a greater impact, and on the SS, in particular at 75% of the span.

The same considerations can be also applied by looking at the secondary flows by using the Q-criterion isosurfaces, for both SBES simulations of the uncooled vane, colored based on the normalized temperature value, as can be seen from Figure 6.9. As a matter of fact, as can be seen, for both cases, the presence of the horse-shoe vortices, due to the interaction between the incoming boundary layer and the solid vane, and the corner vortices, formed at the intersection of two walls where the fluid encounters a corner, is evident, according also to the literature [145] (see Figure 6.10). These flow structures have a strong impact on the distribution of the HTC along the vane: in fact, these, transporting cold fluid coming from the nuggets away from the endwalls over the NGV surface, leave a trace over the SS, leading to a local decrease in HTC. This is in agreement with the work of Thomas et al. [95], where the impact of coherent flow structures was studied, concluding that the corner vortices are the most persistent ones, having an impact on temperature distribution on the airfoil.

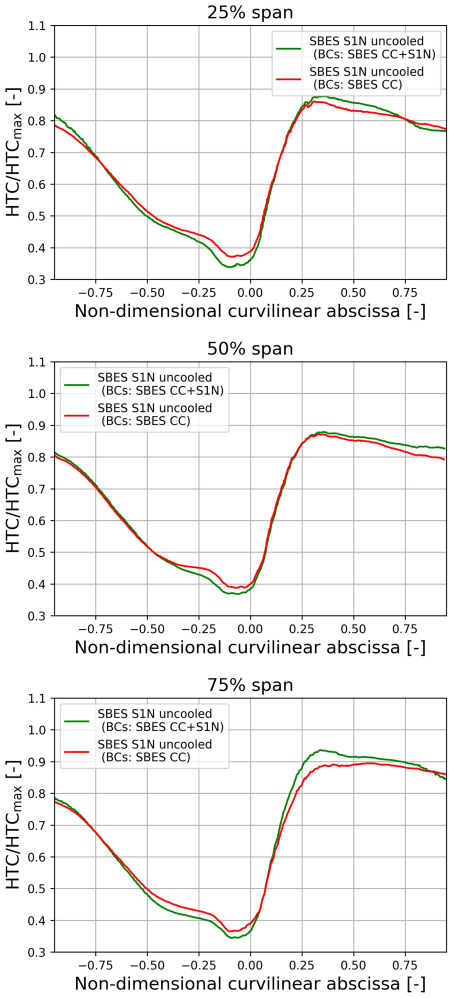

Figure 6.8: Heat Transfer Coefficient profiles at 25%, 50% and 75% of the span for SBES uncooled (BCs: SBES CC+S1N) and SBES uncooled (BCs: SBES CC) ***(©2024 Baker Hughes Company—All rights reserved)****.*

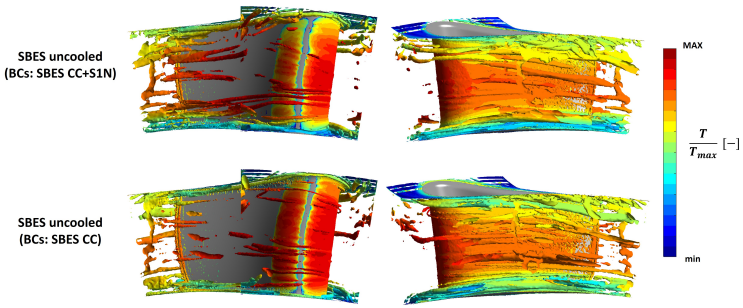

Figure 6.9: Q-criterion isosurfaces colored by static temperature for SBES uncooled (BCs: SBES CC+S1N) and SBES uncooled (BCs: SBES CC) ***(©2024 Baker Hughes Company—All rights reserved)****.*

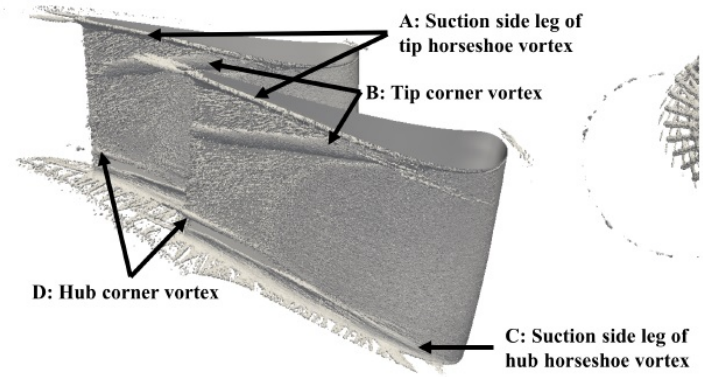

Figure 6.10: Secondary flow structures on a airfoil according to Wang et al. [95, 145].

6.2 HTC scaling from lab-scaled data

Finally, the objective is to obtain a scaling criterion for the HTC obtained in lab-scaled conditions in order to get representative HTC values in engine-like conditions. In fact, when the engine operates in realistic

conditions at full speed and full load, direct experimental measurements are not available and therefore the introduction of a scaling criterion becomes necessary. In particular, the scaling process is applied to the HTC obtained by performing numerical simulation in lab-scaled condition (SBES Integrated SST, see chapter 3) and the obtained results are then compared to the ones obtained by performing the CFD calculations under engine-like conditions, reported in this chapter. In order to carry out such scaling process, the HTC values obtained in lab-scaled conditions are scaled by extracting significant quantities in the prediction of heat exchange, such as the Reynolds number and the Prandtl number, only at the inlet and outlet of the stator, as average quantities. In conclusion, in this way, it is possible to obtain a relationship such that it allows to scale the HTC, obtained in test rig conditions, as standard practice, into a representative HTC in full speed and full load engine-like conditions, where typically there are no experimental measurements available.
The simulations in lab-scaled conditions, reported in chapter 3, are conducted on the same engine, with the only difference being the S1N, that was previously redesigned in order to have the same count of nozzles and burners, thus a 1:1 ratio for the simulations in engine-like conditions (see chapters 4 and 5). In particular, the CFD simulation in lab-scaled conditions that is chosen for the scaling of HTC is the SBES Integrated SST (see chapter 3), where the SBES model was used to study the fully integrated CC+NGV configuration by prescribing mass flow inlets from the experiments at the swirler and nuggets inlets. In this simulation, transition phenomena are not taking into account (fully turbulent). In the following sections, the theoretical approach employed for the scaling process will be presented, along with the results.

6.2.1 Description of the theoretical approach

According to the common procedure used for the calculation of the heat transfer coefficient on an airfoil, the surfaces of interest are distinguished between LE, which is approximated to a cylindrical surface, and the PS

and SS, which are considered as flat plates.
As regards the LE, the correlation used is the following [146]:

$$Nu_D^\star = C \cdot Re_D^m \cdot Pr^{1/3} \cdot \left(\frac{T_{avg,w}}{T_{avg,inlet}} \right)^{0.8} \tag{6.2}$$

from which the heat transfer coefficient is obtained as:

$$HTC_{LE}^\star = C \cdot Re_D^m \cdot Pr^{1/3} \cdot \left(\frac{T_{avg,w}}{T_{avg,inlet}} \right)^{0.8} \cdot \frac{k}{D} \tag{6.3}$$

where k is the thermal conductivity of the fluid evaluated and averaged on the inlet plane, while C and m are constants that are worth $C = 0.1738$ and $m = 0.6642$. The subscript D indicates that the characteristic variable used to calculate the Reynolds number is the diameter of curvature at the LE, while the other quantities for the Reynolds number calculation (velocity, density and dynamic viscosity) are calculated as mean values over the area at the inlet plane of stator (plane 39.5). It is important to point out that the original version of this correlation took into account the dependence on the angular position (in terms of curvilinear abscissa). In this work, instead, this aspect is neglected in order to simply the calculation. However, the correlation is used within its validity range, $-0.17 < s < 0.21$, as indicated by the authors. Furthermore, given the obvious difference between lab-scaled and engine-like operating conditions, the ratio between average temperature on the stator vane surface ($T_{avg,w}$) and the temperature average flow on the inlet plane ($T_{avg,inlet}$) was taken into account according to [147]. The exponent $\star$ indicates that the considered quantity, i.e. the HTC, is evaluated through correlation, to distinguish it from that predicted by numerical analysis.
To calculate the HTC on the PS and SS, assumed as flat plates, the following correlation is instead used:

$$HTC_{PS,SS}^\star = 0.0287 \cdot Re_{C_{ax}}^{0.8} \cdot Pr^{0.6} \cdot \left(\frac{T_{avg,w}}{T_{avg,inlet}} \right)^{0.8} \cdot Ma_{outlet} \cdot \frac{k}{D} \tag{6.4}$$

where the characteristic variable used to evaluate the Reynolds number is the axial chord of the vane (C_{ax}), while Ma indicates the isentropic Mach number averaged on the exit plane of the stator. This correlation comes from [127], with the additional introduction of the ratio between temperatures and isentropic Mach number. In particular, the latter has been added since the acceleration in the vane passage is different between the two simulations due to the different operating conditions. This correlation was validated for turbulent flows [127].
The scaling procedure is applied as follows: firstly, the $HTC^{\star}$ is evaluated for all the considered simulations by correlation, by applying Eq. 6.3 and Eq. 6.4, extracting data from the CFD simulations, both in lab-scaled and engine-like conditions; then, the HTC predicted by the lab-scaled CFD simulation is scaled to engine-like conditions as follows:

$$HTC_{scaled} = HTC_{lab,scaled} \cdot \left(\frac{HTC^{\star}_{engine}}{HTC^{\star}_{lab}} \right) \tag{6.5}$$

6.2.2 Results

In Figure 6.11, the comparison between the HTC predicted by the simulation SBES uncooled (BCs: CC+S1N) and HTC calculated by scaling the HTC numerically predicted in lab-scaled conditions is reported. It is important to point out that this comparison is limited to at the 25%, 50% and 75% of the span to simplify the calculations but has still a general relevance on the entire vane surface. In the same picture, the effect of the different correlations, according to Eq. 6.3 and Eq. 6.4, is reported in order to highlight the advantages of using two different correlations based on the area of the vane considered, as indicated by the literature. In fact, it is clear that, regardless of the percentage of span from which the profile is extracted, using the correlation reported in Eq. 6.3 allows much better scaling of HTC on the LE compared to using Eq. 6.4, which instead provides much better results on the PS and SS, as is particularly evident at 25% and 50% of the span.
By comparing the HTC predicted by the simulation SBES uncooled (BCs: CC+S1N) and HTC calculated by scaling the HTC numerically predicted

in lab-scaled conditions in Figure 6.11, it is so important to recall that for $-0.17 < s < 0.21$, the HTC is scaled by using relation Eq. 6.3, according to its validity range, while along remaining portion of the vane the HTC is scaled by using Eq. 6.4. The peaks that are so visible around the LE are attributed to the switch from a correlation to another, and it was decided to keep them without proceeding with smoothing precisely to highlight this transition.

As can be seen from the Figure 6.11, the HTC scaling process leads to very close values compared to the SBES simulation runned in realistic operating conditions. In fact, the relative error reported at 50% of the span as an example, gives further confirmation: it, in fact, remains globally contained between 15% and 20% along the entire length of the vane. However, the 20% peak located around $s = 0.2$ is certainly influenced by the switch between one correlation to another, as described above. The results reported so far are referred to SBES uncooled (BCs: SBES CC+S1N), however the same considerations can be also applied to SBES uncooled (BCs: SBES CC), as visible in the Figure 6.12.

As mentioned previously, the scaling process of HTC from lab-scaled to engine-like conditions was conducted taking as reference the SBES Integrated SST CFD simulation (see chapter 3), where the turbulence in the RANS zone is modeled with the $k-\omega$ SST model, which does not takes into account the transition phenomena, similarly to what was done in the engine-like condition calculations. In fact, by applying the scaling process to the experimental data (see chapter 3) in the same ways described above, as shown in the Figure 6.13, much more marked differences are noted compared to applying the scaling process to a fully-turbulent CFD in the same operating conditions: these discrepancies can be attributed to the fact that, despite the elevated levels of turbulence at the inlet, the experimental data show a strong impact of the BL transition on the airfoil. The transition with high free stream turbulence in fact, as seen in the chapter 3, remains a complex phenomenon to model. Furthermore, it is important to point out that the correlations used to predict HTC do not also take into account the transition phenomenon. However, despite

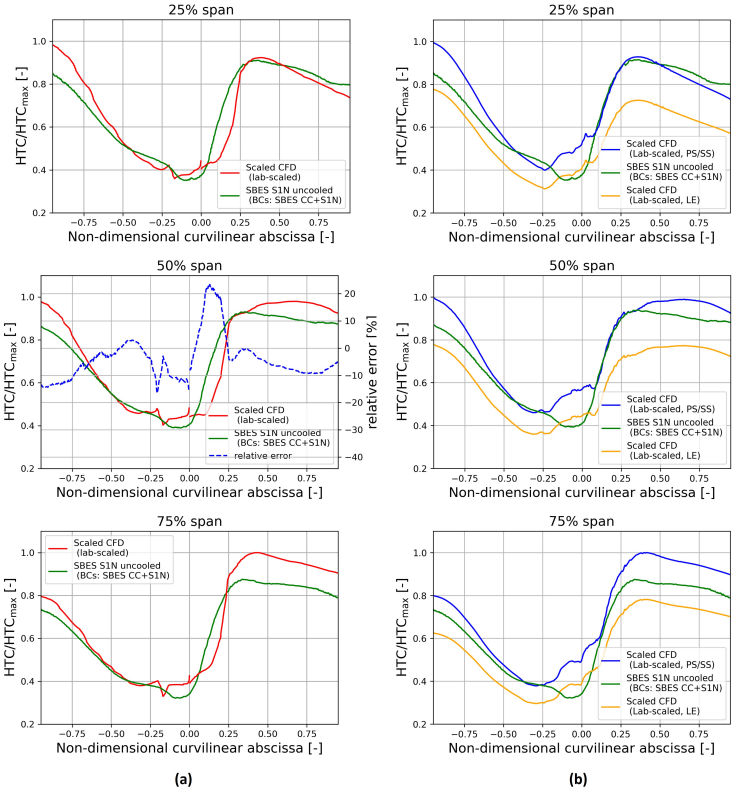

Figure 6.11: Heat Transfer Coefficient profiles at 25%, 50% and 75% of the span obtained by scaling the CFD performed at lab-scaled conditions to engine-like conditions. (a) the results are compared to the HTC obtained for the SBES uncooled (BCs: SBES CC+S1N). (b) the effect of the different correlations, valid for LE and PS/SS, are reported ***(©2024 Baker Hughes Company—All rights reserved).***

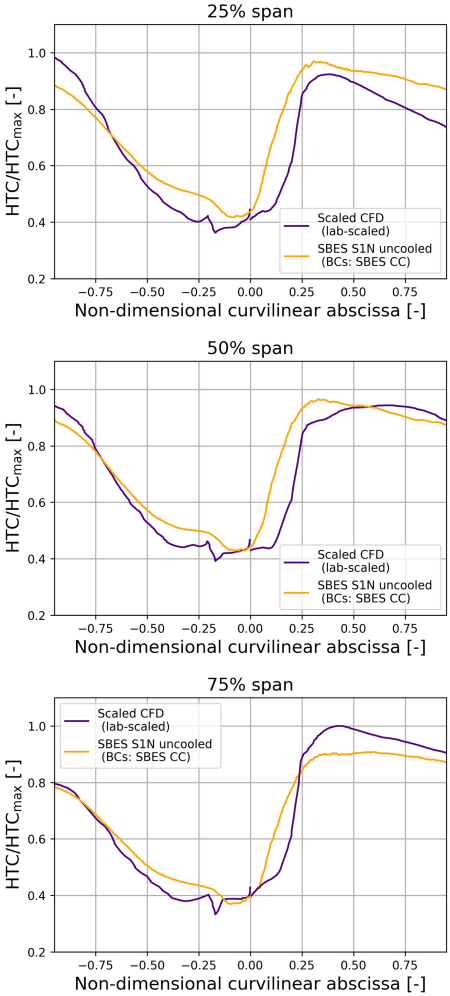

Figure 6.12: Heat Transfer Coefficient profiles at 25%, 50% and 75% of the span obtained by scaling the CFD performed at lab-scaled conditions to engine-like conditions. The results are then compared to the HTC obtained for the SBES uncooled (BCs: SBES CC) ***(©2024 Baker Hughes Company—All rights reserved)****.*

these differences, it is believed that the scaling process described above remains valid for two reasons: firstly, it is hypothesized that all the SBES CFD simulations, characterized by the same general setup, differ from the experimental data in a similar way, regardless of the fact that the calculations were conducted in lab-scaled or engine-like conditions; furthermore, given that the heat exchange is studied on the first high pressure nozzle, this nozzle will certainly be equipped with a complex cooling system - not taken into account in the experiments - which will induce the transition much earlier than it occurs for an uncooled nozzle. In conclusion, for this reason, using an HTC scaling procedure in fully-turbulent conditions remains valid to scale the HTC, obtained in test rig conditions, as standard practice, into a representative HTC in full speed and full load engine-like conditions, where typically there are no experimental measurements available.

6.3 Concluding remarks

In this chapter, a section of a Baker Hughes heavy-duty gas turbine comprising a single set of uncooled vanes, was analyzed through numerical simulations with the objective of assessing the heat transfer coefficient under engine-like conditions. Two different numerical models, RANS and SBES, were used to evaluate potential improvements in employing scale-resolved model with respect to the traditional RANS as per standard design practice. Inlet flow conditions to the first stage nozzles were set as time-averaged 2D maps for RANS, and time-varying 2D maps for SBES, as already discussed for the cooled vanes configuration. These conditions were derived from two different SBES calculations: the first one was conducted on the integrated geometry comprising the combustor and downstream stator while the other one was performed on the stand-alone combustor. From these analyses, it can concluded that, generally speaking, an overestimation of the HTC in the RANS simulation with respect to the companion SBES can be observed, especially on the LE e SS. However, despite the clear discrepancies especially in terms of absolute

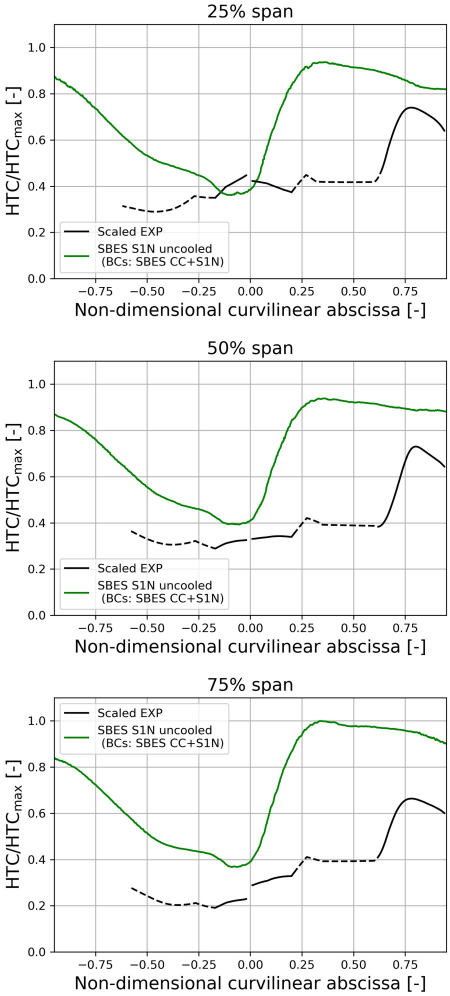

Figure 6.13: Heat Transfer Coefficient profiles at 25%, 50% and 75% of the span obtained by scaling the experimental data, obtained in lab-scaled conditions, to engine-like conditions. The results are then compared to the HTC obtained for the SBES uncooled (BCs: SBES CC+S1N) ***(©2024 Baker Hughes Company—All rights reserved)***.

values between the two modelling, it is important to point out that some similarities can be still noted in terms of distribution: at the LE, all the simulations indeed predict a minimum in HTC, even if the position of this area is delayed downstream along the PS for the RANS case. Regarding the different sets of inlet boundary conditions that were employed, it is noted that they have a limited impact in predicting the HTC on an uncooled vane.

Finally, the objective is to obtain a scaling criterion for the HTC obtained in lab-scaled conditions in order to obtain representative HTC values in engine-like conditions. In fact, when the engine operates in realistic conditions at full speed and full load, direct experimental measurements are not available and therefore the introduction of a scaling criterion becomes necessary. In particular, the scaling process is applied to the HTC obtained by performing numerical simulation in lab-scaled condition (SBES Integrated SST, see chapter 3) and the obtained results are then compared to the ones obtained by performing the CFD calculations under engine-like conditions above described. As a matter of fact, the simulations in lab-scaled conditions, reported in chapter 3, are conducted on the same engine, with the only difference being the S1N, that was previously redesigned in order to have the same count of nozzles and burners, thus a 1:1 ratio for the simulations in engine-like conditions (see chapters 4 and 5).

In order to carry out such scaling process, the HTC values obtained in lab-scaled conditions were scaled by extracting significant quantities in the prediction of heat exchange, such as the Reynolds number and the Prandtl number, only at the inlet and outlet of the stator, as average quantities. The application of such HTC scaling process, independently from the employed sets of inlet boundary conditions, leads to very close values compared to the SBES simulation runned under realistic operating conditions, keeping the relative error limited to the 20% at the 50% of the span. However, by applying the scaling process to the experimental data in the same way described above, much more marked differences are noted: these discrepancies can be attributed to the fact that, despite the

elevated levels of turbulence at the inlet, the experimental data show a strong impact of the BL transition on the airfoil. The transition with high free stream turbulence in fact, as seen in the chapter 3, remains a complex phenomenon to model. However, despite these differences, it is believed that the scaling process described above remains valid for two reasons: firstly, it is hypothesized that all the SBES CFD simulations, with the same setup, differ from the experimental data in a similar way, regardless of the fact that the calculations were conducted in lab-scaled or engine-like conditions; furthermore, given that the heat exchange is studied on the first high pressure nozzle, this nozzle will certainly be equipped with a complex cooling system - not taken into account in the experiments - which will induce the transition well much earlier than it occurs for an uncooled nozzle. In conclusion, for this reason, using an HTC scaling procedure in fully-turbulent conditions remains valid to scale the HTC, obtained in test rig conditions, as standard practice, into a representative HTC in full speed and full load engine-like conditions, where typically there are no experimental measurements available.

Conclusions

The present research focused on the numerical study of the combustor-turbine interaction in modern gas turbines. In fact, a complex and unsteady flow field, characterized by a high level of turbulence and temperature distortions, usually can be found at the interface plane between the two hot gas path components, especially with the implementation of lean-burn combustors that allow the reduction of NO_x emissions, but at the cost of requiring highly swirled and turbulent flows to stabilize the flame. Such severe conditions at the inlet of the first stage nozzle can have a potential impact on the performance of the component, resulting into a perturbation of the heat transfer, the aerodynamics and the effectiveness of the cooling system. For this reason, a better understanding of the physical processes related to the combustor-turbine interaction nozzle have aroused an ever-increasing interest in the recent years, becoming a mandatory step for a reliable the aerothermal design. The main objective of this work is to study the behaviour of film cooling system and the heat loads on the first stage nozzle in lab-scaled and engine-like conditions. To do so, the entire work was carried out by performing coupled and decoupled combustor-turbine RANS/SBES CFD simulations by using the commercial code ANSYS Fluent.

Firstly, an annular sector rig, made by a non-reactive, trisector combustor simulator and nozzle cascade, where both adiabatic effectiveness and HTC measurements had been carried out, was investigated by performing a systematic computational study by using RANS and SBES.

To do so, coupled and decoupled simulations were performed by using RANS and SBES modelling as well. Moreover, the comparison between numerical predictions and the available experimental results was exploited to:

- assess the capability of advanced scale-resolving methods in the characterization of the mutual combustor-turbine interaction, along with the heat transfer coefficient and film cooling system behavior;
- assess if such more advanced and more time-consuming methods than RANS, including also turbulence models able to capture the transition, can be more reliably used for a proper prediction of the vane thermal loads.

The results demonstrated that:

- the employment of the SBES modelling leads to a further improvement in results compared to RANS cases, both by employing uncooled or cooled vanes to predict HTC or adiabatic effectiveness, respectively. As a matter of fact, the results demonstrated a good agreements with the experiments in both cases, especially on LE of the stator. This is especially true, when predicting HTC, by using SBES jointly with a turbulence model able to capture the transition phenomena, even if these ones remain complex to be modelled.

Then, to highlight the risks and uncertainties associated with carrying out decoupled simulations, scale-resolving simulations (SBES) were performed to guarantee an accurate resolution of most of the flow structures while keeping the computational cost low. Firstly, a fully integrated combustor-nozzle setup, including a realistic turbine nozzle cooling system was investigated under realistic operating conditions. The results were then compared with those coming from a SBES decoupled simulation of the first stage nozzle alone. In this case, the prescribed time-varying inlet boundary conditions were extracted from a SBES of the stand-alone combustor. Moreover, in order to assess the discrepancies between different CFD approaches, the results coming from the correspondent preliminary

RANS NGV simulation were here also included, by imposing as inlet boundary conditions two-dimensional maps from the time-averaged solution of the precursor SBES of the stand-alone combustor. In this way, the work focused on the comparison and the analysis of numerical SBES simulations of an integrated combustor-NGV configuration and isolated NGV RANS and SBES simulations to assess the impact of the presence of the combustor under realistic operating conditions and realistic annular geometry. The results of these analyses demonstrated that:

- the presence of the combustion chamber does have a not negligible impact on the film cooling system behaviour due to the non-negligible blockage effect of the NGV on the combustor velocity field, even by employing advanced CFD approaches to study the NGV in a decoupled way.

This study was then developed applying two-dimensional unsteady boundary conditions extracted from the fully integrated combustor-NGV SBES simulation, in order to better identify the differences when using boundary conditions coming from a SBES decoupled simulation of the stand-alone combustor. Additionally, the POD technique was applied, considering three different numbers of POD modes, corresponding to a descending level of energy content relative to the total energy of the flow. The results of these analyses demonstrated that:

- this type of post-processing technique can be successfully used in order to identify the proper coherent structures of turbulent flows and to reduce the complexity of the dynamics of a system, just taking into account the most important modes;

- this way of proceeding, by taking into account the mutual interaction between combustor and turbine, leads to the generation and application of highly representative and reliable boundary conditions at the inlet of the first-stage nozzle to perform decoupled simulations.

Finally, the work focused on the prediction of heat loads in engine-like conditions by simulating a single set of uncooled vanes, similarly to what

was done in lab-scaled conditions. To do so, two different numerical models, RANS and SBES, were used to evaluate potential improvements in employing scale-resolved model with respect to the traditional RANS as per standard design practice. The main objective of these analyses is to obtain a scaling criterion for the HTC obtained in lab-scaled conditions in order to obtain representative HTC values in engine-like conditions. In fact, when the engine operates in realistic conditions at full speed and full load, direct experimental measurements are not available and therefore the introduction of a scaling criterion becomes necessary. It was then demonstrated that:

- the application of such HTC scaling process leads to very satisfactory results, even if the boundary layer transition remains complex to be modelled.

Future numerical analyses on this topic could include a sensitivity analysis on the parameters that characterize the Transition SST model when coupled with SBES. As a matter of fact, the results are supposed to improve further if particular attention is paid in employing such turbulence models by improving their application also to SBES calculations.

In conclusion, the present study demonstrates the importance of accurately capture the mutual combustor-turbine interaction, by employing advanced scale-resolving methods such as SBES calculations, for a reliable aerothermal design of the first stage nozzle also under representative and realistic engine-like operating conditions. To the author's knowledge, a very limited number of studies have been carried out with this kind of EXP-CFD benchmarking, due to the very limited amount of experimental data under representative combustor outflow conditions. In this context, to author's knowledge, this research represents also one of the few study present in literature in studying the impact of the combustor-turbine interaction phenomena on the aerodynamics and thermal fields, including a realistic turbine nozzle cooling system, with realistic inlet conditions representative of the engine marching at full speed and full load.

List of Figures

List of Tables

Bibliography

[1] Frank Whittle inventor of the jet engine. https://www.solarnavigator.net/inventors/frank_whittle.htm. (Accessed on 11/01/2023).

[2] Tang, K., Rao, A.G., and van Buijtenen, J.P. "Conceptual Study of a Hybrid Turbofan Engine With Inter Turbine Burner." Volume 1: Aircraft Engine; Ceramics; Coal, Biomass and Alternative Fuels; Education; Electric Power; Manufacturing Materials and Metallurgy: 239–248, 06 2010. doi: 10.1115/GT2010-22719. URL https://doi.org/10.1115/GT2010-22719.

[3] Ballal, D.R. and Zelina, J. "Progress in aeroengine technology (1939–2003)." *Journal of aircraft*, 41(1):43–50, 2004.

[4] Airbus, SAS. "Global Market Forecast: Growing Horizons 2017/2036." *Art & Caractere, April (4)*, pages 1–127, 2017.

[5] Kallas, S., Geoghegan-Quinn, M., Darecki, M., Edelstenne, C., Enders, T., Fernandez, E., and Hartman, P. "Flightpath 2050 europe's vision for aviation." *Report of the high level group on aviation research, European commission, Brussels, Belgium, Report No. EUR*, 98, 2011.

[6] Rao, A.G. and Bhat, A. "Hybrid combustion system for future aero engines." pages 1–9, 2015.

[7] European energy agency. greening the power sector: benefits of an ambitious implementation of europe's environment and climate policies. https://www.eea.europa.eu/themes/industry/industrial-pollution-in-europe/benefits-of-an-ambitious-implementation.htm. (Accessed on 11/01/2023).

[8] Lefebvre, A.H. and Ballal, D.R. *Gas turbine combustion: alternative fuels and emissions*. CRC press, 2010.

[9] Liu, Y., Sun, X., Sethi, V., Nalianda, D., Li, Y.G., and Wang, L. "Review of modern low emissions combustion technologies for aero gas turbine engines." *Progress in Aerospace Sciences*, 94:12–45, 2017. ISSN 0376-0421. doi: https://doi.org/10.1016/j.paerosci.2017.08.001. URL https://www.sciencedirect.com/science/article/pii/S037604211630118X.

[10] Cubeda, S. "Impacts of gas-turbine combustors outlet flow on the aero-thermal performance of film-cooled first stage nozzles." 2020.

[11] Bacci, T. "Experimental investigation on a high pressure NGV cascade in the presence of a representative lean burn aero-engine combustor outflow." 2018.

[12] Innocenti, A. "Numerical analysis of the dynamic response of practical gaseous and liquid fuelled flames for heavy-duty and aero-engine gas turbines." 2016.

[13] Talpallikar, M.V., Smith, C.E., Lai, M.C., and Holdeman, J.D. "CFD Analysis of Jet Mixing in Low NOx Flametube Combustors." *Journal of Engineering for Gas Turbines and Power*, 114(2):416–424, 04 1992. ISSN 0742-4795. doi: 10.1115/1.2906607. URL https://doi.org/10.1115/1.2906607.

[14] Micklow, G.J., Roychoudhury, S., Nguyen, H.L., and Cline, M.C. "Emissions Reduction by Varying the Swirler Airflow Split in Advanced Gas Turbine Combustors." *Journal of Engineering for Gas*

Turbines and Power, 115(3):563–569, 07 1993. ISSN 0742-4795. doi: 10.1115/1.2906744. URL `https://doi.org/10.1115/1.2906744`.

[15] Giusti, A., Andreini, A., Facchini, B., Vitale, I., and Turrini, F. *Thermoacoustic Analysis of a Full Annular Aero-engine Lean Combustor with Multi-perforated Liners*. doi: 10.2514/6.2013-2099. URL `https://arc.aiaa.org/doi/abs/10.2514/6.2013-2099`.

[16] Ford, C.L., Carrotte, J.F., and Walker, A.D. "The impact of compressor exit conditions on fuel injector flows." 2012.

[17] Hilt, M.B. and Waslo, J. "Evolution of NOx Abatement Techniques Through Combustor Design for Heavy-Duty Gas Turbines." *Journal of Engineering for Gas Turbines and Power*, 106(4):825–832, 10 1984. ISSN 0742-4795. doi: 10.1115/1.3239646. URL `https://doi.org/10.1115/1.3239646`.

[18] McKnight, D. "Development of a Compact Gas Turbine Combuster to Give Extended Life and Acceptable Exhaust Emissions." *Journal of Engineering for Power*, 101(3):349–357, 07 1979. ISSN 0022-0825. doi: 10.1115/1.3446583. URL `https://doi.org/10.1115/1.3446583`.

[19] Meher-Homji, C.B., Matthews, T., Pelagotti, A., and Weyermann, H.P. "Gas Turbines And Turbocompressors For LNG Service." 2007.

[20] Poeschl, G., Ruhkamp, W., and Pfost, H. "Combustion With Low Pollutant Emissions of Liquid Fuels in Gas Turbines by Premixing and Prevaporization." Volume 3: Coal, Biomass and Alternative Fuels; Combustion and Fuels; Oil and Gas Applications; Cycle Innovations:V003T06A044, 06 1994. doi: 10.1115/94-GT-443. URL `https://doi.org/10.1115/94-GT-443`.

[21] Huang, Y. and Yang, V. "Dynamics and stability of lean-premixed swirl-stabilized combustion." *Progress in Energy and Combustion*

Science, 35(4):293–364, 2009. ISSN 0360-1285. doi: https://doi.org/10.1016/j.pecs.2009.01.002. URL https://www.sciencedirect.com/science/article/pii/S0360128509000094.

[22] Andreini, A., Facchini, B., Becchi, R., Picchi, A., and Turrini, F. "Effect of Slot Injection and Effusion Array on the Liner Heat Transfer Coefficient of a Scaled Lean-Burn Combustor With Representative Swirling Flow." *Journal of Engineering for Gas Turbines and Power*, 138(4), 10 2015. ISSN 0742-4795. doi: 10.1115/1.4031434. URL https://doi.org/10.1115/1.4031434. 041501.

[23] Andreini, A., Becchi, R., Facchini, B., Mazzei, L., Picchi, A., and Turrini, F. "Adiabatic Effectiveness and Flow Field Measurements in a Realistic Effusion Cooled Lean Burn Combustor." *Journal of Engineering for Gas Turbines and Power*, 138(3), 09 2015. ISSN 0742-4795. doi: 10.1115/1.4031309. URL https://doi.org/10.1115/1.4031309. 031506.

[24] Andreini, A., Becchi, R., Facchini, B., Mazzei, L., Picchi, A., and Peschiulli, A. "Effusion Cooling System Optimization for Modern Lean Burn Combustor." Volume 5B: Heat Transfer, 06 2016. doi: 10.1115/GT2016-57721. URL https://doi.org/10.1115/GT2016-57721. V05BT17A015.

[25] Berrino, M., Satta, F., Ubaldi, M., Zunino, P., Colantuoni, S., and Di Martino, P. "Experimental Characterization of the Flow-Field Downstream of an Innovative Ultra Low NOx Injection System." Volume 4A: Combustion, Fuels and Emissions, 06 2014. doi: 10.1115/GT2014-25459. URL https://doi.org/10.1115/GT2014-25459. V04AT04A031.

[26] Berrino, M., Lengani, D., Satta, F., Ubaldi, M., Zunino, P., Colantuoni, S., and Di Martino, P. "Investigation of the Dynamics of an Ultra Low NOx Injection System by POD Data Post-Processing." Volume 4A: Combustion, Fuels and Emissions, 06 2015. doi: 10.1115/

GT2015-42638. URL https://doi.org/10.1115/GT2015-42638. V04AT04A049.

[27] WANG, SHANWU, YANG, VIGOR, HSIAO, GEORGE, HSIEH, SHIH-YANG, and MONGIA, HUKAM C. "Large-eddy simulations of gas-turbine swirl injector flow dynamics." *Journal of Fluid Mechanics*, 583:99–122, 2007. doi: 10.1017/S0022112007006155.

[28] Roux, S., Lartigue, G., Poinsot, T., Meier, U., and Bérat, C. "Studies of mean and unsteady flow in a swirled combustor using experiments, acoustic analysis, and large eddy simulations." *Combustion and Flame*, 141(1):40–54, 2005. ISSN 0010-2180. doi: https://doi.org/10.1016/j.combustflame.2004.12.007. URL https://www.sciencedirect.com/science/article/pii/S0010218005000039.

[29] Selle, L., Lartigue, G., Poinsot, T., Koch, R., Schildmacher, K.-U., Krebs, W., Prade, B., Kaufmann, P., and Veynante, D. "Compressible large eddy simulation of turbulent combustion in complex geometry on unstructured meshes." *Combustion and Flame*, 137(4): 489–505, 2004. ISSN 0010-2180. doi: https://doi.org/10.1016/j.combustflame.2004.03.008. URL https://www.sciencedirect.com/science/article/pii/S0010218004000768.

[30] Kern, M., Marinov, S., Habisreuther, P., Zarzalis, N., Peschiulli, A., and Turrini, F. "Characteristics of an Ultra-Lean Swirl Combustor Flow by LES and Comparison to Measurements." Volume 2: Combustion, Fuels and Emissions, Parts A and B:321–330, 06 2011. doi: 10.1115/GT2011-45300. URL https://doi.org/10.1115/GT2011-45300.

[31] Marinov, S., Kern, M., Merkle, K., Zarzalis, N., Peschiulli, A., Turrini, F., and Sara, O.N. "On Swirl Stabilized Flame Characteristics Near the Weak Extinction Limit." Volume 2: Combustion, Fuels and Emissions, Parts A and B:259–268, 06 2010. doi: 10.1115/GT2010-22335. URL https://doi.org/10.1115/GT2010-22335.

[32] Hall, B.F., Chana, K.S., and Povey, T. "Design of a Non-Reacting Combustor Simulator With Swirl and Temperature Distortion With Experimental Validation." Volume 3C: Heat Transfer, 06 2013. doi: 10.1115/GT2013-95499. URL https://doi.org/10.1115/GT2013-95499. V03CT17A010.

[33] Zhou, S., Guo, P., and Stolle, D.F.E. "Interaction Model for "Shelled Particles" and Small-Strain Modulus of Granular Materials." *Journal of Applied Mechanics*, 85(10), 06 2018. ISSN 0021-8936. doi: 10.1115/1.4040408. URL https://doi.org/10.1115/1.4040408. 101001.

[34] Cha, C.M., Hong, S., Ireland, P.T., Denman, P., and Savarianandam, V. "Experimental and Numerical Investigation of Combustor-Turbine Interaction Using an Isothermal, Nonreacting Tracer." *Journal of Engineering for Gas Turbines and Power*, 134 (8), 06 2012. ISSN 0742-4795. doi: 10.1115/1.4005815. URL https://doi.org/10.1115/1.4005815. 081501.

[35] Cha, C.M., Ireland, P.T., Denman, P.A., and Savarianandam, V. "Turbulence Levels are High at the Combustor-Turbine Interface." Volume 8: Turbomachinery, Parts A, B, and C:1371–1390, 06 2012. doi: 10.1115/GT2012-69130. URL https://doi.org/10.1115/GT2012-69130.

[36] Hall, B.F., Chana, K.S., and Povey, T. "Design of a Nonreacting Combustor Simulator With Swirl and Temperature Distortion With Experimental Validation." *Journal of Engineering for Gas Turbines and Power*, 136(8), 02 2014. ISSN 0742-4795. doi: 10.1115/1.4026809. URL https://doi.org/10.1115/1.4026809. 081501.

[37] Shi, L., Huang, H., Lu, Y., Xu, S., and Ge, C. "The Combined Influences of Hot Streak and Swirl on the Cooling Performances of C3X Guide Vane with or without TBCs." *Coatings*, 11(6), 2021. ISSN 2079-6412. doi: 10.3390/coatings11060688. URL https://www.mdpi.com/2079-6412/11/6/688.

[38] Mansouri, Z. and Belamadi, R. "The influence of inlet swirl intensity and hot-streak on aerodynamics and thermal characteristics of a high pressure turbine vane." *Chinese Journal of Aeronautics*, 34 (11):66–78, 2021. ISSN 1000-9361. doi: https://doi.org/10.1016/j.cja.2020.12.036. URL https://www.sciencedirect.com/science/article/pii/S100093612030604X.

[39] Povey, T. and Qureshi, I. "Developments in Hot-Streak Simulators for Turbine Testing." *Journal of Turbomachinery*, 131(3), 04 2009. ISSN 0889-504X. doi: 10.1115/1.2987240. URL https://doi.org/10.1115/1.2987240. 031009.

[40] Qureshi, I., Beretta, A., and Povey, T. "Effect of Simulated Combustor Temperature Nonuniformity on HP Vane and End Wall Heat Transfer: An Experimental and Computational Investigation." *Journal of Engineering for Gas Turbines and Power*, 133 (3), 11 2010. ISSN 0742-4795. doi: 10.1115/1.4002039. URL https://doi.org/10.1115/1.4002039. 031901.

[41] Insinna, M., Griffini, D., Salvadori, S., and Martelli, F. "Conjugate Heat Transfer Analysis of a Film Cooled High-Pressure Turbine Vane Under Realistic Combustor Exit Flow Conditions." Volume 5A: Heat Transfer:V05AT11A007, 06 2014. doi: 10.1115/GT2014-25280. URL https://doi.org/10.1115/GT2014-25280.

[42] Andreini, A., Bacci, T., Insinna, M., Mazzei, L., and Salvadori, S. "Modelling strategies for the prediction of hot streak generation in lean burn aeroengine combustors." *Aerospace Science and Technology*, 79:266–277, 2018. ISSN 1270-9638. doi: https://doi.org/10.1016/j.ast.2018.05.030. URL https://www.sciencedirect.com/science/article/pii/S1270963817319399.

[43] Shih, T. I-P. and Lin, Y.-L. "Controlling Secondary-Flow Structure by Leading-Edge Airfoil Fillet and Inlet Swirl to Reduce Aerodynamic Loss and Surface Heat Transfer ." *Journal of Turbomachinery*,

125(1):48–56, 01 2003. ISSN 0889-504X. doi: 10.1115/1.1518503. URL https://doi.org/10.1115/1.1518503.

[44] Lin, Y.-L., Schock, H.J., Shih, T.I-P., and Bunker, R.S. "Effects of Inlet Swirl Angle on Flow and Heat Transfer in Contoured Turbine Nozzle Guide Vanes." Heat Transfer: Volume 5 — Computational, Aerospace and Environmental Heat Transfer: 279–288, 11 2001. doi: 10.1115/IMECE2001/HTD-24312. URL https://doi.org/10.1115/IMECE2001/HTD-24312.

[45] Koupper, C. *Unsteady multi-component simulations dedicated to the impact of the combustion chamber on the turbine of aeronautical gas turbines*. PhD thesis, 2015.

[46] Khanal, B., He, L., Northall, J., and Adami, P. "Analysis of Radial Migration of Hot-Streak in Swirling Flow Through High-Pressure Turbine Stage." *Journal of Turbomachinery*, 135(4), 06 2013. ISSN 0889-504X. doi: 10.1115/1.4007505. URL https://doi.org/10.1115/1.4007505. 041005.

[47] Barringer, M.D., Polanka, M.D., and Thole, K.A. "An Experimental Study of Combustor Exit Profile Shapes on Endwall Heat Transfer in High Pressure Turbine Vanes." Volume 4: Turbo Expo 2007, Parts A and B:1323–1334, 05 2007. doi: 10.1115/GT2007-27156. URL https://doi.org/10.1115/GT2007-27156.

[48] Colban, W.F., Lethander, A.T., Thole, K.A., and Zess, G. "Combustor Turbine Interface Studies—Part 2: Flow and Thermal Field Measurements." *Journal of Turbomachinery*, 125(2):203–209, 04 2003. ISSN 0889-504X. doi: 10.1115/1.1561812. URL https://doi.org/10.1115/1.1561812.

[49] Radomsky, R.W. and Thole, K.A. "Flowfield Measurements for a Highly Turbulent Flow in a Stator Vane Passage ." *Journal of Turbomachinery*, 122(2):255–262, 02 1999. ISSN 0889-504X. doi: 10.1115/1.555442. URL https://doi.org/10.1115/1.555442.

[50] Ligrani, P. "Aerodynamic losses in turbines with and without film cooling, as influenced by mainstream turbulence, surface roughness, airfoil shape, and mach number." *International Journal of Rotating Machinery*, 2012, 2012.

[51] Denton, J.D. "Loss Mechanisms in Turbomachines." Volume 2: Combustion and Fuels; Oil and Gas Applications; Cycle Innovations; Heat Transfer; Electric Power; Industrial and Cogeneration; Ceramics; Structures and Dynamics; Controls, Diagnostics and Instrumentation; IGTI Scholar Award, 05 1993. doi: 10.1115/93-GT-435. URL `https://doi.org/10.1115/93-GT-435`. V002T14A001.

[52] Dixon, S.L. and Hall, C. *Fluid mechanics and thermodynamics of turbomachinery*. Butterworth-Heinemann, 2013.

[53] Bindon, J.P. "The Measurement and Formation of Tip Clearance Loss." *Journal of Turbomachinery*, 111(3):257–263, 07 1989. ISSN 0889-504X. doi: 10.1115/1.3262264. URL `https://doi.org/10.1115/1.3262264`.

[54] Lakshminarayana, B. and Horlock, J.H. "Review: Secondary flows and losses in cascades and axial-flow turbomachines." *International Journal of Mechanical Sciences*, 5(3): 287–307, 1963. ISSN 0020-7403. doi: https://doi.org/10.1016/0020-7403(63)90055-9. URL `https://www.sciencedirect.com/science/article/pii/0020740363900559`.

[55] Langston, L.S. "Secondary flows in axial turbines—a review." *Annals of the New York Academy of Sciences*, 934(1):11–26, 2001.

[56] Qureshi, I., Smith, A.D., and Povey, T. "HP Vane Aerodynamics and Heat Transfer in the Presence of Aggressive Inlet Swirl." *Journal of Turbomachinery*, 135(2), 11 2012. ISSN 0889-504X. doi: 10.1115/1.4006610. URL `https://doi.org/10.1115/1.4006610`. 021040.

[57] Langston, L.S. "Crossflows in a Turbine Cascade Passage." *Journal of Engineering for Power*, 102(4):866–874, 10 1980. ISSN 0022-

0825. doi: 10.1115/1.3230352. URL https://doi.org/10.1115/1.3230352.

[58] Sharma, O.P. and Butler, T.L. "Predictions of Endwall Losses and Secondary Flows in Axial Flow Turbine Cascades." *Journal of Turbomachinery*, 109(2):229–236, 04 1987. ISSN 0889-504X. doi: 10.1115/1.3262089. URL https://doi.org/10.1115/1.3262089.

[59] Ekkad, S.V. and Han, J.C. "A transient liquid crystal thermography technique for gas turbine heat transfer measurements." *Measurement Science and Technology*, 11(7):957, 2000.

[60] L'Ecuyer, M.R. and Soechting, F.O. "A model for correlating flat plate film cooling effectiveness for rows of round holes." *AGARD Heat Transfer and Cooling in Gas Turbines 12p (SEE N86-29823 21-07)*, 1985.

[61] Pedersen, D.R., Eckert, E.R.G., and Goldstein, R.J. "Film Cooling With Large Density Differences Between the Mainstream and the Secondary Fluid Measured by the Heat-Mass Transfer Analogy." *Journal of Heat Transfer*, 99(4):620–627, 11 1977. ISSN 0022-1481. doi: 10.1115/1.3450752. URL https://doi.org/10.1115/1.3450752.

[62] Eckert, V.L. E.R.G .and Eriksen, Goldstein, R.J., and Ramsey, J.W. Film cooling following injection through inclined circular tubes. Technical report, 1969.

[63] Baldauf, S., Scheurlen, M., Schulz, A., and Wittig, S. "Correlation of Film Cooling Effectiveness From Thermographic Measurements at Engine Like Conditions." Volume 3: Turbo Expo 2002, Parts A and B:149–162, 06 2002. doi: 10.1115/GT2002-30180. URL https://doi.org/10.1115/GT2002-30180.

[64] Jose, N., Jayakumar, J.S., and Yepuri, G.B. "Numerical Investigation of Adiabatic Film Cooling Effectiveness over a Flat Plate

Model with Cylindrical Holes." *Procedia Engineering*, 127:398–404, 2015. ISSN 1877-7058. doi: https://doi.org/10.1016/j.proeng.2015.11.387. URL https://www.sciencedirect.com/science/article/pii/S1877705815037479. INTERNATIONAL CONFERENCE ON COMPUTATIONAL HEAT AND MASS TRANSFER (ICCHMT) - 2015.

[65] Bons, J.P., MacArthur, C.D., and Rivir, R.B. "The Effect of High Free-Stream Turbulence on Film Cooling Effectiveness." *Journal of Turbomachinery*, 118(4):814–825, 10 1996. ISSN 0889-504X. doi: 10.1115/1.2840939. URL https://doi.org/10.1115/1.2840939.

[66] Schmidt, D.L. and Bogard, D.G. "Effects of Free-Stream Turbulence and Surface Roughness on Film Cooling." Volume 4: Heat Transfer; Electric Power; Industrial and Cogeneration, 06 1996. doi: 10.1115/96-GT-462. URL https://doi.org/10.1115/96-GT-462. V004T09A049.

[67] Ito, S., Goldstein, R.J., and Eckert, E.R.G. "Film Cooling of a Gas Turbine Blade." *Journal of Engineering for Power*, 100(3):476–481, 07 1978. ISSN 0022-0825. doi: 10.1115/1.3446382. URL https://doi.org/10.1115/1.3446382.

[68] Schwarz, S.G. and Goldstein, R.J. "The Two-Dimensional Behavior of Film Cooling Jets on Concave Surfaces." *Journal of Turbomachinery*, 111(2):124–130, 04 1989. ISSN 0889-504X. doi: 10.1115/1.3262246. URL https://doi.org/10.1115/1.3262246.

[69] Han, J.-C., Dutta, S., and Ekkad, S. *Gas turbine heat transfer and cooling technology*. CRC press, 2012.

[70] ZXingdan, Z., Jingzhou, Z., and Xiaoming, T. "An Experimental Investigation of Showerhead Film Cooling Performance on a Turbine Blade." *Procedia Engineering*, 99:634–645, 2015. ISSN 1877-7058. doi: https://doi.org/10.1016/j.proeng.2014.12.583. URL https://www.sciencedirect.com/science/article/

pii/S1877705814036972. 2014 Asia-Pacific International Symposium on Aerospace Technology, APISAT2014 September 24-26, 2014 Shanghai, China.

[71] Fric, T.F. and Roshko, A. "Vortical structure in the wake of a transverse jet." *Journal of Fluid Mechanics*, 279:1–47, 1994.

[72] Andreopoulos, J. "On the structure of jets in a crossflow." *Journal of Fluid Mechanics*, 157:163–197, 1985.

[73] Walters, D.K. and Leylek, J.H. "A Detailed Analysis of Film-Cooling Physics: Part I—Streamwise Injection With Cylindrical Holes." *Journal of Turbomachinery*, 122(1):102–112, 02 1997. ISSN 0889-504X. doi: 10.1115/1.555433. URL https://doi.org/10.1115/1.555433.

[74] Dyson, T.E., Helmer, D.B., and Tallman, J.A. "Large-Scale Simulation of the Clocking Impact of 2D Combustor Profile on a Two Stage High Pressure Turbine." Volume 5B: Heat Transfer, 06 2014. doi: 10.1115/GT2014-25883. URL https://doi.org/10.1115/GT2014-25883. V05BT14A008.

[75] Roux, S., Cazalens, M., and Poinsot, T. "Outlet-boundary-condition influence for large eddy simulation of combustion instabilities in gas turbines." *Journal of Propulsion and Power*, 24(3):541–546, 2008.

[76] Klapdor, E.V. "Simulation of combustor-turbine interaction in a jet engine." 2011.

[77] Morata, E.C. *Impact of the unsteady aerothermal environment on the turbine blades temperature*. PhD thesis, Institut National Polytechnique de Toulouse-INPT, 2012.

[78] Werschnik, H., Hilgert, J., Wilhelm, M., Bruschewski, M., and Schiffer, H.-P. "Influence of Combustor Swirl on Endwall Heat Transfer and Film Cooling Effectiveness at the Large Scale Turbine Rig." *Journal of Turbomachinery*, 139(8):081007, 03 2017. ISSN

0889-504X. doi: 10.1115/1.4035832. URL https://doi.org/10.1115/1.4035832.

[79] Jacobi, S., Mazzoni, C., Rosic, B., and Chana, K. "Investigation of Unsteady Flow Phenomena in First Vane Caused by Combustor Flow With Swirl." *Journal of Turbomachinery*, 139(4):041006, 01 2017. ISSN 0889-504X. doi: 10.1115/1.4035073. URL https://doi.org/10.1115/1.4035073.

[80] Zhang, W., Wang, Z., Wang, Z., Li, R., and Feng, Z. "Study on heat transfer characteristics of NGVs influenced by non-reacting lean burn combustor simulator flow." *International Journal of Thermal Sciences*, 172:107313, 2022. ISSN 1290-0729. doi: https://doi.org/10.1016/j.ijthermalsci.2021.107313. URL https://www.sciencedirect.com/science/article/pii/S1290072921004725.

[81] Mansouri, Z. "Numerical prediction of heat transfer characteristics on a turbine nozzle guide vane under various combustor exit hot-streaks." *Heat Transfer*, 51(1):976–997, 2022. doi: https://doi.org/10.1002/htj.22338. URL https://onlinelibrary.wiley.com/doi/abs/10.1002/htj.22338.

[82] Koupper, C., Bonneau, G., Gicquel, L., and Duchaine, F. "Large Eddy Simulations of the Combustor Turbine Interface: Study of the Potential and Clocking Effects." Volume 5B: Heat Transfer, 06 2016. doi: 10.1115/GT2016-56443. URL https://doi.org/10.1115/GT2016-56443. V05BT17A003.

[83] Phan, H.M., Duan, P.H., and Dinh, C.T. "Numerical aero-thermal study of high-pressure turbine nozzle guide vane: Effects of inflow conditions." *Physics of Fluids*, 32(3):034111, 03 2020. ISSN 1070-6631. doi: 10.1063/1.5144418. URL https://doi.org/10.1063/1.5144418.

[84] Barringer, M.D., Thole, K.A., and Polanka, M.D. "Effects of Combustor Exit Profiles on Vane Aerodynamic Loading and Heat Trans-

fer in a High Pressure Turbine." *Journal of Turbomachinery*, 131 (2), 01 2009. ISSN 0889-504X. doi: 10.1115/1.2950051. URL https://doi.org/10.1115/1.2950051. 021008.

[85] Nasir, S., Carullo, J.S., Ng, W.F., Thole, K.A., Wu, H., Zhang, L.J., and Moon, H.K. "Effects of Large Scale High Freestream Turbulence and Exit Reynolds Number on Turbine Vane Heat Transfer in a Transonic Cascade." *Journal of Turbomachinery*, 131(2), 02 2009. ISSN 0889-504X. doi: 10.1115/1.2952381. URL https://doi.org/10.1115/1.2952381. 021021.

[86] Bacci, T., Picchi, A., Lenzi, T., Facchini, B., and Innocenti, L. "Effect of Surface Roughness and Inlet Turbulence Intensity on a Turbine Nozzle Guide Vane External Heat Transfer: Experimental Investigation on a Literature Test Case." Volume 7C: Heat Transfer: V07CT13A011, 09 2020. doi: 10.1115/GT2020-14622. URL https://doi.org/10.1115/GT2020-14622.

[87] Kanani, Y., Acharya, S., and Ames, F. "Large Eddy Simulation of the Laminar Heat Transfer Augmentation on the Pressure Side of a Turbine Vane Under Freestream Turbulence." *Journal of Turbomachinery*, 141(4):041004, 01 2019. ISSN 0889-504X. doi: 10.1115/1.4041599. URL https://doi.org/10.1115/1.4041599.

[88] Jenkins, S., Varadarajan, K., and Bogard, D.G. "The Effects of High Mainstream Turbulence and Turbine Vane Film Cooling on the Dispersion of a Simulated Hot Streak ." *Journal of Turbomachinery*, 126(1):203–211, 03 2004. ISSN 0889-504X. doi: 10.1115/1.1643911. URL https://doi.org/10.1115/1.1643911.

[89] Jenkins, S.C. and Bogard, D.G. "Superposition Predictions of the Reduction of Hot Streaks by Coolant From a Film-Cooled Guide Vane." *Journal of Turbomachinery*, 131(4), 06 2009. ISSN 0889-504X. doi: 10.1115/1.2948964. URL https://doi.org/10.1115/1.2948964. 041002.

[90] Martin, D. and Thorpe, S.J. "Experiments on Combustor Effusion Cooling Under Conditions of Very High Free-Stream Turbulence." Volume 4: Heat Transfer, Parts A and B:1001–1013, 06 2012. doi: 10.1115/GT2012-68863. URL https://doi.org/10.1115/GT2012-68863.

[91] Salvadori, S., Riccio, G., Insinna, M., and Martelli, F. "Analysis of Combustor/Vane Interaction With Decoupled and Loosely Coupled Approaches." Volume 8: Turbomachinery, Parts A, B, and C: 2641–2652, 06 2012. doi: 10.1115/GT2012-69038. URL https://doi.org/10.1115/GT2012-69038.

[92] James, S., Zhu, J., and Anand, M.S. "Large-eddy simulations as a design tool for gas turbine combustion systems." *AIAA journal*, 44 (4):674–686, 2006.

[93] Boudier, G., Gicquel, L.Y.M., Poinsot, T., Bissières, D., and Bérat, C. "Comparison of LES, RANS and experiments in an aeronautical gas turbine combustion chamber." *Proceedings of the Combustion Institute*, 31(2):3075–3082, 2007. ISSN 1540-7489. doi: https://doi.org/10.1016/j.proci.2006.07.067. URL https://www.sciencedirect.com/science/article/pii/S1540748906000824.

[94] Thomas, Ma., Duchaine, F., Gicquel, L., and Koupper, C. "Advanced Statistical Analysis Estimating the Heat Load Issued by Hot Streaks and Turbulence on a High-Pressure Vane in the Context of Adiabatic Large Eddy Simulations." Volume 2B: Turbomachinery, 06 2017. doi: 10.1115/GT2017-64648. URL https://doi.org/10.1115/GT2017-64648. V02BT41A041.

[95] Thomas, M., Dombard, J., Duchaine, F., Gicquel, L., and Koupper, C. "Large Eddy Simulation of Combustor and Complete Single-Stage High-Pressure Turbine of the FACTOR Test Rig." Volume 2A: Turbomachinery, 06 2019. doi: 10.1115/GT2019-91206. URL https://doi.org/10.1115/GT2019-91206. V02AT45A016.

[96] Pope, S.B. "Ten questions concerning the large-eddy simulation of turbulent flows." *New Journal of Physics*, 6(1):35, mar 2004. doi: 10.1088/1367-2630/6/1/035. URL https://dx.doi.org/10.1088/1367-2630/6/1/035.

[97] Gicquel, L.Y.M., Staffelbach, G., and Poinsot, T. "Large Eddy Simulations of gaseous flames in gas turbine combustion chambers." *Progress in Energy and Combustion Science*, 38(6):782–817, 2012. ISSN 0360-1285. doi: https://doi.org/10.1016/j.pecs.2012.04.004. URL https://www.sciencedirect.com/science/article/pii/S0360128512000366.

[98] Spalart, P.R. "Comments on the Feasibility of LES for Wings and on the Hybrid RANS/LES Approach." pages 137–147, 1997.

[99] Menter, F.R. and Egorov, Y. "Revisiting the turbulent scale equation." pages 279–290, 2006.

[100] Menter, F.R. and Egorov, Y. *A Scale Adaptive Simulation Model using Two-Equation Models*. doi: 10.2514/6.2005-1095. URL https://arc.aiaa.org/doi/abs/10.2514/6.2005-1095.

[101] Bacci, T., Lenzi, T., Picchi, A., Mazzei, L., and Facchini, B. "Flow Field and Hot Streak Migration Through High Pressure Cooled Vanes With Representative Lean Burn Combustor Outflow." Volume 5C: Heat Transfer, 06 2018. doi: 10.1115/GT2018-76728. URL https://doi.org/10.1115/GT2018-76728. V05CT17A009.

[102] Bacci, T., Becchi, R., Picchi, A., and Facchini, B. "Adiabatic Effectiveness on High-Pressure Turbine Nozzle Guide Vanes Under Realistic Swirling Conditions." *Journal of Turbomachinery*, 141 (1), 11 2018. ISSN 0889-504X. doi: 10.1115/1.4041559. URL https://doi.org/10.1115/1.4041559. 011009.

[103] Andreini, A., Bacci, T., Insinna, M., Mazzei, L., and Salvadori, S. "Hybrid RANS-LES Modeling of the Aerothermal Field in an Annular Hot Streak Generator for the Study of Combustor–Turbine

Interaction." *Journal of Engineering for Gas Turbines and Power*, 139(2), 09 2016. ISSN 0742-4795. doi: 10.1115/1.4034358. URL `https://doi.org/10.1115/1.4034358`. 021508.

[104] Cubeda, S., Mazzei, L., and Andreini, A. "External heat transfer on nozzle guide vanes under highly swirled combustor outlet flow." 2019.

[105] Menter, F.R. "Stress-blended eddy simulation (SBES)—A new paradigm in hybrid RANS-LES modeling." pages 27–37, 2018.

[106] Verma, I., Rida, S., Zori, L., Basani, J., Kamrath, B., and Brandt, D. "Modeling of Combustor-Turbine Vane Interaction Using Stress-Blended Eddy Simulation." Volume 2D: Turbomachinery — Multidisciplinary Design Approaches, Optimization, and Uncertainty Quantification; Radial Turbomachinery Aerodynamics; Unsteady Flows in Turbomachinery, 06 2021. doi: 10.1115/GT2021-59344. URL `https://doi.org/10.1115/GT2021-59344`. V02DT39A008.

[107] Duchaine, F., Dombard, J., Gicquel, L.Y.M., and Koupper, C. "On the importance of inlet boundary conditions for aerothermal predictions of turbine stages with large eddy simulation." *Computers & Fluids*, 154:60–73, 2017. ISSN 0045-7930. doi: https://doi.org/10.1016/j.compfluid.2017.05.024. URL `https://www.sciencedirect.com/science/article/pii/S0045793017302001`. ICCFD8.

[108] Martin, B., Duchaine, F., Gicquel, L., and Odier, N. "Generation of Realistic Boundary Conditions at the Combustion Chamber/Turbine Interface Using Large-Eddy Simulation." *Energies*, 14(24), 2021. ISSN 1996-1073. doi: 10.3390/en14248206. URL `https://www.mdpi.com/1996-1073/14/24/8206`.

[109] Martin, B., Duchaine, F., Gicquel, L., Odier, N., and Dombard, J. "Accurate Inlet Boundary Conditions to Capture Combustion Chamber and Turbine Coupling With Large-Eddy Simulation." *Journal of Engineering for Gas Turbines and Power*, 144

(2), 11 2021. ISSN 0742-4795. doi: 10.1115/1.4052099. URL https://doi.org/10.1115/1.4052099. 021007.

[110] Thomas, M. *Combustor-turbine interactions: Hot spot migration and thermal environment prediction for a better understanding and design of helicopter engines*. PhD thesis, 2021.

[111] Gründler, J., Schiffer, H.-P., and Lehmann, K. "An Efficient Unsteady 1-Way Coupling Method of Combustor and Turbine." Volume 10D: Turbomachinery — Multidisciplinary Design Approaches, Optimization, and Uncertainty Quantification; Turbomachinery General Interest; Unsteady Flows in Turbomachinery, 06 2022. doi: 10.1115/GT2022-78056. URL https://doi.org/10.1115/GT2022-78056. V10DT37A003.

[112] Gründler, J., Lehmann, K., and Schiffer, H.-P. "The Effect of Unsteady Inlet Boundary Conditions on the Aero-Thermal Behavior of High-Pressure Turbine Vanes: A Numerical Study Using Scale-Resolving Simulations." Volume 13D: Turbomachinery — Multidisciplinary Design Approaches, Optimization, and Uncertainty Quantification; Radial Turbomachinery Aerodynamics; Unsteady Flows in Turbomachinery:V13DT36A001, 06 2023. doi: 10.1115/GT2023-100884. URL https://doi.org/10.1115/GT2023-100884.

[113] Mendez, M.A., Balabane, M., and Buchlin, J.M. "Multi-scale Modal Analysis of Complex Fluid Flows." *preprint available in*, 2018.

[114] Mendez, M.A., Balabane, M., and Buchlin, J.M. "Multi-scale proper orthogonal decomposition of complex fluid flows." *Journal of Fluid Mechanics*, 870:988–1036, 2019.

[115] Lumley, J.L. *Stochastic tools in turbulence*. Courier Corporation, 2007.

[116] Sirovich, L. "Turbulence and the dynamics of coherent structures. I. Coherent structures." *Quarterly of applied mathematics*, 45(3): 561–571, 1987.

[117] Sirovich, L. "Chaotic dynamics of coherent structures." *Physica D: Nonlinear Phenomena*, 37(1-3):126–145, 1989.

[118] Bacci, T., Caciolli, G., Facchini, B., Tarchi, L., Koupper, C., and Champion, J.L. "Flowfield and Temperature Profiles Measurements on a Combustor Simulator Dedicated to Hot Streaks Generation." Volume 5C: Heat Transfer:V05CT17A001, 06 2015. doi: 10.1115/GT2015-42217. URL `https://doi.org/10.1115/GT2015-42217`.

[119] Cubeda, S., Bacci, T., Mazzei, L., Salvadori, S., Facchini, B., Fiorineschi, L., and Volpe, Y. "Design of a Non-Reactive Warm Rig With Real Lean-Premix Combustor Swirlers and Film-Cooled First Stage Nozzles." Volume 7A: Heat Transfer:V07AT11A001, 09 2020. doi: 10.1115/GT2020-14186. URL `https://doi.org/10.1115/GT2020-14186`.

[120] Bacci, T., Picchi, A., Facchini, B., and Cubeda, S. "A New Experimental Approach for Heat Transfer Coefficient and Adiabatic Wall Temperature Measurements on a Nozzle Guide Vane With Inlet Temperature Distortions." *Journal of Turbomachinery*, 144(3): 031007, 10 2021. ISSN 0889-504X. doi: 10.1115/1.4052407. URL `https://doi.org/10.1115/1.4052407`.

[121] Bacci, T., Picchi, A., Babazzi, G., Facchini, B., and Cubeda, S. "Heat Transfer Coefficient and Adiabatic Wall Temperature Measurements on High-Pressure Turbine Nozzle Guide Vanes With Representative Inlet Swirl and Temperature Distortions." *Journal of Turbomachinery*, 145(7):071010, 02 2023. ISSN 0889-504X. doi: 10.1115/1.4056713. URL `https://doi.org/10.1115/1.4056713`.

[122] Menter, F.R. "Best practice: scale-resolving simulations in ANSYS CFD." *ANSYS Germany GmbH*, 1:1–70, 2012.

[123] Menter, F.R. "Zonal two equation kw turbulence models for aerodynamic flows." page 2906, 1993.

[124] Griffini, D., Insinna, M., Salvadori, S., and Martelli, F. "Clocking Effects of Inlet Nonuniformities in a Fully Cooled High-Pressure Vane: A Conjugate Heat Transfer Analysis." *Journal of Turbomachinery*, 138(2):021006, 11 2015. ISSN 0889-504X. doi: 10.1115/1.4031864. URL https://doi.org/10.1115/1.4031864.

[125] Qureshi, I., Smith, Andy D., and Povey, T. "HP Vane Aerodynamics and Heat Transfer in the Presence of Aggressive Inlet Swirl." *Journal of Turbomachinery*, 135(2):021040, 11 2012. ISSN 0889-504X. doi: 10.1115/1.4006610. URL https://doi.org/10.1115/1.4006610.

[126] Shaikh, F. and Rosic, B. "Unsteady phenomena at the combustor-turbine interface." *Journal of the Global Power and Propulsion Society*, 5:202–215, 2021.

[127] Kays, W.M., Crawford, M.E., and Weigand, B. *Convective heat and mass transfer*, volume 4. McGraw-Hill New York, 1980.

[128] Kreith, F. and Bohn, M.S. "Principles of heat transfer, St." *Paul: West Publishing Company*, 1993.

[129] Cubeda, S., Mazzei, L., Bacci, T., and Andreini, A. "Impact of Predicted Combustor Outlet Conditions on the Aerothermal Performance of Film-Cooled High Pressure Turbine Vanes." *Journal of Engineering for Gas Turbines and Power*, 141(5):051011, 12 2018. ISSN 0742-4795. doi: 10.1115/1.4041038. URL https://doi.org/10.1115/1.4041038.

[130] Cerutti, M., Giannini, N., Ceccherini, G., Meloni, R., Matoni, E., Romano, C., and Riccio, G. "Dry Low NOx Emissions Operability Enhancement of a Heavy-Duty Gas Turbine by Means of Fuel Burner Design Development and Testing." Volume 4B: Combustion, Fuels, and Emissions, 06 2018. doi: 10.1115/GT2018-76587. URL https://doi.org/10.1115/GT2018-76587. V04BT04A029.

[131] Meloni, R., Nassini, P.C., and Andreini, A. "Model development for the simulation of the hydrogen addition effect onto the NOx emission

of an industrial combustor." *Fuel*, 328:125278, 2022. ISSN 0016-2361. doi: https://doi.org/10.1016/j.fuel.2022.125278. URL `https://www.sciencedirect.com/science/article/pii/S0016236122021135`.

[132] Pope, S.B. *Turbulent flows*. Cambridge university press, 2000.

[133] Zimont, V.L. and Lipatnikov, A.N. "A numerical model of premixed turbulent combustion of gases." *Chem. Phys. Reports*, 14(7):993–1025, 1995.

[134] Tay-Wo-Chong, L., Scarpato, A., and Polifke, W. "LES Combustion Model With Stretch and Heat Loss Effects for Prediction of Premix Flame Characteristics and Dynamics." Volume 4A: Combustion, Fuels and Emissions, 06 2017. doi: 10.1115/GT2017-63357. URL `https://doi.org/10.1115/GT2017-63357`. V04AT04A029.

[135] Romano, S., Meloni, R., Riccio, G., Nassini, P.C., and Andreini, A. "Modeling of Natural Gas Composition Effect on Low NOx Burners Operation in Heavy Duty Gas Turbine." *Journal of Engineering for Gas Turbines and Power*, 143(3), 02 2021. ISSN 0742-4795. doi: 10.1115/1.4049819. URL `https://doi.org/10.1115/1.4049819`. 031018.

[136] Meloni, R., Gori, S., Andreini, A., and Nassini, P. C. "CO Emission Modeling in a Heavy Duty Annular Combustor Operating With Natural Gas." *Journal of Engineering for Gas Turbines and Power*, 144(1), 10 2021. ISSN 0742-4795. doi: 10.1115/1.4052028. URL `https://doi.org/10.1115/1.4052028`. 011011.

[137] Meloni, R., Andreini, A., and Nassini, P.C. "A Novel LES-Based Process for NOx Emission Assessment in a Premixed Swirl Stabilized Combustion System." Volume 3A: Combustion, Fuels, and Emissions, 06 2021. doi: 10.1115/GT2021-59215. URL `https://doi.org/10.1115/GT2021-59215`. V03AT04A046.

[138] Nassini, P.C., Pampaloni, D., Meloni, R., and Andreini, A. "Lean blow-out prediction in an industrial gas turbine combustor through a

LES-based CFD analysis." *Combustion and Flame*, 229:111391, 2021. ISSN 0010-2180. doi: https://doi.org/10.1016/j.combustflame.2021.02.037. URL https://www.sciencedirect.com/science/article/pii/S0010218021001061.

[139] Meneveau, C. and Poinsot, T. "Stretching and quenching of flamelets in premixed turbulent combustion." *Combustion and Flame*, 86(4): 311–332, 1991. ISSN 0010-2180. doi: https://doi.org/10.1016/0010-2180(91)90126-V. URL https://www.sciencedirect.com/science/article/pii/001021809190126V.

[140] Goodwin, D.G., Moffat, H.K., and Speth, R.L. Cantera: An object-oriented software toolkit for chemical kinetics, thermodynamics, and transport processes, 2018.

[141] Bowman, C.T., Hanson, R.K., Davidson, D.F., Gardiner Jr., W.C., Lissianski, V., Smith, G.P., Golden, D.M., Frenklach, M., Wang, H., and Goldenberg, M. GRI-Mech version 3.0. http://www.me.berkeley.edu/gri_mech/. Accessed: 2023-03-19.

[142] Menter, F.R., Kuntz, M., and Langtry, R. "Ten years of industrial experience with the SST turbulence model." *Turbulence, heat and mass transfer*, 4(1):625–632, 2003.

[143] Meneveau, C. and Lund, T.S. "The dynamic Smagorinsky model and scale-dependent coefficients in the viscous range of turbulence." *Physics of fluids*, 9(12):3932–3934, 1997.

[144] Meloni, R., Chiarizia, N., Nassini, P. C., and Andreini, A. "E-POD investigations of turbulent premixed flame dynamics approaching lean blow-out conditions." *International Journal of Spray and Combustion Dynamics*, 15(1):51–69, 2023.

[145] Wang, H.P., Olson, S.J., Goldstein, R.J., and Eckert, E.R.G. "Flow Visualization in a Linear Turbine Cascade of High Performance Turbine Blades." *Journal of Turbomachinery*, 119(1):1–8, 01 1997.

ISSN 0889-504X. doi: 10.1115/1.2841006. URL `https://doi.org/10.1115/1.2841006`.

[146] Bacci, T. Comparison of experimental results with available correlations. Experimental characterization of external flow path across gas turbine nozzle guide vane, 2021.

[147] Humble, L.V., Lowdermilk, W.H., and Desmon, L.G. Measurements of average heat-transfer and friction coefficients for subsonic flow of air in smooth tubes at high surface and fluid temperatures. Technical report, 1951.